



**Calhoun: The NPS Institutional Archive**  
**DSpace Repository**

---

Theses and Dissertations

1. Thesis and Dissertation Collection, all items

---

1990-03

An assessment of data requirements for  
quasigeostrophic nowcasts and hindcasts of a  
mesoscale eddy field in the California Current  
System with application to fall transition

Johnson, John Edward.

Monterey, California. Naval Postgraduate School

---

<http://hdl.handle.net/10945/30696>

---

This publication is a work of the U.S. Government as defined in Title 17, United States Code, Section 101. Copyright protection is not available for this work in the United States.

*Downloaded from NPS Archive: Calhoun*



Calhoun is the Naval Postgraduate School's public access digital repository for research materials and institutional publications created by the NPS community. Calhoun is named for Professor of Mathematics Guy K. Calhoun, NPS's first appointed -- and published -- scholarly author.

**Dudley Knox Library / Naval Postgraduate School**  
**411 Dyer Road / 1 University Circle**  
**Monterey, California USA 93943**

<http://www.nps.edu/library>

# NAVAL POSTGRADUATE SCHOOL Monterey, California

AD-A231 394



## DISSERTATION

**S** DTIC  
ELECTE  
FEB 04 1991  
**E D**

An Assessment of Data Requirements for Quasi-geostrophic Nowcasts and Hindcasts of a Mesoscale Eddy Field in the California Current System with Application to Fall Transition

by

John Edward Johnson

March 1990

Dissertation Supervisor: C.N.K. Mooers

Approved for public release; distribution unlimited

91 2 01 036

**Best  
Available  
Copy**

UNCLASSIFIED

SECURITY CLASSIFICATION OF THIS PAGE

REPORT DOCUMENTATION PAGE				Form Approved OMB No 0704-0188	
1a REPORT SECURITY CLASSIFICATION <b>Unclassified</b>			1b RESTRICTIVE MARKINGS <b>None</b>		
2a SECURITY CLASSIFICATION AUTHORITY			3 DISTRIBUTION/AVAILABILITY OF REPORT <b>Approved for public release; distribution unlimited</b>		
2b DECLASSIFICATION/DOWNGRADING SCHEDULE					
4 PERFORMING ORGANIZATION REPORT NUMBER(S)			5 MONITORING ORGANIZATION REPORT NUMBER(S)		
6a NAME OF PERFORMING ORGANIZATION <b>Naval Postgraduate School Monterey, California</b>		6b OFFICE SYMBOL (If applicable) <b>68</b>	7a NAME OF MONITORING ORGANIZATION		
6c ADDRESS (City, State, and ZIP Code) <b>Naval Postgraduate School Monterey, California 93943-5008</b>			7b ADDRESS (City, State, and ZIP Code)		
8a NAME OF FUNDING/SPONSORING ORGANIZATION <b>Office of Naval Research</b>		8b OFFICE SYMBOL (If applicable) <b>(1120 PO)</b>	9 PROCUREMENT INSTRUMENT IDENTIFICATION NUMBER <b>N000146WR24027</b>		
8c ADDRESS (City, State, and ZIP Code) <b>Arlington, VA 22217</b>			10 SOURCE OF FUNDING NUMBERS		
			PROGRAM ELEMENT NO <b>61153N</b>	PROJECT NO <b>RR0310306</b>	TASK NO
					WORK UNIT ACCESSION NO
11 TITLE (Include Security Classification) <b>An Assessment of Data Requirements for Quasigeostrophic Nowcasts and Hindcasts of a Mesoscale Eddy Field in the California Current System (cont)</b>					
12 PERSONAL AUTHOR(S) <b>John Edward Johnson</b>					
13a TYPE OF REPORT <b>Dissertation</b>		13b TIME COVERED FROM _____ TO _____		14 DATE OF REPORT (Year, Month, Day) <b>90 March 29</b>	
15 PAGE COUNT <b>370</b>					
16 SUPPLEMENTARY NOTATION <b>The views expressed in this thesis are those of the author and do not reflect the official policy or position of the Department of Defense or the U.S. Government.</b>					
17 COSATI CODES			18 SUBJECT TERMS (Continue on reverse if necessary and identify by block number)		
FIELD	GROUP	SUB-GROUP	Mesoscale Ocean Models Fall Transition		
			Data Requirements AVHRR		
			California Current System GEOSAT Altimetry		
19 ABSTRACT (Continue on reverse if necessary and identify by block number)					
<p>An extensive Ocean Prediction Through Observation, Modeling, and Analysis (OPTOMA) domain, off Northern and Central California, was surveyed in November 1986, during OPTOMA 23. Surface dynamic height (SDH), sea surface temperature (SST), and other fields were mapped with a Gandin objective analysis (OA) model; stream function nowcasts and hindcasts of the mesoscale oceanic field were generated by a quasi-geostrophic (QG) model, initialized and updated with OA fields of dynamic topography.</p> <p>The westward propagation, at 5-to-10 km/day, of an anticyclone was the predominant mesoscale event; cyclonic features were quasi-stationary. Surface velocities, estimated from changes in SST patterns observed in pairs of satellite images, were consistent in direction with geostrophic surface velocities and ca. twice the magnitude, as expected from their</p>					
20 DISTRIBUTION/AVAILABILITY OF ABSTRACT <input checked="" type="checkbox"/> UNCLASSIFIED/UNLIMITED <input type="checkbox"/> SAME AS RPT <input type="checkbox"/> DTIC USERS			21 ABSTRACT SECURITY CLASSIFICATION <b>Unclassified</b>		
22a NAME OF RESPONSIBLE INDIVIDUAL <b>John Edward Johnson</b>			22b TELEPHONE (Include Area Code) <b>601-688-2561</b>		22c OFFICE SYMBOL <b>INO</b>



Block 11 continued. with Application to Fall Transition  
Block 19 continued. increased spatial resolution. Altimetric sea surface height (SSH) fields were consistent with SDH fields. A simulation of the GEOSAT sampling pattern reproduced the SDH field accurately using two ascending and four descending orbits. Hence, GEOSAT altimetry can be effective in mapping the mesoscale variability of the California Current System (CCS).

The impact of data upon QG nowcasts/hindcasts was evaluated by incorporating wind stress and bottom topography and subsampling an in situ data set. Ten-day hindcasts of the upper level stream function and the temperature at 100m (T100), derived from an empirical relation with the vertical derivative of the stream function, were compared with climatology, persistence, and a verification field. The optimal QG model configuration, for this case, was: interpolated boundary conditions, no bottom topography, and no wind stress curl forcing

The Generalized Digital Environmental Model (GDEM), the Navy standard climatology, had accurate averages and ranges of values, but it did not represent the mesoscale field. Because the mesoscale field did not change much over the ten-day period, persistence fields scored well. QG hindcasts were most sensitive to data density: the one-half subsampled fields scored well and the one-eighth fields were poor. Even in the latter case, the model filled data gaps and areas of cyclonic and anticyclonic activity were adequately delineated. Poorly initialized fields were recovered with good boundary condition updates; hindcasts using simulated GEOSAT and Sofar data located features accurately, but were noisy and had a range of values lower than the verification field. T100 fields extracted from the hindcasts were accurate.

The Fall Transition of 1986 in the CCS was a chronic event; winds favorable for upwelling fluctuated and diminished in late October, but occurred during short periods through December. A balance of alongshore pressure gradient and wind stress at Monterey shifted from maximum southward in late November to maximum northward two weeks later. The northward nearshore flow was observed in satellite imagery, SDH and SSH OA fields, and in QG hindcasts. An increase in SST at NDBC buoys and Granite Canyon was also consistent with the Fall Transition. Near surface warming, expected nearshore during the Transition, was observed to ca. 300 km offshore in OA and T100 fields.

Approved for public release; distribution unlimited

An Assessment of Data Requirements for Quasigeostrophic Nowcasts  
and Hindcasts of a Mesoscale Eddy Field in the California  
Current System with Application to Fall Transition

John Edward Johnson  
Commander, United States Navy  
B.S., United States Naval Academy, 1973  
M.S., Naval Postgraduate School, 1980

Submitted in partial fulfillment of the  
requirements for the degree of

DOCTOR OF PHILOSOPHY

from the

Naval Postgraduate School  
March 1990

Author

*John Edward Johnson*

Approved by:

*Christopher K. Moore*  
C.N.K. Mooers, Professor of  
Oceanography  
DISSERTATION SUPERVISOR

*M.L. Batteen*

M.L. Batteen, Associate Professor  
of Oceanography

*J.V. Sanders*  
J.V. Sanders, Associate Professor  
of Physics

Approved by:

*C.A. Collins*  
C. A. Collins, Chairman  
Department of Oceanography

Approved by:

*Harvey Shull*  
Provost/Academic Dean

Accession For

NTIS GRA&I

DTIC TAB

Unannounced

Justification

By

Distribution/

Availability Codes

Dist

Avail and/or  
Special

*A-1*



## Abstract

An extensive Ocean Prediction Through Observation, Modeling, and Analysis (OPTOMA) domain, off Northern and Central California, was surveyed in November 1986, during OPTOMA 23. Surface dynamic height (SDH), sea surface temperature (SST), and other fields were mapped with a Gandin objective analysis (OA) model; stream function nowcasts and hindcasts of the mesoscale oceanic field were generated by a quasigeostrophic (QG) model, initialized and updated with OA fields of dynamic topography.

The westward propagation, at 5-to-10 km/day, of an anticyclone was the predominant mesoscale event; cyclonic features were quasi-stationary. Surface velocities, estimated from changes in SST patterns observed in pairs of satellite images, were consistent in direction with geostrophic surface velocities and ca. twice the magnitude, as expected from their increased spatial resolution. Altimetric sea surface height (SSH) fields were consistent with SDH fields. A simulation of the GEOSAT sampling pattern reproduced the SDH field accurately using two ascending and four descending orbits. Hence, GEOSAT altimetry can be effective in mapping the mesoscale variability of the California Current System (CCS).

The impact of data upon QG nowcasts/hindcasts was evaluated by incorporating wind stress and bottom topography and subsampling an in situ data set. Ten-day hindcasts of the upper level stream function and the temperature at 100 m (T100), derived from an empirical relation with the vertical derivative of the stream function, were compared with climatology, persistence, and a verification field. The optimal QG model

configuration, for this case, was: interpolated boundary conditions, no bottom topography, and no wind stress curl forcing.

The Generalized Digital Environmental Model (GDEM), the Navy standard climatology, had accurate averages and ranges of values, but it was not representative of the mesoscale field. Because the mesoscale field did not change much over the ten-day period, persistence fields scored well. QG hindcasts were most sensitive to data density: the one-half subsampled fields scored well and the one-eighth fields were poor. Even in the latter case, the model filled data gaps and areas of cyclonic and anticyclonic activity were adequately delineated. Poorly initialized fields were recovered with good boundary condition updates; hindcasts using simulated GEOSAT and Sofar data located features accurately, but were noisy and had a range of values lower than the verification field. T100 fields extracted from the hindcasts were accurate.

The Fall Transition of 1986 in the CCS was a chronic event; winds favorable for upwelling fluctuated and diminished in late October, but occurred during short periods through December. A balance of alongshore pressure gradient and wind stress at Monterey shifted from maximum southward in late November to maximum northward two weeks later. The northward nearshore flow was observed in satellite imagery, SDH and SSH OA fields, and in QG hindcasts. An increase in SST at NDBC buoys and Granite Canyon was also consistent with the Fall Transition. Near surface warming, expected nearshore during the Transition, was observed to ca. 300 km offshore in OA and T100 fields.

## TABLE OF CONTENTS

I.	INTRODUCTION .....	1
A.	STATEMENT OF THE PROBLEM .....	1
B.	ELEMENTS OF THE PROBLEM .....	4
C.	RESEARCH PHASES .....	7
II.	BACKGROUND LITERATURE REVIEW .....	8
A.	CALIFORNIA CURRENT SYSTEM .....	8
	1. General .....	8
	2. Currents and Mean Flow .....	9
	3. Coastal Upwelling and Transition .....	12
	4. Mesoscale Activity .....	13
B.	OCEAN MODELS .....	18
	1. General .....	18
	2. Objective Analysis .....	18
	3. Quasigeostrophic Model .....	24
	4. Evaluation of Sampling Schemes .....	35
C.	REMOTE SENSING FROM SATELLITES .....	36
	1. General .....	36
	2. Vertical Coherence of Oceanic Fields .....	37
	3. Summary of IR Imagery .....	40
	4. Summary of Satellite Altimetry .....	43
D.	SUMMARY OF BACKGROUND LITERATURE REVIEW .....	46
III.	DATA ACQUISITION, PROCESSING, AND ANALYSIS .....	47
A.	INTRODUCTION .....	47
B.	ANALYSIS OF IN SITU DATA .....	49
	1. General .....	49
	2. Data Processing .....	53
	3. Extension of Shallow Fields to Depth .....	56
	4. Objective Analysis .....	57
	5. Evaluation of Model Output.....	64
	6. Inverse Distance OA .....	66

C.	WINDS, COASTAL, AND BUOY DATA .....	67
1.	General .....	67
2.	Wind Stress .....	70
3.	Bakun Upwelling Indices .....	71
4.	Granite Canyon SST .....	71
5.	Filtering .....	72
D.	CLIMATOLOGY .....	73
1.	General .....	73
2.	Generalized Digital Environmental Model .....	73
E.	ANALYSIS OF REMOTELY SENSED DATA .....	75
1.	AVHRR .....	75
2.	GEOSAT .....	82
F.	SUMMARY OF DATA ACQUISITION, PROCESSING, AND ANALYSIS .....	84
IV.	DESCRIPTION OF OPTOMA 23 FIELDS .....	87
A.	INTRODUCTION .....	87
1.	General .....	87
2.	GDEM Fields .....	87
3.	A Review of OPTOMA 18 and OPTOMA 22 .....	96
B.	ENVIRONMENTAL SUMMARIES .....	100
1.	Weather Summary .....	100
2.	Ocean Summary .....	101
C.	INDIVIDUAL SURVEYS AND TIME SERIES .....	101
1.	23P1 and P2 .....	101
2.	23P4 .....	105
3.	23P5 and P6 .....	107
4.	Time Series .....	110
5.	Mean Temperature-Depth Profiles .....	118
D.	SATELLITE FIELDS .....	123
1.	General Description .....	123
2.	MCSST .....	124
3.	Satellite Surface Vectors and Comparisons ..	126
4.	SSH .....	133

E.	VERTICAL COHERENCE AND AVERAGE VALUES .....	144
1.	Vertical Coherence .....	144
2.	Comparisons with OPTOMA Ensemble Averages ..	148
F.	SUMMARY AND DISCUSSION OF OPTOMA 23 FIELDS ....	150
V.	QUASIGEOSTROPHIC "NOWCASTS" AND "HINDCASTS" .....	154
A.	GENERAL .....	154
B.	FULL FIELD INITIALIZATIONS AND SENSITIVITY ANALYSIS .....	157
1.	Model Parameters .....	157
2.	Stratification .....	159
2.	Boundary Conditions .....	159
3.	Bottom Topography Effects.....	163
4.	Wind Forcing .....	167
C.	OPTIMAL CONFIGURATION HINDCASTS .....	172
1.	Optimal Hindcast Fields .....	172
2.	Diagnostics .....	182
3.	GEOSAT SSH Hindcast (86329) .....	186
4.	Temperature Extractions .....	186
D.	DATA SUBSAMPLING .....	193
1.	Subsampling Techniques .....	193
2.	Standard Subsampling .....	199
3.	Initialization and Boundary Condition Subsampling .....	203
4.	GEOSAT and Sofar Simulation .....	208
5.	Temperature Extraction from Subsampled Hindcasts .....	210
E.	SUMMARY AND DISCUSSION OF QG MODELING .....	218
VI.	THE FALL TRANSITION OF 1986 .....	220
A.	GENERAL .....	220
B.	COASTAL DATA PROCESSING .....	221
C.	DESCRIPTION OF THE TRANSITION .....	224
D.	CHANGES IN THE MESOSCALE FIELDS .....	234
E.	DISCUSSION OF THE FALL TRANSITION OF 1986 .....	245

VII. SUMMARY, CONCLUSIONS, AND RECOMMENDATIONS .....	256
A. SUMMARY .....	256
1. General .....	256
2. Synopsis .....	257
B. CONCLUSIONS .....	263
1. General .....	263
2. Observations .....	263
3. Modeling .....	267
4. Fall Transition .....	270
C. RECOMMENDATIONS .....	271
1. General .....	271
2. Observations .....	273
3. Modeling .....	274
APPENDIX A: LITERATURE REVIEW ON SATELLITE REMOTELY SENSED DATA .....	276
APPENDIX B: PRT-5 DATA .....	284
APPENDIX C: DRIFTING BUOY .....	290
APPENDIX D: PRT-5 DATA SUBSAMPLING .....	293
APPENDIX E: SATELLITE IMAGES .....	301
APPENDIX F: INVERSIONS .....	313
APPENDIX G: EXAMPLE OF QG MODEL INPUTS AND DYNAMIC DYNAMIC TOPOGRAPHY DATA SUBSAMPLING .....	318
APPENDIX H: COMNAVOCEANCOM INDEPENDENT MODEL REVIEWS PANEL (CIMREP) .....	329
LIST OF REFERENCES .....	331
INITIAL DISTRIBUTION LIST .....	344



## LIST OF TABLES

1.	AUTOCORRELATION RESULTS FOR DATA ENSEMBLES OPTOMA 23	....60
2.	AVHRR IMAGERY AVAILABLE DURING SELECTED OPTOMA SURVEYS	..77
3.	OPTOMA 23 IR IMAGERY	.....79
4.	AVHRR TEMPERATURE STATISTICS	.....81
5.	GDEM BASIC STATISTICS	.....91
6.	OA FORECAST COMPARISON FIGURES	.....122
7.	SUMMARY OF IR OBSERVATIONS DURING OPTOMA 23	.....125
8.	COMPARISONS OF SATELLITE MCSST AND IN SITU SST OA FIELDS	.....129
9.	SATELLITE SURFACE VECTORS AND SDH GEOSTROPHIC VELOCITIES	.....129
10.	COMPARISONS OF IN SITU, SDH, GEOSAT SSH, AND SIMULATED SSH	.....141
11.	COMPARISONS OF OPTOMA 23 FIELDS IN THE VERTICAL	.....145
12.	MATRIX OF QG MODEL RUNS	.....156
13.	NON-DIMENSIONAL $N_0/N(z)$ , $\sigma$ , QG MODEL VALUES	.....160
14.	FULL FIELD QG COMPARISONS	.....180
15.	SUBSAMPLED QG COMPARISONS	.....211
16.	QUALITATIVE SUMMARY OF COASTAL SIGNALS	.....251
17.	DRIFTING BUOY DATA	.....291
18.	PRT-5 OA DATA SUBSAMPLING COMPARISONS	.....299
19.	OPTOMA 23 INVERSIONS (STRENGTHS AND WIDTHS GREATER OR EQUAL TO 0.2° C AND 5 M RESPECTIVELY)	.....316
20.	EXAMPLE OF QG MODEL INPUTS	.....318
21.	SUBSAMPLED OA DH FIELDS (FOR QG MODEL INPUT) COMPARISONS	.....320

## LIST OF FIGURES

1.1	Block diagram of the components in this study .....	6
2.1	Area of interest, OPTOMA NOCAL and CENCAL domains .....	10
2.2	CalCOFI Station Spacing (Lynn et al., 1982) .....	14
3.1	A summary of data types and survey times from July through December 1986: Bakun indices at 36 N (top), Monterey sea level (middle), Granite Canyon SST (bottom), and OPTOMA 23 activity (right corner) .....	48
3.2	Flight tracks for OPTOMA 23, November 1986. NOCAL and CENCAL surveys were flown twice, boundary condition update once .....	51
3.3	Observation positions (dots), OPTOMA 23. Observation positions were spaced 30 km except for the boundary condition update flight (40 km) .....	52
3.4	OPTOMA 23 T-S relationship, derived from CTD observations (filled circle), compared with CalCOFI data (line 60 is open circle, line 70 is open square) and OPTOMA 13 data (filled square). The dashed lines are CalCOFI standard deviations from line 70 .....	56
3.5	PRT-5 SST autocorrelations; 900 point OPTOMA 23 ensemble (left), 150 point individual survey from day 86313 (right). Calculated correlation is solid line, 95% CI is shaded, fitted form is dashed .....	59
3.6	OA SDH fields, error fields, and observational positions superimposed on grid .....	63
3.7	PRT-5 OA fields. Inverse distance weighted method (left), Gandin method (center), and data distribution (right) .....	68
3.8	Positions of NDBC buoys, sea level stations, and Bakun upwelling index calculations .....	69
3.9	GEOSAT ascending (A) and descending (D) sub-orbital tracks off Central California (OPTOMA 23 domain is highlighted) .....	83
4.1	SDH (ref 450 m) and SST from in situ data, 9 and 19 November 1986 (Julian Dates 86313 and 86323) .....	88
4.2	SDH (referenced to 450 m) from GDEM climatology for the months of October, November, and December, and gridplot (Gridplot is valid for all GDEM fields) .....	89

4.3	Observed SST; SST, T50, and T100 from GDEM climatology for the month of November .....	92
4.4	Observed Z08; MLD, Z08, and Z10 from GDEM climatology for the month of November .....	93
4.5	November GDEM dynamic heights at surface, 50, 100, and 200 m (all referenced to 450 m). A weak cyclonic feature in the southeast corner of the domain is evident at depth ....	94
4.6	SDH (referenced at various levels) from GDEM climatology for the month of November. SDH from in situ data is for comparison .....	95
4.7	OPTOMA 18, 31 October - 2 November 1985, SDH, SST, T50, Z08 maps (Rienecker et al., 1987) .....	98
4.8	OPTOMA 22, 25 July - 5 August 1986, SDH, SST, T50, Z08 maps (Rienecker et al., 1987) .....	99
4.9	Synoptic surface weather depiction 9 and 10 November 1986 during OPTOMA 23P1 and P2 surveys. A two-day weather composite .....	103
4.10	SDH, SST, T50, and Z08 OA fields from OPTOMA 23 P1 and P2 surveys .....	104
4.11	Example of cold dome associated with cyclonic feature, center of surface expression and 70 dyn cm contour marked, along track A-B and E-F during OPTOMA 23P2 (Johnson et al., 1988) .....	106
4.12	Synoptic surface weather depiction 16 and 17 November 1986 when OPTOMA 23P4 was in progress .....	108
4.13	SDH, SST, T50, and Z08 OA fields from OPTOMA 23 P4 survey .....	109
4.14	Synoptic surface weather depiction 19 November 1986 when OPTOMA 23P5 and 23P6 were in progress .....	111
4.15	SDH, SST, T50, and Z08 OA fields from OPTOMA 23 P5 and 23P6 surveys .....	112
4.16	SDH OA error fields generated from composite of OPTOMA 23 data. Contour interval is 5%. The time window is 3 or 7 days; a 5 km/day westward phase speed was used.....	113
4.17	Time series of SDH contoured at 2 dyn cm. Cyclonic features are labelled C1 and C2; Anticyclones, AC1 and AC2 .....	114

4.18	Time series of SST contoured at 0.5 °C. Warm features (W) and cold (C) features are labelled .....	116
4.19	Time series of Z08 contoured at 10 m. SDH labels applied ....	117
4.20	SDH OA "forecast" experiment. The initial data fields from day 86313 were used in an OA routine with a 5 km/day westward phase propagation to forecast the field at day 86323 .....	119
4.21	SST OA "forecast" experiment. The initial data fields from day 86313 were used in an OA routine with a 5 km/day westward phase propagation to forecast the field at day 86323 .....	120
4.22	Z08 OA "forecast" experiment. The initial data fields from day 86313 were used in an OA routine with a 5 km/day westward phase propagation to forecast the field at day 86323 .....	121
4.23	SST, MCSST, and satellite grid and observations plot from image 86315N. The image was cloud-free. There was high correlation between the fields (0.85) and the RMS difference was 0.7 °C .....	126
4.24	SST, MCSST, and satellite grid and observations plot from image 86314A. The were mid and high-level clouds in the image. The correlation was low (0.22) and the RMS difference was 1.4 °C .....	127
4.25	Geostrophic surface velocity vectors on day 86314 at same scale as satellite image from day 86314 .....	130
4.26	SDH and SSH OA fields on day 86312; and SDH and SSH OA fields on day 86329. Contour interval is 2 cm .....	135
4.27	GEOSAT ERM orbital subtracks through the OPTOMA domain. Data are averaged alongtrack every second, or ca. 7 km. Ascending orbits (A) have a few, random gaps. Descending orbits (D) have large data gaps .....	136
4.28	SDH OA (Day 86312) and SSH OA error fields from GEOSAT ERM orbits through the OPTOMA domain on days 86312 and 86329. Contour interval is 5% .....	138

4.29	GEOSAT sampling experiment; survey pattern is same as the ERM on day 86312. SDH OA field on day 86312 is the sampled and verification field .....	140
4.30	GEOSAT sampling experiment; survey pattern consists of all six orbits through the OPTOMA domain. SDH OA field on day 86312 is the sampled and verification field .....	142
4.31	GEOSAT sampling experiment; survey pattern consists of all six orbits through the OPTOMA domain plus an ascending orbit to the west. SDH OA field on day 86312 is the sampled and verification field .....	143
4.32	Surface, 50, 100, 200, and 300 m dynamic heights (all referenced to 450 m) on day 86313 .....	146
4.33	Time series of correlations between SDH and SST during OPTOMA surveys (top) and SDH and Z08 (bottom). OPTOMA 23 values have been added to a figure from Rienecker et al. (1987) .....	147
4.34	Time series of SDH (top), SST (center), and Z08 (bottom) averaged during the individual OPTOMA surveys ( $\sigma$ are dashed). OPTOMA 23 was the last survey .....	149
5.1	Full field SDH and dynamic height (referenced to 450 m) QG model input fields at 50, 150 and 400 m for days 86313 (top), 86320 (middle), and 86323 (bottom) .....	158
5.2	QG hindcasts with persisted boundary conditions and OPTOMA 23 stratification. Four mesoscale features were identified (AC1 and AC2, C1 and C2). (The hindcast plots were scaled) .....	161
5.3	OPTOMA 23 hindcast from day 86313 to 86323; boundary conditions were interpolated and data from day 86320 were incorporated; there was no wind stress curl forcing or bottom topography (The plots were scaled and the contour interval changed on day 86320) .....	162
5.4	Bottom topography, contoured at 500 m intervals, from NAVOCEANO DBDB5 data base. The bottom topography in the OPTOMA domain slopes slightly, except for a small seamount in the southwest and the continental slope to the northeast .....	164
5.5	OA Bottom topography field from NAVOCEANO DBDB5 data base. Contour interval is 250 m .....	166

- 5.6 OPTOMA 23 hindcast, surface level, from day 86313 to 86323 using EOF extension, and incorporating bottom topography; boundary conditions were interpolated; there was no wind stress curl forcing. (The hindcast plots were scaled) .....168
- 5.7 The OPTOMA 23 domain with MBL gridpoints (x), at 2.5 degree resolution, and NDBC buoy positions (dots). Wind stress curl was calculated at the northern gridpoint (N), the central (C), the southern (S), and area-averaged .....170
- 5.8 Wind stress curl in the OPTOMA 23 domain (north, central, southern and area-averaged) during the month of November 1986. OPTOMA 23 survey took place between 9 and 19 November .....171
- 5.9 OPTOMA 23 hindcast, surface level, from day 86313 to 86323. Wind stress curl forcing was provided from values calculated at the center grid point. (The hindcast plots were scaled) .....173
- 5.10 QG optimal hindcast: OPTOMA 23 stratification, initialization at three levels (extended by EOF), interpolated boundary conditions, no bottom topography, and no wind stress curl forcing. (The hindcast plots were scaled) .....174
- 5.11 Hindcast from day 86313 to 86323 initialized with GDEM. The upper three levels were extended to the lower three by EOF's; boundary conditions were persisted; there was no wind stress curl forcing or bottom topography. The southern feature is cyclonic. (The hindcast plots were scaled) .....176
- 5.12 Correlation (left) and RMSN (right) for boundary condition (BC) variations: interpolated BC's between days 86313 and 86323 (solid), a BC update on day 86320 (dash), persisted BC's with data from 86313, 86320, and 86323 (dot). For comparison, persistence (chain dot), and climatology (chain dash) were added .....177
- 5.13 Correlation (left) and RMSN (right) for wind stress curl forcing (stress) and bottom topography (topo) variations: center gridstress (solid), no stress (dash), average stress (dot), center stress with topo (chain dot), and the optimal case of no stress and no topo (chain dash) .....178

5.14	Correlation (left) and RMSN (right) for BC, stress, and topo variations: the optimal case of no stress and no topo (solid), center grid stress and topo (dash), no stress but topo included (dot), persisted BC's (chain dot), and data on days 86313 and 86323 only (chain dash) .....	179
5.15	Area-integrated thermal and relative vorticity (Z) and kinetic energy (NRG) (left) and potential vorticity (Q) (right). Level one values and total, over all six levels .....	183
5.16	Area-integrated thermal and relative vorticity (Z) and kinetic energy (NRG) (left) and potential vorticity (Q) (right). Level two values and total, over all six levels .....	184
5.17	Area-integrated thermal and relative vorticity (Z) and kinetic energy (NRG) (left) and potential vorticity (Q) (right). Level three values and total, over all six levels .....	185
5.18	QG hindcast from day 86323 to day 86329, a GEOSAT 17-day ERM; no wind stress curl or bottom topography forcing was incorporated. (The hindcast plots were scaled) .....	187
5.19	T100 OA (verification) and QG-derived fields on days 86313 and 86323. The in situ method of Glenn and Robinson (1989) was used to determine T from $\psi$ .....	190
5.20	T100 OA (verification) and QG-derived fields on days 86313 and 86323. The vertical derivative method was used to determine T from $\delta\psi/\delta z$ .....	191
5.21	T100 86323 minus T100 86313 (verification, and QG-derived fields). The in situ method (left) does not reproduce the verification field as well as the vertical derivative method (right) .....	192
5.22	Full and randomly subsampled observations positions (dots) and grid plots (crosses) for day 86313. Full field is made up of ca. 120 observations. The other days are qualitatively similar .....	194
5.23	OA dynamic height fields (left to right, surface, 50, 150, and 400 m ) from one-half (top), one-quarter (middle), and one-eighth (bottom) random subsamples of data on day 86313 .....	196

5.24	OA dynamic height fields (left to right, surface, 50, 150, and 400 m) from one-half (top), one-quarter (middle), and one-eighth (bottom) random subsamples of data on day 86320 .....	197
5.25	OA dynamic height fields (left to right, surface, 50, 150, and 400 m) from one-half (top), one-quarter (middle), and one-eighth (bottom) random subsamples of data on day 86323 .....	198
5.26	QG ten-day hindcasts using the optimal model configuration with one-half day subsampled initialization (day 86313) and boundary condition updates (days 86320 and 86323). The mesoscale field was reproduced well. (The hindcasts were scaled) .....	200
5.27	QG ten-day hindcasts using the optimal model configuration with one-quarter day subsampled initialization (day 86313) and boundary condition updates (days 86320 and 86323). The mesoscale field was reproduced well. (The hindcasts were scaled) .....	201
5.28	QG ten-day hindcasts using the optimal model configuration with one-quarter day subsampled initialization (day 86313) and boundary condition updates (days 86320 and 86323). The mesoscale field was reproduced poorly; however, the QG model accurately delineated the cyclonic and anticyclonic zones accurately. (The hindcasts were scaled) .....	202
5.29	Correlation (left) and RMSN (right) for standard subsampled hindcasts. Full field (solid), one-half field (dashed), one-quarter (dot), and one-eighth (chain dot) .....	204
5.30	QG ten-day hindcasts using the optimal model configuration with one-half subsampled initialization (day 86313) and full boundary condition updates (days 86320 and 86323). The mesoscale field was reproduced well .....	205
5.31	QG ten-day hindcasts using the optimal model configuration with one-quarter subsampled initialization (day 86313) and full boundary condition updates (days 86320 and 86323). The mesoscale field was reproduced fairly well .....	206
5.32	QG ten-day hindcasts using the optimal model configuration with one-eighth subsampled initialization (day 86313) and full boundary condition updates (days 86320 and 86323). The mesoscale field was reproduced poorly; however, the QG model filled data gaps and delineated the cyclonic and anticyclonic zones .....	207



- 5.33 Correlation (left) and RMSN (right) for poor initialization and full boundary condition subsampled hindcasts. Full field (solid), one-half field (dashed), one-quarter (dot), and one-eighth (chain dot) .....209
- 5.34 QG ten-day hindcasts using the optimal model configuration initialized with level one data and climatology at depth (day 86313) to simulate GEOSAT data. Boundary conditions were interpolated to GEOSAT simulated data on day 86323. Features in the mesoscale field were well located; the range of values was reduced and the fields are noisier .....212
- 5.35 QG ten-day hindcasts using the optimal model configuration initialized with level one data and climatology at depth (day 86313) to simulate GEOSAT data. Boundary conditions were interpolated to full fields on day 86323 .....213
- 5.36 QG ten-day hindcasts simulating Sofar data using the optimal model configuration initialized with level two data (day 86313) and climatology in the upper and lower levels .....214
- 5.37 QG ten-day hindcasts simulating Sofar data using the optimal model configuration initialized with level two data (day 86313) and climatology in the upper and lower levels and boundary conditions updated by full fields (day 86323) .....215
- 5.38 T100 OA (verification) and QG-derived fields on days 86313 and 86323 using one-half subsampled fields. The vertical derivative method was used to determine T from  $\delta\psi/\delta z$  .....216
- 5.39 Correlation (left) and RMSN (right) for T100 extractions on days 86313 and 86323 from standard subsampled hindcasts. Full field (solid), one-half field (dash), one-quarter (dot), and one-eighth (chain dot) .....217
- 6.1 Gridpoints for MBL winds (X) and the positions of the six NDBC moored buoys (circles). Time series of wind stress were analyzed at grids labelled 1 through 5. Bakun indices were calculated at 33, 36, 39, and 42 N (squares) .....223
- 6.2 1986 daily (vertical bars) and weekly average (short horizontal bars) Bakun upwelling indices at 39 N (top) and 36 N (bottom). Positive values indicate offshore transport .....225
- 6.3 Daily Bakun upwelling indices at 33 N (solid), 36 N (chain dash), 39 N (dash), and 42 N (chain dot) from 14 October to 14 December 1986. Four strong upwelling episodes occur near the time of transition: November 7th, November 23rd, December 1st, and December 9th .....226

- 6.4 Low pass filtered wind vectors from 14 October to 14 December 1986. The scale is in m/s and the vector is towards the direction the wind is blowing; direction has not been rotated. The vertical lines identify the four episodes of winds favorable for upwelling .....227
- 6.5 Low pass filtered hourly alongshore wind stress (dynes/cm<sup>2</sup>), top, and low pass filtered hourly cross-shore wind stress, bottom, calculated from NDBC 10 m winds at the four northern buoys from 14 October to 14 December 1986. Buoy 46014 is the solid line; 46013, dotted; 46026 dashed; and, 46012, chain .....229
- 6.6 Hydrostatically adjusted low pass filtered hourly sea level deviations from 14 October to 14 December 1986. The solid line is the northern-most station, Crescent City; the dotted line, Point Reyes; the dashed line, San Francisco; the chain-dot, Monterey; and the chain-dash is Port San Luis .....230
- 6.7 Low pass filtered hourly SST from the northern three NDBC buoys (top) and the southern three NDBC buoys plus Granite Canyon daily SST (bottom) from 14 October to 14 December 1986 .....231
- 6.8 CTD and XBT positions during the two R/V POINT SUR surveys in November 1986. A-A' identifies the seven XBT's in the offshore group; B-B', the three CTD's in the "off-filament" group .....235
- 6.9 OPTOMA 23 fields at the beginning of the survey, 9 November (left), and at the end of the survey, 19 November (right). Surface dynamic height referenced to 450 m and contoured at 2 dyn cm intervals .....237
- 6.10 OA fields off Monterey Bay on 16 November 1986. SDH (top) is referenced to 450 m and contoured at one dyn cm. SST (bottom) is contoured at 0.25 °C. The crosses are data from the R/V POINT SUR; the dots are data from OPTOMA 23P3; OPTOMA 23P4 data were also used .....238
- 6.11 OA fields off Monterey Bay on 16 November 1986. T200 (top) is contoured at 0.25 °C. Salinity at 200 m (bottom) is contoured at one PPT. The crosses are data from the R/V POINT SUR; the dots are data from OPTOMA 23P3; OPTOMA 23P4 data were also used .....239

6.12	OPTOMA 23 difference fields calculated by subtracting fields on 9 November from the same fields observed on 19 November. SST and T50 are contoured at 0.2 °C intervals, T200 at 0.05 °C and Z08 at 10 m .....	241
6.13	R/V POINT SUR CTD and XBT temperature (left) and salinity (right) average differences (solid lines) and one standard deviation (dashed lines) calculated from positions (17) common to the surveys .....	243
6.14	$\Delta T$ from the northern line perpendicular to the coast at Monterey, group A XBT's (left), and $\Delta T$ and salinity difference (right) from the observations off the cool filament, group B CTD's .....	244
6.15	SDH and SSH OA fields from Julian date 86312 and 86329 (8 and 25 November 1986). The SDH field on day 86329 is generated from data on days 86321 and 86323. The contour interval is 2 dyn cm (or cm) .....	247
6.16	The balance of alongshore PGF and wind stress forces at Monterey Bay, from 1 July to 31 December 1986. In October and November, they both were southward. Near 2 December, the PGF became northward .....	253
A.1	A definition sketch for the altimetric measurement of sea height (Calman, 1987) .....	282
B.1	PRT-5 (solid) and gradient (dash) versus elapsed time of flight for OPTOMA 23 P1 survey. This plot is similar to that from other surveys .....	285
B.2	OA of SST (PRT-5) for days 86313, 86320, and 86323. The grid spacing is 20 km. The high gradients noted in figure B.1 have been smoothed by the OA procedure .....	288
B.3	Objective analysis of difference field (PRT-AXBT) 86313, 86320, and 86323 .....	289
C.1	Buoy track from 18 November to 6 December 1986 superimposed upon SST and SDH fields with central date of 18 November .....	292
D.1	PRT-5 data distribution using randomly selected observations. The alternate method had more evenly distributed data and the "smart" method concentrated observations near features .....	294

D.2	OA (Gandin) PRT-5 fields. Alternate (top), random (middle), and smart (bottom) fields. Contour interval is 0.2 °C .....	295
D.3	OA (Inverse distance) PRT-5 fields. Alternate (top), random (middle), and smart (bottom) fields. Contour interval is 0.2 °C. No error estimate is available .....	296
D.4	OA (Gandin) error fields for PRT-5 data. Alternate (top), random (middle), and smart (bottom) fields. Contour interval is 5% .....	298
E.1	AVHRR IR image from NOAA-10, channel 4, of OPTOMA domain on Julian Day 86314 at 16:23 GMT .....	301
E.2	AVHRR IR image from NOAA-9, channel 4, of OPTOMA domain on Julian Day 86314 at 21:55 GMT. Land is masked white .....	302
E.3	AVHRR IR image from NOAA-9, channel 4, of OPTOMA domain on Julian Day 86315 at 12:03 GMT. Land is masked white .....	303
E.4	AVHRR IR image from NOAA-9, channel 4, of OPTOMA domain on Julian Day 86315 at 21:45 GMT .....	304
E.5	AVHRR IR image from NOAA-9, channel 4, of OPTOMA domain on Julian Day 86319 at 22:42 GMT .....	305
E.6	AVHRR IR image from NOAA-9, channel 4, of OPTOMA domain on Julian Day 86321 at 22:21 GMT .....	306
E.7	AVHRR IR image from NOAA-9, channel 4, of OPTOMA domain on Julian Day 86323 at 21:59 GMT .....	307
E.8	AVHRR IR image from NOAA-9, channel 4, of OPTOMA domain on Julian Day 86325 at 11:57 GMT. Land is masked white .....	308
E.9	Surface velocity vectors superimposed on channel 4 IR image from day 86315 (12:03 GMT). Vectors were calculated from day 86314 (16:23 GMT). $\Delta t$ is ca. 20 hours. 10 cm/s scale in upper left corner. Land is masked white .....	309
E.10	Surface velocity vectors superimposed on channel 4 IR image from day 86315 (21:45 GMT). Vectors were calculated from day 86314 (16:23 GMT). $\Delta t$ is ca. 29 hours. 10 cm/s scale in upper right corner .....	310
E.11	Surface velocity vectors superimposed on channel 4 IR image from day 86315 (12:03 GMT). Vectors were calculated from day 86314 (21:55 GMT). $\Delta t$ is ca. 14 hours. 10 cm/s scale in upper left corner. Land is masked white .....	311

- E.12 Surface velocity vectors superimposed on channel 4 IR image from day 86315 (21:45 GMT). Vectors were calculated from day 86315 (12:03 GMT).  $\Delta t$  is ca. 10 hours. 10 cm/s scale in upper left corner .....312
- F.1 Inversions (marked by X). OPTOMA 23P1 and P2 (left); 23P4 (center); 23P5 and P6 (right). Isotherms from SST OA (solid) T50 (dashed) outline the cool filaments .....317

## Acknowledgements

Many people played an important role in the completion of this dissertation: I thank Dr Chris Mooers for his patience and guidance; I thank Dr Curt Collins and my committee members for their support.

Others contributed data or helped organize it: LCDR Ron Repper and the aircrew of VXN-8's Project BIRDSEYE aircraft collected the data; at NPS, Ms Melissa Ciandro (now at Scripps Satellite Ocean Facility) organized the AVHRR data (and helped with the survey), Mr Paul Whitmann edited the data, Dr Steve Ramp and Mr Mike McCann provided the data from the R/V Point Sur, and Mr Cal Dunlap provided the drifting buoy. From other sources and from other organizations: Dr Larry Breaker (NOAA) provided the Granite Canyon SST data; Mr Eric Meindel (NDBC), the moored buoy data; Mr Bob Rhodes (NORDA), the marine boundary layer winds from FNOC; Dr Mike Carron (NAVOCEANO), the GDEM climatology, and Dr Ziv Sirkes (INO/WHOI), the GEOSAT data.

I am most thankful for the support and faith from my family and from my friends, in the Navy, at NPS, and at INO.

## I. INTRODUCTION

### A. STATEMENT OF THE PROBLEM

Variable mesoscale ocean features (e.g., eddies, current meanders, and fronts) can have a considerable impact on marine operations, economics, and safety. Mesoscale features have horizontal spatial scales of order 50 to 500 km, vertical scales of order 100 to 1000 m, and temporal scales from days to months. Mesoscale features have been well documented on a world-wide basis (Robinson, 1983).

Regional eddy models (REM) and eddy-resolving global ocean circulation models (EGOCM) have been developed over the past five years for mesoscale ocean simulation and prediction. Generally, these evolved along the same lines as their numerical weather prediction counterparts, many of which are used operationally; however, almost all of the mesoscale ocean models are research models. Two major limiting factors preventing their operational implementation are the lack of data for initialization, updating of boundary conditions, and verification of results, and the expense of running full-basin eddy-resolving models.

Due to financial and logistical constraints, basin-wide in situ observation on an eddy scale is impractical. The data currently available for operational use are sparse, noisy, spatially and temporally irregular, and often restricted (i.e., classified for security). Usually, the fields required to initialize a model (e.g., dynamic topography) are not the same fields readily available in the operational data (e.g., temperature profiles). Also, the acquisition of oceanic data is expensive (e.g., a single airborne AXBT survey costs ca.

\$40,000; a P-3 on a ten hour flight uses fuel at the rate of \$3000/hr and may drop 100 AXBT's at a price of \$125/AXBT).

There will probably never be enough data from contemporary, conventional sources to make most models operational. Short-term solutions require extensive survey work in small domains, feature models which insert canonical structures of mesoscale features, or correlation of surface signals with fields at depth along with judicious use of AVHRR imagery and GEOSAT altimetry. The long-term solution to the problem of ocean prediction may come from EGCM's which link the ocean with the atmosphere and from the use of data from satellite and acoustic remote sensing systems. Both long- and short-term methodologies require evaluation and validation of the model system (i.e., the data stream, the assimilation scheme, the models, and the outputs).

The research emphasis for mesoscale ocean modeling has traditionally been on understanding physical processes. Initialized with climatology, edited historical data, or idealized states, the models have been used as research tools. On the other hand, the operational (i.e., Navy) mesoscale ocean modeling emphasis is on real-time feature location and nowcasting the sound speed field for anti-submarine warfare purposes (Peloquin, 1988). Due to this difference in emphasis, a successful evaluation and validation of a model by research modelers (the scientific process) does not necessarily guarantee success for operational modelers (the operational process), and vice versa.

Ideally, the scientific process of evaluation and validation first determines whether or not a model accurately characterizes mesoscale features and other permanent circulation features. Sensitivity case



studies, or Ocean Prediction Experiments (OPE), then follow to assess model system performance with different parameters and data inputs using synthetic ocean fields or real data. These case studies provide error estimates from which the decision as to whether or not to transition the model can be made.

The operational process of evaluation and validation, done typically after the scientific process, uses similar terminology but answers different questions. Among these are:

- (1) Does the model perform well with an operational data stream (i.e., what is the quantity of data needed to produce a "good" forecast),
- (2) How robust is the model (i.e., how does the model degrade if certain data are not available),
- (3) Does the model fit within the system of models being run, and
- (4) Is it better than what is currently available?

The Harvard Open Ocean Model (HOOM), a quasigeostrophic (QG) dynamic REM, is the first mesoscale ocean prediction model to undergo the transition from the research community to operational use (at the Naval Oceanographic Office, NAVOCEANO). The domain modeled at NAVOCEANO is in the Gulf Stream, roughly from Cape Hatteras to the New England Seamounts, and the version used is known as the Navy Operational Gulf Stream (NOGUSFS) model 1.0 (called GULFCAST at Harvard). Although the model does not provide the fields required for acoustic coupling directly, with proper initialization and boundary condition updating, it does identify and locate features. From this, together with feature models and climatology, the sound speed may be inferred.

Unfortunately, the HOOM was transitioned after a scientific evaluation of its performance, but before an operational evaluation. The model requires intensive resources and is limited in capability and physics; still, there is an implicit push to apply the model in many domains, such as the Northeast Pacific (NEPAC) and the Greenland-Iceland-Norwegian Sea (GINSEA), with little time for further evaluation and validation.

From the scientific standpoint, Robinson et al. (1986 and 1987) have demonstrated the accuracy of the HOOM in the California Current System (CCS) and Gulf Stream, respectively, under research conditions. However, its performance under realistic operational conditions is unknown and case studies with NOGUFs are in progress at the Naval Ocean Research and Development Activity (NORDA). Also unknown is how well the model behaves operationally in an eastern boundary current (e.g., the CCS) and whether or not feature models are required universally to compensate for the lack of data.

#### B. ELEMENTS OF THE PROBLEM

In this data sensitivity case study, mesoscale ocean fields in the CCS are analyzed with the Harvard Ocean Descriptive-Predictive System (ODPS), which consists of the data set, an objective analysis (OA) model for data assimilation, and the HOOM. Data are from the last survey in the Ocean Prediction Through Observation, Modeling and Analysis (OPTOMA) program, an extensive, four-year, joint NPS/Harvard project sponsored by ONR which sought to understand the mesoscale variability and dynamics of

the CCS and to determine the scientific limits to practical mesoscale ocean forecasting (Rienecker et al., 1984).

The OPTOMA 23 survey, which took place in November 1986, consisted of six synoptic survey flights (with a total of ca. 500 AXBT's) and two ship surveys (with ca. 50 XBT's and 50 CTD's). The OPTOMA 23 QG model domain is larger than previous OPTOMA QG experiments (by a factor of 5) and bottom topography and wind forcing are included in the model. Furthermore, the data set is unique in that the fall transition of the CCS (i.e., the onset of the Davidson Current) took place about the same time as the surveys.

The effect of various data types, sampling densities, and analysis techniques upon nowcasts and hindcasts in the OPTOMA domain are explored in this dissertation. This is an evaluation of the ODPS methodology; the mesoscale features are modeled with the QG model, which is initialized, updated, and verified with fields from an OA model. Although the input data fields have gaps in space and time, the model outputs provide a complete and internally consistent time series of ocean fields. These fields, together with sea level, coastal SST, and wind stress time series, are used to describe the thermal structure in the CCS during the Fall Transition period in 1986 (Figure 1.1).

The major question addressed by this research is: What is the sensitivity of the OA and QG models to the spatial resolution of the input surface and subsurface data? Additional questions are: does SST correlate with other surface and subsurface fields during the OPTOMA 23, and, thus, can infrared (IR) imagery help initialize the models?

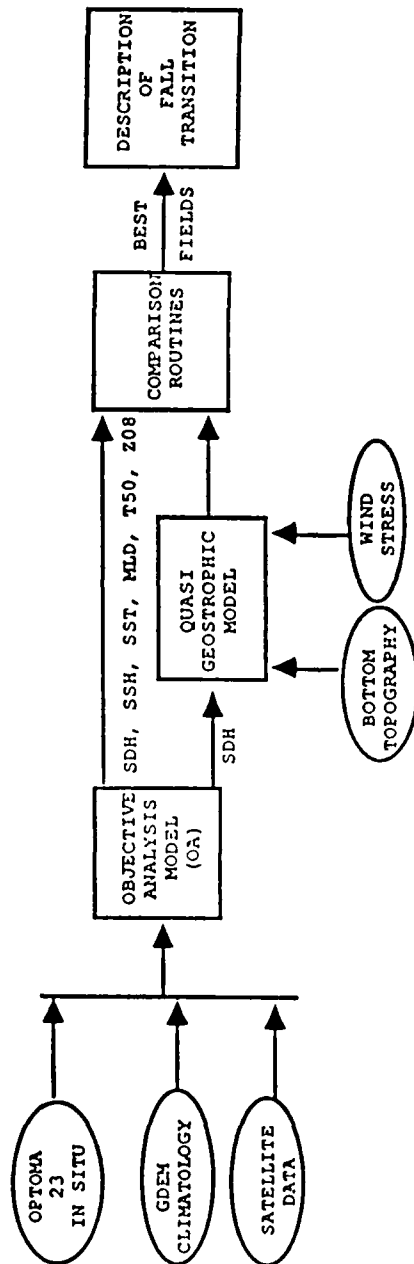


Figure 1.1 Block diagram of the components in this study.

### C. RESEARCH PHASES

Research was conducted in three phases:

- (1) nowcasts were made with statistical and dynamical models using in situ data and various initialization strategies,
- (2) a sensitivity analysis was conducted by varying input data resolution, and
- (3) the mesoscale fields were used in conjunction with nearshore data to describe the 1986 Fall Transition of the CCS.

In Chapter II, previous oceanographic studies along the Central California coast are reviewed in order to describe mesoscale activity from Cape Mendocino south to Point Conception and the techniques and procedures used to analyze this activity (e.g., in situ observations, numerical models, and remotely sensed data). In Chapter III, the procedures for processing and analyzing in situ and remotely sensed data are described. In Chapter IV, surface dynamic topography referenced to 450 m (SDH), sea surface temperature (SST), mixed layer depth (MLD), temperature at 50 m (T50), and the depth of the 8° C isotherm (Z08) are objectively analyzed and compared with each other and satellite data. The full fields are used to describe the offshore mesoscale activity in the domain from 9 to 19 November 1986. In Chapter V, QG nowcasts are generated with full and partial inputs of dynamic height (50 m, 150 m, and 400 m), wind stress, and bottom topography and sensitivity studies are analyzed. In Chapter VI, the offshore mesoscale fields are used in conjunction with an expanded analysis of coastal data to describe the 1986 Fall Transition of the CCS. In Chapter VII, results are summarized, conclusions are drawn, and recommendations are made.

## II. BACKGROUND STUDIES AND LITERATURE REVIEW

### A. CALIFORNIA CURRENT SYSTEM

#### 1. General

The OPTOMA program was an intensive study of the CCS off Central and Northern California, from the coast to ca. 400 km offshore. The general goals of OPTOMA were to understand the dynamics of the mesoscale eddies and jets in the CCS and to develop an ocean prediction system consisting of an observing system and four-dimensional data assimilation into dynamical models (Rienecker et al., 1987).

Starting in March 1982 with OPTOMA 1, an extensive series of 45 separate oceanographic survey cruises and flights were conducted by OPTOMA in the CCS from Cape Mendocino to Point Sur. The program was completed in November 1986 by OPTOMA 23, a survey designed and executed, as a part of this study, to investigate the scientific and operational limits to the ocean prediction system.

As a result of the rich data set, the mesoscale activity, as observed in satellite imagery and in situ data, was well-described (e.g., Rienecker et al., 1989, Rienecker et al., 1985, and Mooers and Robinson, 1984), and modeled (e.g., Robinson et al., 1986 and Rienecker et al., 1987). Other, unexpected results, such as descriptions of cool filaments (Flament et al., 1985) and of the El Nino signal off Central California in 1982-1983 (Rienecker et al., 1986), were obtained.

Most of the OPTOMA ship surveys were in one of two (300 km) sub-domains, Northern California (NOCAL) and Central California (CENCAL); aircraft surveys frequently covered both domains (Rienecker et al.,

1987). The ship surveys were quasi-synoptic; due to the slow ship speed, a few days were required to survey the domain. The aircraft surveys were synoptic.

The area of interest for OPTOMA 23 is a deep ocean (4200 m), 300 by 600 km rectangular domain parallel to and ca. 100 km off Northern California (Figure 2.1). The northern boundary of the domain is offshore of Cape Mendocino and south of the Mendocino Escarpment, which changes depth from approximately 3000 to 4200 m over a distance of 30 km.

## 2. Currents and Mean Flow

The domain is under the influence of the California Current System (CCS), an eastern boundary current with a high level of mesoscale activity which has been well-documented. In the upper ocean, four currents make up the system: the California Current, the California Undercurrent, the Davidson Current, and the Southern California Current (Hickey, 1979). The first three of these currents and the coastal upwelling jet influence the area of interest.

The California Current is part of the North Pacific Subtropical (anticyclonic) Gyre centered near Hawaii. The wind-driven, baroclinic geostrophic current is a continuation of the West Wind Drift in the North Pacific. After splitting, between 40 and 45 N, a portion flows southward along the coast and turns westward between 20 and 30 N becoming part of the North Equatorial Current (Sverdrup et al., 1942).

The current is weak, shallow (0 to 300 m), and broad. It has a mean southward flow of 5 to 10 cm/s with respect to a 500 m reference level (Hickey, 1979); most vertical shear is in the upper 200 m and horizontal variability at 500 m with respect to 1000 m is thought to be

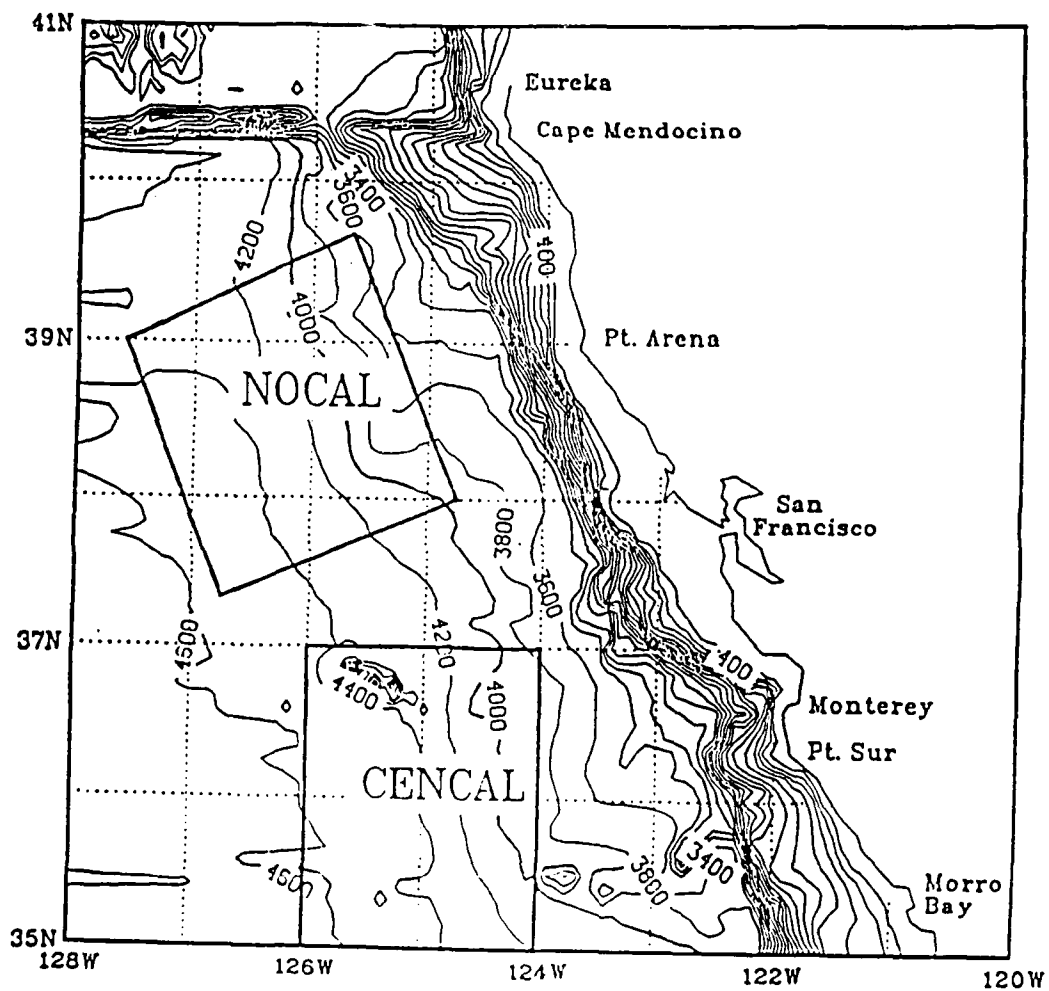


Figure 2.1 Area of interest, OPTOMA NOCAL and CENCAL domains.



negligible (Wyllie, 1966). The main core of the current is ca. 300 to 400 km offshore; its western boundary is ca. 900 km offshore. The water associated with the California Current is a mixture of cool Pacific Subarctic water with a near-surface salinity minimum and warmer North Pacific Central water from the west (Simpson et al., 1986).

The northward subsurface flow over the continental slope is the California Undercurrent, also called the Counter Current. Flow is maximum at 200 to 250 m in the summer and fall and is distinguishable from the California Current by its higher temperature and salinity. Fluctuation events in the flow, on time scales of a few days, appear to be correlated with fluctuations in the alongshore component of the local wind stress (Hickey, 1979).

The Davidson Current is the surface expression of the high speed poleward core of the California Undercurrent which rises from 200 m to the surface during the late fall and winter north of Point Conception coincident with the minimum monthly mean equatorward alongshore wind stress forcing. This flow has a jet-like structure and it extends through the water column over the continental slope. The Davidson Current is near the coast, confined roughly to the continental shelf and slope, inshore of the California Current axis.

An analysis of current meter data acquired by Smith et al. (1986) provides some insight on the magnitude of the barotropic component of the California Current. Preliminary results estimated the ratio of barotropic to first-mode baroclinic variance to be 0.5 in the OPTOMA domain and 2.0 a few hundred kilometers west (Rienecker et al., 1988). For comparison, in the MODE area, McWilliams (1976) statistically

obtained a barotropic kinetic energy to baroclinic first-mode kinetic energy ratio of 0.58.

### 3. Coastal Upwelling and Transitions

Coastal upwelling is an event-type process with a temporal scale of several days to a few weeks, an offshore scale of ca. 10 to 50 km, and a vertical scale of ca. 50 to 200 m. It is caused by offshore Ekman transport due to equatorward wind events which are predominant off California during the spring and summer. The cool water mass close to shore contrasts with the warmer water of the CCS and is easily distinguished in infrared (IR) imagery.

The upwelled water maintains its identity and provides a tracer of mesoscale flow as it is advected hundreds of kilometers offshore in narrow, ca. 40 km, filaments by jets associated with the mesoscale field. Offshore transport is ca.  $1 \times 10^6 \text{ m}^3/\text{s}$ , an order of magnitude greater than Ekman transport. The slower return flow, south of the offshore filament, is still recognizable although the water subsides as it flows around the meander (CTZ Group, 1988 and Flament et al. 1985).

Occurrence of the Davidson Current is associated with the seasonal weakening of equatorward winds favorable for upwelling and the onset of poleward winds. Theoretically, westward radiation of annual Rossby waves may be a relaxation mechanism from the upwelling regime (Mysak, 1983). Such waves have been observed in temperature fields at 300 m between Hawaii and San Francisco, and the West coast was identified as a probable source region by Kang and Maagard (1980) and White and Saur (1981).

The fall transition between California Current and Davidson Current regimes off Central California has been described in only a few studies. The 1978 Fall Transition off Cape San Martin, south of Point Sur, was indicated by a gradual, month-long rise in temperature from the surface to 200 m and an abrupt change from equatorward to poleward flow; there was a gradual rise in SST at Granite Canyon (2.5 °C). There was no evidence of local wind forcing (Wickham et al., 1987). The 1984 Fall Transition was indicated by a gradual, but sporadic, cessation of coastal upwelling, a gradual increase in SST at Granite Canyon (2.0 °C), an abrupt increase in SL along the coast from San Luis Obispo to Crescent City, and an increase in poleward flow off Half Moon Bay and Point Sur (Breaker and Bratkovich, 1988, and Chelton et al., 1987). The fall transitions are accompanied by a deepening of the Aleutian Low, near 50 N and 140 W, and zonal flow at 500 mb (Strub and James, 1988).

Some indicators (e.g., SL) changed abruptly, some (e.g., SST and coastal upwelling indices) changed over a period of months. Nearshore sources of data (e.g., coastal sea levels, SST's on moored buoys and current meters on the shelf) at a few locations were used to describe the transitions; these did not put the transition into context with offshore mesoscale activity or with cool filament activity.

#### 4. Mesoscale Activity

Much of the information about the CCS comes from the California Cooperative Fisheries Investigation (CalCOFI) program. Started in 1950, CalCOFI sampled the CCS along the California coast with a fixed, coarse grid of parallel lines spaced 65 km apart with offshore stations every 74 km (Figure 2.2). Temperature, salinity, density, and dissolved oxygen



data are available at 14 standard levels to 500 m. In 1969, the program was reduced to providing monthly coverage every third year mostly along cardinal lines, 195 km apart, off Southern California (Lynn et al., 1982).

Although the CalCOFI sampling scheme undersamples the mesoscale field, the data show evidence of meanders associated with semi-permanent eddies identified in later mesoscale-oriented surveys (e.g., Simpson et al. 1986 and Rienecker et al., 1987). Wyrski et al. (1976) showed that there was significant mesoscale activity in the CCS from calculations of the ratio of eddy kinetic energy to mean kinetic energy averaged over  $5^\circ$  squares. The data were from daily ship drift observations which had a time scale of 24 hours, a spatial scale of 400 km, and included the effects of wind. Off Central California, the ratio was 20 to one.

Complex meanders with wavelengths 300 to 500 km, eddy formations, and jets with speeds of 20 to 40 cm/s were first observed in satellite IR imagery in the CCS by Bernstein et al. (1977). The predominant wavelengths observed were consistent with the fastest growing, baroclinically unstable waves. Baroclinically unstable waves, with wavelengths of 60 to 200 km, were observed from Vancouver Island to Northern California in winter, summer and fall sequences of high resolution IR images (Emery and Mysak, 1980, and Ikeda and Emery, 1984). Strong vertical shear near 150 m, due to equatorward surface flow over the poleward California Undercurrent, was suggested as an apparent energy source.

To test this hypothesis, a baroclinically unstable vertical profile from Ikeda et al. (1984) with "event" surface speed maxima of 40

cm/s was used to initialize a primitive equation (PE) model with 9 km spacing, 10 vertical levels, and realistic topography of the greater OPTOMA domain (Batteen et al., 1988a). This experiment produced dipole eddies and filaments, while a flow more representative of seasonal averages, 5 cm/s, did not form eddies. Eddies were either stationary or moved to the west and southwest.

The following is a synopsis of mesoscale variability in the area of interest from other numerical and observational studies:

- (a) Numerous investigators, e.g., Hickey (1979), Broenkow (1982), Simpson et al. (1984), Koblinsky et al. (1984), and Huyer et al. (1984) have identified mesoscale features such as a semi-permanent cyclone south of the Mendocino Escarpment, an anticyclone ca. 100 km off the coast between San Francisco and Monterey, and a recurrent anticyclone 400 km southwest of Point Conception. Typical observations and common results are:
  - (1) length scales of about 100 to 200 km,
  - (2) time scales of about 100 days,
  - (3) a depth of influence, in some cases, to at least 1500 m (Koblinsky et al., 1984),
  - (4) near surface velocities of 20 to 50 cm/s,
  - (5) changes in dynamic height of 20 dyn cm,
  - (6) approximate geostrophic balance ( $Ro=0.1$ ), and
  - (7) preferred locations associated with forcing.
- (b) Current meters moored within the OPTOMA domain showed evidence of eddy-like features with diameters of 100 km, speeds at 175 m of ca. 10 cm/s, and high vertical coherence. These propagated to the southwest at ca. three km/day (Smith et al., 1986).
- (c) Narimousa and Maxworthy (1985) used a rotating tank to generate high speed jet-like plumes, standing waves, and semi-permanent eddies associated with modeled topography representative of Cape Mendocino and Point Arena.
- (d) Using a PE model with a straight coast, a flat bottom and steady climatological winds, Batteen et al. (1988b) showed that alongshore variation in wind stress plays a role in determining the location of eddy generation regions.

(e) Mooers and Robinson (1984) and Rienecker et al. (1985) observed eddies and jets in hydrographic data and IR imagery. Point Arena appeared to be the origin of cyclones which move offshore south of the jet. Typical parameters of the jets were:

- (1) speeds of 50 to 80 cm/s (referenced to 450 m),
- (2) widths of 50 to 60 km,
- (3) extensions in depth from the surface to 200 m,
- (4) an offshore extension of 160 to 300 km,
- (5) temperature gradients ca. 2 C/20 km, and
- (6) salinity gradients ca. 0.5 ppt/20 km.

(f) Using the H00M, Robinson et al. (1986) found that vorticity inputs from non-linear interactions were as important for eddy development as the relative vorticity term, and Rienecker and Mooers (1988) determined that both local instability processes and wind stress curl were important to the evolution of the mesoscale field off Northern California.

(g) In a review of all OPTOMA surveys, Rienecker and Mooers (1988) noted propagation in the eddy field which varied from one survey to another (e.g., to the west or south at two to five km/day). Simpson et al. (1986), on the other hand, saw no evidence of westward propagation out of the CCS in a domain to the south.

Some aspects of the mesoscale fields are consistent throughout these studies. Baroclinic instability and wind stress curl were important in forcing mesoscale activity and bottom topography played a role in determining their location. However, the observed and modeled direction of propagation of these features varied (e.g., stationary, west, southwest, and south).

Three zones of offshore mesoscale activity off San Francisco were identified by Simpson et al. (1986) from the seasonal range of surface dynamic height (SDH) and its standard deviation ( $\sigma$ ): coastal, transition (with principally anticyclonic activity 400 to 500 km offshore), and oceanic. Inshore of 200 km, in the coastal zone, there is a complex mean

current structure associated with the CCS and intermittent upwelling. Instantaneous flow is typified by jets, filaments, eddies, meanders and larger scale events (e.g., El Nino and Rossby waves).

## B. OCEAN MODELS

### 1. General

Model studies have several advantages over observational studies; a dynamical or statistical model can interpolate data gaps, temporal and spatial, and forecast. Complete, balanced fields at any level can be accessed at any time step. The major problems, some of which are inherent to numerical techniques, are: limited computer capability and resources, instability of small scale features, poor quality and small quantity of data inputs, complications with data assimilation, and incomplete physics.

The pair of ocean models utilized in this research are a part of the Ocean Descriptive-Predictive System (ODPS) used by OPTOMA. ODPS includes an observational network, a statistical model (i.e., objective analysis), and a dynamical model (i.e., the quasigeostrophic HOOM). ODPS has been used in the CCS for several years.

### 2. Objective Analysis

#### a. General

Initializing the model with observed data generally requires gridding in space and time of typically irregular and asynoptic data. There are a number of Objective Analysis (OA) techniques available for this task. The ODPS OA is the Gandin method introduced to oceanographic



applications by Bretherton et al. (1976) and used, for example, in POLYMODE by Carter and Robinson (1981) and Robinson and Leslie (1985).

#### b. Model Parameters

The method assumes the measurements,  $\Psi_i$ , which could be SST or any other scalar, taken at  $n$  observation points  $p_i(x,y,t)$ , are composed of the true value of the scalar field,  $\theta_i$ , and a random error,  $\epsilon_i$ . The error is not systematic; it is from sampling or instrumental noise. Error is uncorrelated with the true field,  $\overline{\epsilon_i \theta_i} = 0$ , and  $\overline{\epsilon_i \epsilon_j} = E\delta_{ij}$ , where  $E$  is the error variance.

The least squares optimum linear estimator of  $\theta_i$ ,  $\theta_p$ , is:

$$\theta_p = \sum_{i=1}^N C_{pi} \left( \sum_{j=1}^N A_{ij}^{-1} \Psi_{ij} \right) \quad (\text{equation 2.1})$$

where  $A_{ij}^{-1}$  is the inverse of the covariance matrix,  $\overline{\Psi_i \Psi_j}$ , and  $C_{pi}$  is the covariance between the estimated value and the  $i^{\text{th}}$  observation,  $\overline{\theta_p \Psi_i}$ .

The correlation function, the radius of influence (spatial and temporal), the maximum number of data points used at each grid point, and the error value (mean square noise level as a fraction of variance) are unique to each analyzed data set and the mapping has varying degrees of sensitivity to each parameter. Additionally, the mean

or a trend can be removed and the output can be smoothed by a Shapiro filter to remove small scale features.

Of the input parameters, only the error value is carried through the OA calculations. The others determine which data points will be used at each grid point. Selection of a proper radius of influence is crucial in sparse data sets where a choice between recently observed, but physically distant data, and old, but nearby data, must often be resolved.

#### c. Autocorrelation

The autocorrelation function, used to compute the correlation between an interpolation point and an observation, is calculated from the data set. The data are assumed to be isotropic, which is a valid assumption away from the cool filaments and upwelling front near the coast. Data pairs are binned according to the distance between the pair; the product of each data pair is summed for each bin; the sum is normalized by the number of elements in each bin and the variance; finally, a least squares fit of the following function to the calculated correlation function is made over a minimum of three bins, to include the first zero crossing and the first bin (from zero to 1.0 km):

$$C(r) = Co(1-(r/a)^2)\exp(-(r/b)^2) \quad \text{for } r \neq 0,$$

$$C(0) = Co(1+\epsilon) \quad \text{for } r=0 \quad (\text{equation 2.2}),$$

where  $C(r)$  is the fitted correlation value,  $r$  is the range,  $Co$  is the maximum correlation at zero lag,  $\epsilon$  is the ratio of noise to signal

variance, and  $a$  and  $b$  are the calculated coefficients. Equation 2.2 smoothly, and usually accurately, portrays most calculated correlation functions, without the spikiness often observed in the latter, and ensures positive correlations within the range of the first zero crossing.

The OA routine uses the correlation function to determine the set of observations which will influence each interpolation point and the elements of the autocorrelation matrix,  $A_{ij}$ . To help ensure that  $A_{ij}$  is easily inverted, the OA routine biases the matrix towards diagonal dominance by limiting the size of the off-diagonal values, by ensuring no observations are too close to each other, and by adding the noise variance to the diagonal elements.

#### d. Filtering and Detrending

A Shapiro filter is used to reduce small scale features (Shapiro, 1970); this linear filter acts as a horizontal diffusion term. It is a low pass filter with a sharp roll off; maximum damping occurs at short wavelengths with little or no damping at long ones. The Shapiro filter removes small scale noise from the scalar field after the objective analysis is performed. It has no impact upon the error field. A detrending routine calculates a plane which best fits the data set. This plane provides the analysis value at gridpoints where there are no observations within the spatial and temporal windows.

#### e. Other Parameters

The spatial and temporal windows, and the number of data points allowed to influence each gridpoint, determine the available set

of observations at each gridpoint. If a phase propagation is used, the observation positions are moved prior to determining if the observation fits within the radius of influence. Those observations within the radius of influence and temporal window with the highest correlations are used in calculating the value of the field at the gridpoint.

A typical spatial window for the OPTOMA data sets is 75 km; temporal windows vary depending upon the data set, but three to seven days is typical. The number of data points influencing each gridpoint can be varied from two to 15. As the number decreases, apparent small scale noise is introduced and the error estimate increases. As the number increases, the small scale noise disappears, the noise estimate decreases, but the time required to invert the larger matrix increases. For practical purposes, the number of data points influencing each gridpoint was chosen to be five to seven.

When there are no observations within the spatial and temporal windows for a gridpoint provided by a sparse data set, the value assigned to the gridpoint is taken from the plane calculated in the detrending routine. Often, this plane accounts for little of the observed variance in the signal, and the error estimate at that gridpoint is 100%.

#### f. Weaknesses of the OA

Errors in the data arise from instrumental and geophysical noise. These errors can be introduced into the OA model output, and the results can be further affected by the data sampling scheme and imperfect knowledge of the statistics. OA has no dynamics; it is strictly an analysis scheme.

This scheme can also produce space-time dependent, phase propagated statistical forecasts using a single, fixed phase speed. For asynoptic surveys, the observations are moved a distance determined by the phase speed and the difference between the observation time and the central time of the analysis. This could lead to inaccuracies for asynoptic surveys in areas of differential advection. For example, Legeckis and Bane (1983) tried to correlate AVHRR imagery and airborne data from a Precision Radiometric Thermometer (PRT). The AVHRR imagery was copied at night and the aircraft flew the following day, some 6 to 10 hours later. Unaccounted for advection resulted in a 4 to 6 km misalignment of the data sets and low correlations.

For several reasons, the OA field may show little resemblance to the "true" field at a particular time, even if the data are truly synoptic. First, selection of a particular grid scale restricts the scale of variability, and thus dynamical processes, which can be resolved; features of  $2\Delta x$  size and smaller are not resolved and sub-grid scale processes appear as aliased noise. Second, tight gradients, which can be drawn accurately by subjective (hand) analysis, are spread out over many gridpoints, especially when the correlation function zero-crossings are large. This effect can be reduced somewhat near fronts if the selection of observations influencing a gridpoint is restricted to those observations in similar water masses. Third, the OA features are weaker than the observed values (i.e., the variance is lower) as the OA acts as a low pass filter. Finally, the OA scheme in its 2-D form must be applied to the data at individual levels; there is

no guarantee of vertical consistency or stability between OA fields throughout the water column without the use of a 3-D form of OA.

g. Alternative Schemes

The Naval Oceanography Command is replacing its Expanded Ocean Thermal System (EOTS) with a Gandin objective analysis scheme, the Optimum Thermal Interpolation System (OTIS). It is mathematically similar to the model used in ODPS; however, instead of detrending a plane from the data, OTIS uses climatology as a first guess field. Also, the correlation scales are based upon climatology, basin-dependent and much larger than the values used in the CCS; for example, the zonal scale is 200 to 250 km, the meridional scale is 500 to 750 km (Phoebus, 1988). Another technique which weighs the observations with the inverse of the distance between the gridpoint and observation is introduced in Chapter III.

3. Quasigeostrophic Model

a. The Quasigeostrophic Approximation

The quasigeostrophic (QG) approximation is derived from the non-linear equations of motion ( $u, v, w$ ), a thermal equation and the continuity equation with Boussinesq,  $\beta$ -plane and hydrostatic approximations. These equations are non-dimensionalized, expanded about a small parameter ( $\epsilon$ , the Rossby number) and separated by orders of approximation. The zero and first order approximations are:

Zero order

$$V_0 = \partial P_0 / \partial x$$

$$U_0 = -\partial P_0 / \partial y$$

$$\rho_0 = -\partial P_0 / \partial z$$

$$\partial U_0 / \partial x + \partial V_0 / \partial y = 0$$

$$W_0 = 0$$

First order

$$U_{0t} - V_1 - V_0 \beta Y = -\partial P_1 / \partial x$$

$$V_{0t} + U_1 + U_0 \beta Y = -\partial P_1 / \partial y$$

$$-\partial P_1 / \partial z - \rho_1 = 0$$

$$\partial U_1 / \partial x + \partial V_1 / \partial y + \partial W_1 / \partial z = 0$$

$$d_0/dt(\rho_0) - W_1 N^2 = 0$$

(equation 2.3),

where 0 and 1 indicate order of approximation, U, V, and W are velocities in the X, Y, and Z directions, P is pressure,  $\rho$  is density, N is the Brunt-Vaisala frequency, and  $d_0/dt$  is the material derivative with advection by zero order terms.

The diagnostic equations governing the zero order motion are in geostrophic and hydrostatic balance on an f-plane. The flow is horizontally non-divergent, and thus, there is no zero order vertical component of velocity. The zero order density field is prescribed; the first order density field is predicted. There is no wind or thermal forcing; mixing and diffusion are not incorporated.

The zero and first order equations are used to derive the governing equation in terms of the QG vorticity balance:

$$d_0/dt(\xi_0 + \partial/\partial z(1/N^2 \partial P_0/\partial z) + \beta Y) = F \quad (\text{equation 2.4}),$$

where  $\xi_0$  is the zero order relative (vertical) vorticity,  $\partial/\partial z(1/N^2 \partial P/\partial z)$  is the thermal vorticity introduced by density stratification,  $\beta Y$  is the planetary vorticity ( $Y$  is the north-south distance on the  $\beta$ -plane), and  $F$  includes effects of filtering, bottom drag, and wind stress curl, if they are incorporated.

Ignoring  $F$ , the left hand side of equation 2.4 can be expressed as:

$$\xi_t + \alpha J(\psi, \xi) + \Gamma^2 (\sigma \psi_z)_{zt} + \Gamma^2 \alpha J(\psi, (\sigma \psi_z)_z) + \beta \psi_x = 0$$

$$(A) \quad (B) \quad (C) \quad (D) \quad (E)$$

(equation 2.5)

where term (A) is the local rate of change of relative vorticity; (B), the advection of relative vorticity; (C), the local rate of change of thermal vorticity; (D), the advection of thermal vorticity; and, (E), the advection of planetary vorticity.



The process of non-dimensionalization introduces three ratios:  $\alpha$ ,  $\beta$ , and  $\Gamma^2$ .  $\alpha$ ,  $V_0 t/L$ , is the ratio of scaling time to the advective time scale;  $\beta$ ,  $\beta_0 L t$ , is the ratio of scaling time to the planetary wave time scale; and,  $\Gamma$ ,  $f_0 L / N H$ , is the ratio of the length scale,  $L$ , to the baroclinic Rossby radius of deformation.  $H$  is the thermocline depth scale;  $V_0$ , is the velocity scale;  $t$ , the time scale; and,  $f_0$ , the value of the Coriolis parameter.

QG phenomena cover a wide range of dynamic activity including Rossby wave propagation, barotropic and baroclinic instability, Rossby wave solitons, jets, and non-linear interactions. Since potential vorticity is conserved by equation 2.4, neglecting the effects of  $F$ , the direction of flow on surfaces of constant density is along contours of potential vorticity. The QG approximation is valid for mid-latitude interior flows over relatively flat topography (bottom slopes of order  $\varepsilon$  are allowed) in domains with a horizontal scale that is much greater than the vertical scale, but less than the planetary scale, a vertical scale which is ca. the basin depth, and a time scale greater than a day.

There are limitations in the use of a QG model: it lacks complete physics (e.g., higher order terms have been dropped and there is no thermodynamic term) and it assumes small amplitude topographical and interfacial displacements (e.g., outcropping of isopycnals is not allowed).

#### b. HOOM Specifications and Parameters

The HOOM requires initial and boundary conditions for each timestep. These are provided from objectively analyzed fields or feature models. Vorticity ( $\xi$ ) and streamfunction ( $\psi$ ) are initially specified throughout the model; at each timestep,  $\psi$  along the boundary and  $\xi$  at inflow points along the boundary are required. The model is integrated forward in time using an Adams-Bashforth finite differencing scheme (boundary conditions must subsequently be provided). Finite elements are used for horizontal derivatives, and finite differencing or collocation is used for vertical derivatives (Miller et al. 1983).

In past OPTOMA applications, vorticity at the boundaries was computed by using an objective analysis with an extra gridpoint at the edge rather than calculating a one-sided derivative (Rienecker and Mooers, 1989). Vorticity information on the boundary cannot propagate into the interior when the stream function is tangential to the boundary and noise is introduced when this occurs (Robinson and Haidvogel, 1980).

Initialization and boundary condition strategies cover a wide range of options and remain an active issue in attempts to make the HOOM operational. Generally, the term "hindcast" describes use of the model when the boundary conditions, and possibly interior data, are known, persisted from one input (known) field to another, or linearly interpolated between input fields. If new observations are provided for the boundary conditions, the model "nowcasts" the interior. If the boundary conditions are extrapolated or otherwise forecast, it "forecasts" the interior.

The model has a rigid lid. The wind forced layer at the surface,  $z=0$ , is horizontally divergent due to  $\text{curl}_z \tau$ . Vertical velocity in the top layer is calculated at each time step at the top ( $z=0$ ) by the following:

$$w^{QG} + w^E = 0$$

$$\text{where, } w^{QG} = \epsilon V_0 H D^{-1} w_1 \text{ and } w^E = k \{ \bar{\nabla} \times \bar{\tau} / \rho f \} \quad (\text{equation 2.6}).$$

At the bottom ( $z=-1$ ), there is a no slip boundary condition and no normal flow through the bottom. Net transport is to the left of geostrophic flow. Vertical velocity:

$$w = U \cdot \nabla B \quad (\text{equation 2.7})$$

where  $B(x,y)$  is the bottom topography. Bottom topography within QG constraints must have a slope less than  $\epsilon$  (Robinson and Walstad, 1987).

Vertical velocity forces changes in  $\rho$  through the relationship:

$$\Gamma^2 \{ D(\sigma \partial \psi / \partial z) / Dt \} = -w \quad (\text{equation 2.8})$$

and the QG streamfunction is related to the dynamic pressure perturbation,  $P'$ , by:

$$\psi/V_0 L = P' \quad (\text{equation 2.9}).$$

Enstrophy cascades from small wavenumbers to large wavenumbers due to numerical techniques used in the model. If it accumulates, numerical instability results. There is no horizontal or vertical diffusion term in this model; the same Shapiro filter used in the OA is applied to remove the small scale vorticity which may cause instability. With better initialization, and better boundary conditions, use of the filter can be reduced (Robinson et al., 1986).

The HOOM is portable in that it only requires bottom topography and mean stratification in a new domain, as long as the assumptions made in the QG approximation remain valid (Robinson and Walstad, 1987a). With good initialization and boundary conditions, the model can be updated with partial or sparse data to perform as a data interpolation scheme (Robinson and Leslie, 1985).

#### c. HOOM Usage

Robinson and Haidvogel (1980) simulated oceanic conditions in the POLYMODE area using a barotropic version of the HOOM. By introducing errors, gaps in the data, and noise into the initial and boundary conditions, they noted that the forecast error was sensitive to the frequency of updating boundary streamfunction data, but not as sensitive to vorticity error. After four months, the simulated forecast had a root mean square (rms) error of about 10% which was attributed to inadequate dynamic representation, computer error, and observational error (initial and boundary conditions, and verification).

Miller et al. (1981) calibrated the same model with an exact solution (Rossby waves) and simulated observed ocean conditions. After two wave periods (about 160 days), the rms errors were less than 10% (concentrated near the boundaries). Occasionally, large error structures occurred at the boundaries where the flow was tangent to the boundary; however, why they formed at one point and not another has not been explained. Of the two techniques for determining the vertical derivatives, finite differencing was the easier to implement, while the collocation technique was more accurate and efficient.

Robinson and Leblond (1985) ran a set of QG predictive experiments in the POLYMODE area using various data inputs. In one series of tests in small domains (order of 100 km), the interior conditions were set to zero and the boundary conditions were updated continuously; the interiors were accurately forecast. In another series with the initial conditions for the interior provided, fluctuations in the rms error were attributed to bad or unrepresentative hydrocasts.

Modeling groups at the Naval Postgraduate School and Harvard used the QG model extensively in the CCS as part of the OPTOMA program (Rienecker and Mooers, 1988, Rienecker et al. 1985 and Robinson et al. 1986). The model was the principle tool in determining the relative importance of non-linear interactions, baroclinicity, relative vorticity, and surface forcing from Ekman pumping. The domain for these experiments was small, ca. 150 km square, the asynoptic data spanned ca. a month, and, when wind stress was incorporated, a single value was used. Climatology was used, in a limited sense, for the stability profile.

The H00M is currently in use at the Naval Oceanographic Office forecasting the 100 m position of the north wall of the Gulf Stream and its rings. The system, known as GULFCAST or as the Navy Operational Gulf Stream Model (NOGUFMS) 1.0, provides a forecast once a week in a rectangular domain situated between ca. 30 and 46 N and 50 and 72 W. The model has six vertical levels and 15 km grid spacing.

Due to the spatial extent of the GULFCAST domain, it is not feasible to obtain in situ data alone to initialize the model. Instead, "feature models", which are canonical, analytical 3-D structures of the Gulf Stream and rings, are used to provide in situ fields for initialization and the boundary condition updating at positions provided by remote sensing, and mean stratification at mid-thermocline is derived from Levitus climatology. This approach appears to work well in the robust Gulf Stream where major features are coherently structured. The process of producing a forecast takes a week and requires many steps (Glenn et al., 1987):

- (1) The locations of the Gulf Stream and rings are determined from satellite (GEOSAT or AVHRR), AXBT's and the previous forecast.
- (2) Feature models are used to estimate the velocity fields for QG initialization at the appropriate locations using width, maximum velocity, and vertical shear parameters for the Gulf Stream and radius, depth, and maximum swirl velocity parameters for the rings.
- (3) The QG model dynamically adjusts the features, interpolates between the features, and evolves the full fields.
- (4) A dedicated survey flight is flown, for example, to verify the position of features not seen in imagery but carried forward from the previous forecast by model dynamics and to resolve major events (e.g., eddy-stream mergers, eddy pinch-offs, and eddy-eddy interactions). Ca. 20 to 30 AXBT's are dropped. These in situ observations are used in the final forecast.

- (5) Sensitivity analyses using smaller, higher resolution QG models are conducted at inflow and outflow regions to determine the exact positions of the Gulf Stream and rings and the evolution of any Gulf Stream-ring interactions. These determine the best and most probable initial and boundary conditions, and
- (6) The model is re-initialized and a one-week forecast is made.

The domain includes the New England Seamounts which are steep (0.15) and tall (order of 1000 m) enough to invalidate the QG approximation. (However, Adamec (1988) used a three-level QG model to study the southward deflection of the Gulf Stream over the New England Seamounts). The seamounts are either removed, shortened and filtered, or left untouched for short range forecasts. The latter is the technique used operationally. Although wind data are readily available, no surface forcing is incorporated because local atmospheric forcing is assumed to have minimal influence in the dynamics of the overall Gulf Stream and its eddies.

Based upon a limited number of research evaluations, GULFCAST has scientifically "verified" consistently (Robinson et al., 1987). However, a measure of accuracy, other than rms position error, has not been developed and the verification was qualitative and visual (i.e., compared with IR imagery). Generally, some difficulties in forecasting are attributed to misinterpreting weak surface signatures and persisting unobserved rings which may have changed position or shape. Additionally, temperature extractions at isolated points have not been accurate unless the properties for slope, Stream, and Sargasso Sea water masses are manually "tuned".

NORDA is currently evaluating GULFCAST sensitivity to data inputs in a quantitative sense with focus on IR imagery, GEOSAT altimetry, and XBT's (the in situ observations are used in an "all or none" sense). Six case studies have been identified for analysis. This evaluation uses the same GULFCAST process described above with an appropriate operational restriction: there is no sensitivity analysis of initial and boundary conditions (which requires additional resources and an educated staff). In this manner, the model had an rms error in forecasting the position of the Gulf Stream of ca. 50 km, and it did not beat persistence. The main problems cited are: over-development of meanders, phase problems at the outflow, and an inability to handle ring-stream interactions (Martinek, 1989).

Although GULFCAST is manpower and resource intensive, it provides an operationally useful product. Whether or not the HOOM has similar operational value in less vigorous domains (e.g., the CCS) is not known.

#### d. Other Uses of QG Models

Although restricted in physics, QG models have operational roots in numerical weather forecasting (Charney et al. 1950). Compared with a more complete primitive equation model, QG models have been popular because generically they are simple, fast, and inexpensive to run and their applicability to mid-ocean mesoscale flow regimes has been demonstrated in other research ocean modeling studies. Most of the work with QG models, other than the HOOM, has been with a modest number of layers or levels in large domains, with grid spacing of ca. 20 km. For example:



- (1) The Holland (1978) model is a two-layer model which has been used by Malanotte-Rizzoli et al. (1984) to investigate the effects of model parameterization and by Vallis et al. (1987) to study the effects of climatological wind stress in the Pacific. The latter effort employed the Holland model in a coarser resolution (one degree), non-eddy resolving model of the North Pacific basin from 15 N to 45 N latitude and from the coast to 140 W longitude; bottom topography was included.
- (2) Ikeda et al. (1984) and Ikeda et al. (1989) used a two-layer QG model to analyze baroclinic instability of the California Undercurrent off Washington and the Norwegian Coastal Current off Norway, respectively. Both domains were similar in size to the OPTOMA domain and the latter study included the shallow, ca. 300 m, bottom topography.
- (3) Cummins (1989) and Cummins and Myzak (1988) used a three level, climatological wind-driven version to study the effects of wind stress curl in a large (1000 by 3000 km) Northeast Pacific domain. An artificial frictional boundary was used to isolate the interior. The model reproduced many of the expected features, but the lack of in situ data precluded quantitative verification.

#### 4. Evaluation of Sampling Schemes

Robinson and Haidvogel (1980), in their barotropic simulation, also found that, with initial vorticity set to zero and accurate boundary conditions, the model recreated the flow in the domain after a few days. A subsampling of boundary observations by Robinson and Tu (1981), for insertion into the same barotropic model, showed that model errors increased as sampling resolution decreased. Still, their worst-case error, associated with a grid of ca. 62 km in the interior and ca. 16 km on the boundary, was an "acceptable" 15%. Also, persistence boundary conditions adversely affected model accuracy, but the error dropped immediately when the boundaries were updated.

Oceanic sampling strategies have been generally discussed in Ocean Prediction Experiments (OPE) and Observing System Simulation Experiments (OSSE). For example, other than the NORDA GULFCAST work in progress, Batteen et al. (1988a) used simulated observations, subsampled from a PE model, in an OA model to assess sampling strategies in the OPTOMA domain. The resulting maps were verified against the PE model field. They determined that a limited number of observations are best utilized in a regular grid pattern and that the spatial sensitivity was much more important than the temporal sensitivity. However, their data were perfect (i.e., noise-free), complete (i.e., no failures), and the data were used in the OA model only (i.e., no dynamics involved).

## C. REMOTE SENSING FROM SATELLITES

### 1. Introduction

Among the presently available space-based remote sensing systems are the Advanced Very High Resolution Radiometer (AVHRR) and (until January 1990) the satellite altimeter. AVHRR, used since the late 1970's and currently on the NOAA-series polar orbiting satellites, provides images of the ocean surface at various wavelengths including visual, near infrared, and far infrared wavelengths. The altimeter was an active microwave sensor which provided an independent source of all-weather ocean, wind, and geoid measurements. It had been used by oceanographers since late 1986 and data from GEOSAT are still being processed.

High resolution infrared (IR) images of the ocean surface covering large areas of ocean can be obtained rapidly. Accurate sea surface temperatures, corrected for atmospheric water vapor and skin

versus bulk temperature differences, can be derived from a single, cloud-free multi-channel image. Under favorable conditions, complex circulation patterns can be inferred from a sequence of images.

Altimetry data, consisting of specular radar measurements along a narrow orbital subpath, are used to derive several kinds of geophysical information such as ocean currents, wind speed, and significant wave height. Of importance to mesoscale observations is the distance from the satellite to the sea surface; however, there are many error sources in the process of correcting the raw signal to a usable sea surface height (SSH).

## 2. Vertical Coherence of Oceanic Fields

A major limitation of both AVHRR and altimetry is their inability to directly detect subsurface fields. Both data sets consist of a single variable, SST or SSH; but, these variables can be "enhanced and extended" by in situ observations, time series of surface fields, and appropriate ocean models. For studies of subsurface processes, satellite data are useful only if the surface signal contains information about the subsurface signal. This holds in many, but not all, cases of mesoscale variability. In this manner, remote sensing can quantitatively contribute to a 4-dimensional description of the ocean fields (Robinson and Leslie, 1985, and Rienecker et al., 1985).

Bernstein et al. (1977) stated that satellites could provide extensive information on the horizontal gradient of temperature through the upper 100 meters. Evidence throughout the years has tempered such optimism. An "estimation" of the subsurface thermal structure using the surface temperature pattern may be possible in some areas, at certain

times, and under certain conditions; i.e., some observations show high correlation between surface and subsurface structure particularly when the dynamics in the mixed layer have not masked the interior mesoscale variability.

There are many examples in the Pacific of low correlations. In the subtropics, Dorman and Saur (1978) found two uncorrelated levels, one above 60 to 100 m and one below, with contrasting statistical properties and anomaly patterns. They suggested that atmospheric synoptic processes were important in the upper level while ocean mesoscale processes are important at depth. Emery and Mysak (1980) noted that only one-third of eddies in the CCS off Vancouver had surface expressions. Broenkow (1982) observed a tilt in the axis of a CCS eddy resulting in a 35 km displacement of the center at 1000 m from the surface position. Likewise, Roden (1984) noted that subsurface temperature fronts in the Pacific were often displaced great distances from their surface expressions. Also, storms have been noted to decouple or distort the surface signature from the subsurface vortex (Simpson et al., 1986).

In the OPTOMA domain, in August 1982, Rienecker et al. (1985) found a seasonal correlation between the surface and 30 m. At times the SST pattern appeared to be determined by summertime heating, upwelling and advection by the mesoscale flow field with offshore displacement caused by local atmospheric forcing. Surface temperature and dynamic topography were not correlated. Rienecker et al. (1987) correlated objectively analyzed fields of SST and T50 for most of the OPTOMA

surveys. The average correlation was ca. 0.8; however, there were significant periods of decorrelation throughout the surveys.

High correlations between a surface signal and a field at depth have been noted by others. In the Northern Pacific subtropical front during winter, Van Woert (1982) found that temperature and dynamic topography at 800 m were highly correlated with surface values. In the California coastal upwelling zone near Point Sur, Breaker (1983) noted high correlations between the surface and thermocline temperatures.

Using CalCOFI historical data and mean satellite-derived SST, Fiedler (1988) made point-to-point calculations of vertical coherence, mostly south of Point Conception. Off Central California, high vertical coherence at a depth greater than the MLD was most likely in the summer when the mixed layer was shallow and the water column was strongly stratified. Although no problems were mentioned, this was also the time when surface masking would be most apparent.

These studies have inadequately addressed the necessary conditions which allow a correlation between a surface and subsurface signal (e.g., no diurnal layer, no surface masking, and moderate winds) and the time-space scales of the correlation.

### 3. Summary of IR Imagery

#### a. General

The AVHRR imager is carried on the NOAA series of polar-orbiting, sun-synchronous satellites. These satellites (NOAA 6,7,8 and 9) are in ca. 850 km orbits which provide 2500 km swath coverage twice daily with five channels (0.58- 0.68, 0.725-1.10, 3.55-3.93, 10.3-11.3, and 11.5-12.5 microns).

The AVHRR has many advantages as a tool for observing SST: good spatial resolution (1.1 km at nadir), good temperature resolution (Noise Equivalent Differential Temperature, NEDT, ca. 0.1° C in most channels), broad geographic range, and coverage about twice a day. Its major limitations are: inability to view through clouds, a precessing orbit which occasionally prevents viewing a particular area repeatedly, changing atmospheric moisture and aerosol effects, and the fact that it measures a single surface variable which is subject to change through a myriad of mechanisms and processes (Appendix A).

b. AVHRR Imagery Applications

Some researchers simply correct satellite measurements to in situ observations. For example, Vastano and Bernstein (1984) corrected AVHRR measurements to coincide with XBT measurements in the vicinity of the Oyashio Front. Most measurements agreed after the correction with exceptions attributed to satellite-ship asynopticity and position discrepancies. However, they had little data to work with, only 16 data pairs even with a large temporal and spatial window (24 hours and 25 km).

Generally, the following multi-channel correction was used in the OPTOMA domain:

$$SST45 = 1.0346 * T4 + 2.5779 * (T4 - T5) - 0.61 + 1.2 * (\text{SEC}(\phi) - 1.0)$$

(equation 2.10),

where SST45 is SST based upon channel 4 and 5, T4 is channel 4 brightness temperature, T5 is channel 5 brightness temperature, and  $\phi$  is the zenith angle (Bernstein, personal communication, 1988). A comparison of mean differences and rms scatter between in situ and AVHRR data using various algorithms verified the accuracy of equation 2.10; however, in one particular case, a constant correction to channel 4 data was more accurate (Rienecker et al., 1985). To check for cloud-contamination, the data were flagged if  $\sigma$  in a 5X5 array of channel 4 data was greater than an arbitrary threshold of 0.3° C (although strong SST fronts were also be flagged).

Surface motion vector analysis is an application of a meteorological technique, cloud motion analysis, to ocean purposes (Leese et al. 1971). Simply put, the technique is to track the position of the same feature through a series of different images and calculate the displacement, which can be done manually or by automated techniques (Emery et al. 1986). When used successfully, the result is a near-synoptic estimate of surface velocities over a large area.

The features tracked are small enough to be located precisely, yet they must be large enough to maintain their integrity from one image to the other, ca. 10 km in length. The types of thermal features most easily tracked are: cold or warm intrusions, isolated hot or cold spots, seaward extremes of upwelling, and wave pattern "meanders" along sharp fronts.

The motion between the two positions is assumed to be linear, irrotational, and the result of advection. Errors arise from deviation from a linear track due to distortion of the feature, curvilinear motion, rotation, and non-advective processes (e.g., wave propagation), inaccurate registration of the images, and tracking error. The tracks cross SST isotherms, which appears contrary to geostrophy, but the features are typically shallow tracers with no vertical structure. In shallow areas, wind mixing and tides distort the images and near the coast, upwelling is not well-tracked. Surface masking caused by diurnal heating under clear sky and low wind conditions may also be a problem.

In the earliest applications, surface stream functions and dynamic heights were derived in the Oyashio and Kuroshio currents from surface vectors (Vastano and Borders, 1984; Vastano and Bernstein, 1985). A 10 to 20 km thermal feature was tracked as it moved around a large cyclonic eddy in the CCS, but there were no in situ measurements for comparison (Koblinsky et al., 1984). One automated technique matches the displacement from one image to the area of highest correlation, within a small window, in the next image (Emery et al., 1987). Off the Straits of Juan de Fuca, the satellite measured velocities compared well to geostrophic velocities and other types of in situ observations for comparison. A total of 27 comparisons between surface drifters, drogued at 2 m, and satellite vectors were made off Southern California



(Svejkovsky, 1988). The rms difference was 5.9 cm/s with the largest errors near shear zones where the satellite measurements and drifters were not colocated and the separation was enough to put the two in different velocity regions. These works were typified by comparisons to a very limited number of point-to-point, in situ observations even with large spatial and temporal windows of comparison.

#### 4. Summary of Satellite Altimetry

##### a. General

GEOSAT, the satellite altimeter platform, was launched in February 1985 with two goals: the precise measurement of the geoid on a fine mesh, a classified mission, and ocean measurement from an Exact Repeat Mission (ERM). The latter is a 17-day repeat cycle with a track spacing of ca. 135 km at the equator and an orbital period of ca. 100 minutes. GEOSAT completed its first mission in September 1986 and started the ERM in October 1986. The system was declared to be operational in the ERM on 8 November 1986.

Many corrections must be made and large sources of error must be removed before a usable value of sea surface height (SSH) is available (Appendix A). Fortunately, though the competing signals and errors are large compared with the mesoscale signal, they are of different magnitude and have different horizontal scales. This allows processing techniques (e.g., curve fitting, smoothing, and filtering) to separate signal from noise (Calman, 1987). The error budget results in an error of ca. 2 cm over 100 km, about the same as that for dynamic height computed from observed vertical profiles of temperature and

salinity. Difficulties in using altimetry data are: temporal aliasing due to the 17-day repeat, spatial aliasing due to the ca. 100 km track spacing, gaps in the data, an incomplete understanding of the effects of moisture in the atmosphere upon the radar travel time, and the loss of large scale oceanic signals due to geoid and orbit processing techniques.

b. GEOSAT Altimetry Applications

Satellite altimetry bypasses many difficulties of in situ measurement of the velocity field. It is rapid, global, and direct (i.e., there is no reference level assumption). Surface geostrophic currents are related to sea surface slope through the geostrophic balance where the crosstrack surface current component is proportional to along-track slope. In mid-latitudes, a slope of 1 meter over 100 km results in a one meter per second current. To ascertain velocities within 10% on these scales, the rms error associated with the height measurements must be less than 10 cm. The surface velocity is given by:

$$V_s = g/f (d\eta/dx) \quad (\text{equation 2.11}),$$

where  $V_s$  is the absolute cross-track surface geostrophic current,  $g$  is gravity,  $f$  is the Coriolis parameter, and  $d\eta/dx$  is the alongtrack derivative of the vertical displacement of the sea surface.

In the CCS, where the Pacific geoid is not well known (it is classified) and descending tracks are noisy and gappy, there have been few studies using altimetry data. Altimetric topography from an

ascending orbit which passes through the OPTOMA domain close to the coast was compared to ocean topography obtained from 15 CTD stations with an along-orbit spacing of 15 km (Kosro et al., 1988). The dynamic topography referenced to 500 meters was computed and demeaned. The altimeter heights were corrected for the tides, the FNOC troposphere, the ionosphere, the inverse barometric effect, the geoid (obtained by averaging the first 16 repeat cycles) and the orbit error (modeled as a bias and tilt over the latitude band 34 N to 45 N). This process also eliminated mean currents. The heights were interpolated in space and time to the CTD stations and demeaned.

Both data sets depicted a 20 cm perturbation over 50 km due to a strong offshore filament clearly seen in satellite IR imagery. The sea surface topography corresponded to an offshore speed of ca. 50 cm/s over 30 km. The rms differences between the GEOSAT and calculated data sets are 3.2 cm in May 1987 and 4.1 cm in June 1987.

Based on rms difference between altimetric sea level and a one-year mean, four areas of maximum variability along the West Coast were identified, including one within the OPTOMA domain off San Francisco and Cape Mendocino (White and Tai, 1988). A spectral analysis showed a dominant annual cycle with a maximum in the winter, contrary to in situ observations of a maximum rms residual from May to August and a minimum from fall to winter (Rienecker and Mooers, 1988 and Flament et al., 1988).

#### D. SUMMARY OF BACKGROUND LITERATURE REVIEW

The CCS, off Central California, is a complex system of five currents: the California Current, the California Undercurrent, the Davidson Current, the Southern California Current, and a coastal upwelling jet. The system is further complicated by mesoscale variability, coastal upwelling, and transitions during spring and fall.

The OPTOMA domain, a 225 by 550 rectangle ca. 100 km offshore, is an area of year-round mesoscale activity. Mesoscale activity (e.g., eddies with length scales of 100 to 200 km, time scales of 100 days, and flows of 20 to 50 cm/s) has been observed and well-described by CalCOFI, OPTOMA, and other independent surveys using in situ measurements and data from remotely sensed sources (e.g., IR imagery and satellite altimetry). Baroclinic instability, wind stress curl, and bottom topography are important in forcing mesoscale activity and in determining preferred location.

IR imagery, when available, vividly depicts mesoscale activity, both in single images and in surface motion analyses from a pair of images; however, clouds often prohibit the viewing of the sea surface and masking of features sometimes occurs. With careful processing and reduction of the error budget, satellite altimetry also depicts mesoscale activity; however, the 17-day ERM orbits are widely spaced and most descending orbits have many spatial gaps.

The Ocean Descriptive-Predictive System (ODPS), made up in part by OA and QG models, has been used in the OPTOMA domain to map and "nowcast" or "hindcast" fields. A sensitivity analysis on data requirements for the models has not been done previous to this study.

### III. DATA ACQUISITION, PROCESSING, AND ANALYSIS

#### A. INTRODUCTION

This study incorporated data from many sources: in situ data from aircraft, ship and buoys (six moored and one drifting); satellite data (AVHRR and GEOSAT); coastal data (six sea level sites and one SST site); modeled fields (NOGAPS winds); and climatology (the Navy standard and CalCOFI). OPTOMA 23 was unique in two respects: this was the first OPTOMA boundary condition updating experiment using aircraft; and, this was the first OPTOMA effort to integrate concurrent data sources in a comprehensive oceanographic, meteorological and acoustical study of the CCS. The time frame of the initial study, a two-week period in November 1986, was expanded to a six-month review of coastal sea levels, Granite Canyon SST, winds, and data from the National Data Buoy Center (NDBC) buoys off Central California to describe the Fall Transition of the CCS (Figure 3.1).

The key component of the OPTOMA 23 data acquisition was the dedicated use of the Project BIRDSEYE RP-3D aircraft. The aircraft, part of NAVOCEANO Project OS-06-87, flew six flights between 9 and 19 November 1987 (Julian dates 86313 and 86323); five of these were surveys of the OPTOMA domain, and one provided data within 50 km of Monterey Bay which linked the offshore mesoscale fields with coastal data. During the last two flights, the R/V POINT SUR made observations at sea in the CENCAL domain.

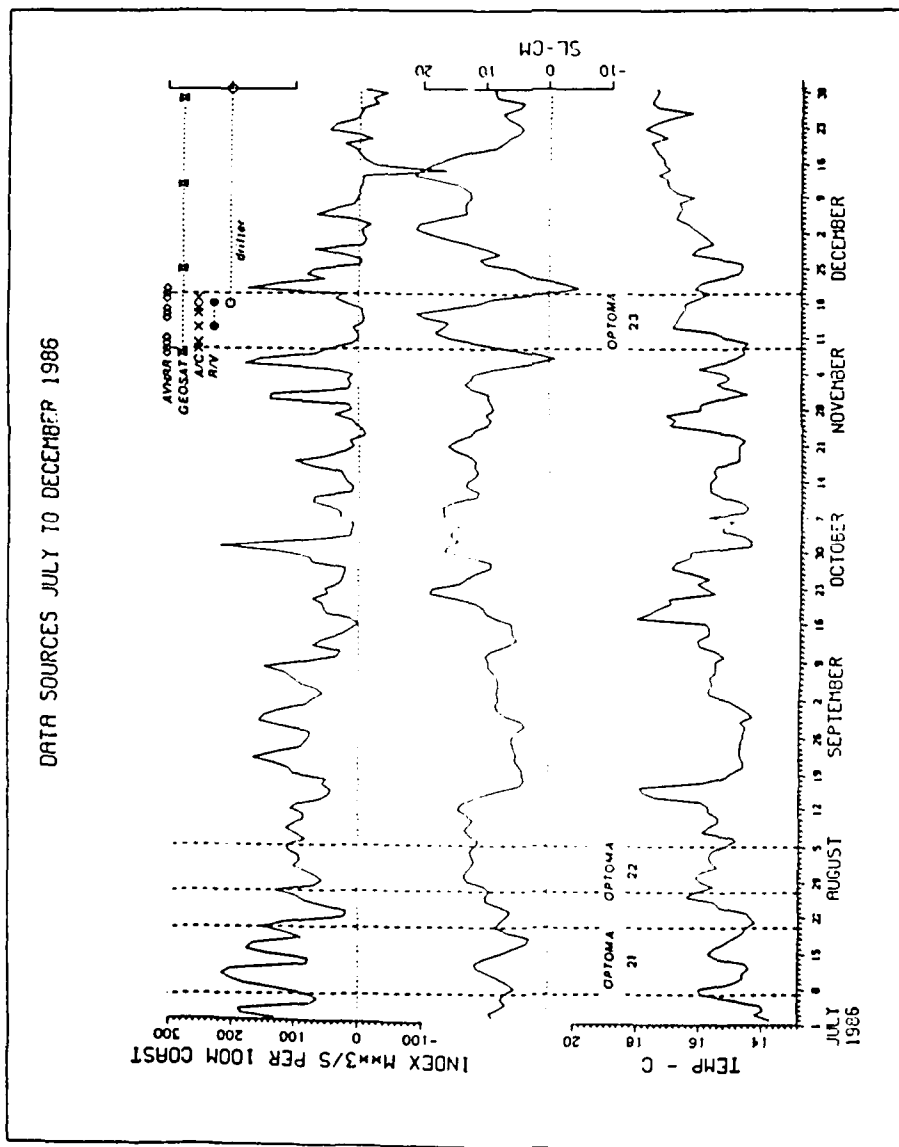


Figure 3.1 A summary of data types and survey times from July through December 1986: Bakun indices at 36°N (top), Monterey sea level (middle), Granite Canyon SST (bottom), and OPTOMA 23 activity (right corner).

## B. ANALYSIS OF IN SITU DATA

### 1. General

The Project BIRDSEYE aircraft was used for the survey; it is a modified P-3A, equipped with a precision radiometric thermistor (PRT-5) which continuously recorded SST within  $0.1^{\circ}$  C (i.e., after correcting for system drift), air and dewpoint sensors, and airborne expendable bathythermograph (AXBT) data acquisition and processing equipment. Position was determined by use of two inertial navigation systems updated hourly with TACAN, a radio navigation system. The cumulative navigation error upon landing was within 2.0 km for all flights.

OPTOMA 23P1 was the first event, a survey on 9 November 1986 (Julian date 86313) of the NOCAL domain. OPTOMA 23P2 was the second event, a survey on 10 November of the CENCAL domain. An acoustics flight, OPTOMA 23P3, in support of a study by the Environmental Acoustic Research Group (EARG) was flown on 13 November within 50 km of Monterey Bay (this provided data for the Fall Transition analysis). The next OPTOMA flight, OPTOMA 23P4, was a boundary condition update flight around the perimeter of the NOCAL and CENCAL domains on 16 November (Julian date 86320). The last two flights, OPTOMA 23P5 and 23P6, flown on 17 and 19 November, respectively (Julian dates 86321 and 86323), were repeats of the NOCAL track and the CENCAL track. These were originally scheduled to take place a week after the boundary condition update flight, but operational commitments for the aircraft and the offshore Pacific Missile Test Center range, which covers the CENCAL domain forced an early end to the mission. Weather was not a factor in

mission scheduling. Each survey took four-to-five hours to complete not including transit time (Figure 3.2).

Buoy spacing was ca. 30 km. Many factors influenced the final survey pattern. The RP-3D can carry ca. 100 AXBT's on an eight hour mission. The typical flight profile on station was a speed of 240 knots at an altitude of 1000 feet. This altitude optimized radio reception range (ca. 50 nm at 1000 feet), weather (the stratus layer was typically higher than 1000 feet and the ocean surface remained in view), and fuel conservation. From this altitude, an AXBT takes ca. one minute for fall and light-off time. Shallow AXBT's (300 m) then transmit for 200 s, deep AXBT's (750 m), for 500 s. AXBT's were available in three radio channels; with three receivers aboard the aircraft and all equipment operating properly, a station spacing of 10 to 15 km was possible in some areas (e.g., near cool filaments).

Approximately 508 AXBT's were dropped in support of the OPTOMA flights (100 per flight) with a relatively high failure rate of 20% due to aged probes. The drop positions were spaced every 30 km for the NOCAL and CENCAL surveys and every 40 km for the boundary condition update flight (Figure 3.3). There were some AXBT's left for reseeded of buoys that failed in "critical" areas (e.g., near the cool filaments). (The AXBT data have been forwarded to the National Oceanographic Data Center by Johnson et al., 1988).

The AXBT signals were recorded on analog tape and digitized onboard the aircraft by the NAVOCEANO data acquisition system and by the Airborne Digital Data Acquisition System (ADDAS), the NPS system (Colton et al., 1984). Temperature-depth profiles were made in flight as the



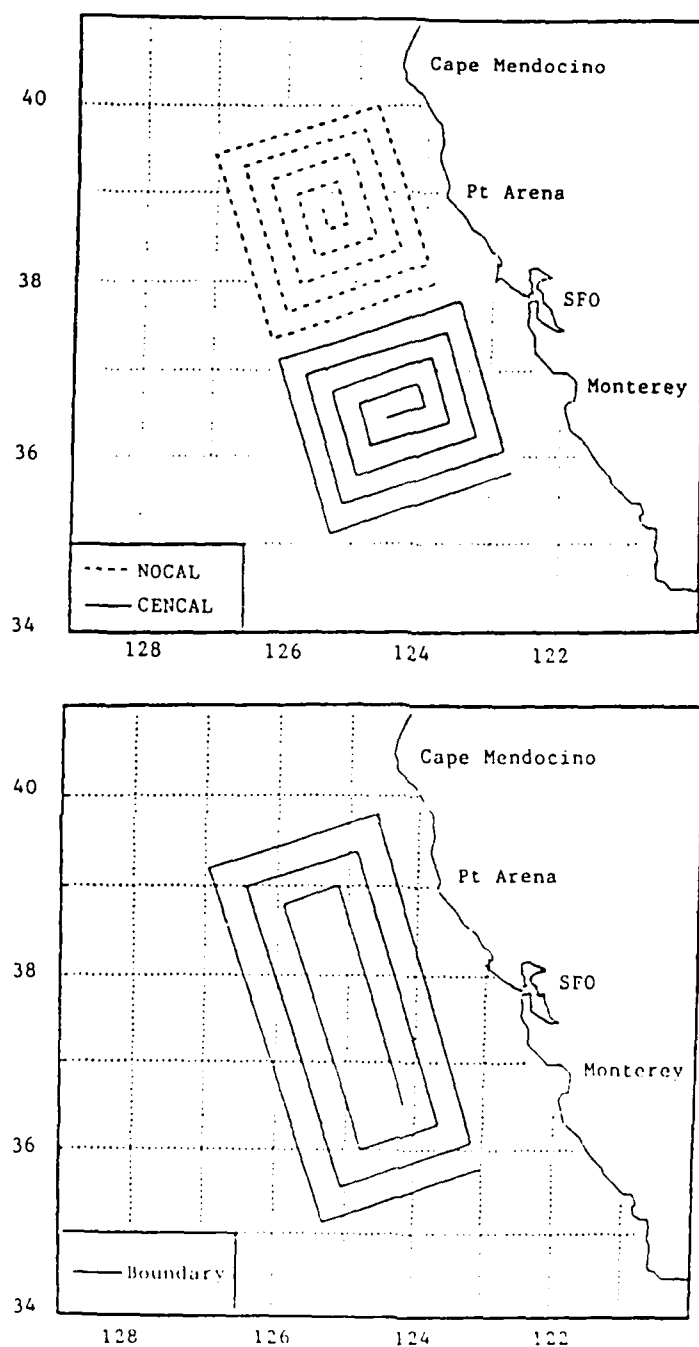


Figure 3.2 Flight tracks for OPTOMA 23. NOCAL and CENCAL surveys were flown twice (on 9 and 17 November 1986 and on 10 and 19 November 1986, respectively); the boundary condition update survey was flown once, on 16 November 1986.

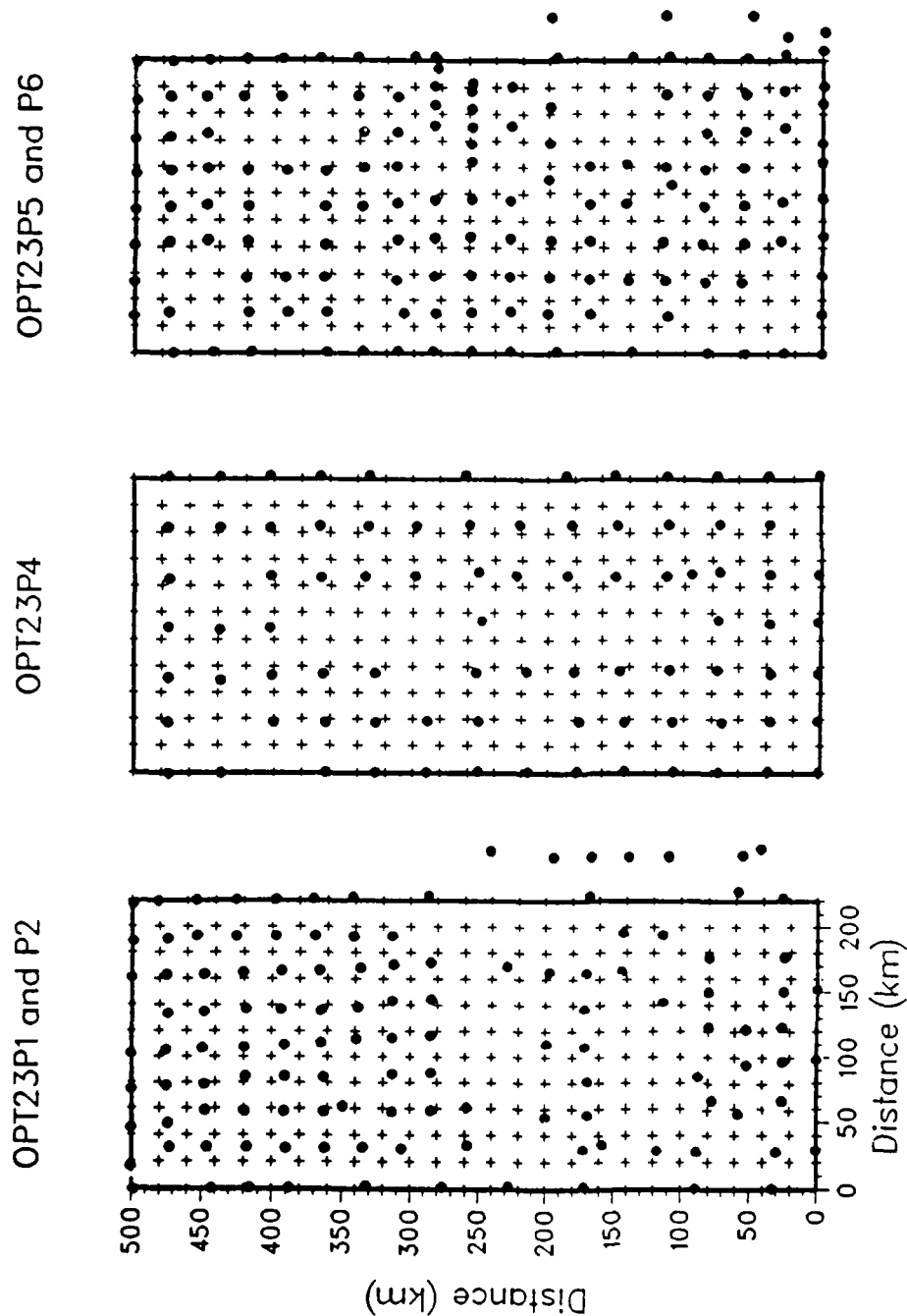


Figure 3.3 Observation positions (dots), OPTOMA 23. Surveys 1,2,5 and 6 had a spacing of 30 km; survey 4 a spacing of 40 km. Survey 3 was from Monterey to Point Sur and is of limited interest for present purposes.

signal was digitized. Data from the PRT-5 (upward scanning and sea scanning sensors), the air and dewpoint temperature were recorded continuously on strip charts. The PRT-5 provided an independent measurement of SST (Appendix B).

The R/V POINT SUR made CTD and XBT profiles in the CENCAL domain 13 to 18 November. The ship survey focused on a cool filament identified in satellite imagery and in the data from the first two survey flights. A drifting buoy was released from the ship north of the cool filament on 18 November (Appendix C).

## 2. Data Processing

The general OPTOMA procedure for creation of dynamic topography fields is summarized:

- (1) the domain is surveyed using ship or aircraft with XBT's, AXBT's, CTD's and other equipment when available (e.g., PRT-5),
- (2) AXBT data are digitized at 0.1 s intervals (or about 15 cm interval in the vertical), edited with a spike removal routine, and smoothed with a 3-point filter,
- (3) a salinity profile for each XBT or AXBT is inferred from a mean T-S relationship derived from CTD observations (or from climatology if necessary),
- (4) fields are extended to depth by adding linear tails, or by adding a mean correction to account for dynamic topography between levels, and
- (5) dynamic heights are calculated.

OPTOMA 23 used a variety of AXBT's (5 different lots from 3 manufacturers) each with presumably subtle differences in temperature-frequency response and drop rate. Although there are improved algorithms for some AXBT's (e.g., Boyd, 1986), the standard Navy equation was used

to convert XBT and AXBT time of fall to depth. The Navy specifications for depth accuracy is 5%. With AXBT's, frequency is converted to temperature using the Sippican (Ghent) temperature equation.

To calculate dynamic heights from AXBT profiles, a corresponding salinity profile is needed and can be estimated (the ratio of the number of CTD's to XBT's is ca. 1 to 10 for the OPTOMA cruises and airborne surveys acquire no salinity data). In previous OPTOMA experiments, a mean T-S relationship derived from concurrent CTD casts had been used to determine salinity at the XBT sites. This is an acceptable procedure when the T-S relationship is stable (e.g., no major variations in the T-S relationship due to variations in water mass, inversions, heating, or river run-off) and it has been used in the OPTOMA domain (Rienecker et al., 1985).

Two mean T-S relationships were used to estimate salinity from the temperature files recorded by the AXBT's. South of 37 N, the mean T-S relationship from ca. 40 concurrent CTD measurements (away from the continental shelf) was used; north of 37 N, a mean T-S relationship from 25 CTD measurements made during OPTOMA 13 in the NOCAL domain in November 1984 was used.

Both T-S relationships were compared with data from the California Cooperative Oceanic Fisheries Investigations (CalCOFI). Other than the OPTOMA surveys, the CalCOFI data set is the most comprehensive data set in the CCS; however, the CalCOFI surveys have been infrequent north of San Francisco and have had alongshore spacing of 195 km in

recent years (Chelton, 1982). The OPTOMA 23 T-S relationships were similar to the mean CalCOFI T-S relationship (Figure 3.4).

The CalCOFI T-S relationship, plus and minus the standard deviations, roughly bracketed the OPTOMA T-S relationships. To ensure that differences in T-S relationships did not quantitatively affect results, the T-S relationship extremes were used, with observed temperatures, to calculate two dynamic topography sets. The two resulting OA fields of SDH correlated perfectly and had a RMSE of less than 3 dyn cm.

### 3. Extension of Shallow Fields to Depth

A linear extension was used to extend AXBT profiles shallower than 450 m but deeper than 300 m. The addition of a linear tail makes no assumptions about the relationship between deep and shallow fields. The technique used the vertical temperature change calculated over the last 25 m of the profile in a manner similar to that used by the OTIS software at FLENUMOCEANCEN. The estimate for each profile was compared with an estimate derived by linear interpolation between the deepest temperature value in the profile and GDEM climatology at 500 m. This extension technique was tested against the 25 deep AXBT's dropped during 23P4; the rms difference between the estimated and the actual recorded temperature at 450 m was 0.5° C.

Another method used to compare dynamic topography referenced to 300 m and that referenced to 450 m was the addition of the average difference between the two levels. Using the deep AXBT's from survey

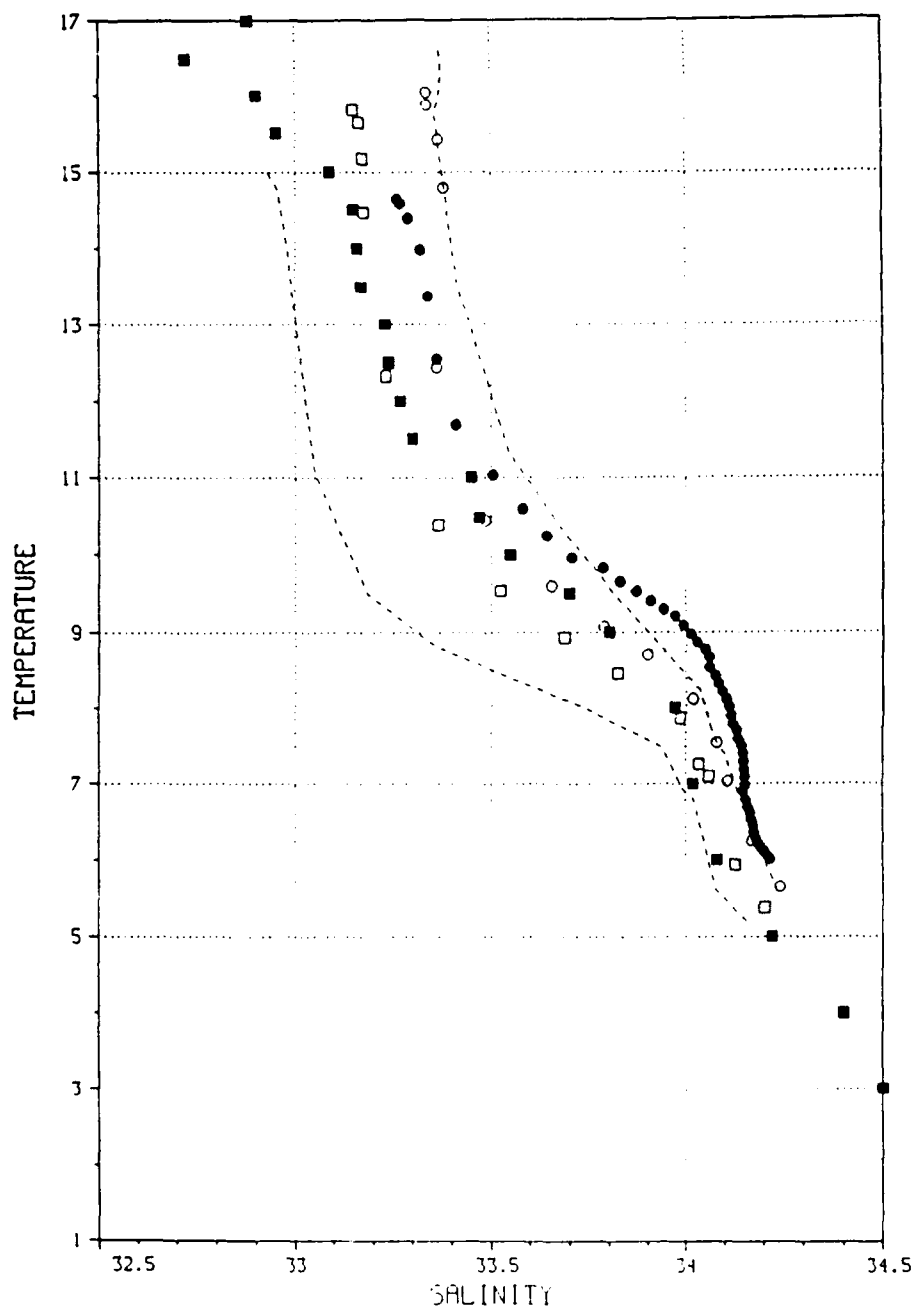


Figure 3.4 OPTOMA 23 T-S relationship, derived from CTD observations (filled circle), compared with CalCOFI data (line 60 is open circle, line 70 is open square) and OPTOMA 13 data (filled square). The dashed lines are the CalCOFI standard deviations from line 70.

23P4 (ca. 25 AXBT's), this was ca. 16.7 dyn cm. The mean difference between 300 and 450 m, over the entire OPTOMA ensemble, is 19 dyn cm with a  $\sigma$  of 1 dyn cm (Rienecker et al., 1987).

#### 4. Objective Analysis

##### a. Introduction

Objective analyses were conducted for a variety of fields: SST (both from XBT and PRT-5 inputs), MLD, the temperature at 50 m (T50), the depth of the thermocline (8° C isotherm, Z8 and 10° C isotherm, Z10) and dynamic height (0, 50, 150, and 400 m referenced to 300 or 450 m).

##### b. Sensitivity Analysis

Prior to running the OA for research purposes, a sensitivity analysis was conducted on the spatial and temporal windows, and on the maximum number of data points influencing each gridpoint to determine the optimal values for the analyses. (The coefficients of the fitted correlation were determined for the data set and fixed).

As a test of the filtering effects, sine waves sampled on a 8.33 km grid with wavelengths from 10 to 200 km were filtered using a second order Shapiro filter applied once (the standard filter used by Robinson et al., 1980). As expected, the shorter waves were affected the most (the reduction averaged ca. 95% for a 10 km wave); little effect was noted at wavelengths of 75 km and above (ca. 2% for a 75 km wave). (This routine was subjected to a sensitivity test with a signal comprised of a plane, random noise, and a sine wave. As expected with only a plane input, the detrend routine fit the input plane perfectly; when the amplitudes of the noise and sine wave components were

increased, the estimates of the input plane were less accurate and the goodness of fit decreased.)

c. Autocorrelation

The autocorrelation functions were calculated for survey ensembles of each field and for each field using data from individual surveys (e.g., SST from all of OPTOMA 23 would make up the ensemble, SST from OPTOMA 23P1 would be an individual survey). For the most part, ensemble values were used in the OA; these values were similar to those calculated from the individual surveys, but, having a larger number of observations, they were more statistically reliable (Figure 3.5).

In fitting the autocorrelation functional form to the data (equation 2.2), typical values for the zero crossing,  $a$ , are between 50 and 100 km; for the radius of curvature,  $b$ , between 75 and 100 km. The 95% confidence interval can be estimated by assuming white noise and a normal distribution using the following:

$$CI = C_b \pm 1.96/\sqrt{NB_b} \quad (\text{equation 3.1}),$$

where CI is the 95% confidence interval,  $C_b$  is the correlation in the bin,  $NB_b$  is the number of elements in the bin, and  $b$  is the respective bin number. The noise at zero lag, determined by extrapolating from the first three range bins, ranged from 0.0 to 0.13, and the fitted functions generally fell within the 95% confidence limits. For all fields, the plane removed by the detrending routine did not account for much of the variance in the signal (Table 1).



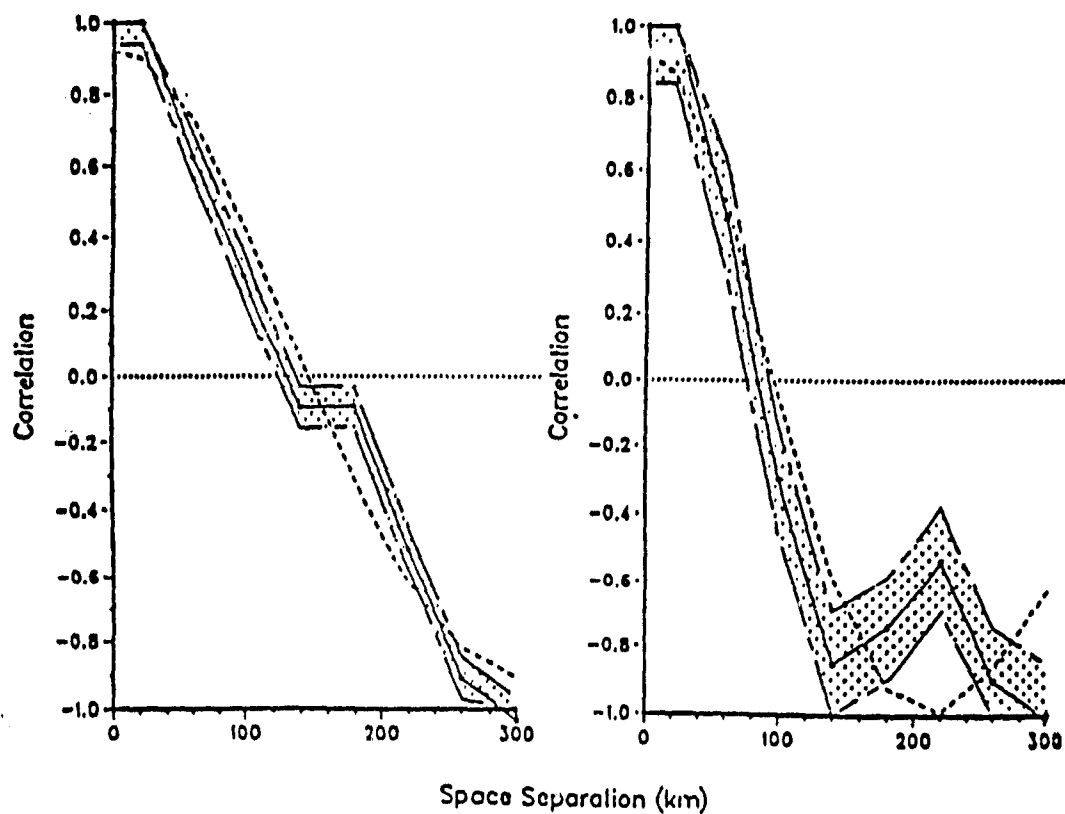


Figure 3.5 PRT-5 SST autocorrelations 900 point OPTOMA 23 ensemble (left), 150 point individual OPT23P1 survey (right). Calculated correlation is solid line, 95% CI is shaded, fitted form is dashed.

TABLE 1. AUTOCORRELATION RESULTS FOR DATA ENSEMBLES OPTOMA 23.

Data Set	#Obs	Range (min) (max)	Mean	Std Dev	Goodness of fit (plane)	Estimate of noise (zero lag)	Zero X-ing (km)
SDH (dyn cm)	411	48.0 66.0	55.0	6.2	0.30	0.02	99
SST(XBT) (° C)	411	10.8 16.8	14.5	0.9	0.46	0.02	99
SST(PRT) (° C)	943	10.2 16.3	13.5	0.9	0.07	0.08	146
MLD (m)	411	00.0 84.0	30.4	15.2	0.07	0.13	95
Z10 (m)	411	10.0 152.0	83.0	19.0	0.14	0.00	104
DIFF (PRT-AXBT) (° C)	327	-2.2 +0.4	-0.74	0.5	0.01	0.00	80
GEOSAT Altimetry (cm)	377	-13.8 +21.3	2.6	0.6	0.25	0.03	108

The effects of slightly different parameters are expected to be negligible with dense data sets. To confirm this, an experiment was conducted using parameters from SST (derived from PRT-5 measurements) during OPTOMA 23. The full ensemble consisted of over 900 measurements taken over 10 days; the individual survey consisted of ca. 150 measurements taken during the first two days. Two OA fields were generated using the same dense (153 point) data input set in the same domain with parameters from either the ensemble or individual survey. Although the autocorrelations for the two data sets are different (the zero crossing for the ensemble is 145 km, and for the individual survey it is 95 km), the two fields correlated perfectly and had an rms difference of  $0.03^{\circ}\text{C}$ , which is much less than the sensor noise level; similar results were obtained using a sparse data set of 20 points. These two fields also correlated perfectly, but had a slightly larger rms difference,  $0.04^{\circ}\text{C}$ . These results should not be expected for all data sets, particularly for those cases when parameters for individual surveys vary and the ensemble values are a non-representative average.

#### d. Objective Analysis

For each survey day, synoptic objective analyses were run on each field. Additionally, daily time series for SST (AXBT) and Z8 were run from day 86313 to 86323 using time windows of two, three, or seven days, depending upon the temporal gap in data coverage. In these asynoptic cases, a westward propagation of 5 km/day, appropriate for Rossby wave propagation and observed in the OPTOMA 23 data set, was used to propagate the observations westward.

A 12 by 26-grid rectangle with 20 km spacing was used to incorporate both the NOCAL and CENCAL domains; some finer scale grids, 8.3 and 12.0 km, were used to analyze the transition off Monterey Bay. The maximum number of observations allowed to influence each grid point was seven; it was noted that values less than five resulted in a significantly noisier field and values higher than seven required more computer time with little difference in the output.

A spatial radius of influence of 75 km was chosen because the error field in the analyses was minimized when the spatial radius of influence was less than the zero crossing, as determined by the autocorrelation calculation, but larger than the station spacing.

The internal Rossby radius,  $\lambda$ , a ratio of baroclinic phase speed to the Coriolis parameter,  $C/fo$ , is fundamental to the length scale of mesoscale features. Emery et al. (1984) averaged data in five-degree squares in the North Pacific and calculated  $\lambda$  seasonally; off Central California,  $\lambda$  was ca. 28 km with little annual change (on a smaller scale in the OPTOMA domain, Rienecker et al. (1985) and Robinson et al. (1986) calculated  $\lambda$  to be ca. 25 km). The radius of influence is about  $3\lambda$ .

Although there were spatial gaps in data coverage, the correlation statistics and sampling coverage produced objective analyses with low error fields (Figure 3.6). All analyses in the time series ensembles between the second and third surveys (10 and 16 November) had error fields with larger values due to the absence of data.

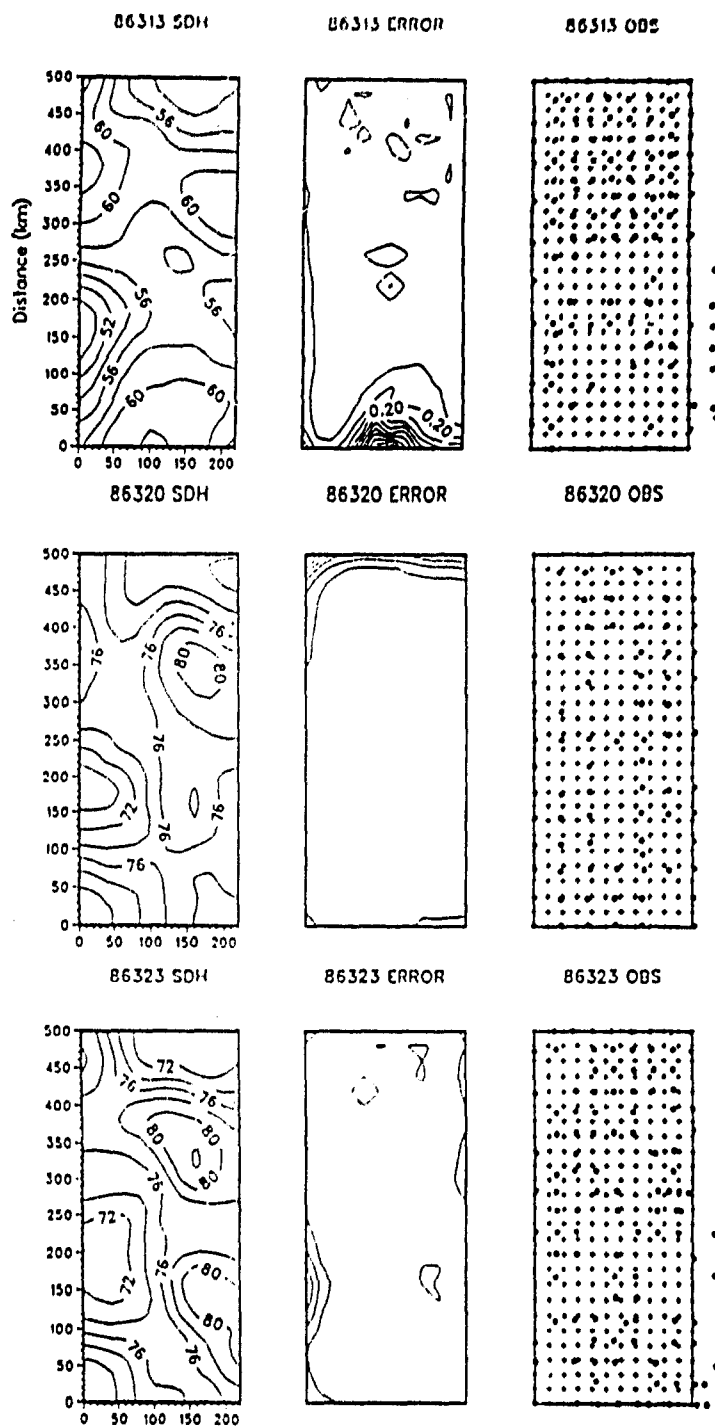


Figure 3.6 OA SDH fields, error fields, and observational positions superimposed on grid.

### 5. Evaluation of Model Output

OA fields are compared against climatology, a persisted field, and a verification field in order to quantify changes and to evaluate model accuracy. All OA fields have been mapped in a consistent manner. The evaluation techniques are field-to-field comparisons and start with a difference field:

$$D = P - O \quad (\text{equation 3.2})$$

where, D is the difference between the model predicted field, P, and the observed field, O. All errors are assumed to be in P.

The Root Mean Square Error, RMSE, is:

$$RMSE = \left[ \left( \sum_{j=1}^N w_j |d_j|^2 \right) / \sum_{j=1}^N w_j \right]^{1/2} \quad (\text{equation 3.3})$$

where, j is the position, and  $w_j$  is a weight factor to adjust for varying grid size, if required.

RMSE decomposes into two parts, Root Mean Square Error systematic ( $RMSE_s$ ), which gives an indication of linear bias or the similarity in pattern recognition, and Root Mean Square Error unsystematic ( $RMSE_u$ ), which gives an indication of precision:

$$RMSE^2 = RMSE_s^2 + RMSE_u^2 \quad (\text{equation 3.4})$$

and

$$RMSE_s = \left[ \sum_{j=1}^N w_j |\hat{P}_j - O_j|^2 / \sum_{j=1}^N w_j \right]^{1/2}$$

$$RMSE_u = \left[ \sum_{j=1}^N w_j |\hat{P}_j - P_j|^2 / \sum_{j=1}^N w_j \right]^{1/2}$$

where  $\hat{P}_j$  is the least squares estimator of  $P_j$ .  $RMSE_u$  is the best measurement in determining which prediction is more accurate since it can be interpreted as a measure of a model's potential accuracy with respect to estimating observed values (Wilmott et al., 1985).

Pattern correlation (Corr) is another index of accuracy; it is used to estimate how closely the pattern, or structure, in one field resembles that in another:

$$Corr = \frac{\sum (P - \bar{P})(O - \bar{O})}{N \sqrt{(\sigma_p^2 \sigma_o^2)}} \quad (\text{equation 3.5}),$$

where  $P$  and  $O$  are the values of field one and two at the gridpoint;  $\bar{P}$  and  $\bar{O}$  are the field averages;  $N$  is the number of points; and,  $\sigma$  are the variances. A 60% correlation is the lower limit of useful skill recognized in the meteorological community (Rosmond, 1989).

Finally, a qualitative assessment of a model's ability to represent mesoscale features, by an experienced analyst, is important. A single index of value can give misleading indications of model performance, particularly near mesoscale features where a slight error in forecasting the position of a feature may lead to large RMS errors.

#### 6. Inverse Distance OA

For a comparison to the standard ODPS OA scheme, another technique which estimates the value of the field at the grid by weighting the neighboring observations with the inverse of the distance between the gridpoint and the observation was encoded from Davis (1973). The final value is:

$$Y_j = (\sum (Y_i/D_{ij})) / (\sum 1/D_{ij}) \quad (\text{equation 3.6}),$$

where  $Y_j$  is the estimated value at the gridpoint  $j$ ,  $Y_i$  is the observed value at position  $i$ , and  $D_{ij}$  is the distance between gridpoint and observation.

Two comparisons were made, SST from PRT-5 measurements on day 86314 and the difference between PRT-5-derived SST and AXBT-derived SST on the same day. Although the basic schemes for calculating the grid values are markedly different, other parameters were kept constant in order to facilitate the comparison (i.e., the domain, the grid, the number of observations influencing each gridpoint, the phase speed used to advect asynoptic observations, the filter, and most, important, the input data field). Data were spaced approximately  $1.5\lambda$ .



The SST OA field using the inverse distance method was compared to the SST OA field using the Gandin method (Figure 3.7). The correlation between the two is 1.0 and the rms difference is 0.09°. Similar results were obtained in the other comparison. It is apparent that when the data are dense as in these two cases, the choice of OA techniques is not critical (Appendix D).

The advantage of the inverse distance technique over the Gandin method is speed of computation. The disadvantages are: there is no a priori estimate of error, there are no statistics utilized as in the Gandin method (thus, there is no statistical significance in the resulting field) and, there are no physics utilized in the scheme (same criticism of the Gandin technique).

### C. WINDS, COASTAL, AND BUOY DATA

#### 1. General

Oceanic conditions along the California coast were examined over a six month period from 1 July 1986 to 31 December 1986; this period more than covered the OPTOMA 23 survey (9 to 19 November 1986). Sea level data from NOAA/NOS tide gauges at six coastal stations; SST, 10 m winds, and sea level pressure data from nine National Data Buoy Center (NDBC) moored buoys; SST data from Granite Canyon (40 km south of Point Sur); Marine Boundary Layer (MBL) winds from the Fleet Numerical Oceanography Center (FNOC); and, Bakun upwelling indices at four positions were analyzed to characterize the Fall Transition (Figure 3.8).

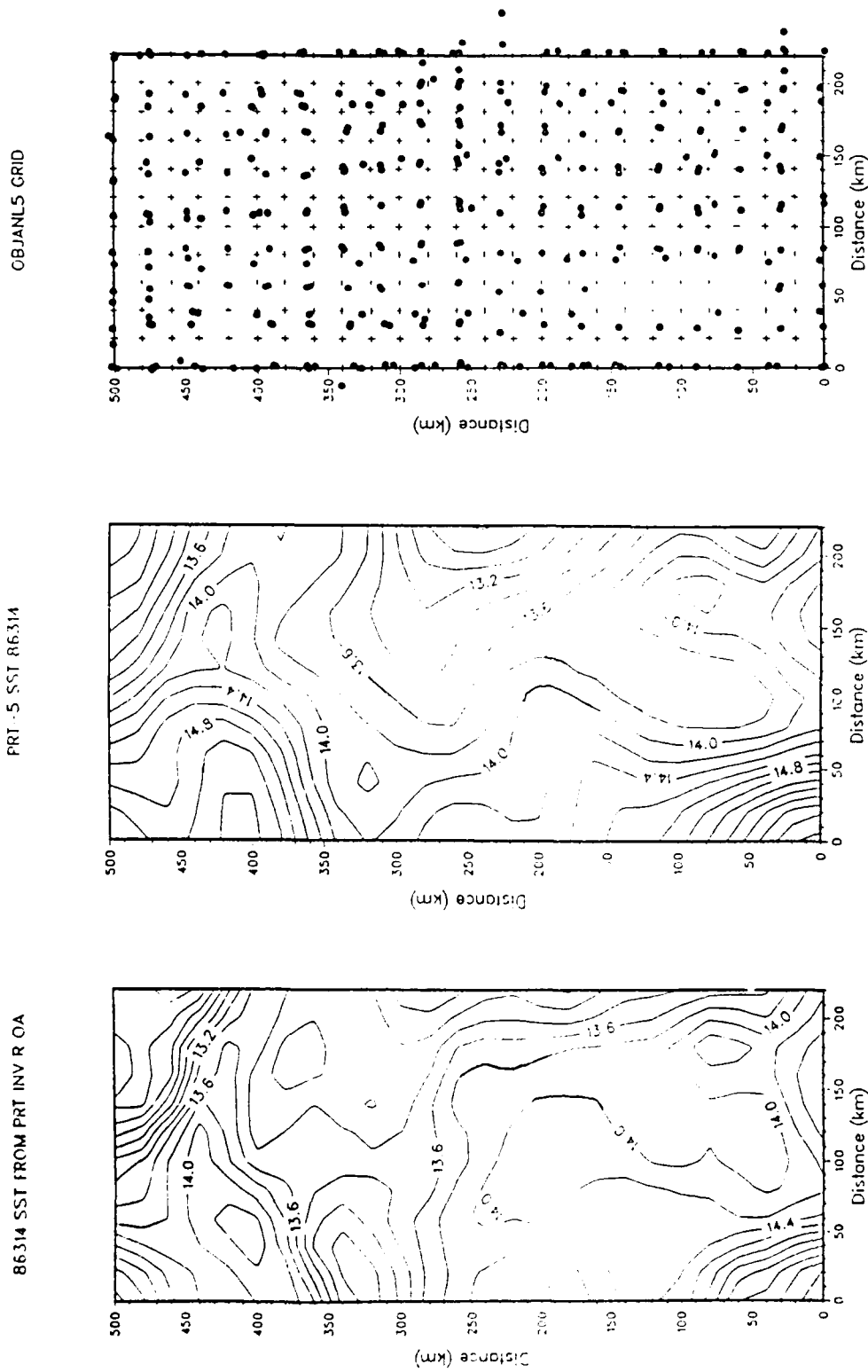


Figure 3.7 PRT-5 OA fields. Inverse distance weighted method (left), Gandin method (center), and data distribution (right).

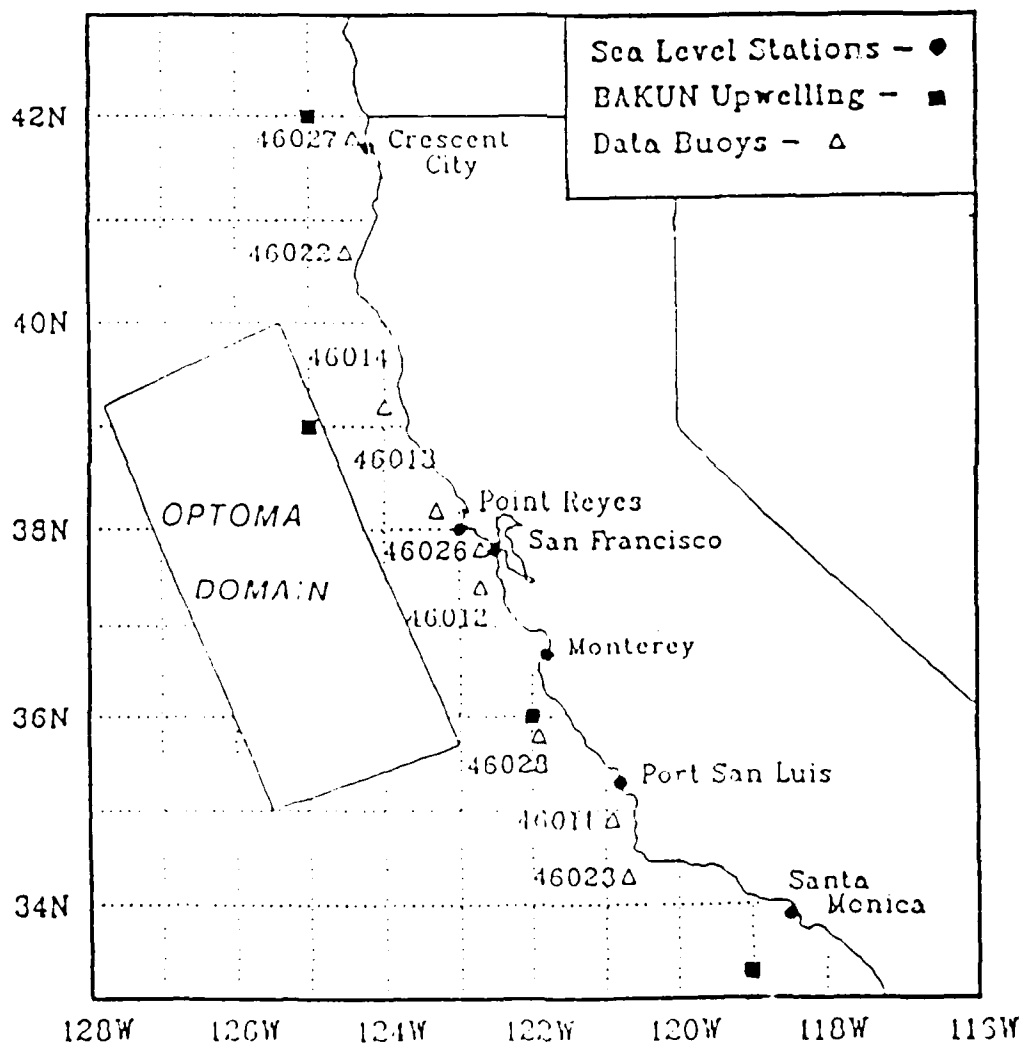


Figure 3.8 Positions of NDBC buoys, sea level stations, and Bakun upwelling index calculations.

## 2. Wind Stress

Wind data were from three sources: aircraft observations at 1000 feet (spaced ca. 50 km), moored buoy data at 10 m, and the MBL winds at 19.5 m. The MBL winds were the only source of daily, globally gridded (2.5 degree) data. The MBL data are a blend of wind data and six-hour forecast data from the Navy Operational Global Atmospheric Weather Prediction System (NOGAPS). The wind stress curl calculated from the MBL grid underestimates the actual wind stress curl because of the large grid spacing. Although measured at altitude, the aircraft winds provided a consistency check on the MBL winds. The NDBC winds were used to check the MBL analysis and they provided an estimate of the change in wind stress along the coast.

Wind stress was used in the analysis of the 1986 Fall Transition, and wind stress curl forces the surface layer of the QG model through Ekman pumping. Wind stress was computed from the 10 m winds using the drag law:

$$\tau = \rho_{\text{air}} C_d U_{10}^2 \quad (\text{equation 3.7})$$

where  $\tau$  is the stress magnitude,  $\rho_{\text{air}}$  is the density of air,  $C_d$  is the drag coefficient from Smith (1988), and  $U_{10}$  is the wind speed at 10 m. Stress from the MBL winds was computed in a similar manner using a drag coefficient for 19.5 m. For the transition analysis, the 10 m winds were decomposed into alongshore and cross-shore components using a counter-clockwise rotation of 20 degrees.

Smith (1988) provides an updated estimate of  $C_d$  which varies with wind speed (increases with higher wind speed) and stability (decreases as stability increases; vertical density gradients can add or remove vertical turbulent kinetic energy) from 0.9 to  $1.3 \times 10^{-3}$ . (Other formulas, e.g., Large and Pond, 1981, have overestimated wind stress). These coefficients are derived from data averaged over time periods less than one hour and are intended for use with observations, not with long period average values.

### 3. Bakun Upwelling Indices

Direct observations of upwelling velocities are not available and indications of upwelling in SST are qualitative. As an alternative, the offshore directed surface Ekman transport is used to define an index. Bakun upwelling indices were computed by the NOAA/NMFS Pacific Environmental Group. These indices describe offshore Ekman transport in cubic meters per second per 100 m of shoreline; the larger the number, the more transport offshore. Values along the coast at 3-degree intervals were calculated from FNOC 6-hourly objectively analyzed synoptic wind/pressure analyses (Bakun, 1973):

$$M = \tau / \rho f \quad (\text{equation 3.8})$$

where  $M$  is the index,  $\rho$  is density, and  $\tau$  is alongshore wind stress.

### 4. Granite Canyon SST

Granite Canyon is a coastal site 15 km south of Monterey (ca. 50 km north of NDBC buoy 46028 and 150 km southeast of NDBC buoy 46012)

included in this analysis to provide a coastal "benchmark" for comparison with SST measured offshore by the NDBC buoys. It is representative of open ocean measurements; the site has excellent exposure to the deep ocean with the continental shelf less than 10 km wide. Bucket SST's are measured to the nearest 0.1° C at ca. 0800 local daily; as such, there is the possibility of aliasing by the predominately semi-diurnal tide (Breaker and Mooers, 1986). The 1986 annual SST range is ca. 3.5° C with a minimum in April/May due to coastal upwelling and a maximum in September/October due to summer heating. In the fall, the mean temperature drops from 13.0° C in early October to 12.5° C in early November. With the fall transition, there is a 0.5° C rise in the middle of November followed by a drop to 12.4° C in early December.

#### 5. Filtering

All of these data, except the MBL winds, Bakun Indices and the Granite Canyon SST, were filtered using a Godin filter, which has a low pass of 0.0 to 0.8 cpd (30 hours) and a half amplitude of 0.4 cpd (66 hours), to eliminate diurnal and semi-diurnal components of the raw signal (Godin, 1972).

A two-week mean was computed and removed from the sea levels at each sea level station. The sea level deviations were hydrostatically corrected for atmospheric pressure:

$$SL_{adj} = (SL(t) - SL_m) - (SLP(t) - SLP_m) \times R \quad (\text{equation 3.9})$$

where  $SL_{adj}$  is the atmospherically adjusted sea level deviation,  $SL(t)$  is the filtered sea level,  $SL_m$  is the sea level mean at that station,  $SLP(t)$  is the filtered sea level pressure,  $SLP_m$  is the sea level pressure mean at the nearest NDBC buoy, and  $R$  is the hydrostatic ratio of 1.0 cm depression in SL for each 1.005 mb increase in atmospheric pressure.

#### D. CLIMATOLOGY

##### 1. General

Climatological or historical data are required to: (1) provide a T-S relationship, (2) benchmark model performance, and (3) to initialize the QG model (by providing a vertical profile of the mean Brunt-Vaisala frequency). CalCOFI data, OPTOMA 13 data, and GDEM climatology were used.

##### 2. Generalized Digital Environmental Model

The Generalized Digital Environmental Model (GDEM), the Navy standard climatology, was initially developed to define homogeneous sound speed provinces. It can provide, among other things, a "synthetic" oceanographic station with temperature and salinity for any location with minimal computer resource requirements and with adequate resolution for acoustic modeling purposes. GDEM consists of monthly coefficients for models of ocean temperature, salinity, and sound speed on a 30 minute grid. The coefficients are derived from fitting observations from the Master Oceanographic Observation Data Set (MOODS) and other data

sets held at the Naval Oceanographic Office, but not yet added to MOODS (Davis et al., 1986). GDEM has not been used in the OPTOMA domain.

The basic functional form in the top 400 m is the squared amplitude response of a Butterworth filter which describes the vertical profile from the surface to the base of the seasonal thermocline and an exponential tail which extends the model to 400 m:

$$T(D) = \frac{(T_0 - T_4) [1 + (\pi_1/A)^{2B}]}{[1 + (D/A)^{2B}] (\pi_1/A)^{2B}} + T_4 - \frac{(T_0 - T_4)}{(\pi_1/A)^{2B}}$$

(equation 3.10)

where,  $T(D)$  is the temperature at depth,  $D$ ,  $A$  is the coefficient describing the depth of the mid-thermocline,  $B$  is the coefficient controlling the vertical derivative,  $\pi_1$  is the depth of the seasonal thermocline,  $T_0$  is the surface temperature, and  $T_4$  is the temperature at the depth of the mid-thermocline. (Observed temperatures are normalized.) This function is fit to historical temperature profiles which have been quality controlled, edited, and binned, geographically and seasonally.

The model is in three layers. The shallow top layer, to 400 m, has temperature in three-month seasons (except for surface temperatures which are monthly) and salinity in five-month bins. The "global" rms error of fit is less than 0.5° and 0.1 ppt, respectively. At mid-depth,



to 2000 m, the bins are six months for both temperature and salinity, and in the deep layer, the bins are 12 months.

## E. ANALYSIS OF REMOTELY SENSED DATA

### 1. AVHRR

#### a. General Processing

AVHRR data are used to update and verify the ODPS outputs by filling in gaps between intensive 3-D samplings. This additional data source is used to provide MCSST fields, surface velocity fields obtained from feature displacement in successive images, and guidance for the selection of conventional data inputs.

The SST variations in the OPTOMA area cover about a 6° C range and have maximum gradients of the order of 1° C/10 km. The minimum wavelength which can be resolved using AVHRR imagery is an order of magnitude smaller than  $\lambda$  and the mesoscale features of interest are about 50 to 100 km in size. Assuming that there is a discernable and persistent surface expression, the features change intensity, advect, and propagate slowly enough so that no details important to the mesoscale field are lost with imagery available every 12 to 48 hours.

Pairs of useful images preferably 12 to 48 hours apart are required to compute surface velocities using a NPS program called OCEANTRAK. This program is based upon a meteorological cloud motion vector analysis technique. An estimate of the error in each approach is of interest.

Satellite data were recorded at the Scripps Satellite Ocean Facility (SSOF). From 1982 through 1985, NOAA-7 passes were routinely

recorded for OPTOMA surveys; NOAA-6 and 8 were recorded only on special occasions. NOAA-9 and NOAA-10 became operational in 1985 and 1986, respectively. OPTOMA 23 images were obtained from the latter two satellites.

Images of the OPTOMA domain from June and July 1985 (OPTOMA 5), May through November 1984 (OPTOMA 11, 12, 13, and 14), July 1985 (pre-OPTOMA 17), April (OPTOMA 20), July, August (OPTOMA 21 and 22), and November 1986 (OPTOMA 23) were reviewed and graded on an arbitrary usefulness scale of 1 to 10. Images with ratings of 8 and above were considered to be excellent; 6 to 8, good but degraded by cloud cover; 4 to 6 usable only in composites. When possible, visual and IR images were viewed side-by-side to help discern low level clouds from sea surface features.

About 300 images (about one-third of the total) were judged to be good to excellent (Table 2). In contrast to the conclusion reached by Fiedler et al. (1985), from his partial review of imagery available during the OPTOMA surveys, it appears that adequate numbers of good images are available as sources for data.

Weather was the most important factor degrading the usefulness of the image. The area off Point Arena is under the regional storm track in winter and low stratus or fog is prevalent in the summer. Satellite precession, and the resulting movement of the field of view, was another prohibitive factor. Every ten days or so, the OPTOMA domain would be on the extreme boundary of or would completely fall out of the field of view.

TABLE 2. AVHRR IMAGERY AVAILABLE DURING SELECTED OPTOMA SURVEYS.

1983	JUN	JUL	AUG	SEP			
excellent	14	11	03	02			
good	15	20	16	12			
total	<u>29</u>	<u>31</u>	<u>19</u>	<u>14</u>			
1984	MAY	JUN	JUL	AUG	SEP	OCT	NOV
excellent	19	09	20	27	20	06	01
good	06	12	20	10	12	08	10
total	<u>25</u>	<u>21</u>	<u>41</u>	<u>37</u>	<u>32</u>	<u>14</u>	<u>11</u>
1985	JUL						
excellent	02						
good	10						
total	<u>12</u>						
1986	MAR	APR	JUN	JUL	AUG	NOV	
excellent	00	01	03	15	02	20	
good	01	05	00	01	00	10	
total	<u>01</u>	<u>06</u>	<u>03</u>	<u>16</u>	<u>02</u>	<u>30</u>	

b. Satellite Images During OPTOMA 23

The OPTOMA 23 images were first viewed on a Chromatics GKS system at the Institute for Naval Oceanography (INO). Channel 2, the visual channel recorded during the day, provided images which were crucial in determining whether or not features near the coast identified in IR channels were low stratus, fog, or sea surface. Images from channel 3 had systematic noise in them, although NOAA-10 was less noisy than NOAA-9. The best cloud free images were recorded on 10, 11, and 21 November, Julian dates 314, 315 and 325, respectively (Appendix E). Usable, partially cloudy images were recorded on 9, 15, 16, 17, and 19 November, Julian dates 86313, 86319, 86320, 86321 and 86323, respectively. The remaining images recorded on 8 and 20 November were too cloudy (Table 3).

Twelve passes over the CCS during the period from 8 November (Julian date 86312) through 21 November (Julian date 86325) were recorded. During the day, channels 2,3,4, and 5 were copied; at night, only the IR channels (3,4, and 5). The resulting 44 images were reduced to 512 by 512 8-bit arrays centered on Point Reyes (38.5 N, 128.3 W). The images were corrected for curvature and earth-located using two landmarks to within ca. one km and sensor counts were converted to relative temperatures at the receiving site.

c. Level-4 Processing

The usable images were further processed. These images were screened for clouds and land contamination using threshold temperatures for clouds and land obtained on the Chromatics system. The 512 by 512 arrays covered the OPTOMA domain north of 35 N. Each pixel was navigated

TABLE 3. OPTOMA 23 IR IMAGERY

<u>DATE</u>	<u>JULIAN</u> <u>DATE</u>	<u>TIME</u> <u>(GMT)</u>	<u>NOAA</u> <u>SAT</u>	<u>CLOUD</u> <u>COVER</u>	<u>TIME OF</u> <u>A/C SURVEY</u>
07 Nov	86311				
08 Nov	86312	2216	9	CLOUDY	
09 Nov	86313	2206	9	PARTIAL	1800-2359 (P1)
10 Nov	86314	1623	10	CLEAR	
		2154	9	CLEAR	1900-0130 (P2)
11 Nov	86315	1203	9	CLEAR	
		2145	9	CLEAR	
12 Nov	86316				
13 Nov	86317				
14 Nov	86318				
15 Nov	86319	2242	9	PARTIAL	
16 Nov	86320	1110	9	PARTIAL	1700-0200 (P3)
17 Nov	86321	2221	9	PARTIAL	2000-0130 (P4)
18 Nov	86322				
19 Nov	86323	2159	9	PARTIAL	
20 Nov	86324	1207	9	PARTIAL	2100-0200 (P5)
21 Nov	86325	1157	9	CLEAR	

to a latitude and longitude grid (estimated accuracy of 1.2 km) and channels 4 and 5 were screened for clouds and land mass (Table 4). Those pixels within the OPTOMA domain, ca. 57% of the total, were used in calculating absolute SST from a split-channel algorithm (equation 2.11).

The Interactive Digital Environmental Analysis (IDEA) Laboratory at NPS was used to enhance the images and to perform surface motion vector analysis using OCEANTRAK. The enhancement curve assigned an 8-bit gray shade value of 0 to temperatures warmer than 18° C and a value of 255 to temperatures colder than 9° C. Temperatures in between were linearly interpolated. These values highlighted the oceanic features in the OPTOMA domain.

The OCEANTRAK system produced nine sets of vectors (a total of 220) from eight images. All of the images had numerous small-scale features, ca. 10 km in diameter, suitable for tracking. The usable time difference between images was from 6 to 48 hours. (Svejkovsky, 1988, tracked somewhat larger features through a maximum of 36 hours time difference off Southern California in the winter.) Six hours was the minimum separation time between sequential images. Motion was hard to discern except near filaments. Beyond 48 hours, the small scale features became unrecognizable. Masking of parts of the domain by clouds was the most prohibitive factor.

Qualitatively, there is good agreement between the geostrophic fields and the satellite surface vector fields. Differences are attributed to errors within the vector analysis approach (e.g., non-linear flow, distortion of surface features, and operator error), ageostrophic effects, and a different level of no motion than that

TABLE 4. AVHRR TEMPERATURE STATISTICS

<u>Image</u>	<u>% Cloud or Land</u>		<u>Range</u>		<u>Mean</u>	<u>Std Dev</u>
	<u>Screened from</u>		<u>(° C)</u>			
	<u>Channel:</u>		<u>From</u>	<u>To</u>	<u>(° C)</u>	<u>(° C)</u>
	<u>4</u>	<u>5</u>				
312	27	29	10.2	20.2	14.1	1.2
313	34	45	9.0	20.5	12.9	1.8
314A	9	9	8.4	19.9	13.7	1.3
314B	12	12	7.8	14.3	11.4	1.3
315N	12	11	6.9	15.7	13.3	1.3
315	34	34	8.2	23.1	13.2	1.5
319	36	39	7.7	20.8	13.5	1.7
320	44	55	7.5	15.5	12.9	1.4
321	32	33	9.3	21.0	14.1	1.4
323	14	18	9.2	22.1	13.6	1.7
324	71	72	8.9	13.7	11.4	1.0
325	17	18	9.2	15.9	13.6	1.1

assumed in this analysis. The satellite vector fields are apparently repeatable.

An estimate of error includes navigation errors, operator errors and non-translational errors. All errors have a different impact depending upon the time difference between images. For the navigation error, with the images registered to within one pixel, the minimum discernable motion over a 48 hr period equates to advection of ca. one cm/s; the same translation observed in images over a six hour period equates to advection of ca. five cm/s. For operator error, the minimum translation discernable for a 10 km diameter feature could result in a five km displacement of the true position.

## 2. GEOSAT

GEOSAT data, provided by Dr Ziv Sirkes of the Institute for Naval Oceanography but visiting at the Woods Hole Oceanographic Institution, were originally acquired at the Applied Physics Laboratory (APL) at Johns Hopkins University. APL created Geophysical Data Records with time, latitude, longitude, altitude (ten measurements per second), statistics, and flags. These records were available through the National Environmental Satellite Data and Information Service (NESDIS).

There are 244 ERM orbits world-wide, spaced ca. 164 km apart at the equator. The "Bermuda Orbit" is designated A000. Six orbital sub-tracks pass through the OPTOMA domain (Figure 3.9); two are ascending orbits, which pass parallel to the coast, but perpendicular to the cool filaments, A119 and A162; four are descending orbits which cross offshore, D042, D085, D128, and D171. The first four 17-day repeat



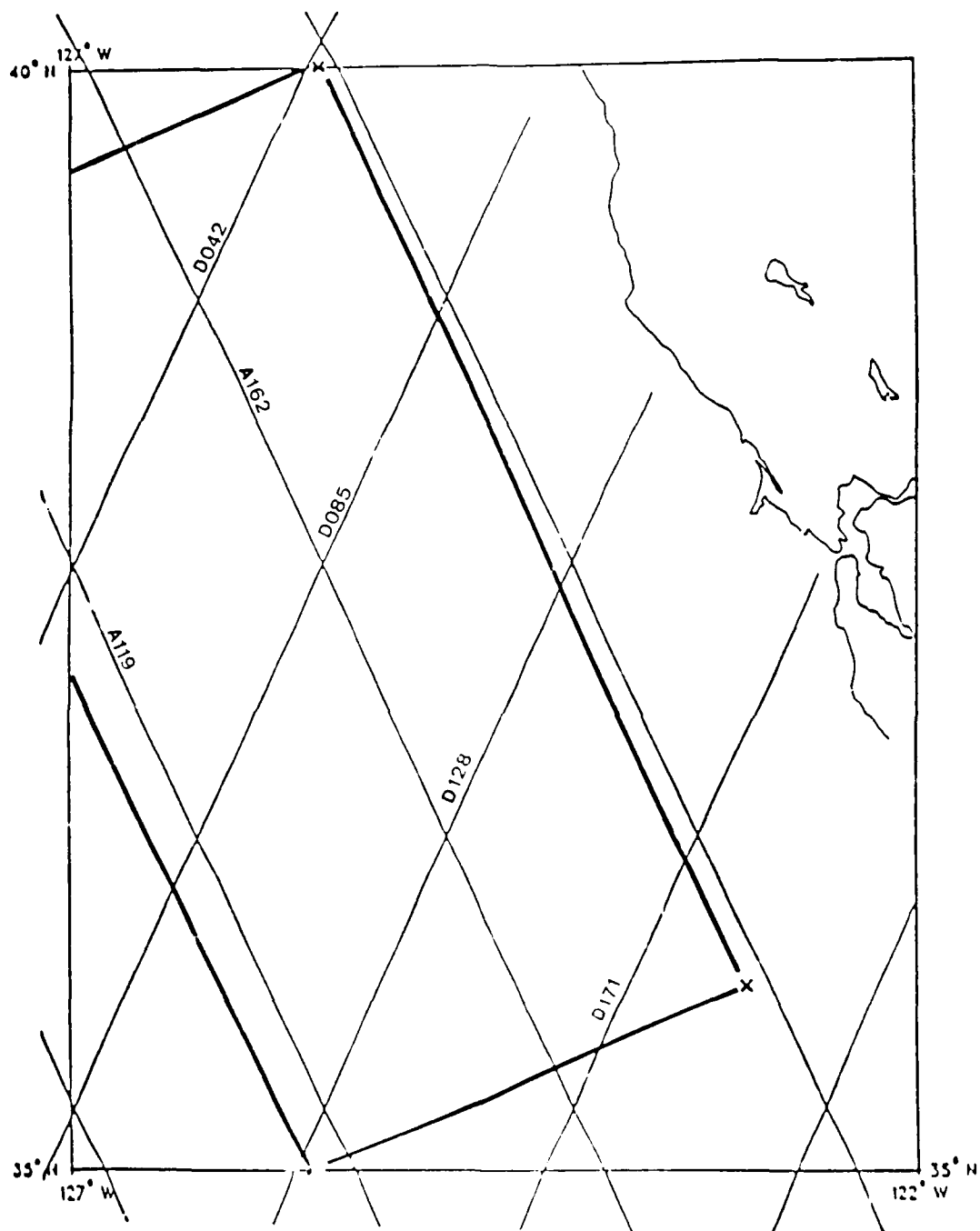


Figure 3.9 GEOSAT ascending (A) and descending (D) sub-orbital tracks off Central California (OPTOMA 23 domain is highlighted).

orbits are of interest. These were on 8 Nov 86 (the ERM was declared stable and operational on this day), 25 Nov 86, 12 Dec 86, and 29 Dec 86 (Julian dates 86312, 86329, 86346, and 86363, respectively).

The data were processed with the colinear technique and two corrections were applied by Dr Sirkes: the long term mean, based upon the 46 repeat orbits then available, was removed from 30-degree arcs through the domain, and tides were corrected using the Schwiderski tidal model. Unfortunately, removal of the long term mean not only removes the geoid, but also the steady and long-period ocean phenomena. No moisture corrections were made. The final records contained position (latitude and longitude) and sea surface height (SSH) measurements every second (ca. 7 km alongtrack spacing).

Autocorrelations were calculated for each 17-day orbit ensemble. The zero crossing for the autocorrelation was ca. 110 km, roughly the same as the zero crossing for in situ observations of SDH. The range of values and standard deviations were also similar, ca. 20 and 30 cm, respectively. OA fields of SSH were calculated for each day using the same OA routine as used for in situ fields.

#### F. SUMMARY OF DATA ACQUISITION, PROCESSING, AND ANALYSIS

OPTOMA 23 incorporated data from many sources: in situ data (aircraft, ship and buoys), satellite data (AVHRR and GEOSAT), coastal data (SL and SST), and climatology. The key component of the survey was the dedicated use of the Project BIRDSEYE RP-3D which flew six flights from 9 to 19 November 1986 (Julian dates 86313 and 86323, respectively).

Ca. 100 AXBT's were dropped at 30 km intervals during surveys of NOCAL and CENCAL (two in each subdomain), and at 40 km intervals during a boundary condition update flight. A salinity profile was estimated for each AXBT using either a historical or an observed (from the ship survey in the southern part of the domain) T-S relationships. Both T-S relationships were similar to CalCOFI climatology.

Daily OA maps were generated for SST, MLD, T50, Z08, Z10, and dynamic heights. The "standard" OA statistical method used: ensemble autocorrelation functions (with zero crossings ca. 100 km) specific to each data type, a temporal window of 3 days, a spatial window of 75 km, a westward propagation of 5 km/day (for the days between surveys), and a Shapiro filter.

Subsampling of the densest data set, the PRT-5 data, indicated that relatively accurate (with correlations of 0.70 or better) OA fields could be reproduced with one-quarter densities when care was taken in selection of data. An inverse distance OA technique produced roughly similar fields, without error estimates.

For an analysis of the 1986 Fall Transition, hourly SL at six coastal locations were filtered (to remove diurnal effects) corrected for the inverse barometer effect, and daily-averaged. Hourly wind data from NDBC buoys were also filtered and daily-averaged. Wind stress was calculated, using drag coefficients from Smith (1988), from both NDBC winds and FNOC MBL winds. As indicators of upwelling, daily Bakun Upwelling indices (at 33, 36, 39, and 42 N latitude), hourly SST from NDBC buoys (filtered and daily-averaged) and Granite Canyon SST (daily) were processed and plotted.

For quantitative comparison, evaluation techniques focused upon difference fields, RMSE, and pattern correlation between various fields (Willmott et al., 1985). GDEM climatology was processed in the same manner as observed data to provide a first order comparison.

Although the domain was often cloudy, 12 AVHRR useable images were recorded and processed. These produced MCSST OA fields and nine sets of surface motion vectors (from pairs of images as much as 48 hours apart).

The first four GEOSAT17-day ERM orbits were on 8 November, 25 November, 12 December, and 29 December (the first two bracket the OPTOMA 23 survey). Six orbits (two ascending and four descending) were colinearly processed for each ERM orbit; the long term means were removed (taking care of geoid and orbit error) and the data were corrected for tides. The resulting SSH had ranges of values and autocorrelations similar to those for in situ SDH. OA fields of SSH were mapped for each of the four Exact Repeat Mission days.

#### IV. DESCRIPTION OF OPTOMA 23 FIELDS

##### A. INTRODUCTION

###### 1. General

The OPTOMA 23 domain was dynamically active with two anticyclonic features and two cyclonic features (AC1 off Point Arena, AC2 off Monterey Bay, C1 off Cape Mendocino, and C2 on the western boundary, Figure 4.1). There was one cool filament, off Point Reyes, which extended westward into and, eventually, through the domain (other cool filaments, visible in IR imagery, off Point Arena and Point Sur, did not extend into the domain).

The observed (and later the QG-predicted) fields were qualitatively compared to earlier OPTOMA surveys, OPTOMA 18 and 22, and quantitatively compared to two benchmarks: climatology and persistence. The climatological benchmarks were objective analyses of GDEM-derived data. The persisted benchmarks were objective analyses of data from the first two surveys. (Wind forcing, bottom topography, and in situ data from the OPTOMA 23P3 survey off Monterey Bay are discussed in later chapters).

###### 2. GDEM Fields

OA climatology fields of SDH (referenced to 450 m) for the months of October, November, and December were qualitatively similar with broad and slow (ca. 7 cm/s) southward flow of the California Current and large meanders with wavelengths of ca. 500 km. There was a persistent anticyclonic feature, with a diameter of ca. 200 km, in the northwest corner of the domain. It weakened from 90 dyn cm in October to 85 in

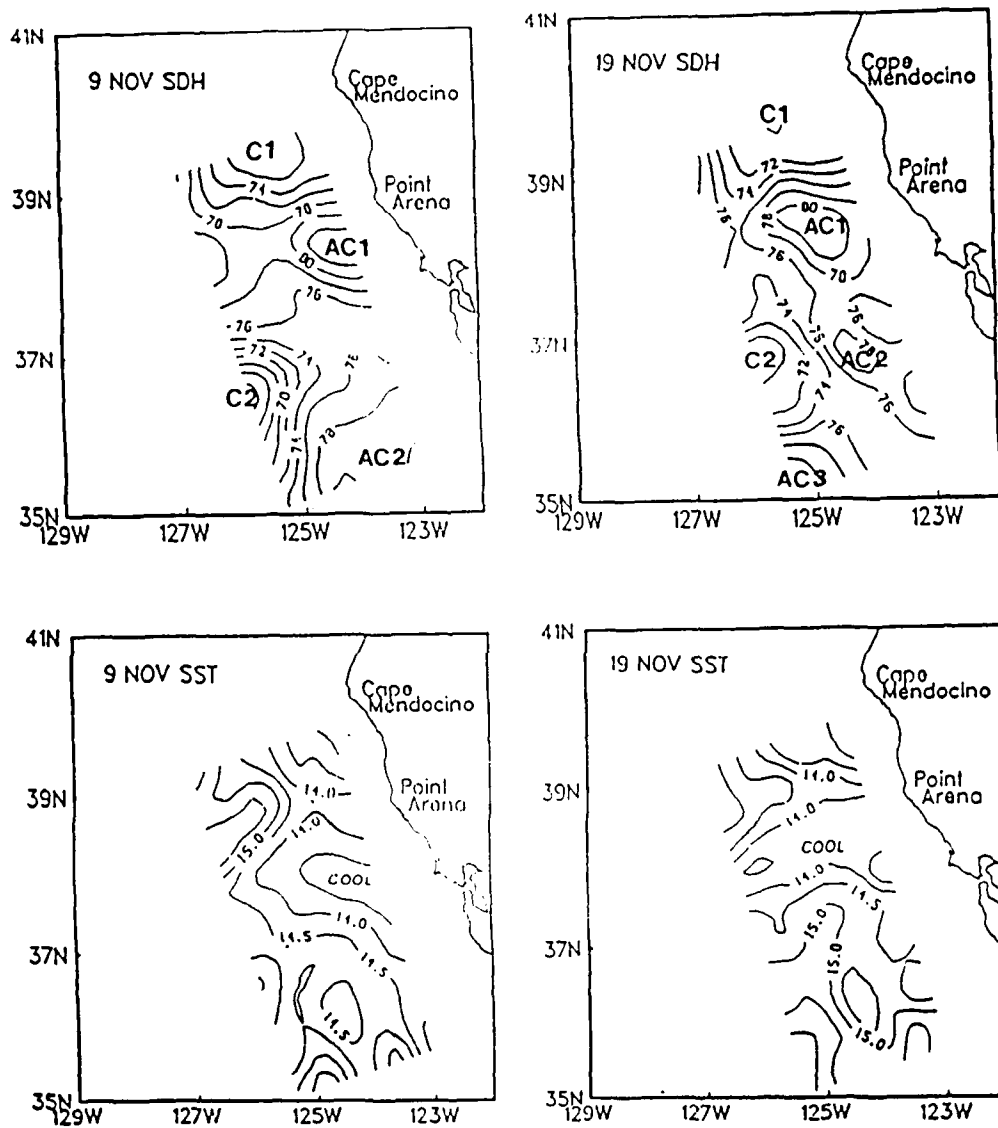


**Figure 4.1** SDH (contoured at 2 dyn cm intervals, ref 450 m) and SST (contoured at 0.5 °C) from in situ data, 9 and 19 November 1986 (Julian Dates 86313 and 86323). AC2 apparently moved northwest and another anticyclonic feature (AC3) formed on the southeast border.

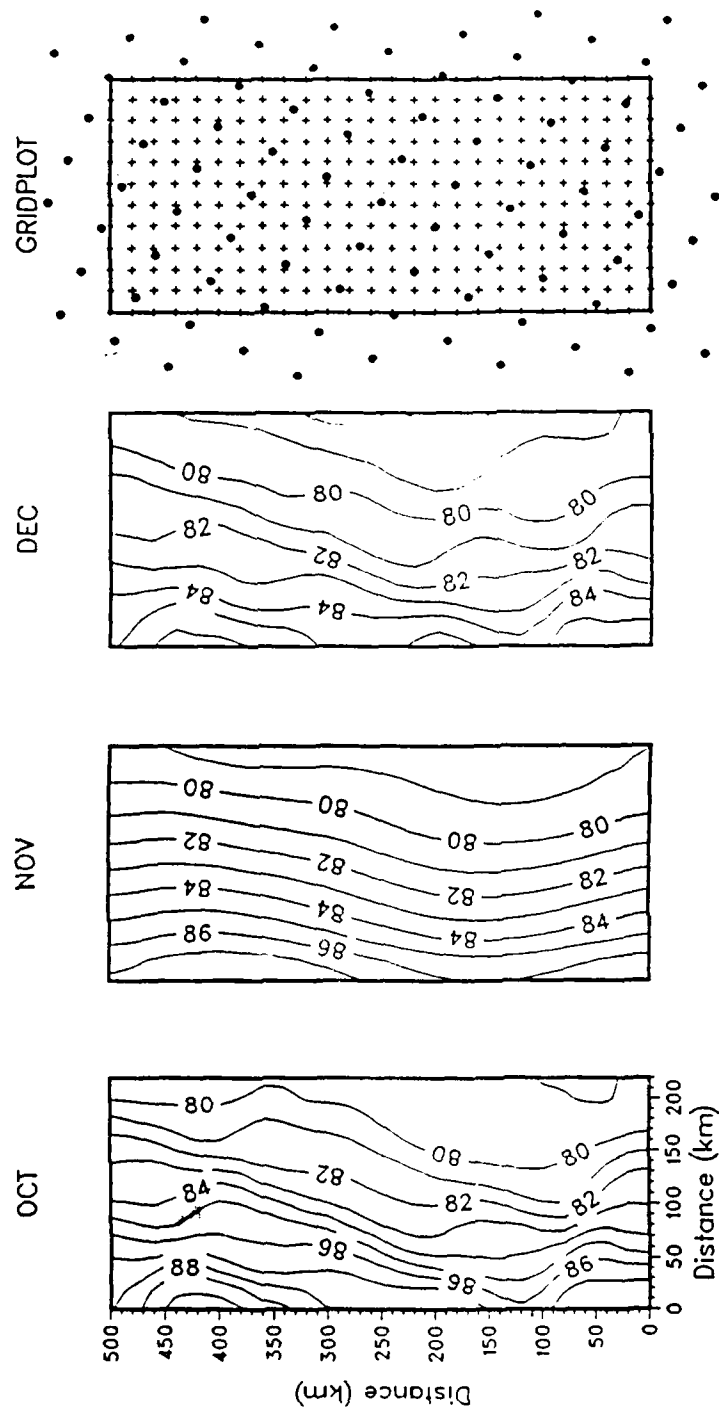


Figure 4.2 SDH (referenced to 450 m) from GDEM climatology for the months of October, November, and December and gridplot. (Gridplot is valid for all GDEM fields).

December (Figure 4.2). The range of values was consistent with the observed range; also consistent were the slight decreases in dynamic range, mean, and standard deviation ( $\sigma$ ) from October through November (Table 5).

OA climatology fields of SST, T50, T100, MLD, Z08, and Z10 also had similar means and ranges as observations (Figures 4.3 and 4.4). Of note, the T100, Z08, and Z10 fields had features on the eastern boundary indicative of the California Undercurrent (CUC). However, instead of flowing northward through the domain, the apparent CUC reversed cyclonically to join the California Current. The weak cyclonic feature in the southeast corner of the domain was distinguishable in dynamic topography at subsurface levels through the water column (Figure 4.5).

The difference in November climatological SDH, referenced to 300 m, and that referenced to 450 m, was 19.3 dyn cm (16.7 and 19.0 dyn cm were the differences calculated from OPTOMA 23 data and the entire OPTOMA ensemble, respectively). The SDH with a 300 m reference level had a dynamic range of 10.1 dyn cm and a maximum velocity of 6.5 cm/s; the 450 m reference level, 9.9 dyn cm and 6.9 cm/s; and, the 750 m reference level, 9.5 dyn cm and 6.5 cm/s (Figure 4.6).

450 m was not a "true" reference level, i.e., a level of no motion. This was demonstrated in the tilt of the temperature field at 450 m. The climatological temperature at 450 m was ca. 5.8 °C. The depth of the 5.8 °C isotherm shoaled from 500 to 400 m across the domain (over 225 km); the north-south variation in depth was ca. 50 m (over 550 km). However, the selection of a shallow reference level, at 300 or 450 m, was satisfactory in that topographies referenced to these levels



TABLE 5. GDEM BASIC STATISTICS

<u>Field</u> <u>(Units)</u>	<u>Range</u> <u>from</u> <u>to</u>		<u>Mean</u>	<u><math>\sigma</math></u>
GDEM SDH FIELDS				
SDH (OCT)	79.0	90.2	83.3	3.2
SDH (NOV)	78.4	88.3	82.2	3.0
SDH (DEC)	77.8	86.4	81.7	2.4
(dyn cm)				
OCTOBER				
SST	12.8	16.9	14.9	0.9
T50	10.7	14.4	11.8	0.9
T100	9.2	10.4	9.6	0.2
(°C)				
MLD	8.4	47.2	28.8	8.0
Z10	62.7	119.9	81.4	11.6
Z08	204.6	268.8	227.5	11.6
(m)				
NOVEMBER				
SST	12.4	15.5	14.0	0.7
T50	10.6	14.0	11.9	0.9
T100	9.1	10.4	9.5	0.2
(°C)				
MLD	13.0	30.8	22.7	4.1
Z10	66.5	120.5	79.4	10.9
Z08	188.1	251.6	216.3	12.5
(m)				
DECEMBER				
SST	10.9	14.5	12.8	0.8
T50	10.4	13.5	11.6	0.7
T100	9.1	10.4	9.6	0.2
(°C)				
MLD	9.0	42.2	22.6	7.4
Z10	64.8	115.5	83.5	10.3
Z08	192.0	262.8	225.8	14.0
(m)				

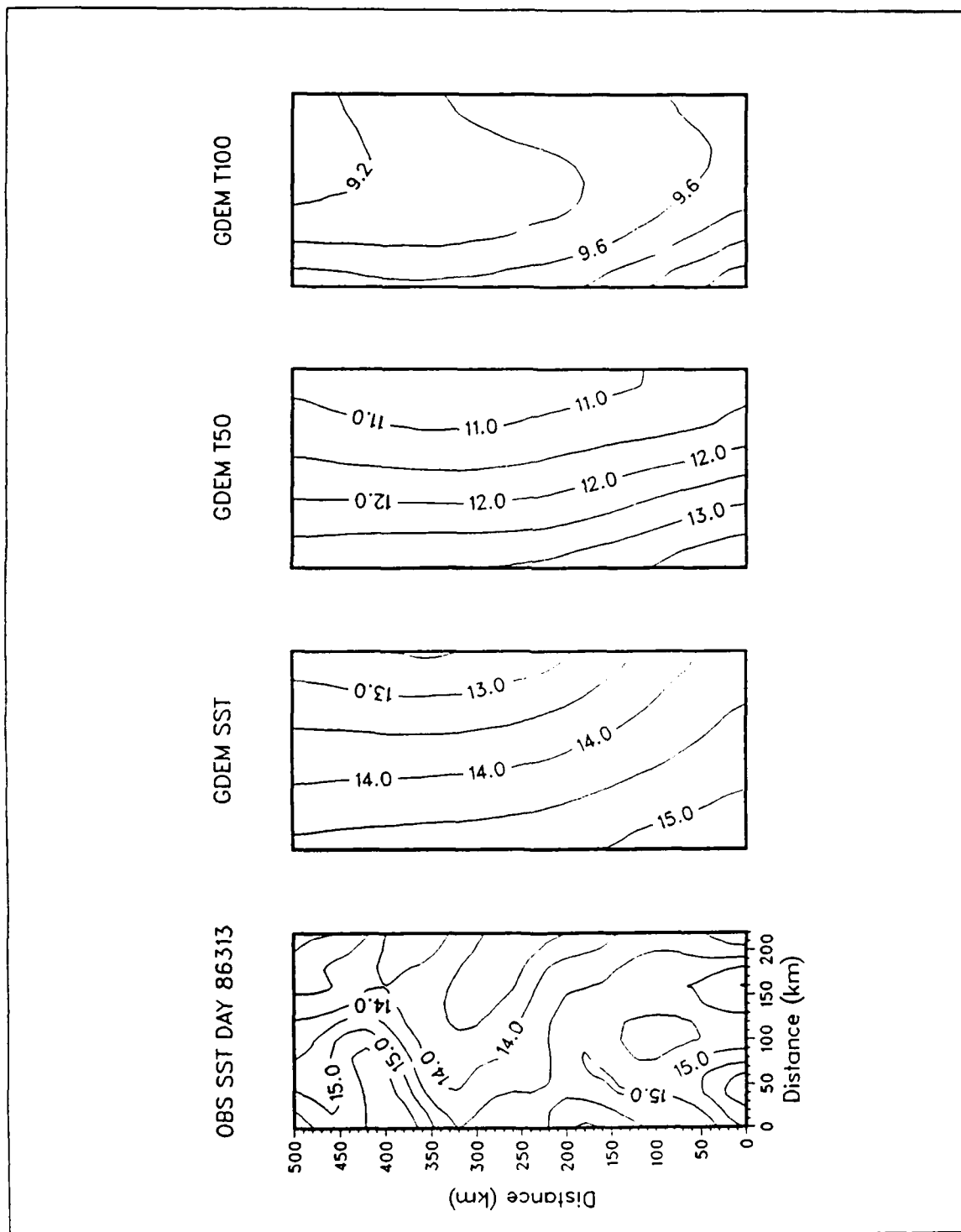


Figure 4.3 Observed SST; SST, T50, and T100 from GDEM climatology for the month of November.

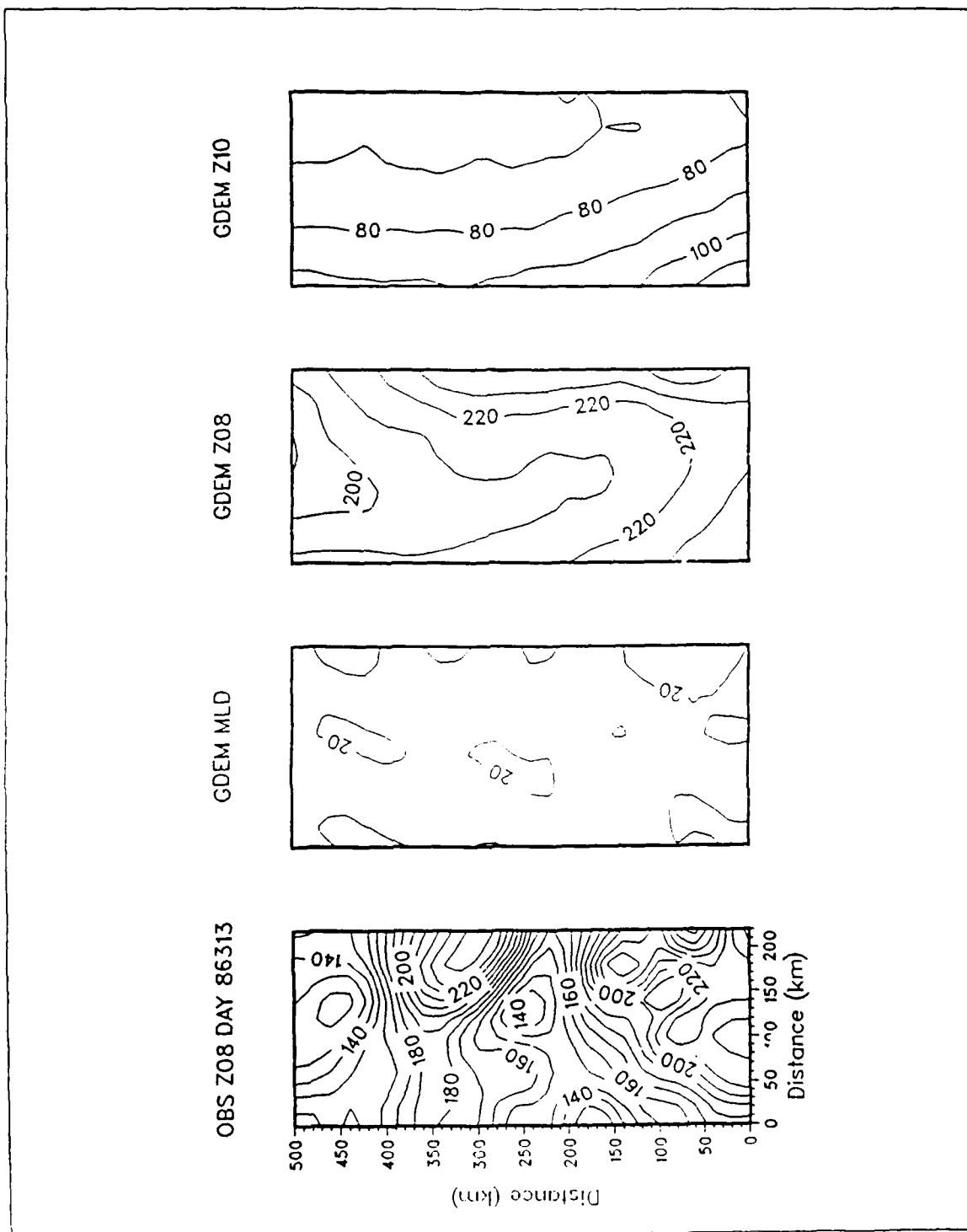


Figure 4.4 Observed Z08; MLD, Z08, and Z10 from GDEM climatology for the month of November.

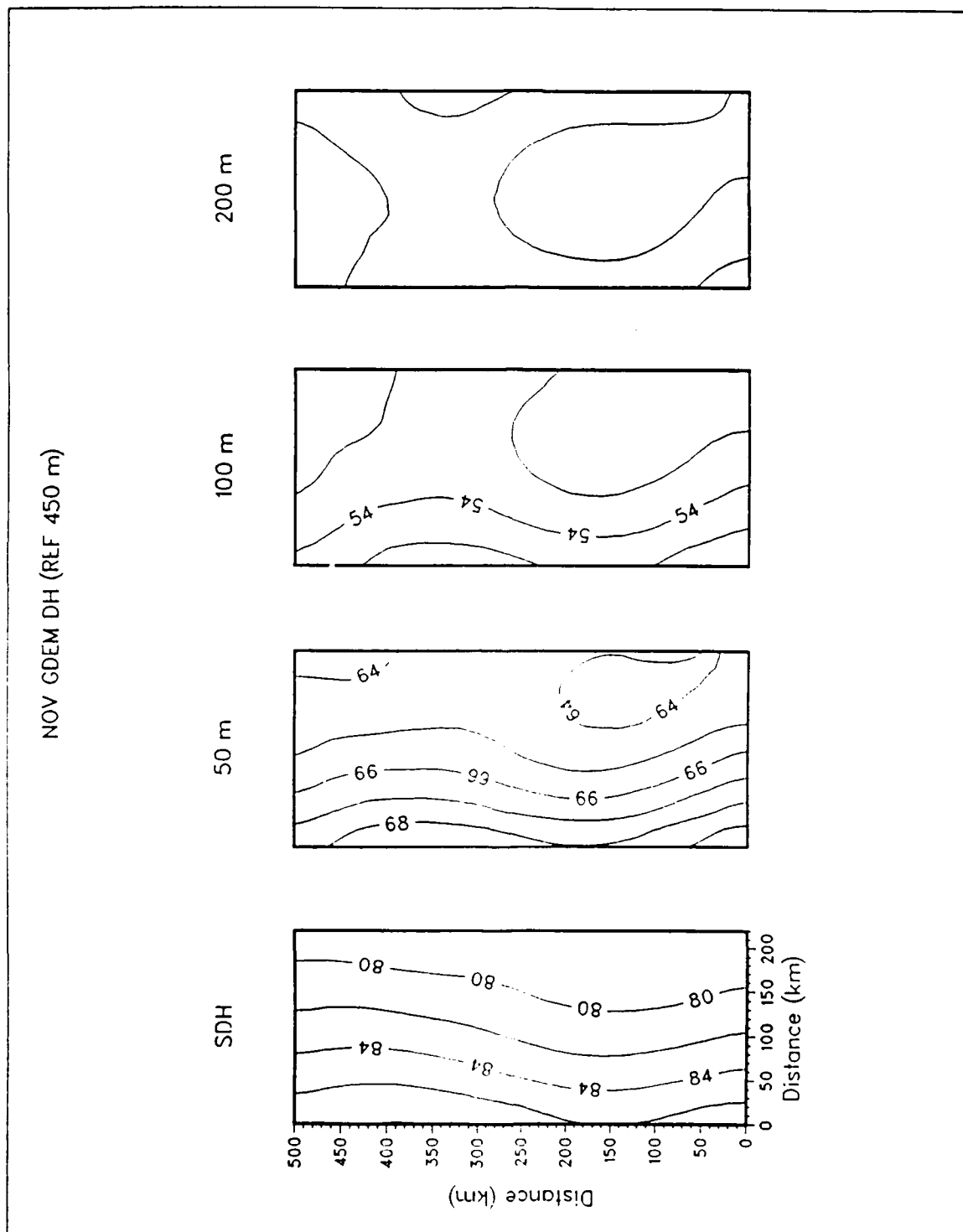


Figure 4.5 November GDEM dynamic heights at the surface, 50, 100 and 200 m (all referenced to 450 m). A weak cyclonic feature in the southeast corner of the domain is evident at depth.

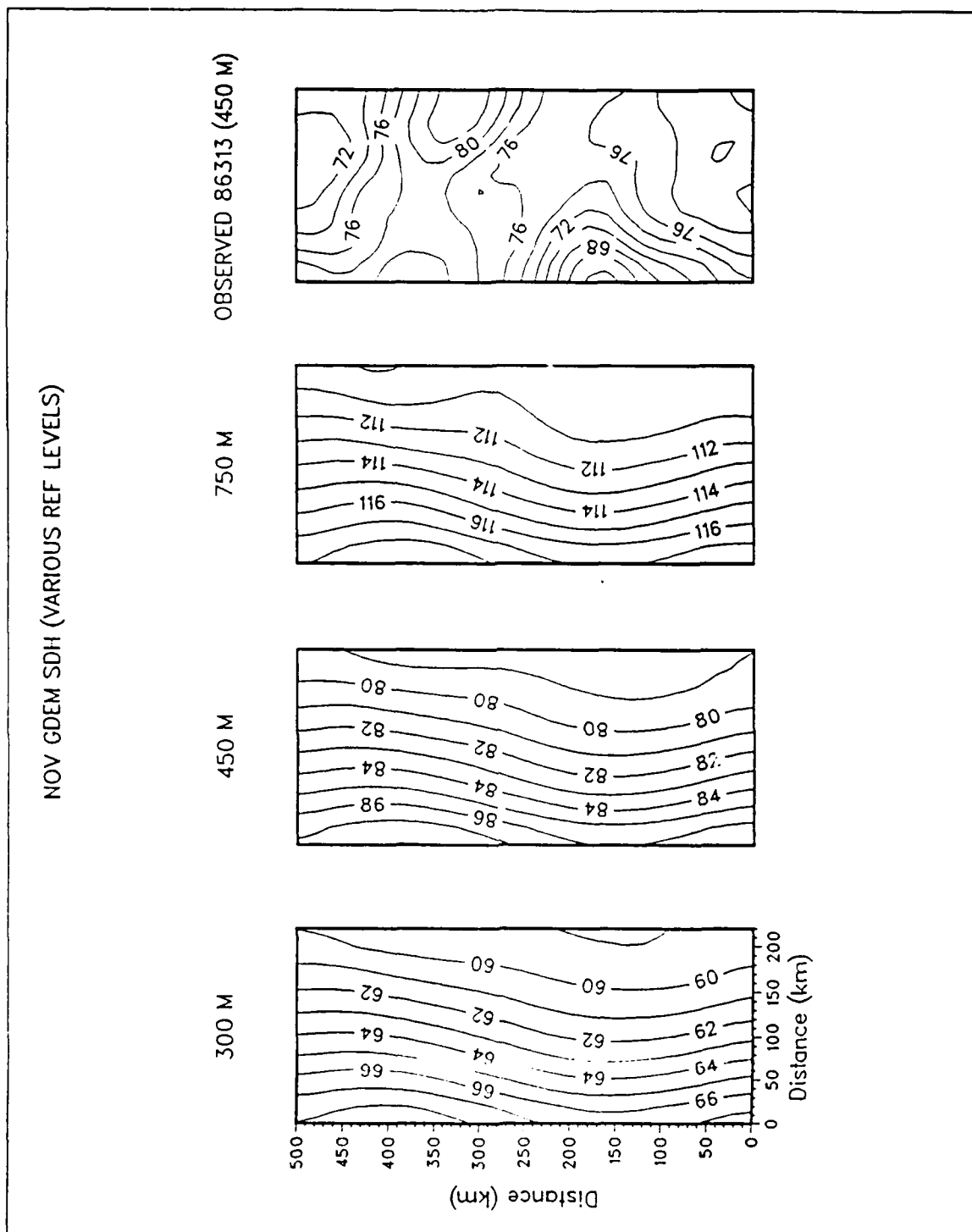


Figure 4.6 SDH (referenced at various levels) from GDEM climatology for the month of November. SDH from in situ data is for comparison.

adequately depicted the flow. (The use of the abbreviation SDH will imply a 450 m reference level, hereafter).

### 3. A Review of OPTOMA 18 and OPTOMA 22

The entire domain from Cape Mendocino to Point Sur was surveyed four times during the OPTOMA program (twice by aircraft, OPTOMA 18 and 23). November surveys were conducted each year from 1982 through 1986; however, all but one, OPTOMA 18 in 1985, were in domains too small to provide useful comparisons to OPTOMA 23. Prior to OPTOMA 23, from 27 July to 5 August 1986, OPTOMA 22 surveyed the NOCAL domain and the inshore area to the continental shelf (by ship).

OA fields of SDH, SST, MLD, Z08, and T50 were produced for most OPTOMA surveys using the ODPS OA routine with a single covariance function, based upon the SDH covariance with a zero crossing of 79 km, and a single phase propagation, 5 km/day to the west (Rienecker et al., 1987). In general, throughout the OPTOMA program, meanders during the summer were "sharper" and eddies were more densely packed than those during the winter. The means and standard deviations ( $\sigma$ ) of SDH were larger in the summer than in the winter. The mean SDH of anticyclones in the summer was 100 dyn cm; in the winter, 88 dyn cm. There was a smaller difference for cyclones, 83 and 80 dyn cm, respectively (Rienecker and Mooers, 1988).

OPTOMA 18, surveyed the same domain as OPTOMA 23, from 31 October to 2 November 1985 (this was not an anomalous El Nino period). A meandering southward jet, with an apparent wavelength of ca. 300 km, was ca. 200 km offshore and had a speed of ca. 15 cm/s. Two cold nearshore cyclonic features, one located off Point Arena and the other off Point

Reyes, were south of cool filaments. There was warm anticyclonic activity on the western boundary with one feature off San Francisco and another off Monterey (Figure 4.7). The maximum SDH and SST gradients, associated with the jet, were ca. 12 dyn cm and  $3.2^{\circ}$  C/100 km. T50 was much cooler towards the coast and the front was easily distinguished at 50 m where the maximum temperature gradient increased to ca.  $4.4^{\circ}$  C/100 km. Z08 showed well-defined features and was shallow (ca. 150 m) nearshore and in cyclones, and deep (ca. 270 m) in anticyclones. These observations were consistent with coastal upwelling conditions. All fields were highly correlated with each other.

The observed fields during the OPTOMA 18 and 23 surveys were qualitatively similar. The mesoscale features were of the same size and the fields had a similar range of values. However during OPTOMA 18, the positions of the major features were reversed from OPTOMA 23 (i.e., the cyclonic activity was nearshore during OPTOMA 18 and offshore during OPTOMA 23), the jet meandered southward through the entire domain between the zones of cyclonic and anticyclonic activity, and the SDH gradients were tighter.

The survey just prior to OPTOMA 23, a ship survey in July and August 1986 (also not an El Nino period), covered the NOCAL domain off Point Arena and Point Reyes. A southward jet, with a speed of ca. 23 cm/s, was ca. 200 km offshore between a trough parallel to the coast (100 km offshore) and warm anticyclonic features along the western boundary (Figure 4.8). The maximum SDH and SST gradients associated with the offshore jet, were 18 dyn cm and  $2.4^{\circ}$  C/100 km, respectively. The temperature gradient for this front increased to  $4.0^{\circ}$  C/100 km in the

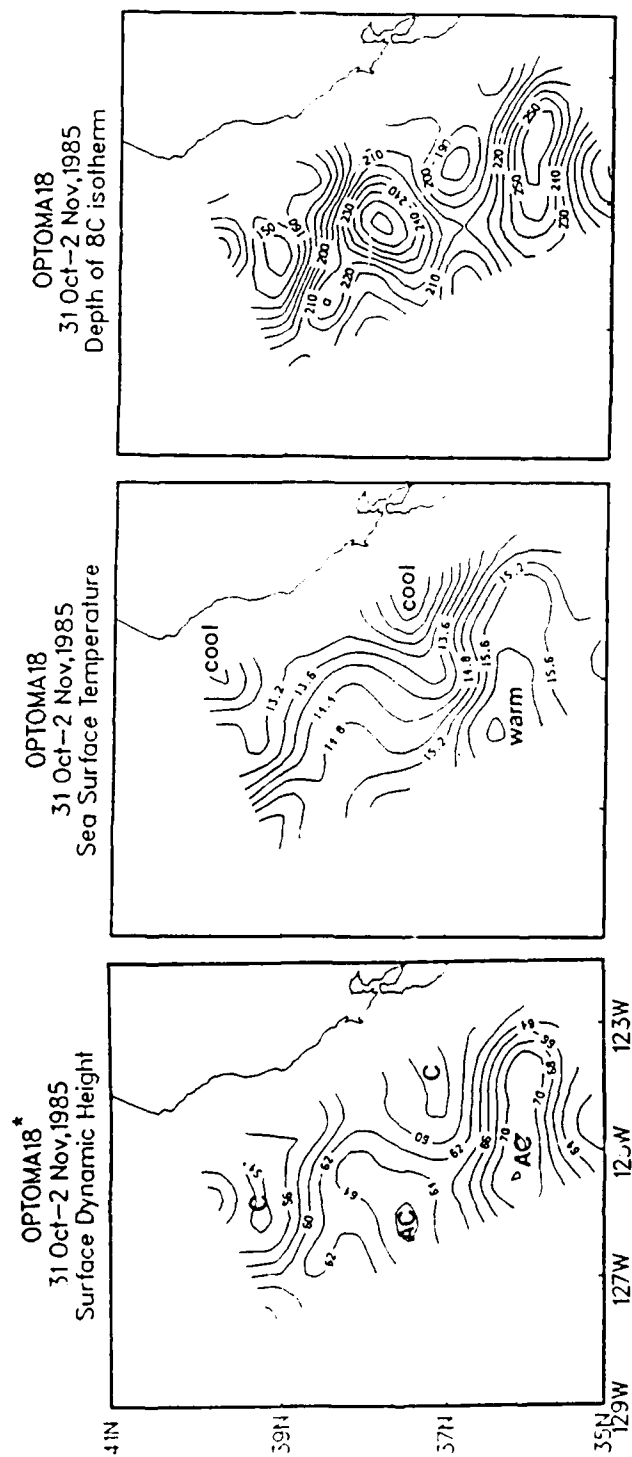
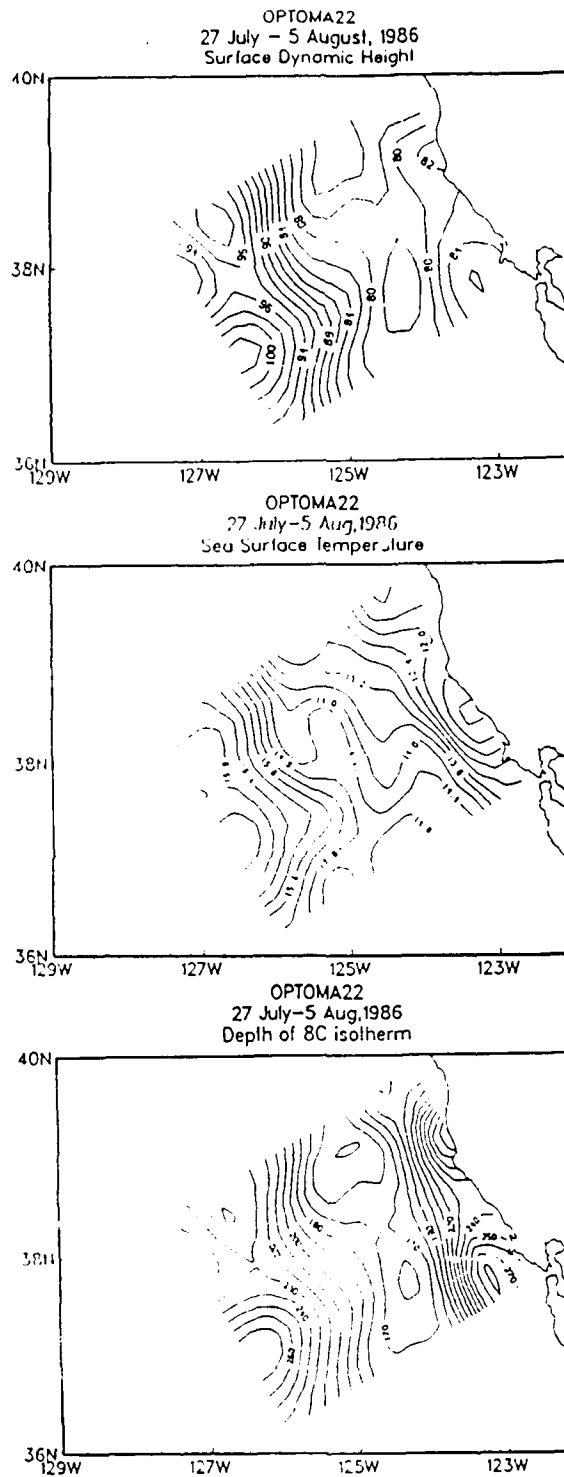


Figure 4.7 OPTOMA 18, 31 October - 2 November 1985, SDH, SST, T50, Z08  
Maps (Rienecker et al., 1987).





**Figure 4.8** OPTOMA 22. 25 July - 5 August 1986. SDH, SST, T50, Z08 Maps (Rienecker et al., 1987).

T50 field. There was a nearshore, northward flowing, jet within 100 km of the coast. A second front, presumably the upwelling front within 50 km of the coast, was also distinguishable in the SST field (with a gradient of  $2.4^{\circ}$  C/ 50 km), but not in the T50 field. Z08 was shallow (170 m) in the trough and deep (270 m) in the anticyclones.

The equatorward wind stress relaxed during July 1986. The observed effects were an increase in the coastal poleward flow, as compared with observations during OPTOMA 21 (7 to 20 July), and a decrease in width of a cool filament off Point Arena from 40 to 10 km (Rienecker and Mooers, 1989).

## B. ENVIRONMENTAL SUMMARY

### 1. Weather Summary

The weather throughout the two-week period for OPTOMA 23 was typical for the season. The OPTOMA domain and central coast area were often in a neutral point between the quasi-stationary North Pacific High pressure system ca. 1000 km to the west, a weaker high pressure system over the Sierras and Rockies, a thermal trough over Southern California, and low pressure systems to the north over the Pacific Northwest. In the fall and winter the Aleutian low is strong, so the NOCAL wind field is dominated by storm systems at three to five-day intervals.

During OPTOMA 23, three storms passed from the Gulf of Alaska through the Pacific Northwest along the principal storm track, 1500 km to the north of the domain. Another storm traveled along a secondary storm track, from an area about 1500 km southwest of San Diego, to Southern California. The period from 9 to 20 November was often cloudy,

but there was only one frontal passage through the domain, on 14 and 15 November, with numerous low stratus clouds and high clouds.

## 2. Ocean Summary

Two anticyclones, two cyclones, a meandering jet, and a cool filament directly influenced the OPTOMA 23 domain. The two anticyclones (100 km radius) extended from the surface to depth; one, off Point Arena (AC1) propagated westward (ca. 5 km/day) from the eastern boundary to the center of the domain north of the cool filament axis. The development and progression of the second anticyclone (AC2), to the south off Monterey, was less certain. It appeared to have strengthened and moved west. The two cyclones, one in the north (C1) and one in the southwest (C2), were quasi-stationary. There was one cool filament off Point Reyes, which extended westward through the domain. Another off Point Sur, approached the domain from the southeast, but did not reach it until late in the survey period. Both filaments were easily identified in satellite images. None of the eddies were identifiable in single satellite images; however, sequences of images highlighted the surface flow around the eddies.

The CCS during this period was not under the anomalous influence of El Nino. The El Nino signal of January 1987 was first identified as a Kelvin wave in the tropical mid-ocean in altimetry data (Cheney, 1989).

## C. INDIVIDUAL SURVEYS AND TIME SERIES

### 1. Surveys 23P1 and 23P2

On 9 November, during OPTOMA 23P1, most of the NOCAL survey domain was overcast with broken mid-level stratus. Approximately one-

fourth of the track, particularly in the quadrant closest to Cape Mendocino was undercast (i.e., an obscuration between the aircraft and the surface) with low stratus or fog. Aircraft winds at altitude (1000 feet) were steady from the northwest (330 to 345 degrees) at 9 to 15 m/s and were consistent with 850 mb winds (4800 feet). On the following day, 10 November, during OPTOMA 23P2 in CENCAL, only a small portion of the domain along the western and southern borders was overcast with broken stratus. The western central area and the southeastern corner were undercast. Aircraft winds (700 to 1000 feet) were from the north (000 to 010 degrees) at 5 to 10 m/s. There was a small area of wind divergence northwest of the central low cloudy area where the winds were from the northeast (035 degrees) at 10 m/s. The quasi-stationary North Pacific High was 1000 km west, a stationary frontal system was oriented east to west near the Oregon border, and a warm front was rapidly approaching the Washington coast (Figure 4.9).

There were two cyclonic features, one to the northeast (C1) and one to the southwest (C2), and two anticyclonic features, one in the center (AC1) and one to the south (AC2), depicted in the SDH field (Figure 4.10). The apparent wavelength of the jet meandering between these features was ca. 350 km. A cool filament extended offshore from Point Reyes on the central eastern border. Mixed layer depths, ranging from 0 to 70 m, were shallower to the north of the filament and along the eastern boundary and deeper to the south and west. Between AC1 and C2, there was a broad offshore flow ca. 150 km wide. This flow was highly geostrophic; the Rossby number ( $R_o$ ),  $U/f_o L$ , was ca. 0.02 (with  $U$

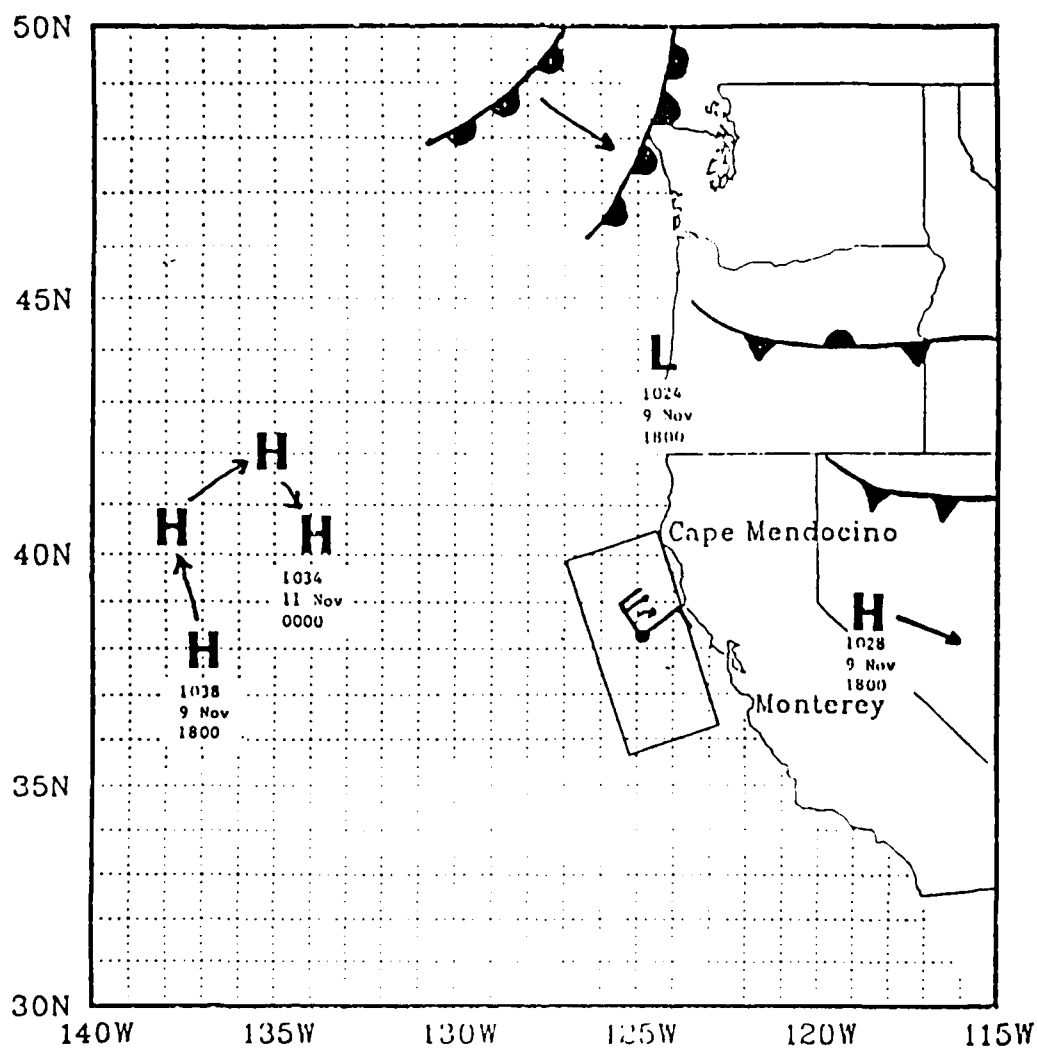


Figure 4.9 Synoptic surface weather depiction 9 and 10 November 1986 during OPTOMA 23P1 and P2 surveys. A two-day surface weather composite.

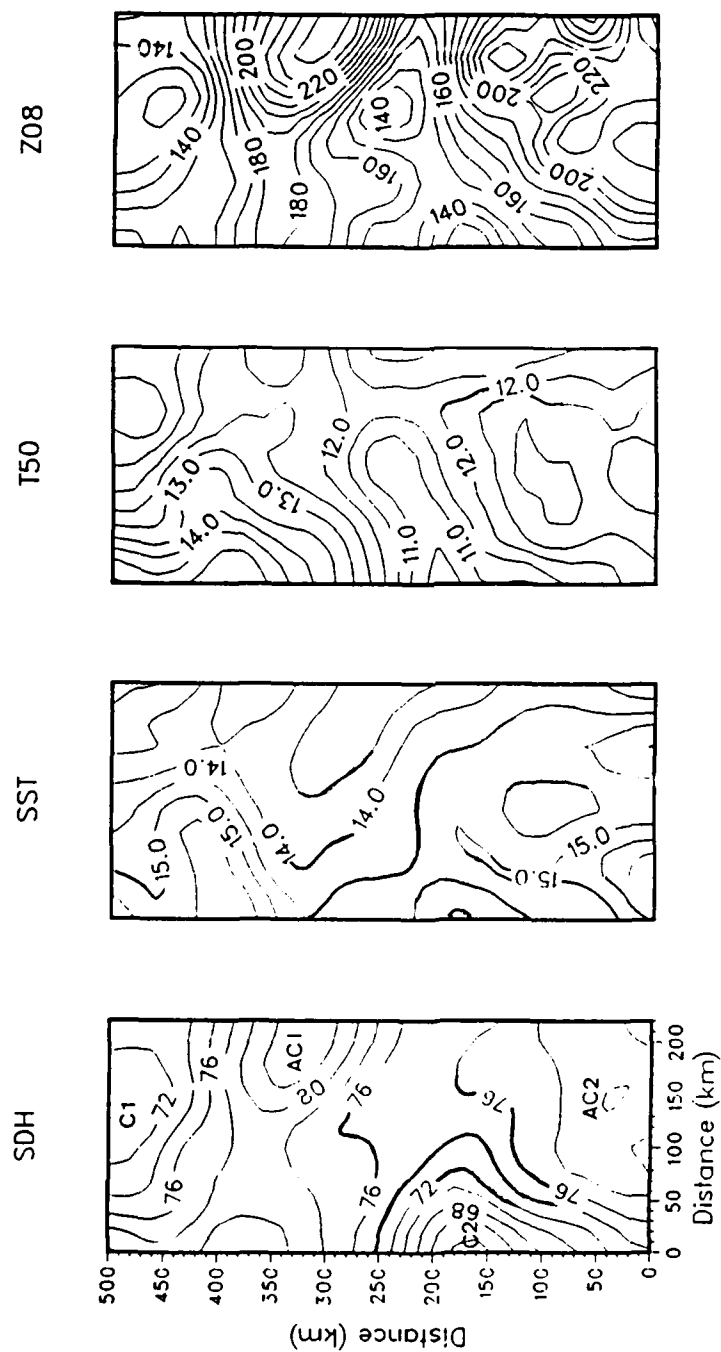


Figure 4.10 SDH, SST, T50 and Z08 OA fields from OPTOMA 23 P1 and P2 surveys.

ca. 20 cm/s and L ca. 100 km). (SST and Z08 OA fields from OPTOMA 23P1 and 23P2 were used to coordinate the survey conducted by the R/V POINT SUR in the southern part of the CENCAL domain).

All the mesoscale features had strong vertical support (i.e., they were evident in surface and subsurface fields), which was persistent throughout the survey period (Figure 4.11). The cold core cyclonic feature in the northeast corner (C1) was over a large cold dome with vertical changes in isotherms of ca. 30 m. The dome had a discernable tilt with depth towards the southwest. The anticyclone off Point Arena (AC1) had a warm core at depth and a layer of cooler water over it from the surface to ca. 50 m, apparently from upwelled water (the MLD was 20 to 30 m). On the southwestern boundary, the cyclonic feature (C2) had a cold dome with a diameter of ca. 200 km at a depth of 100 m and isotherms had vertical changes of ca. 100 m. The southern anticyclonic feature (AC2) was better defined in the Z08 field than in the SDH field.

## 2. Survey 23P4

A week later, on 16 November, the weather situation had deteriorated. OPTOMA 23P4 was a boundary updating survey. In the southern half of this larger domain, there was a stratus overcast. Undercast areas were in the southwestern corner and to the north off Point Reyes; otherwise, the domain was clear. Aircraft winds were varied; in the cloudy southern area, the winds were from the east (025 to 090 degrees) at 3 to 10 m/s; in the clear northern area, the winds were from the north (350 to 020 degrees) at 7 to 15 m/s.

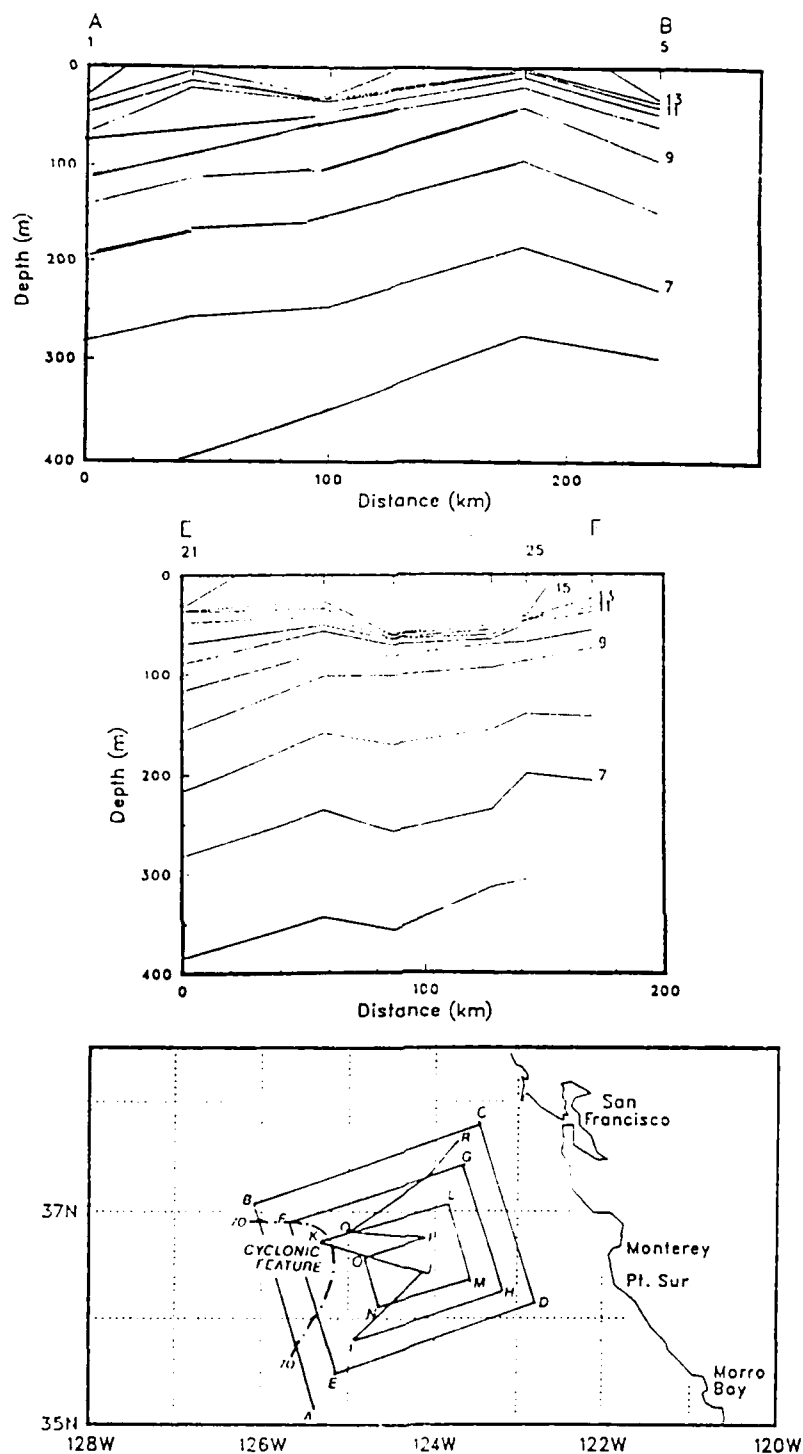


Figure 4.11 Example of cold dome associated with cyclonic feature, center of surface expression and 70 dyn cm contour marked, along track A-B and E-F during OPTOMA 23P2 on 10 November 1986 (Johnson et al., 1988).



A strong storm and frontal system was moving southeast at 25 knots from a position 1200 km to the northwest of the domain (Figure 4.12). There was an east-to-west oriented dissipating front 200 km north of the survey area. A low pressure system and trough moving northeast at 15 knots were 1000 km to the south.

In the SDH field, there was continuity in the positions and strengths of the two cyclones and two anticyclones from a week earlier. While the cyclonic features remained stationary, AC1 moved westward ca. 40 km (best seen in Z08), and AC2 apparently strengthened and moved slightly north. The cool filament off Point Arena extended through the domain and shifted northward (Figure 4.13). Another filament, off Point Sur, can be identified in satellite imagery to the east of the domain. The MLD (not shown) was consistent with earlier surveys.

### 3. Surveys 23P5 and 23P6

On 17 November, during OPTOMA 23P5, the sky was almost entirely cloud free. There was some scattered stratus near the grid center, but no undercast. Aircraft winds were generally north-northeasterly (005 to 035) at 5 to 10 m/s. Some cyclonic turning was evident in the southeastern corner with winds from the northwest (320 to 340) at 5 to 10 m/s. Two days later, on 19 November during OPTOMA 23P6, there was a scattered overcast in the western half of the domain over a solid and heavy low stratus deck (fog). The eastern half was clear. There was some anticyclonic turning of the winds progressing from north to south. In the north, winds were from the northwest at 5 to 8 m/s; in the south, they were from the north at 5 to 10 m/s.

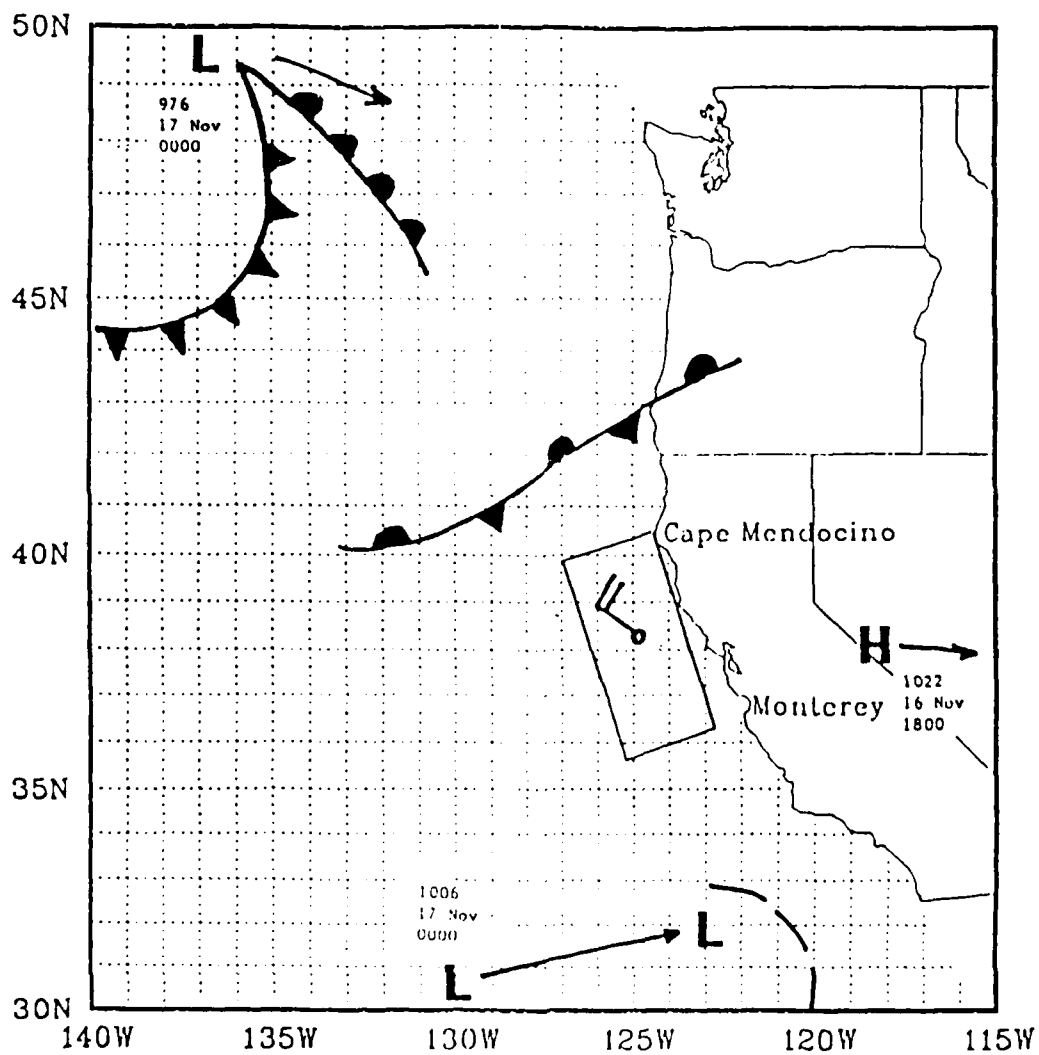


Figure 4.12 Synoptic surface weather depiction 16 and 17 November when OPTOMA 23P3 was in progress.

OPT 23 P4 86320

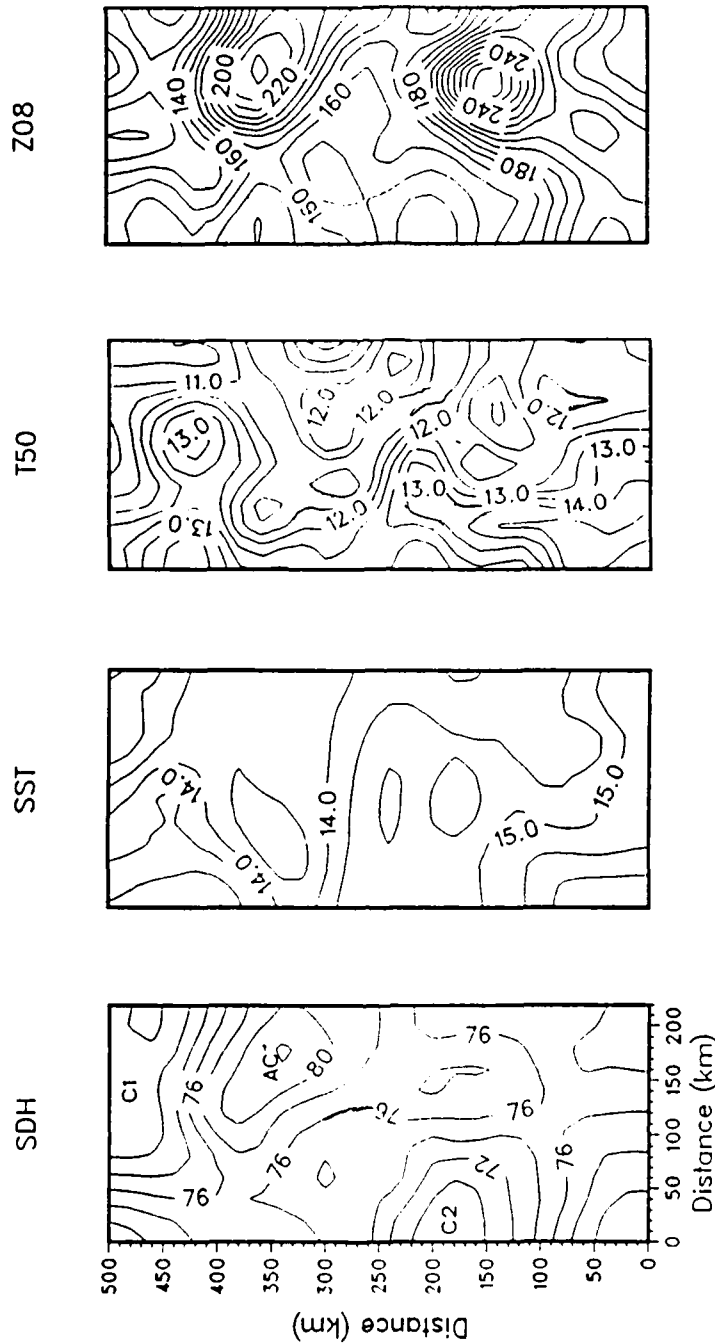


Figure 4.13 SDH, SST, T50, and Z08 OA fields from OPTONA 23 P4 survey.

The storm from the northwest identified on 16 November made landfall near Vancouver. A cold front from this system extended to the north and west of the survey area. The southern storm passed through California and was situated over Nevada. A weak and dissipating front extended from this system through central California (Figure 4.14).

The cyclones, anticyclones, and cool filaments identified earlier persisted in the SDH, SST, T50, and Z08 fields (Figure 4.15). The northern filament, off Point Reyes, extended offshore and the southern filament, off Point Sur, extended to the southeast about 50 km with a well-defined cold feature, particularly notable in the T50 field.

#### 4. Time Series From OA

Since OPTOMA 23 covered a 10-day period, only a part (i.e., a third to a quarter) of the expected eddy life cycle was surveyed. Still, to track the evolution of the features identified in the individual surveys, and to determine the persistence of the features, time series of three representative fields, SDH, SST and Z08, were created from objective analyses using 3 and 7-day time windows (a westward advection of 5 km/day was assumed). The error fields were small, generally less than 5%, except along the southern border during the first four days, where the 23P2 data were gappy, and in the NOCAL domain during days 86317 and 86318, prior to the boundary condition update flight, 23P4 (Figure 4.16).

In the SDH time series, the anticyclone on the eastern border off Point Reyes (AC1) and the anticyclone in the southern part of the domain (AC2) moved west at ca. 10 km/day (Figure 4.17). The cyclone on the

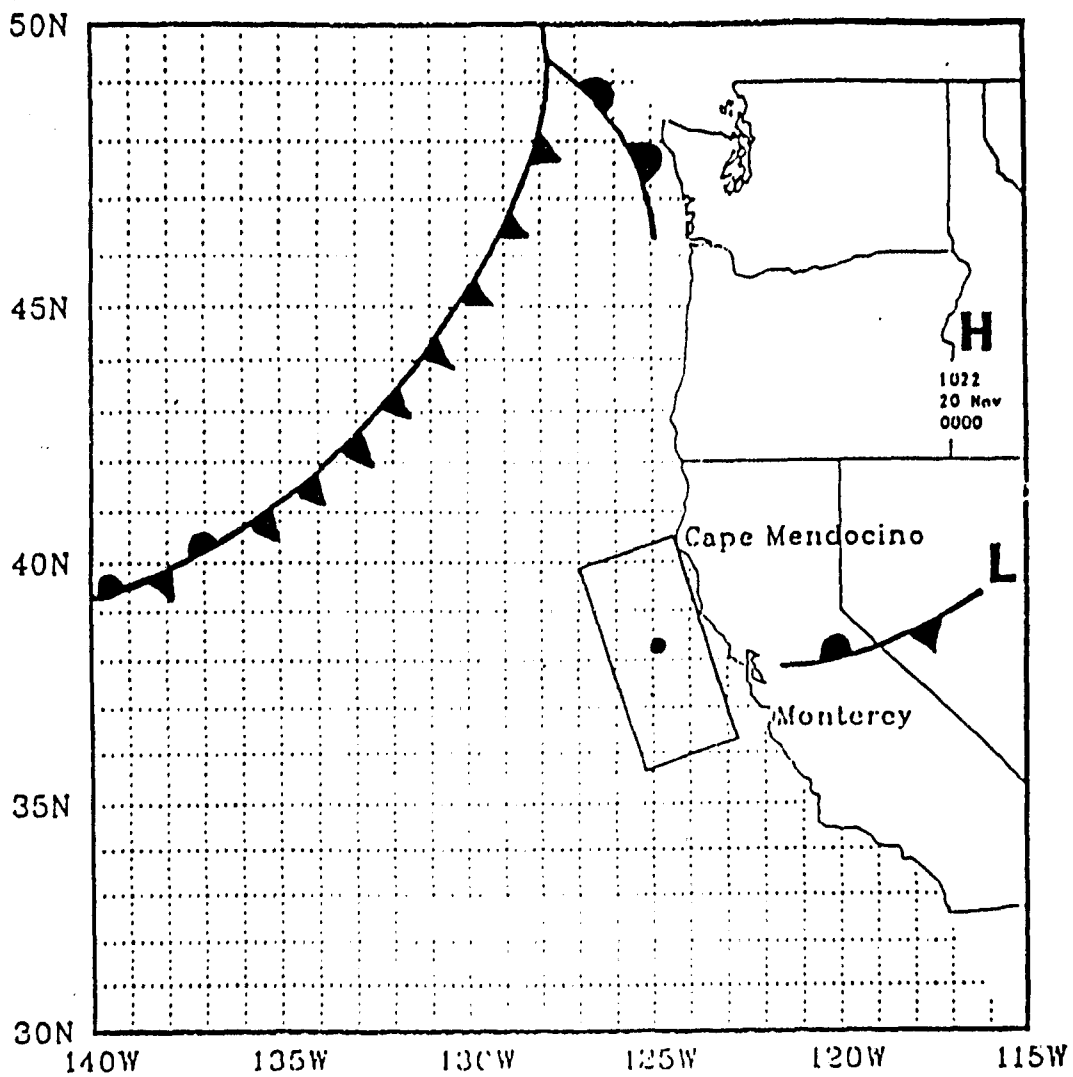


Figure 4.14 Synoptic surface weather depiction 19 November when OPTOMA 23P5 and 23P6 were in progress.

OPT 23 P4 86323

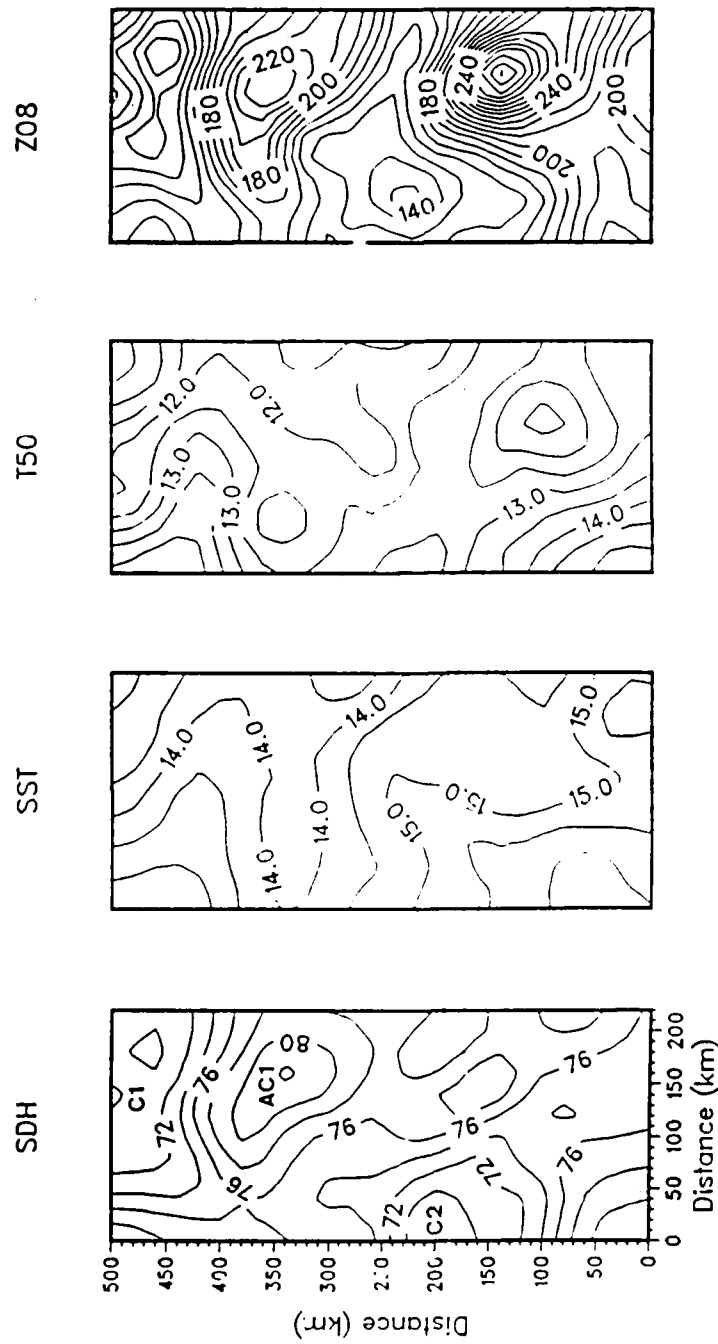


Figure 4.15 SDH, SST, T50, and Z08 OA fields from OPTOMA 2CP5 and P6 surveys.

# OPT23 SDH ERROR FIELD - TIME SERIES FROM OA MODEL

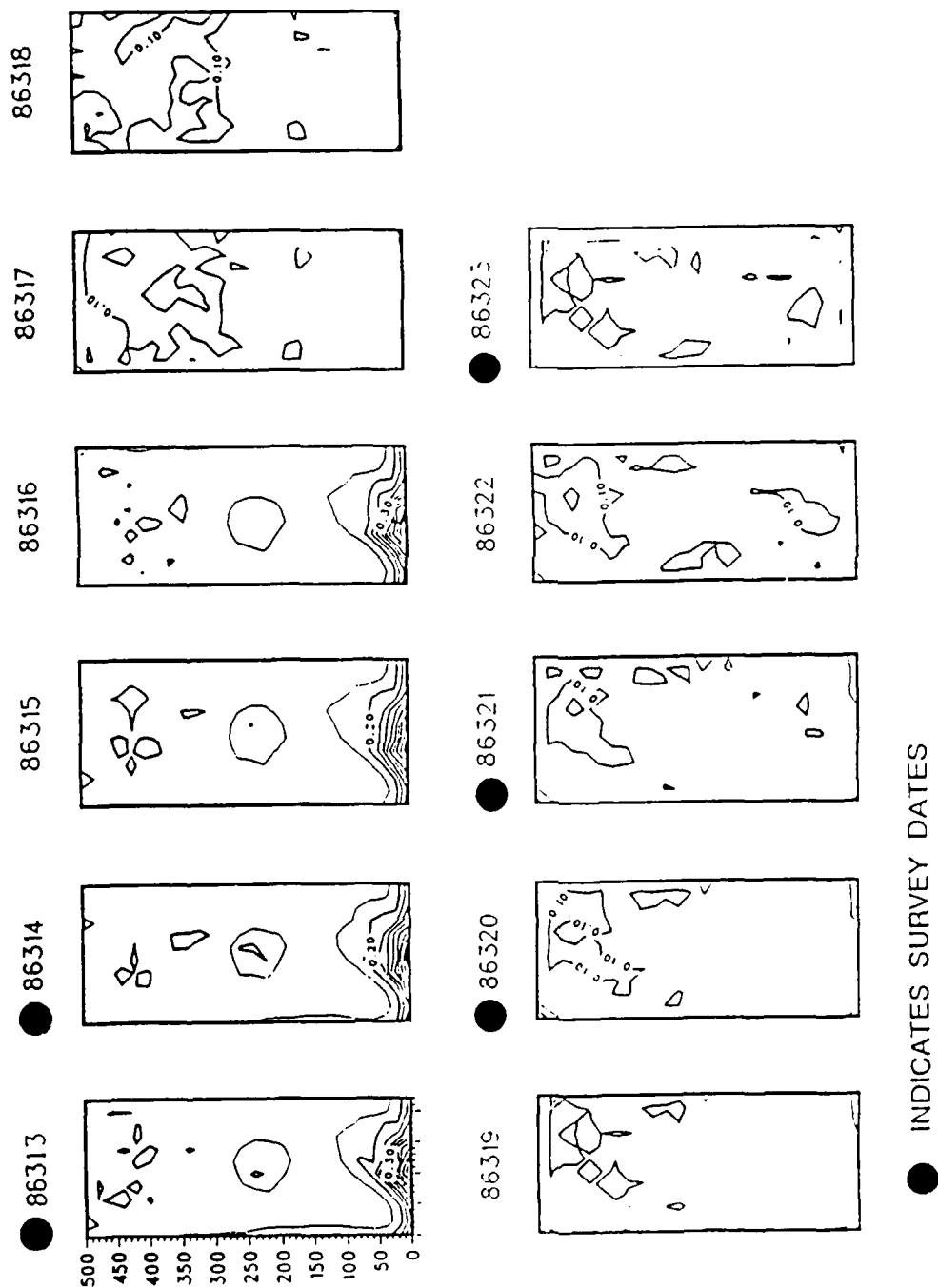


Figure 4.16 SDH OA error fields generated from composite of OPTOMA 23 data. Contour interval is 5%. The time window is 3 or 7 days; a 5 km/day westward phase speed was used.

OPT23 SDH TIME SERIES FROM OA MODEL

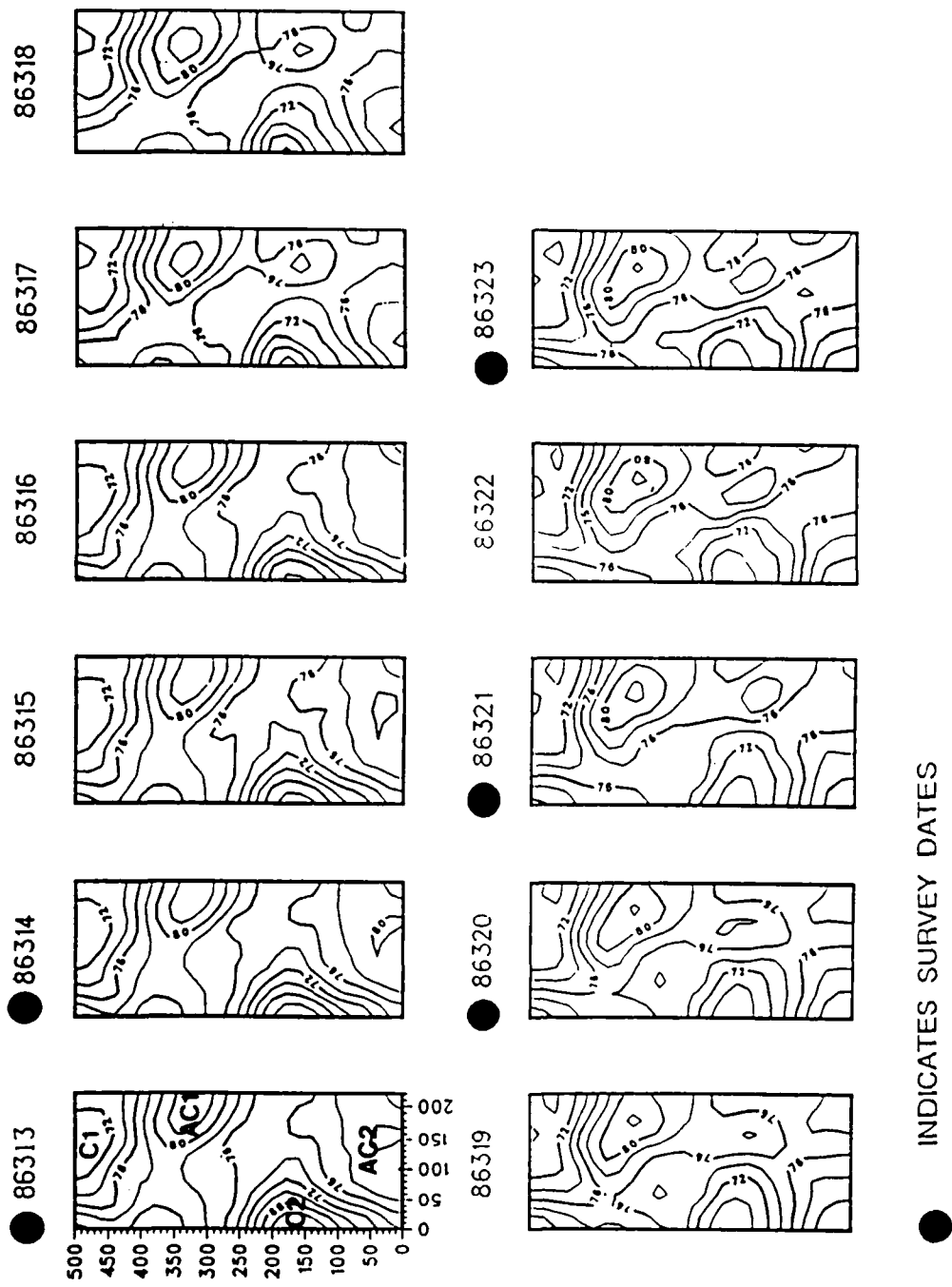


Figure 4.17 Time series of SDH contoured at 2 dyn cm. Cyclonic features are labelled C1 and C2; Anticyclones, AC1 and AC2.



northern boundary (C1) and the cyclone on the southwest border (C2) were quasi-stationary; C1 "deepened" and C2 "filled" slightly, 2 dyn cm, over the period.

In the SST times series, the cool filament located off Point Arena, right of center and extending from the eastern border, persisted throughout the series and eventually moved westward across the entire domain, at ca. 10 km/day (Figure 4.18). The shape of the cool filament was smeared out by the OA routine. To the northwest, there was a persistent warm tongue. Advection by the anticyclonic eddy to the north of the filament (AC1) accounted for the penetration of warm surface water along the northern axis of the filament; and, the cyclonic eddy on the southwest border (C2) advected another warm tongue northward (ca. 20 cm/s).

In the Z08 time series, the anticyclonic and cyclonic eddies were distinct deep and shallow features, respectively (Figure 4.19). The Z08 fields behaved similarly to the SDH fields; however, the movement of the deep feature associated with AC2 can be more easily followed in the Z08 field. It moved northwestward for the first five days and became stationary at day 86319.

SDH, SST, and Z08 were "forecast" from the initial observations from the first two surveys (day 86313) to day 86323 using the OA routine with a westward propagation of 5 km/day. These 10-day forecasts were compared with the verification fields, from the last two surveys, on day 86323. For a benchmark, persistence and climatology comparisons were also made.

OPT23 SST (AXBT) - TIME SERIES FROM OA MODEL

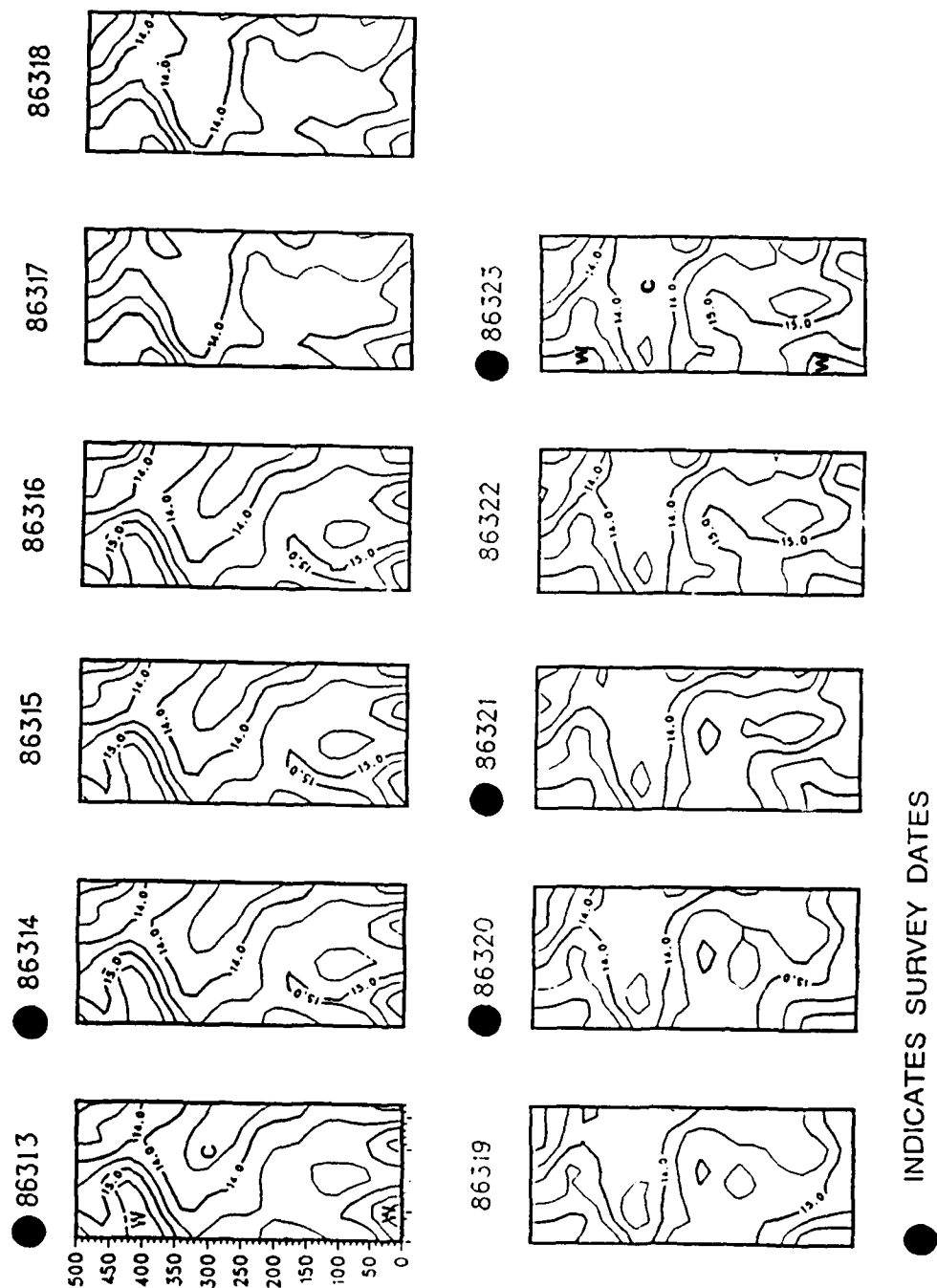


Figure 4.18 Time series of SST contoured at 0.5 °C. Warm features (W) and cold (C) features are labelled.

OPT23 Z08 — TIME SERIES FROM OA MODEL

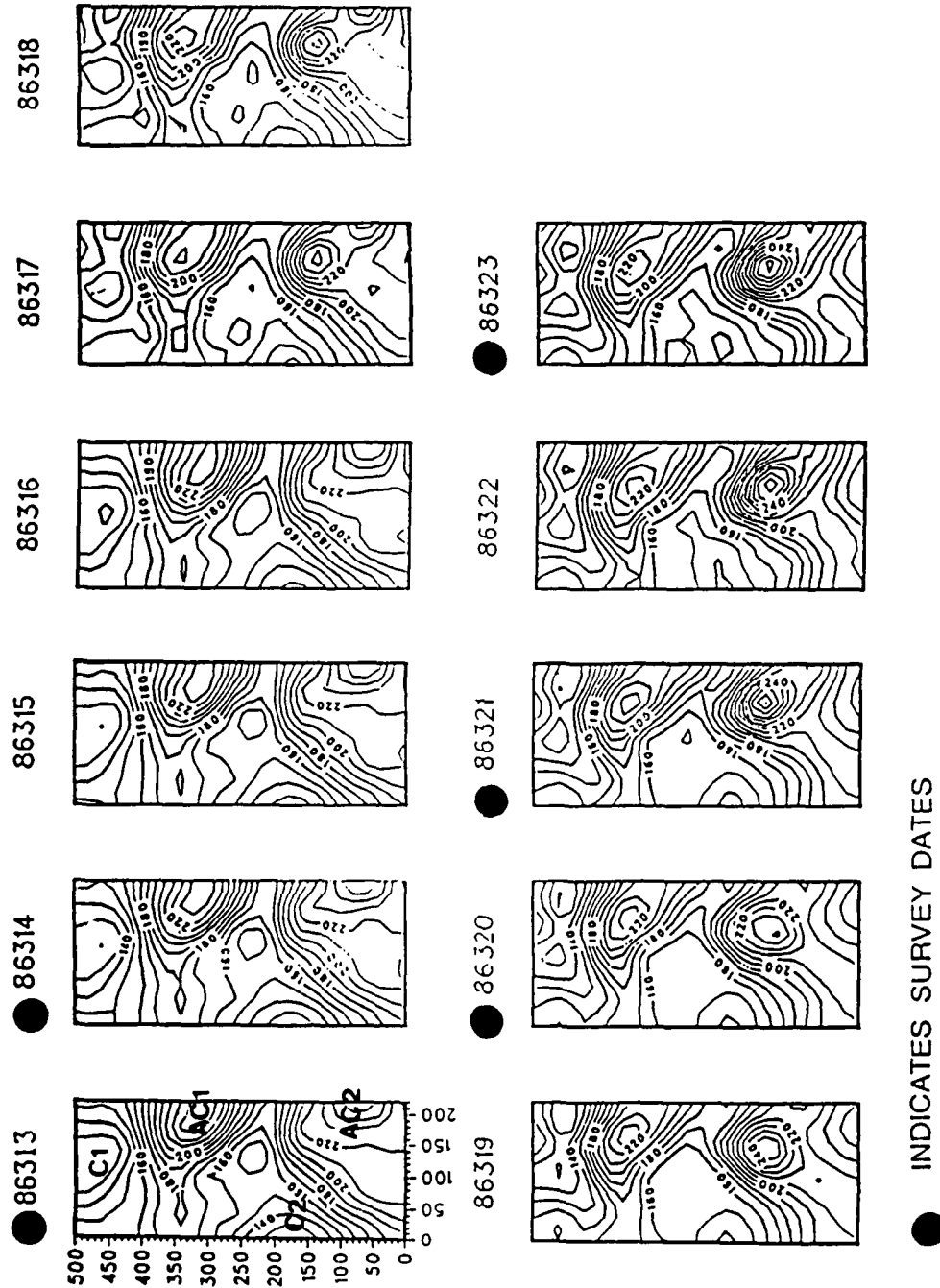


Figure 4.19 Time series of Z08 contoured at 10 m. SDH labels applied.

Qualitatively, the SDH forecast, compared to the verification field, looked "fair"; the forecast best depicted the activity of AC1 (Figure 4.20). The SST forecast looked "poor" with the exception of the northern and southern boundaries where SST was fairly constant; the forecast did not account for the reorientation and rapid westward extension of the cool filament off Point Arena (Figure 4.21). The Z08 forecast looked "good", although the forecast did not account for the deepening of AC2 (Figure 4.22).

Quantitatively, using correlation and RMS error as measures, the SDH forecast was slightly better than persistence and significantly better than climatology. The SST forecast was about the same as persistence and worse than climatology. The Z08 forecast was slightly worse than persistence and significantly better than climatology (Table 6).

## 5. Mean Temperature-Depth Profiles

### a. OPTOMA 18 and 22

In comparison to OPTOMA 18 (Wittmann et al., 1985), also a large domain survey in October 1985, the average temperature profile for OPTOMA 23 (November 1986) was 0.7 °C warmer from the surface to 150 m and somewhat warmer to 300 m. The average temperature profiles for the northern surveys, P1 and P4, were the same as OPTOMA 18; the average profiles for P2 and P5, the southern surveys, were the same at the surface, slightly warmer to 75 m, and slightly cooler from there to 300 m.

OPTOMA 22 was a survey of the NOCAL domain and the inshore area to the upwelling zone over the continental shelf in July and August

# SDH OA "FORECAST" EXPERIMENT

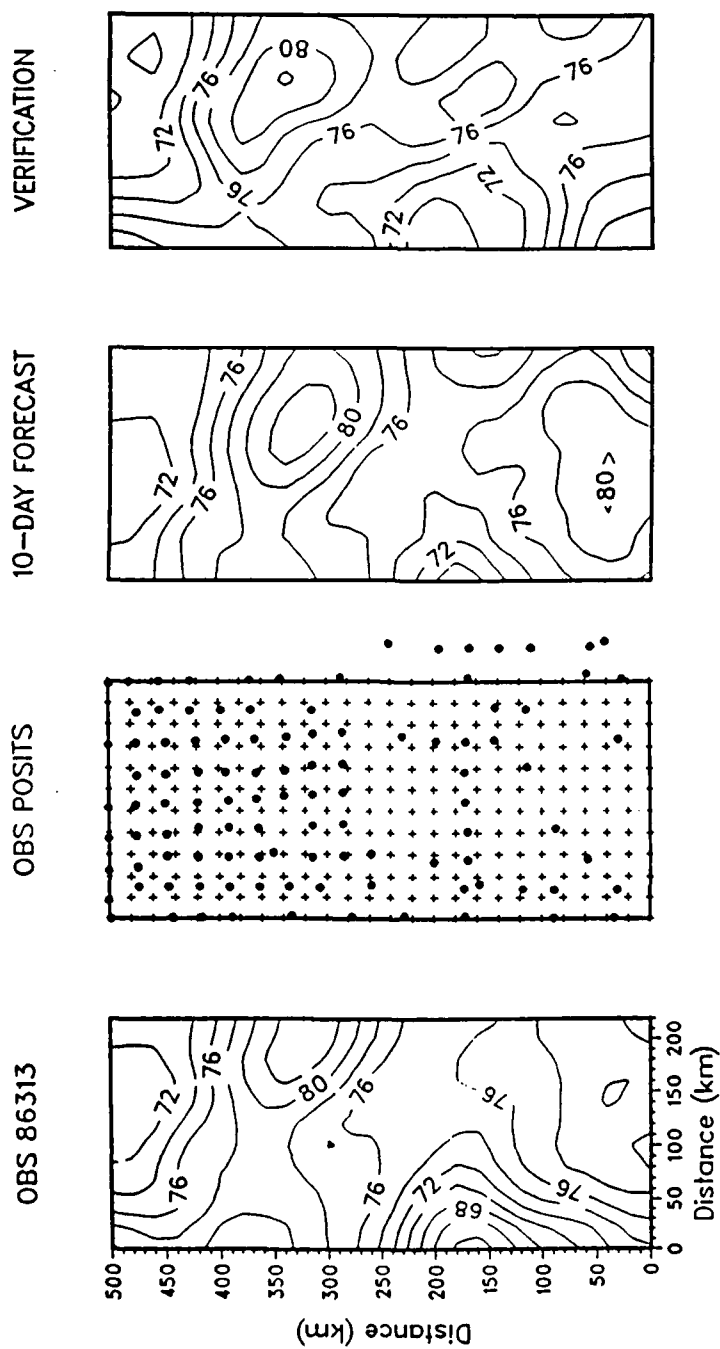


Figure 4.20 SDH OA "forecast" experiment. The initial data fields from day 86313 were used in an OA routine with a 5 km/day westward phase propagation to forecast the field at day 86323.

# SST OA "FORECAST" EXPERIMENT

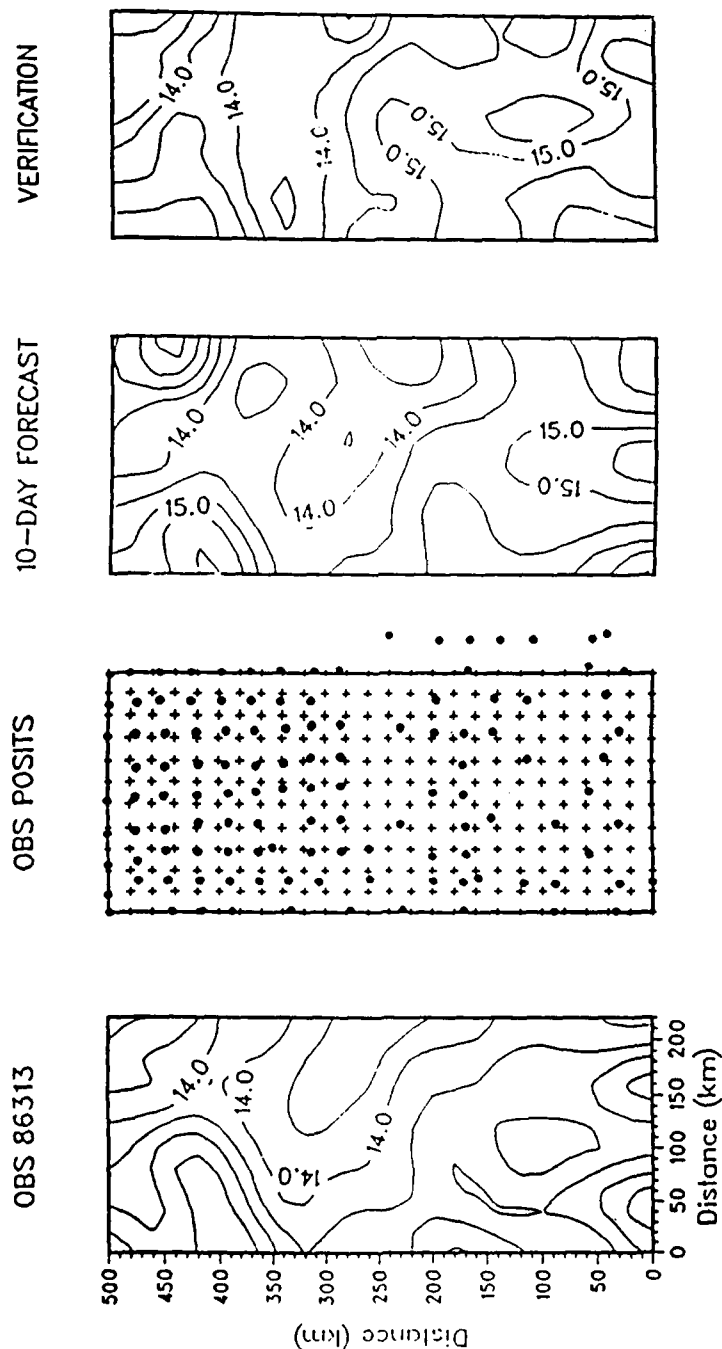


Figure 4.21 SST OA "forecast" experiment. The initial data fields from day 86313 were used in an OA routine with a 5 km/day westward phase propagation to forecast the field at day 86323.

# Z08 OA "FORECAST" EXPERIMENT

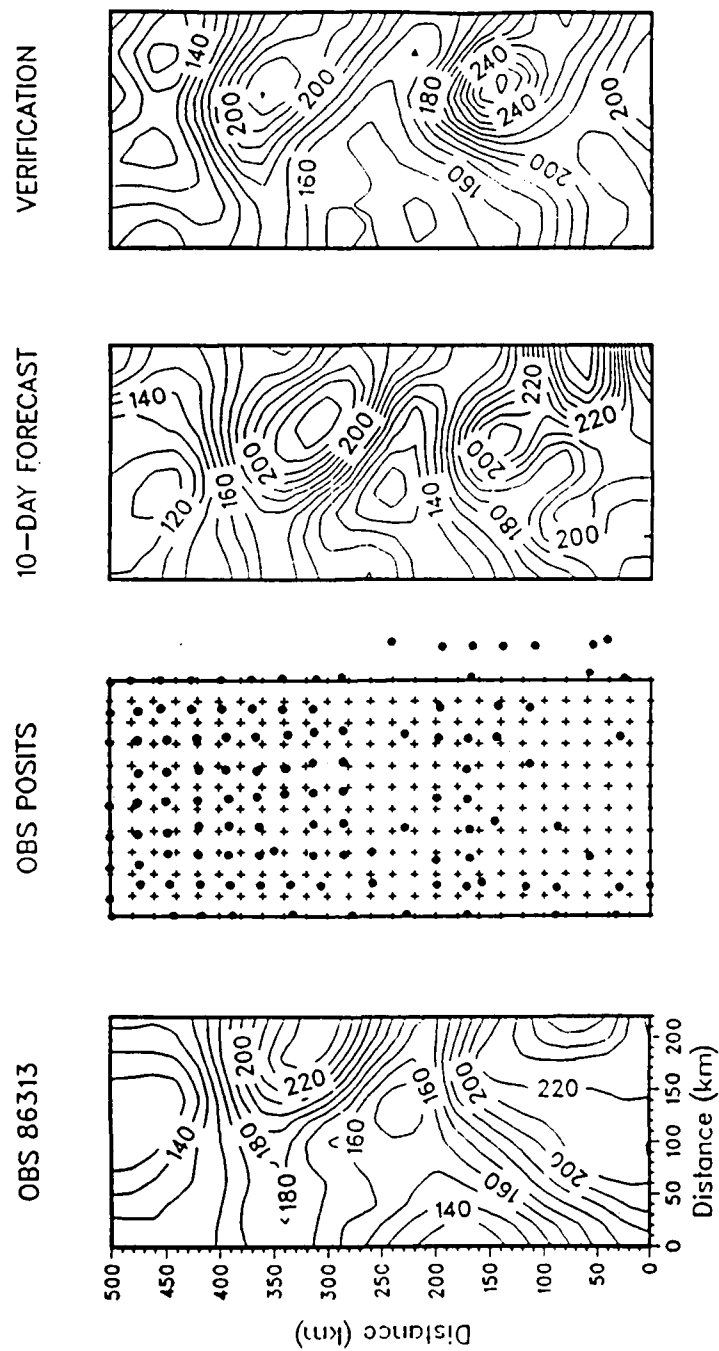


Figure 4.22 Z08 OA "forecast" experiment. The initial data fields from day 86313 were used in an OA routine with a 5 km/day westward phase propagation to forecast the field at day 86323.

TABLE 6. OA FORECAST COMPARISON FIGURES

<u>Field 1</u>	<u>Compared to</u>	<u>CORR</u>	<u>MAE</u>	<u>RMS</u>	<u>RMSN</u>
SDH 86323	OA 10-day	0.71	2.0 <sup>1</sup>	2.3 <sup>1</sup>	.80
	SDH 86313	0.69	2.1	2.8	.75
	(Persistence)				
	SDH GDEM	-0.16	6.7	8.0	2.80
	(Climatology)				
SST 86323	OA 10-day	0.67	0.49 <sup>2</sup>	0.62 <sup>2</sup>	.80
	SST 86313	0.66	0.47	0.61	.87
	(Persistence)				
	SST GDEM	0.73	0.67	0.77	1.06
	(Climatology)				
Z08 86323	OA 10-day	0.79	18.9 <sup>3</sup>	24.0 <sup>3</sup>	.62
	Z08 86313	0.83	15.1	19.5	.57
	(Persistence)				
	Z08 GDEM	0.54	41.4	46.7	3.38
	(Climatology)				

CORR - correlation;

MAE - Mean Absolute Error;

RMS - Root Mean Square;

RMSN - Root Mean Square Normalized (by variance field 2)

## Notes:

1 - Units are dyn cm.

2 - Units are °C.

3 - Units are m.



1986 (Ciandro et al., 1986). The average temperature profile for OPTOMA 23 was warmer than OPTOMA 22 above 100 m (0.6 °C at the surface and 1.0 °C at 50 m). Below 100 m the profiles were the same.

b. Changes during OPTOMA 23

In the northern part of the domain, from survey P1 to P5, eight days apart, the average SST remained the same, the water column from the surface to 75 m warmed by 0.2 °C, and between 75 and 300 m, it remained the same. In the southern part of the domain, from survey P2 to P6, nine days apart, the average SST cooled by 0.4 °C, the column from the surface to 100 m cooled by 0.2 °C, and between 75 and 300 m, it remained the same. On a shorter time scale of a few days, from P4 to P5, the water column between 40 and 70 m warmed 0.3 °C; otherwise, it remained the same. From P4 to P6, the upper 300 m warmed slightly, with SST warmer by 1.0 °C (Johnson et al., 1988). These changes are further analyzed in Chapter VI.

D. SATELLITE FIELDS

1. General Description

Eight five-channel AVHRR images were analyzed for OPTOMA 23: 86314 (day), 86314 (evening), 86315 (day), 86315 (evening), 86319, 86321, 86323, and 86325. The cool coastal water, cool filaments off Point Arena, Point Reyes and Point Sur, and numerous small-scale features (diameter ca. 10 km) were vividly obvious in the IR channels (Appendix E). (The 512 X 512 pixel images were centered on Point Reyes; therefore, they are truncated on the southern boundary at 35 N). Throughout OPTOMA 23, the identification of mesoscale features from a single IR image was difficult due to the complicated pattern of multiple

small-scale features, particularly along the periphery of the cool filaments, and surface masking, either by cool upwelled water or the warm surface water offshore in the CCS.

In the IR imagery (e.g., Figures E.1 and E.3 on Julian Days 86314 and 86315, respectively), the broad (100 km wide measured on the eastern boundary of the domain), cool filament, identified in the SST OA fields between Point Reyes and Point Arena (Figure 4.1), was a narrow (ca. 10 to 30 km measured on the eastern boundary of the domain) filament anchored nearshore at Point Reyes. It was embedded in a wider (ca. 200 km), cool body of water. At the beginning of the survey, the upwelling front was 25 to 75 km offshore and the cool filament was 30 km wide and 350 km long; at the end of the survey, the upwelling front was 10 to 40 km offshore and the cool filament had lost integrity. The relaxation of the upwelling front and dissipation of the filament were consistent with the weakening and cessation of winds favorable for upwelling as seen in the Bakun indices (Table 7).

## 2. MCSST

The high-resolution AVHRR data were navigated, screened for clouds, converted to MCSST, and objectively analyzed to the same grid used for the other fields. As with other OA fields, the MCSST input data were smoothed and averaged by the OA routine.

Qualitatively, some of the MCSST OA fields were similar to the SST fields. The best are 86314A, 86315N, 86315, 86321, and 86325 (Figure 4.23). The worst, with gaps in the data due to high and mid-level clouds, were 86314B, 86319, 86320, and 86324 (Figure 4.24). Quantitatively, all of the MCSST fields were ca. 0.8 °C cooler than the

TABLE 7. SUMMARY OF IR OBSERVATIONS DURING OPTOMA 23

<u>Satellite</u>	<u>Bakun Index</u> <sup>1</sup>		<u>Distance of Upwelling</u>			<u>Filament</u>	
<u>Image</u>	<u>36N</u>	<u>39N</u>	<u>Front Offshore (km)</u>			<u>length</u>	<u>width</u> <sup>2</sup>
<u>Cal/Julian</u>			<u>Mendocino</u>	<u>Pt Arena</u>	<u>Pt Reyes</u>	<u>(km)</u>	
<u>Date</u> <sup>3</sup>							
10/314A	10	80	75	25	50	Note 4	30
10/314B	10	80	75	40	50	350	30
11/315N	-1	45	75	40	50	350	20
11/315	-1	45	75	25	50	300	15
15/319	-9	5	Note 4	10	40	Note 4	10
17/321	-8	12	50	10	50	Note 5	
19/323	36	-4	Note 4	40	30		
21/325	23	-3	Note 4				

## Notes:

- 1 - Units are m<sup>3</sup>/s per 100 m of coastline
- 2 - Measured at eastern boundary of OPTOMA domain, ca. 100 km offshore
- 3 - Calendar date is in November 1986; Julian year is 1986
- 4 - Viewing prohibited by clouds
- 5 - Filament lost integrity and "broke apart"

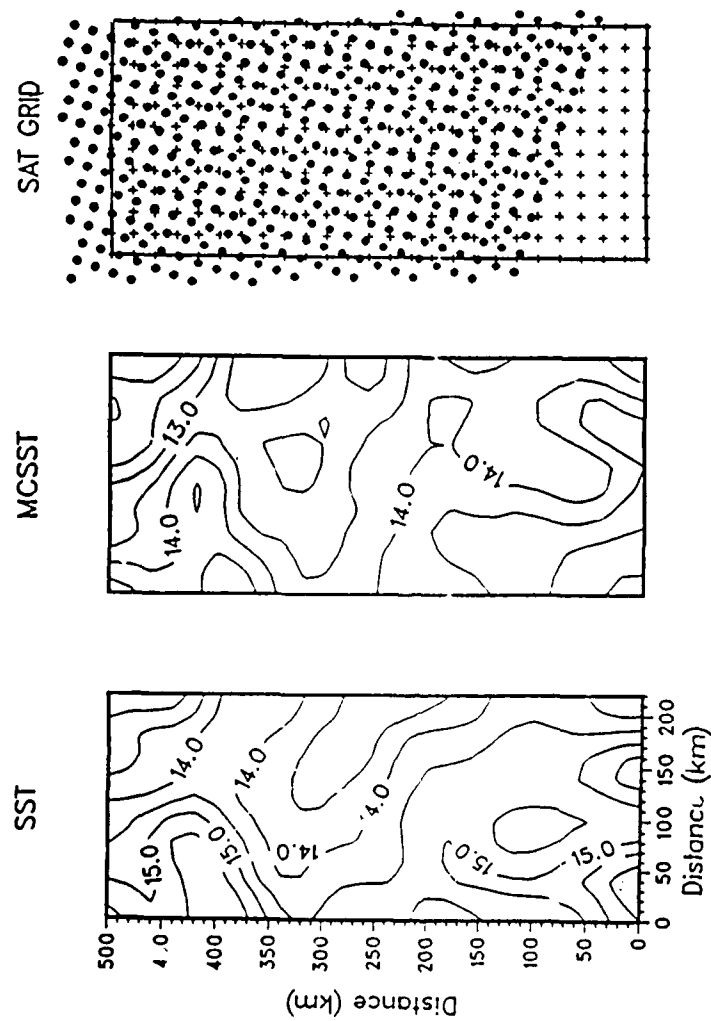


Figure 4.23 SST, MCSST, and satellite grid and observations plot from image 86315N. The image was cloud-free. The image was centered on Point Reyes and truncated the domain below 35°N. There was high correlation between the fields (0.85) and the RMS difference was 0.7 °C.

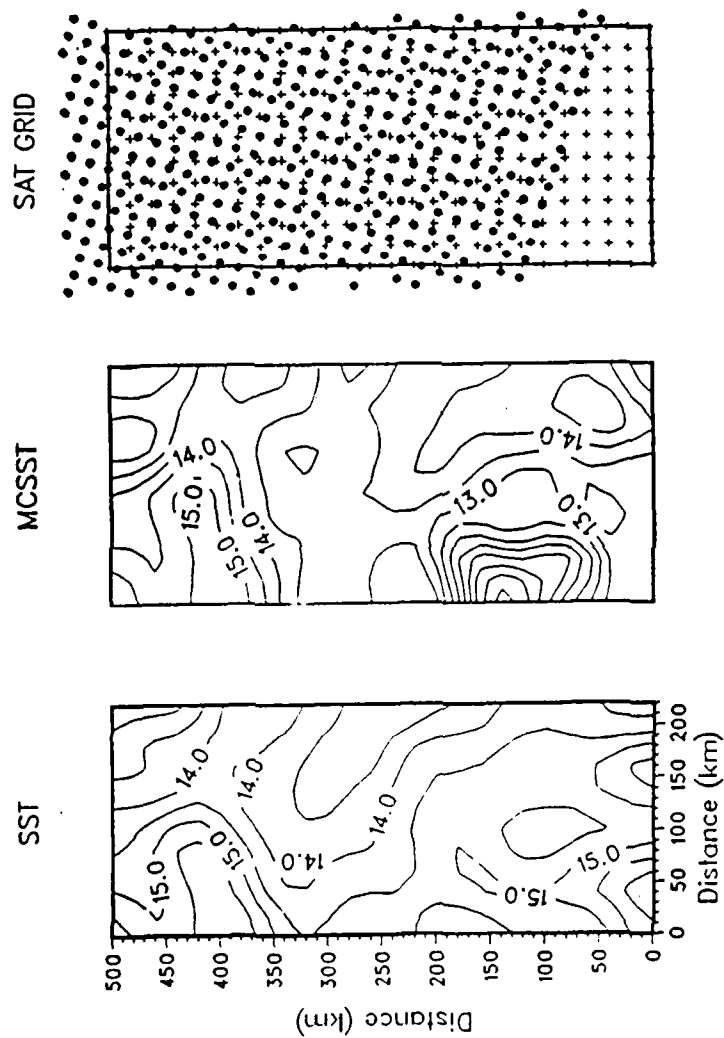


Figure 4.24 SST, MCSST, and satellite grid and observations plot from image 86314A. There were mid and high-level clouds in the image. The image was centered on Point Reyes and was truncated below 35 N. The correlation was low (0.22) and the RMS difference was 1.4 °C.

SST OA fields and had standard deviations ( $\sigma$ ) ca. 0.3 °C higher. The lower average temperature in the satellite data was consistent with the presence of sub-pixel size clouds or low stratus with cool temperatures close to that of the ocean surface, but not cool enough for the pixel to be screened out as "cloudy". The numerous small scale features in each satellite image account for the higher standard deviation (Table 8).

### 3. Satellite Surface Vectors and Comparisons

Although the eddies in the CCS during OPTOMA 23 did not have well-defined and easily discernable surface signals, cold upwelled water did act as a tracer and could be observed as it was advected in filaments between eddies (encirclement of an eddy by cold water did not occur). The flow field was more apparent and identifiable in pairs or series of images, especially near filaments.

Satellite surface vectors were processed with the OCEANTRAK (manual) technique from eight pairs of images. The time intervals ( $\Delta t$ ) were as short as six hours (between images on day 86314) and as long as 48 hours. The shortest  $\Delta t$  gave a rich "sense" of motion; however, it was difficult to pinpoint the center of features accurately (a 20 cm/s flow over six hours displaces a feature ca. four pixels). Other pairs of images with  $\Delta t$  from 48 to 96 hours were analyzed; features lost their identity beyond 48 hours. The optimal  $\Delta t$  was ca. 20 hours. Three sets of surface vectors were obtained (Table 9). Although the method is quite subjective, the results were consistent from one set to another.

Qualitatively, some of the vectors (Figure E.10) compared well with geostrophic velocities derived from SDH fields (Figure 4.25). The areas of agreement were away from the coast where circulation in the CCS

TABLE 8. COMPARISONS OF SATELLITE MCSST AND IN SITU SST OA FIELDS

<u>Field 1</u> <u>MCSST</u>	<u>Compared to</u> <u>SST OA</u>	<u>CORR</u>	<u>MAE</u> <sup>1</sup>	<u>RMS</u> <sup>1</sup>	<u>RMSN</u>
86314A	SST 86314	0.22	0.9	1.4	1.4
86314B	SST 86314	0.62	0.9	1.2	1.1
86315N	SST 86315	0.85	0.6	0.7	0.9
86315	SST 86315	0.82	0.6	0.8	1.0
86319	SST 86319	0.56	0.9	1.3	1.1
86321	SST 86321	0.70	0.7	1.0	1.1
86323	SST 86323	0.36	0.9	1.3	1.2
86325	SST 86325	0.83	0.8	0.9	1.7

CORR - Correlation;

MAE - Mean Absolute Error;

RMS - Root Mean Square;

RMSN - Root Mean Square Normalized (by variance field 2)

Note:

1 - Units are °C.

TABLE 9. SATELLITE SURFACE VECTORS AND SDH GEOSTROPHIC VELOCITIES<sup>1</sup>

<u>Data</u> <u>Set</u>	<u>Number</u> <u>of Obs</u>	<u>Range</u> <u>(cm/s)</u>	<u>Mean</u> <u>(cm/s)</u>	<u><math>\sigma</math></u> <u>(cm/s)</u>	<u><math>\Delta t</math></u> <u>(hrs)</u>
314-315	67	4.4-40.0	17.1	7.4	14:08
86314	312 <sup>2</sup>	0.0-19.8	07.7	4.6	N/A
315-315	48	9.5-54.0	27.5	10.0	19:40
86315	312 <sup>2</sup>	0.0-20.0	07.8	4.7	N/A
323-325	16	6.5-25.7	24.3	11.2	37:58
86323	312 <sup>2</sup>	0.0-16.3	07.4	3.6	N/A

Notes:

1 - Satellite surface vectors are separate measurements;  
SDH geostrophic velocities are from OA fields

2 - 12 X 26 grid

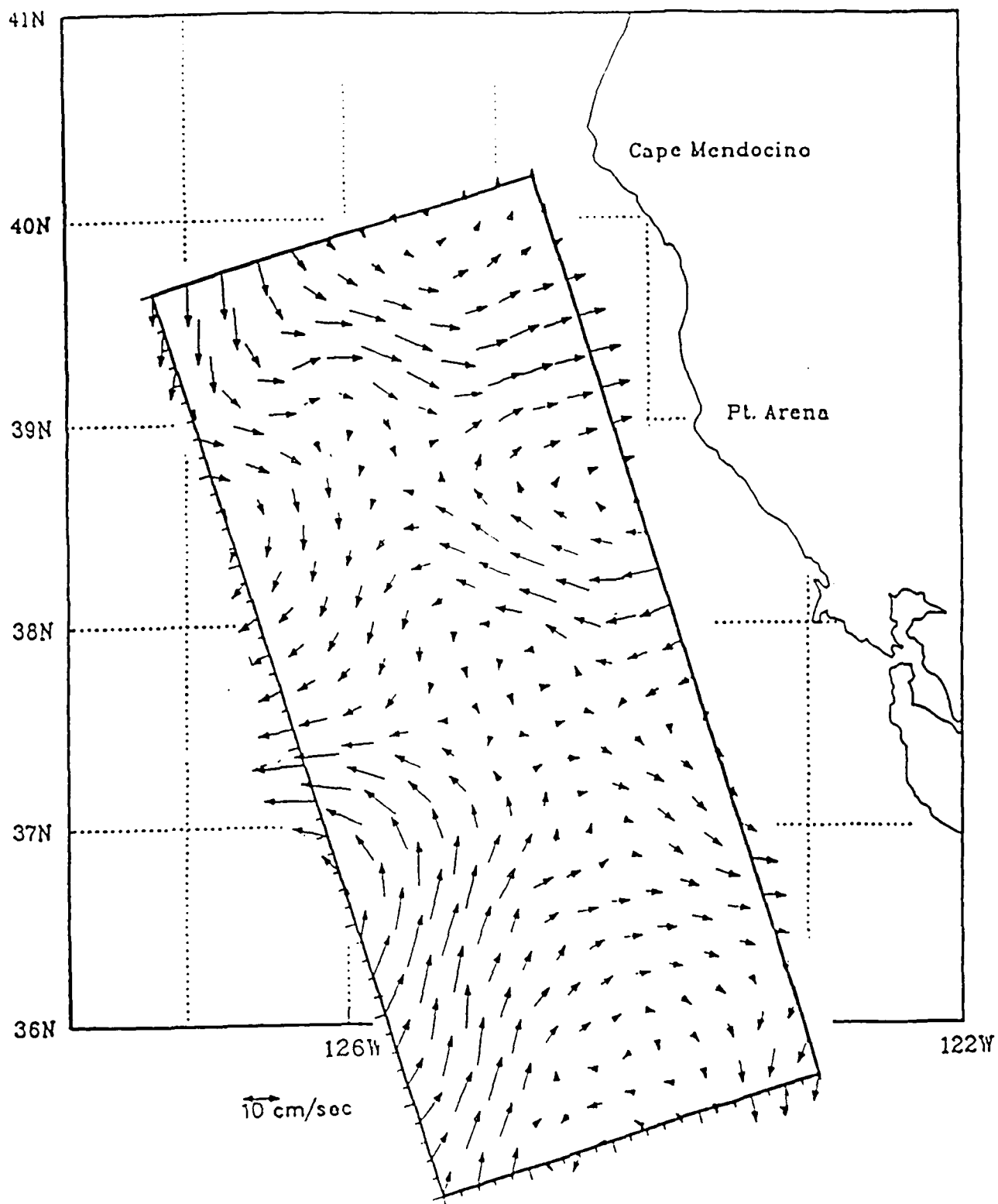


Figure 4.25 Geostrophic surface velocity vectors on day 86314 at same scale as satellite image from day 86314.



and around the mesoscale features was easily determined. Areas of disagreement were in the northeast where the upwelling front reached the domain near C1 (the area closest to shore, ca. 80 km offshore), and in the filaments off Point Reyes and Point Sur.

The geostrophic velocities near C1 were cyclonic and weak (ca. 2 cm/s) around the feature. The satellite surface vectors were also weak (ca. 5 cm/s), and they were inconsistent in direction (both in the same image pair, but in a slightly different position, and in different image pairs, but in the same area). Satellite-derived speeds were higher than geostrophic speeds in the filament and there was differential motion, or horizontal shear, across the filament due to the recirculation pattern.

Quantitatively, 60 satellite vectors, from the three vector sets, were compared, vector-by-vector, with geostrophic velocities. In all comparisons, the two measurements were within 10 km and 24 hours of each other. Two-thirds of the pairs had directions within 20° of each other; the exceptions were all within the cyclone to the north (C1) or the filaments off Point Reyes and Point Sur.

Of the vectors away from these areas of disagreement (40), the satellite-derived speeds were higher than geostrophic speeds in all but seven instances (five of these were the same). The satellite-derived average speeds were almost twice the geostrophic average speeds (11.5 versus 6.7 cm/s) and the standard deviation was slightly higher (4.5 versus 3.5 cm/s). The mean absolute difference was 5.1 cm/s (standard deviation of 4.2 cm/s).

The Ekman drift during the first two periods, on days 86314 and 86315, was ca. three to four cm/s (directed offshore) and was calculated from:

$$V = \tau(\rho)^{-1} H (\sqrt{2} \nu)^{-1} \quad (\text{equation 4.1}),$$

where  $V$  is the Ekman drift at the surface,  $\tau$  is the wind stress,  $H$  is the depth of influence (assumed to be the average mixed layer depth, ca. 20 m),  $\nu$  is the assumed vertical eddy viscosity ( $10^3 \text{ cm}^2/\text{s}$ ) and  $\rho$  is the average density of sea water. The wind stresses were obtained from three NDBC moored buoys on the eastern boundary of the domain (buoys 46013, 46014, and 46028). The Ekman drift estimates were of the same magnitude and direction as those derived from the Bakun indices, at 36 and 39 N, assuming the mixed layer moved like a slab (average MLD ca. 20 m). During the last period, on days 86323 and 86325, the wind stress increased and the Ekman drift was estimated to be ca. 10 cm/s to the west. The Bakun-derived estimate was an order of magnitude smaller.

The Ekman drift improved the comparison between satellite-derived and geostrophic speeds, when added to geostrophic speeds (without regard to direction) and accounted for most of the difference (ca. 75%). However, the mesoscale field had velocities in all directions while the Ekman drift was predominantly offshore.

There appeared to be a bias away from low velocities due to the technique; displacements of many pixels were easier to mark than displacement of a few pixels. The lowest limit of measurement was

estimated to be one pixel over 12 hours (2 to 3 cm/s); the practical limit was two to three times this.

The geostrophic velocities were spatially smoothed and, thus, underestimated maximum velocities. Differences may also be attributed to the geostrophic technique, which integrated dynamic topography over depth and introduced level-of-no-motion errors, the higher resolution of the satellite image compared with the SDH field, which spread the gradient over many gridpoints, and ageostrophic effects.

### 3. SSH

#### a. General

The in situ survey covered a 10-day period, which was insufficient to observe a complete cycle in eddy evolution. GEOSAT altimetry data were available every 17 days for the ERM, starting on 8 November 1989 (Julian Date 86312) and, though aliased for periods less than 34 days, it added useful observations from the beginning of OPTOMA 23 through the end of the year. Both ascending and descending orbits were used to generate OA fields of SSH; in the past, only ascending orbits were used in the CCS because the descending orbits are often gappy and missing data.

#### b. Description of SSH Fields

The SSH data were objectively analyzed in the same manner used for other fields. The GEOSAT observations alongtrack are nearly simultaneous (the satellite takes less than a minute to cross the OPTOMA domain), but from orbit to orbit, the data were asynoptic and as much as 72 hours apart. Six repeat orbits were used to provide data for five OA fields on days 86312, 86329, 86346, 86363, and 87015 (no more than four

orbits were available for any one analysis). The first field was on the day before the survey started and it provided the only reliable comparison with in situ data (OPT23P1 and OPT23P2 data were used to generate an SDH field for 86312). The second field was ca. one week after the survey and it provided insight into the 1986 Fall Transition (for comparison purposes, OPT23P5 and OPT23P6 were used to generate an SDH field for 86329).

Mesoscale activity was evident in all SSH OA fields (Figure 4.26). The size of the mesoscale features, and the range of heights, were both consistent with expected values and the observations. However, on day 86312, the location of derived features was not entirely consistent with direct observations. In the northern half of the domain, where there were two ascending and one descending tracks (Figure 4.27), the cyclone in the northeast corner of the domain (C1) and the anticyclone on the eastern boundary (AC1) were in the same location as noted in the SDH field. In the southern half of the domain, where there were two ascending tracks, there was an apparent anticyclone where the in situ data indicated a cyclone was located. The anomaly was ca. 10 cm higher than expected, a reasonable figure for a moisture correction. However, a review of imagery for this day showed no discontinuities in the cloud cover which may have caused the anomaly. Instead, there was a continuous stratus cloud cover throughout the domain, and a moisture correction would be applied equally over the domain. (This image was not analyzed for MCSST because of the cloud cover).

SDH AND SSH OA FIELDS (GEOSAT 17-day ERM)

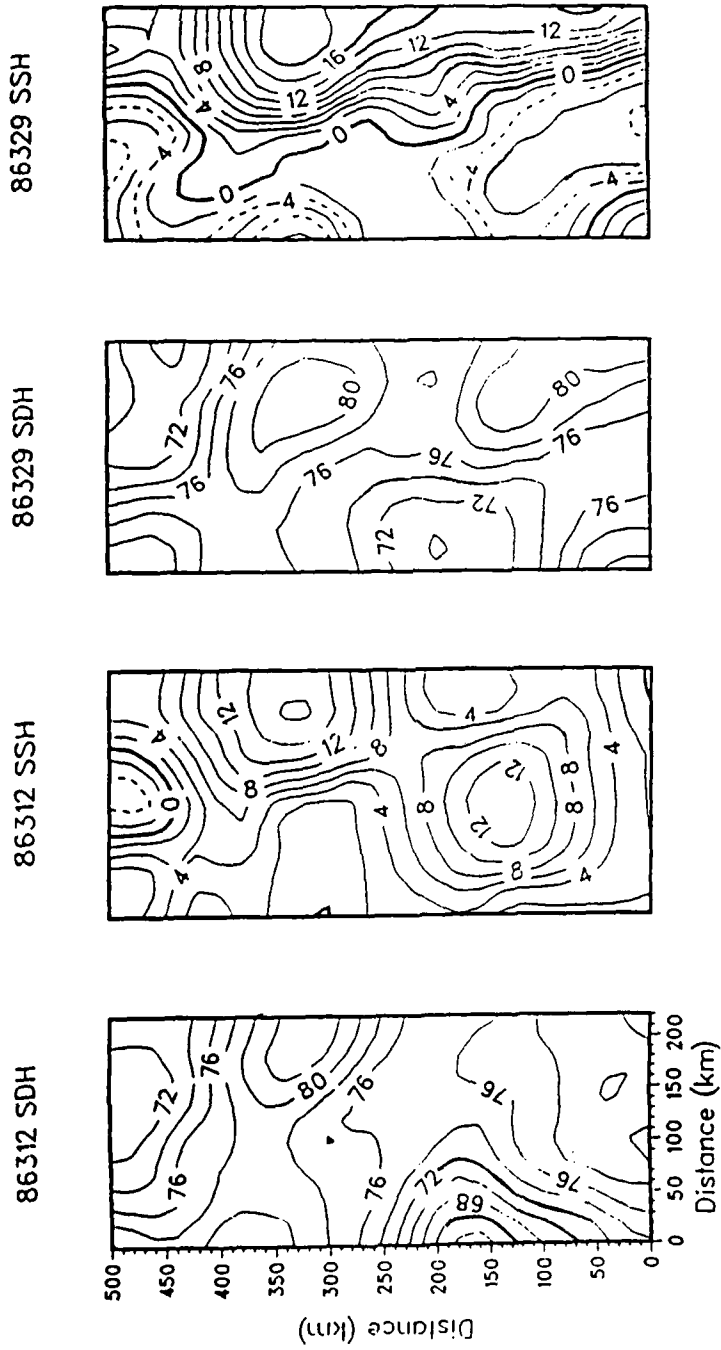


Figure 4.26 SDH and SSH OA fields on day 86312; and SDH and SSH OA fields on day 86329. Contour interval is 2 cm.

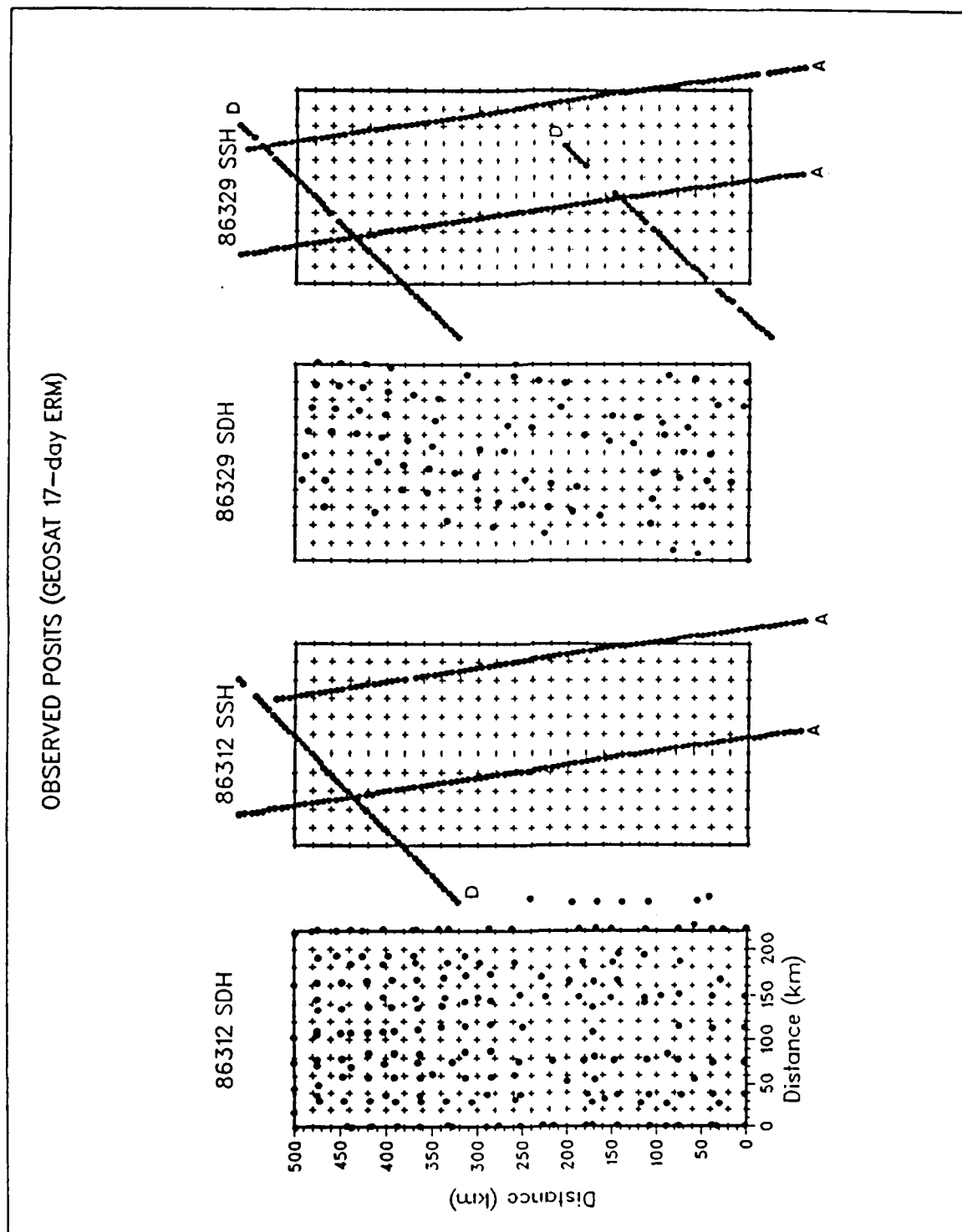


Figure 4.27 GEOSAT ERM orbital subtracks through the OPTOMA domain. Data are averaged alongtrack every second, or ca. 7 km. Ascending orbits (A) have a few, random gaps. Descending orbits (D) have larger data gaps.

Quantitatively, the SSH and SDH fields on day 86312 had the same range of values, ca. 20 cm (or dyn cm, respectively), and the same standard deviation, ca. 4 cm (dyn cm). The fields did not correlate well over the entire domain, 0.27. When the northern half of both fields were compared, however, the correlation increased to 0.73, indicative of the positive impact of data from the descending orbit in the north.

Qualitatively, the SSH field on day 86329 was similar to the SDH OA forecast field. Both had anticyclonic features near the eastern boundary and an offshore trough. The range of values and standard deviation for the SSH field were larger than those for the SDH field (30 cm versus 20 dyn cm, and 7 cm versus 3 dyn cm). Although there was visual similarity, the correlation between the two fields was low (0.47). A strong, meridional, northward jet of ca. 33 cm/s (gradient of 20 cm over 85 km) dominated the SSH field. (The strongest jet in the SDH field was half this). This analysis had a lower error field than the previous case because of the additional orbital track to the south (Figure 4.28). The 1986 Fall Transition of the CCS took place between days 86312 and 86329, 8 and 25 November, respectively (Chapter 6).

#### c. Evaluation of GEOSAT Sampling Strategy

The six GEOSAT orbital subtracks in the OPTOMA domain, plus one to the west, were superimposed over the SDH field on day 86312 and the field was sampled at 7 km intervals. (The SDH field was extrapolated to the west). The "simulated" data were then objectively analyzed to assess the impact of additional subtracks.

# ERROR FIELDS (GEOSAT 17-day ERM)

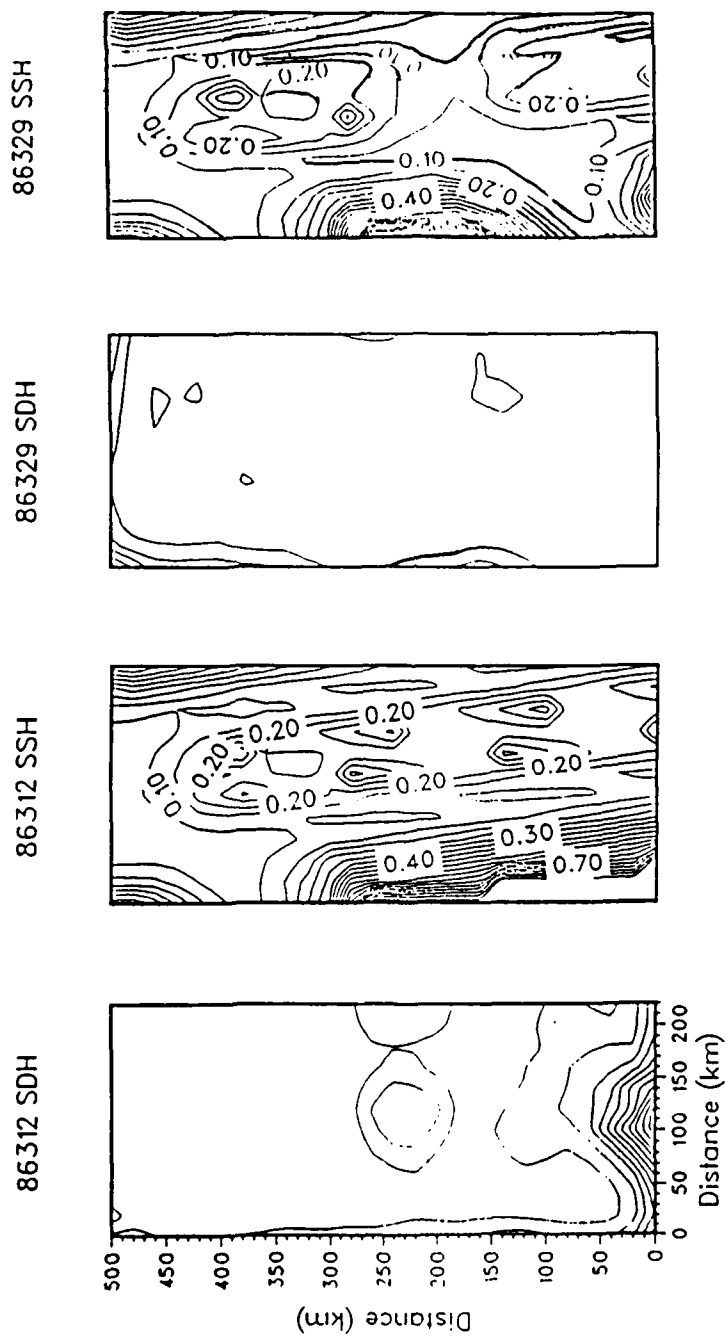


Figure 4.28 SDH OA (Day 86312) and SSH OA error fields from GEOSAT ERM orbits through the OPTOMA domain on days 86312 and 86329. Contour interval is 5 %.



The first experiment, Simulation 1, followed the sampling pattern on day 86312 (i.e., two ascending tracks and one descending track to the north) and had 104 observations. Qualitatively, the SDH field to the north was reproduced fairly well and the anomalous anticyclone to the south was introduced (Figure 4.29). The OA error field was high, ranging from 5 to 100 %, and averaging 27%. Quantitatively, it correlated with the SDH field and showed skill (0.74), but had high error measurements (Table 10).

The second experiment, Simulation 2, added three descending tracks, all in the domain to the south of the first descending track, and had 167 observations. Qualitatively, the SDH field over the whole domain was well reproduced (Figure 4.30). Quantitatively, the OA error field decreased, ranging from 4 to 86%, averaging 14%, with a standard deviation of 10%; the correlation increased markedly (0.93) and the error measurements decreased.

The third experiment, Simulation 3, added an ascending track, to the west of the domain, and had 218 observations. Qualitatively, the SDH field was well reproduced (Figure 4.31) and the OA error field decreased slightly. It ranged from 4 to 86%, averaged 13%, and had a standard deviation of 8%; the correlation increased to 0.97 and the error measurements, MAE and RMS, were 1 cm.

OA maps of SSH reproduced the in situ field accurately (with a correlation greater than 0.90) using perfect data from six orbits (two ascending and four descending). The addition of another ascending orbit (a seventh orbit) improved the correlation slightly.

# GEOSAT SAMPLING PATTERN TEST

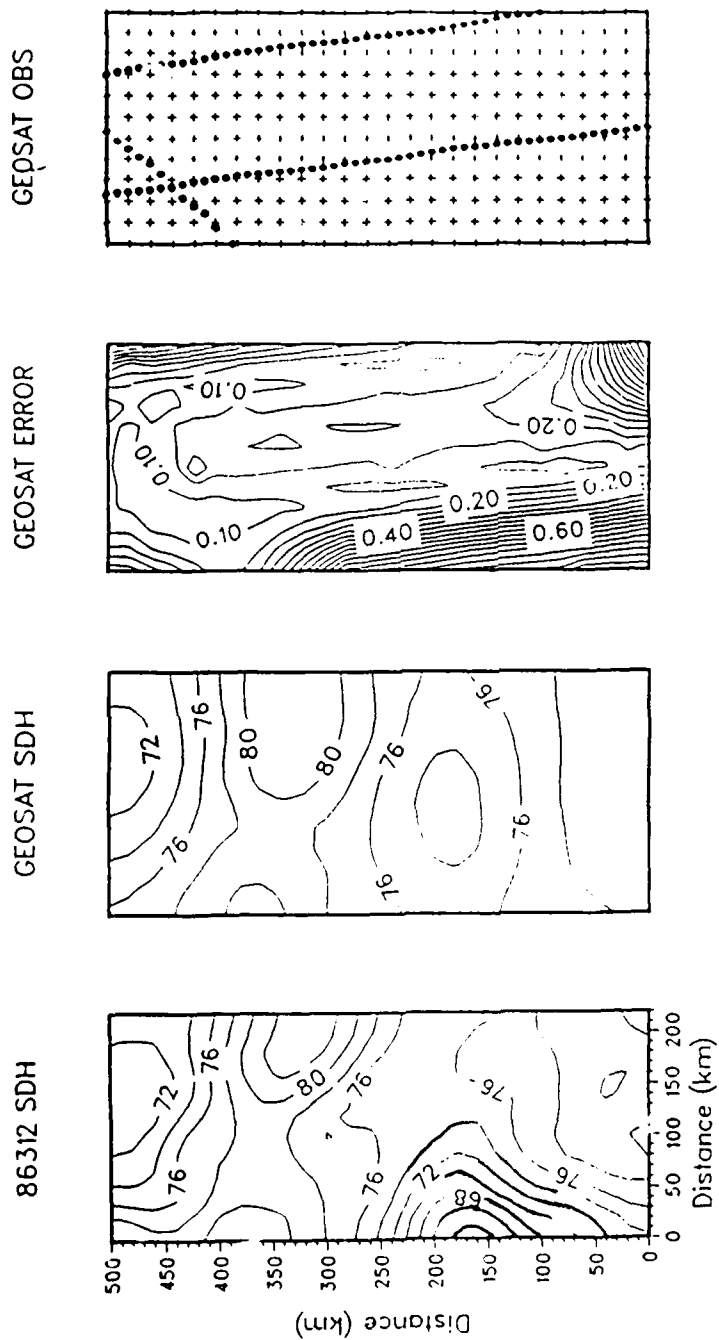


Figure 4.29 GEOSAT sampling experiment; survey pattern is same as the ERM on day 86312. SDH OA field on day 86312 is the sampled and verification field.

TABLE 10. COMPARISONS OF IN SITU SDH, GEOSAT SSH, AND SIMULATED SSH<sup>1</sup>

<u>Field 1</u> <u>Field 2</u>	<u>Range</u> <u>from to</u>	<u>Mean</u>	<u><math>\sigma</math></u>	<u>CORR</u>	<u>MAE</u>	<u>RMS</u>	<u>RMSN</u>
GEOSAT SSH 86312 SDH 86312	-5 to 16 63 to 83	6. 76.	4. 4.	0.27			
GEOSAT SSH 86312 SIMULATION 1	-5 to 16 71 to 82	6. 76.	4. 3.	0.74	2.	3.	1.1
GEOSAT SSH 86312 SIMULATION 2	-5 to 16 71 to 83	6. 76.	4. 3.	0.93	1.	1.	0.5
GEOSAT SSH 86312 SIMULATION 3	-5 to 16 66 to 83	6. 76.	4. 3.	0.97	1.	1.	0.3
GEOSAT SSH 86312 DEMEANED SIMULATION	-5 to 16 71 to 82	6. 77.	4. 3.	0.25			

CORR - Correlation;

MAE - Mean Absolute Error;

RMS - Root Mean Square;

RMSN - Root Mean Square Normalized (by variance field 2)

Note:

1 - Units are cm for GEOSAT fields, and dyn cm for simulations.

# GEOSAT SAMPLING PATTERN TEST

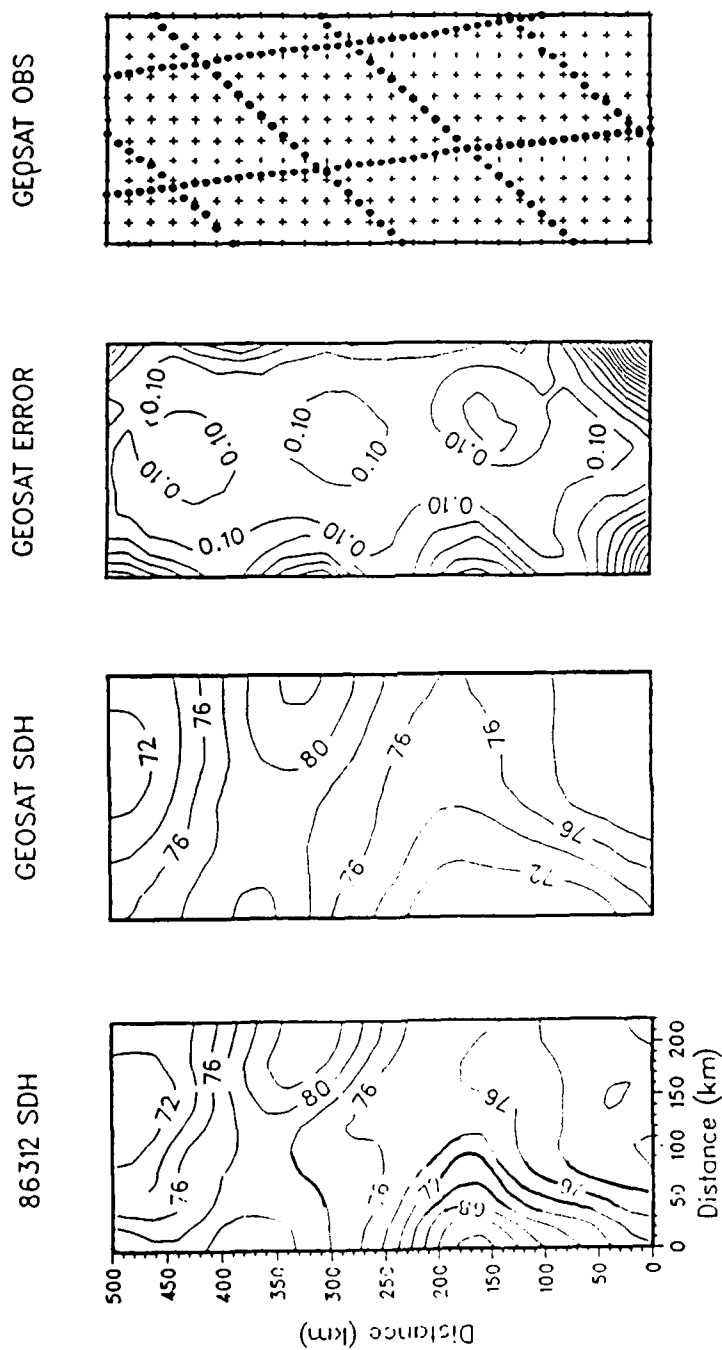


Figure 4.30 GEOSAT sampling experiment; survey pattern consists of all six orbits through the OPTOMA domain. SDH OA field on day 86312 is the sampled and verification field.

# GEOSAT SAMPLING PATTERN TEST

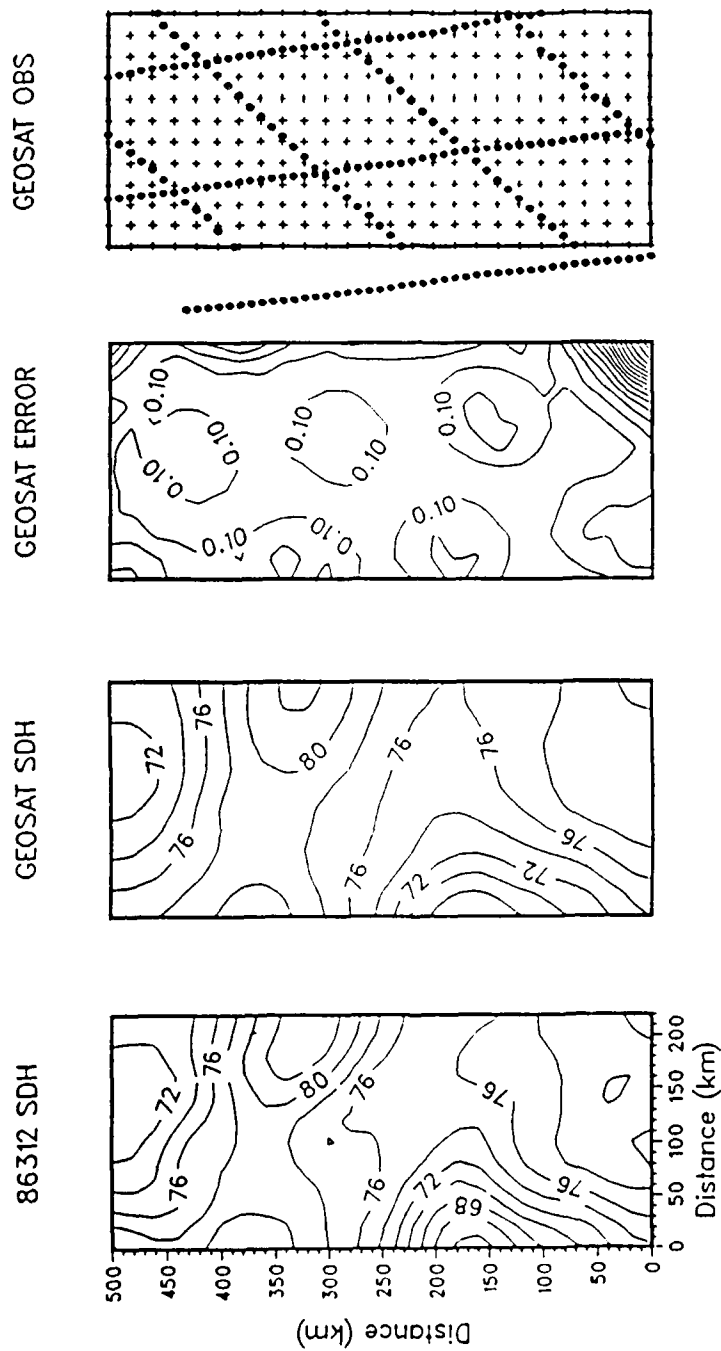


Figure 4.31 GEOSAT sampling experiment; survey pattern consists of all six orbits through the OPTOMA domain plus an ascending orbit to the west. SDH OA field on day 86312 is the sampled and verification field.

## E. VERTICAL COHERENCE AND AVERAGE VALUES

### 1. Vertical Coherence

During OPTOMA 23, there was little correlation between SST and fields at depth. However, the dynamic topography, from the surface to at least 300 m, and Z08 were all highly correlated throughout the survey (Table 11). The cyclonic features (C1 and C2) on the northeast and western borders and the anticyclonic feature (AC1) on the eastern border extended in depth through the water column from the surface to 300 m (Figure 4.32). The anticyclonic features on the southern border (AC2) was distinguishable at depth only by a weak ridge. The range in dynamic height appeared to have an e-folding depth of ca. 360 m, decreasing from ca. 14 dyn cm at the surface to ca. 4 dyn cm at 360 m. (There were numerous temperature inversions near the filaments, Appendix F).

Correlations between SDH and SST and between SDH and Z08 throughout the OPTOMA surveys were high (Figure 4.33). The correlation between SDH and SST averaged 0.65 with a  $\sigma$  of 0.11. The time series of the correlation between SDH and SST had significant deviations from the average, particularly during August 1982 and October 1983. The correlation between SDH and SST during OPTOMA 23 was 0.06 (during OPTOMA 18, it was 0.70).

The correlation between SDH and Z08 averaged 0.83 with a  $\sigma$  of 0.17. Deviations occurred during October 1983, the summer of 1984, and the spring of 1986. The correlation between SDH and Z8 during OPTOMA 23 was 0.71 (during OPTOMA 18, it was 0.80).

TABLE 11. COMPARISONS OF OPTOMA 23 FIELDS IN THE VERTICAL<sup>1</sup>

<u>Comparison</u> <u>Field</u>	<u>Range</u> <u>from</u> <u>to</u>	<u>Mean</u>	<u><math>\sigma</math></u>	<u>CORR</u>
SDH <sup>2</sup>	63 to 83	76.	4.	N/A
DH 50 m	50 to 68	60.	3.	0.97
DH 100 m	42 to 56	49.	4.	0.88
DH 200 m	27 to 37	32.	2.	0.81
DH 300 m	15 to 21	18.	1.	0.77
DH 400 m	4 to 6	6.	1.	0.71
SST <sup>3</sup>	12.9 to 16.4	14.4	0.7	0.06
Z08 <sup>4</sup>	120 to 258	179.	34.	0.71
MCSST <sup>3</sup>	9.3 to 15.5	13.5	1.0	0.57

CORR - Correlation;

MAE - Mean Absolute Error;

RMS - Root Mean Square;

RMSN - Root Mean Square Normalized (by variance field 2)

Notes:

1 - All fields are compared with SDH.

2 - Units are dyn cm.

3 - Units are °C.

4 - Units are m.

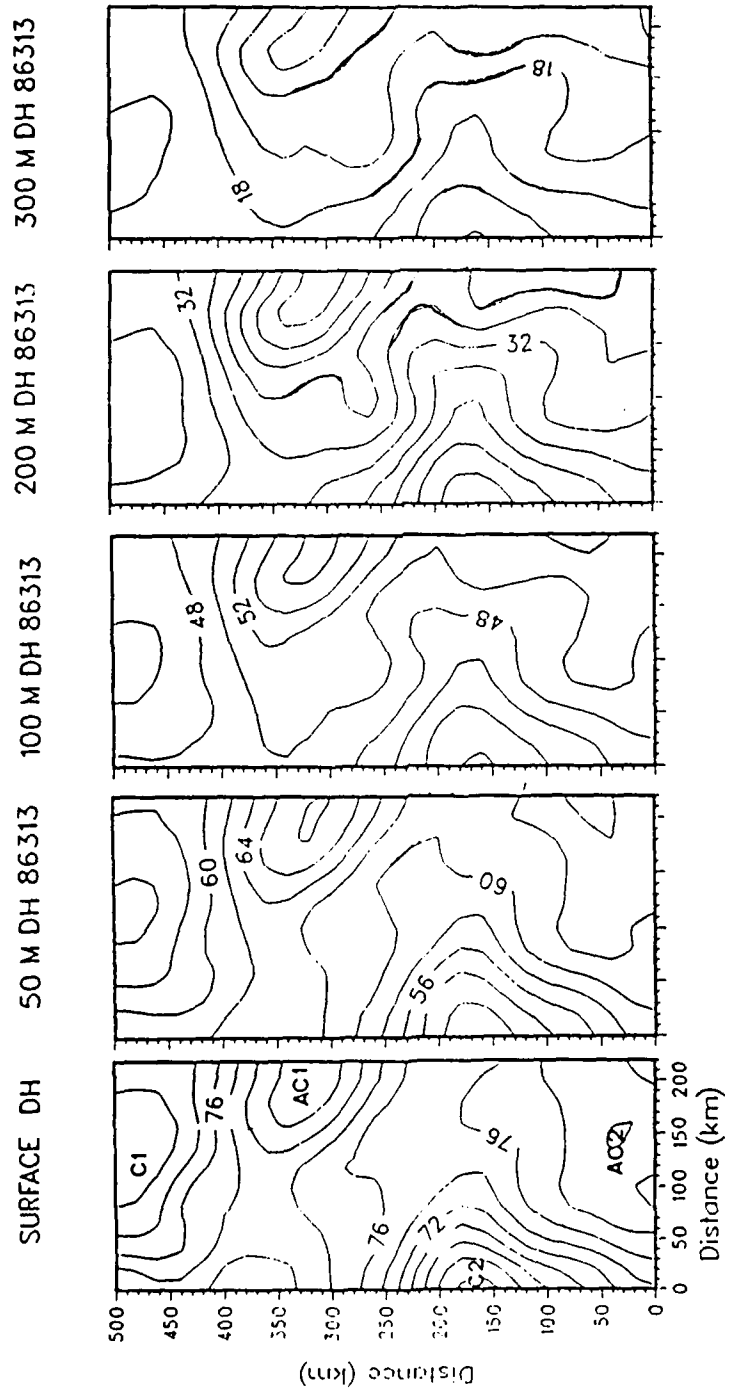


Figure 4.32 Surface, 50, 100, 200, and 300 m dynamic heights (all referenced to 450 m) on day 86313.





## 2. Comparisons with OPTOMA Ensemble Averages

Rienecker et al. (1987) calculated SDH, SST, and Z08 averages and  $\sigma$  for each OPTOMA survey through OPTOMA 22 (42 cruises and flights). For comparison, SDH, SST, and Z08 basic statistics were calculated for the OPTOMA 23 ensembles and plotted with the other surveys (Figure 4.34). To plot SDH from AXBT and CTD/XBT surveys on the same plot, the SDH from the P-3 surveys (referenced to 300 m) were corrected to the SDH from the ship surveys (referenced to 450 m) by adding 19 dyn-cm. This was the average difference over the entire OPTOMA survey ensemble and the difference in GDEM climatology between the SDH referenced at the two levels.

The SDH time series had seasonal variations each year. The SDH during each November, when the fall transition is expected, was lower than the SDH during the previous summer; the  $\sigma$  for the winter was less than that during the summer. Both observations were consistent with the decrease in mesoscale activity in the winter. The maximum signal occurred during the 1982-1983 El Nino. The total range covered was ca. 20 dyn-cm. The OPTOMA 23 SDH were the lowest in the ensemble.

The SST time series had seasonal variations with no long term trend evident. The total range covered was ca. 7 °C. The OPTOMA 23 SST were typical of SST values during the other fall surveys. The summer of 1983 had the highest SST, consistent with the El Nino (ca. 2 °C warmer than other summers). The following summer had the lowest SST, perhaps indicative of stronger upwelling and offshore transport.

There was no seasonal variation in the Z08 time series. As expected, it was similar to, but out of phase with the SDH time series

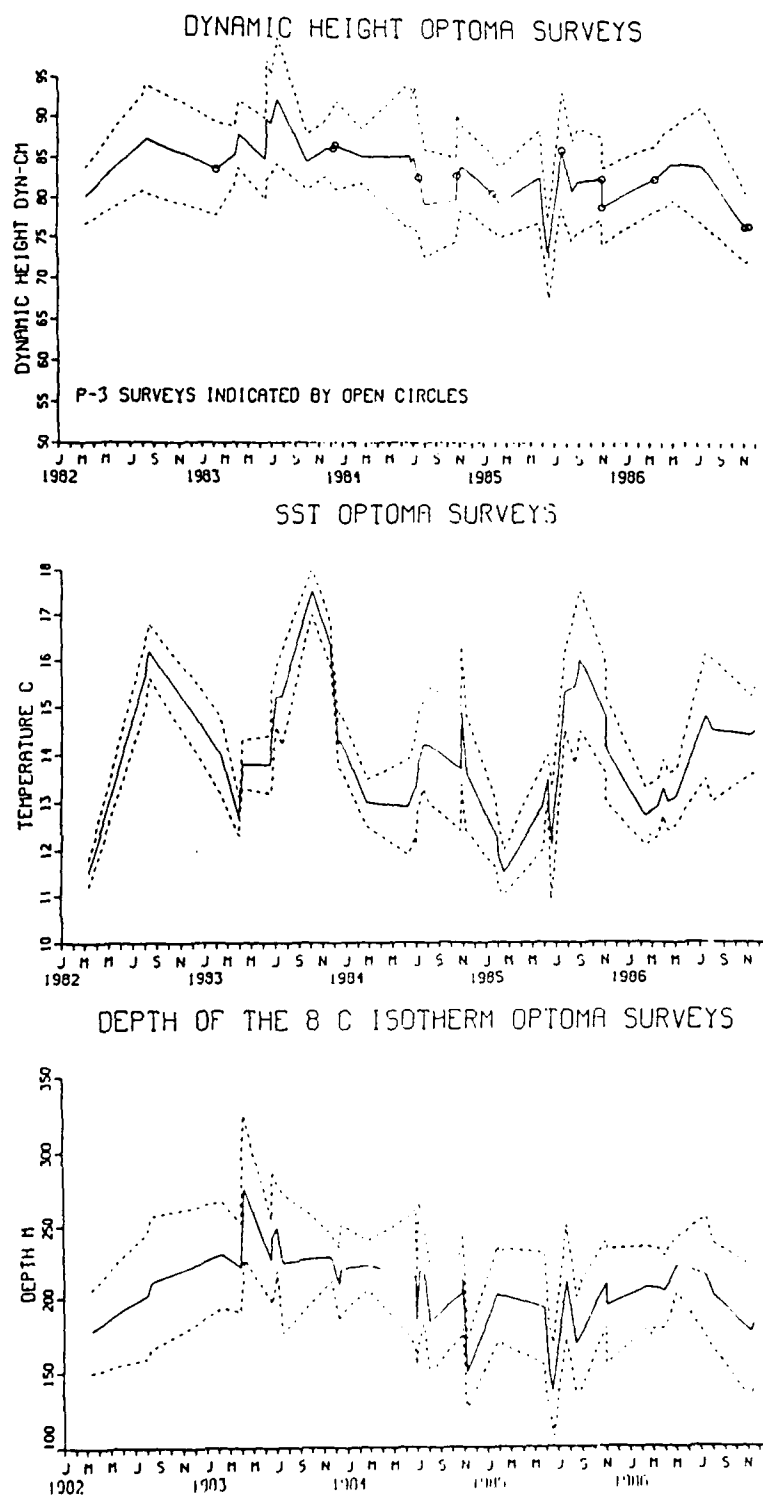


Figure 4.34 Time series of SDH (top), SST (center), and Z08 (bottom) averaged during the individual OPTOMA surveys ( $\sigma$  are dashed). OPTOMA 23 was the last survey.

(i.e., higher SDH, more anticyclonic activity, and deeper Z08). The 1982-1983 El Nino signal was identifiable: Z08 was at its deepest during this period reflecting the warmer water at shallower depths. Z08 was at a minimum during the summer of 1984, coincident with the cooler SST (and upwelling). The total range covered was ca. 200 m. Z08 during OPTOMA 23 was typical of the other surveys.

#### F. SUMMARY AND DISCUSSION OF THE OPTOMA 23 FIELDS

Two anticyclonic features and two cyclonic features were in the OPTOMA 23 domain (AC1 off Point Arena, AC2 off Monterey Bay, C1 off Cape Mendocino, and C2 on the western boundary). There was one cool filament, which extended westward from Point Reyes into and, eventually, through the domain. The two anticyclones (100 km radius) extended from the surface to 300 m; AC1 propagated westward (ca. 5 km/day), the other appeared to strengthen and move west. The two cyclones were larger than the anticyclones, they were quasi-stationary, and they extended from the surface to 300 m.

OA fields of SDH, SST, T50, T100, MLD, Z08, and Z10 during OPTOMA 23 were roughly comparable (in the range of values, but not in pattern) with GDEM climatology and past OPTOMA surveys. The OPTOMA 23 mean and standard deviation of SDH were lower than summer OPTOMA surveys, and meanders and eddies were not as "sharp" or as "densely packed". OA time series of three representative fields, SDH, SST and Z08, had small error fields, generally less than 5%. OA "10-day forecasts" of SDH, SST, and Z08 were about as accurate as persistence and generally better than climatology (except for SST).

The cool coastal water, cool filaments off Point Arena, Point Reyes and Point Sur, and numerous small-scale features (diameter ca. 10 km) were vividly obvious in the IR channels. However, eddies could not be distinguished in a single IR image due to the complicated pattern of multiple small-scale features and surface masking. In the imagery, the broad cool filament, identified in the SST OA fields between Point Reyes and Point Arena, was a narrow filament embedded in a wider cool body of water. During the survey, the upwelling front moved closer to shore and the cool filament lost integrity as winds favorable for upwelling ceased.

Some of the MCSST OA fields were similar to the SST OA fields; those that were not had gaps due to high and mid-level clouds. The MCSST fields were ca. 0.8 °C cooler than the SST OA fields and had standard deviations ca. 0.3 °C higher, consistent with the presence of sub-pixel size clouds, low stratus and numerous small scale oceanic features.

OCEANTRAK satellite surface vectors were processed with time intervals ( $\Delta t$ ) as short as six hours and as long as 48 hours; the optimal  $\Delta t$  was ca. 20 hours. The shortest  $\Delta t$  gave a rich "sense" of motion, but it was impossible to pinpoint the center of features accurately and beyond 48 hours, features lost their identity and were impossible to follow.

Although the method was quite subjective, the resulting vectors were consistent from one set to another and most of the vectors compared well with geostrophic velocities derived from SDH fields. Areas of disagreement were in the northeast corner of the domain (near a cyclone and where the upwelling front reached the domain) and near the cool

filament. Satellite-derived speeds were generally higher than geostrophic speeds by a factor of two. A correction for Ekman drift improved the comparison between satellite-derived and geostrophic speeds, and accounted for most of the difference in speed (ca. 75%).

Satellite surface velocity vectors were biased away from low velocities due to the technique; displacements of many pixels were easier to mark than displacement of a few pixels and the lowest limit of measurement was estimated to be one pixel over 12 hours (2 to 3 cm/s); the practical limit was two to three times this. The geostrophic velocities underestimated maximum velocities due to spatial smoothing, the integration of dynamic topography over depth, and level-of-no-motion errors. Also, there may have been ageostrophic effects.

Mesoscale activity was evident in the GEOSAT data (SSH OA fields). The size of the mesoscale features, the range of heights, and standard deviations were similar to those in SDH observations. However, on day 86312, the location of derived features was not entirely consistent with in situ observations; the sampling pattern accounted for the difference.

The mesoscale field apparently changed after the survey was completed (86323). The SSH field on day 86329, similar to the SDH OA forecast field, had anticyclonic features near the eastern boundary and an offshore trough resulting in a strong, meridional, northward jet of ca. 33 cm/s (gradient of 20 cm over 85 km). It was estimated that the 1986 Fall Transition in the CCS started between days 86312 and 86329 (8 and 25 November, respectively).

Simulations of GEOSAT data reproduced in situ fields accurately (with a correlation greater than 0.90) using perfect data from six orbits (two ascending and four descending). The addition of another ascending orbit (a seventh orbit) improved the correlation slightly.

During OPTOMA 23, there was little correlation between SST and fields at depth (0.06, compared to the OPTOMA average and  $\sigma$  of 0.65 and 0.11, respectively). However, the dynamic topography, from the surface to at least 300 m, and Z08 were all highly correlated (0.71, compared to the OPTOMA average and  $\sigma$  of 0.83 and 0.17, respectively). The cyclonic features (C1 and C2) on the northeast and western borders and the anticyclonic feature (AC1) on the eastern border extended in depth through the water column from the surface to 200 m while the anticyclonic features were distinguishable at depth only by a weak ridge. The average SDH during OPTOMA 23 was the lowest in the OPTOMA series; the average SST and Z08 were typical of values during other fall surveys.

## V. QUASIGEOSTROPHIC "NOWCASTS" AND "HINDCASTS"

### A. GENERAL

To determine sensitivity to different initial and boundary conditions, the QG model was used to "nowcast" and "hindcast" the streamfunction ( $\psi$ ) fields in the OPTOMA 23 domain. In nowcasting, OA fields of observed dynamic topography (converted to  $\psi$ ) initialized the model and were dynamically balanced by the model (within the limits of QG physics). In hindcasting, the future fields were generated from the initial field with specified boundary conditions. The boundary conditions were either persisted, from the initialization and from updates supplied to the model at later times, or linearly interpolated between initial and final fields.

Generally, the hindcasts were for ten days, from the initialization on day 86313 to day 86323, and these provided continuity between survey dates and determined the quasigeostrophic development of mesoscale features. The exceptions were 30-day hindcasts to determine model behavior beyond the OPTOMA 23 time period and a 15-day hindcast to compare with the GEOSAT SSH field on day 86329.

The QG model output fields for comparison were upper level  $\psi$  and the temperature at 100 m (T100), a derived quantity. For  $\psi$  verification purposes, nowcasts were generated for each day, from day 86313 to day 86323; the nowcasts were initialized with OA fields of dynamic topography at 50, 150, and 400 m on the same days (see Figure 4.17), boundary conditions were persisted, and neither wind stress curl forcing nor bottom topography were incorporated. For T100 verification purposes,



OA fields of T100 were generated from full-field in situ data on days 86313 and 86323. As with the OA time series of dynamic topography, the nowcasts and T100 fields were expected to most accurately depict the state of the ocean on OPTOMA 23 survey days (86313, 86321, and 86323). Climatology (from GDEM) and persistence (from day 86313) hindcasts were generated to provide baseline comparisons. Model accuracy (score) was ranked by pattern correlation (CORR) and root mean square error (RMSE), normalized by the standard deviation of the verification field (RMSN).

The impact of model parameters and data inputs, for initial and boundary conditions, on nowcast and hindcast accuracy was rigorously tested (OPTOMA 23 was a specific case study in the CCS during autumn, thus, the modeling results and comparisons were not expected to be statistically representative of general conditions). Variations included changes in the stability profile, the use of persisted or forecast boundary conditions, the incorporation of wind stress curl forcing and bottom topography, and different data subsamples (Table 12). The subsampling test scheme focused on simulations of: incomplete in situ data, poor initializations with good boundary condition updates, good surface fields with poor subsurface fields, and poor surface fields with good subsurface fields. The first two were referred to as 'Standard Subsampling' and the later two as 'Simulated GEOSAT' and 'Simulated Sofar' subsampling.

TABLE 12. MATRIX OF QG MODEL RUNS

I. GDEM (NOVEMBER) CLIMATOLOGY INITIALIZATION

3 LEVELS  
(Extended by EOF)

II. STRATIFICATION

GDEM            OPTOMA (Ensemble)            OPTOMA 23

III. BOUNDARY CONDITIONS

PERSISTED                      INTERPOLATED

From all three surveys (86313, 86320, 86323) or  
from the first and last surveys (86313, 86323)

IV. WIND STRESS CURL FORCING

NOT INCLUDED                      INCLUDED

If included, one of four wind stress curl values,  
calculated within the OPTOMA 23 domain, was used  
(north, central, southern, or spatially averaged)

V. BOTTOM TOPOGRAPHY

NOT INCLUDED                      INCLUDED

If included, an unlimited topography or one restricted  
to depths greater than 3400 m was used.

VI. "OPTIMAL" RUN<sup>a</sup>

PERSISTENCE FIELD                      VERIFICATION FIELD

With data from all three surveys (86313, 86320, and  
86323) or from the first and last surveys (86313, 86323)

VII. DATA SUBSAMPLING<sup>a</sup>

FULL            ONE-HALF    ONE-QUARTER    ONE-EIGHTH

With combinations of data from 50, 150, and 150 m

Notes:

- a - These model runs used the optimal configuration determined  
from previous sensitivity tests (i.e., 6 levels, OPTOMA 23  
stratification, interpolated boundary conditions, no wind  
stress curl, and no bottom topography).

## B. FULL FIELD INITIALIZATION AND SENSITIVITY ANALYSIS

### 1. Model Parameters

The domain of the QG model was increased from a 150 km by 150 km square, used in past OPTOMA experiments (e.g., Rienecker and Mooers, 1989) to a 225 km by 500 km domain. Initialization and boundary conditions were provided from OA dynamic topography in the three upper levels (50, 150, and 400 m, referenced to 450 m) for OPTOMA 23 survey days (86313, initialization; 86320, boundary condition update; and, 86323, verification, Figure 5.1). Fields for the three lower levels (at 1050, 2150, or 3400 m) were provided by an internal routine, which extended data from the three upper levels to the lower three levels using Empirical Orthogonal Functions (EOFs).

The QG model was run with model parameters specific to the OPTOMA domain and verified during past OPTOMA experiments (Rienecker and Mooers, 1989). The advective time scale in the domain ( $d/V$ ) was ca. three days and the planetary time scale ( $1/\beta d$ ) was ca. 23 days (with  $d = 50$  km,  $V = 20$  cm/s, and  $\beta = 10^{-11} \text{ s}^{-1} \text{ m}^{-1}$ ). (Other scaling parameters were: thermocline depth,  $H_t = 150$  m and depth,  $H = 4000$  m). The grid spacing was 20 km and the model had 11 X 25 lateral gridpoints. The six vertical levels were at 100, 200, 600, 1533, 2767, and 4000 m.

The Adams-Bashforth finite difference method for time derivatives was conditionally stable with a time step of two hours (i.e., the scheme was stable when the time step,  $\Delta t$ , was not greater than the amount of time necessary for a signal to move one grid). Occasionally, with subsampled fields or with some wind stress curl forcing cases, the time

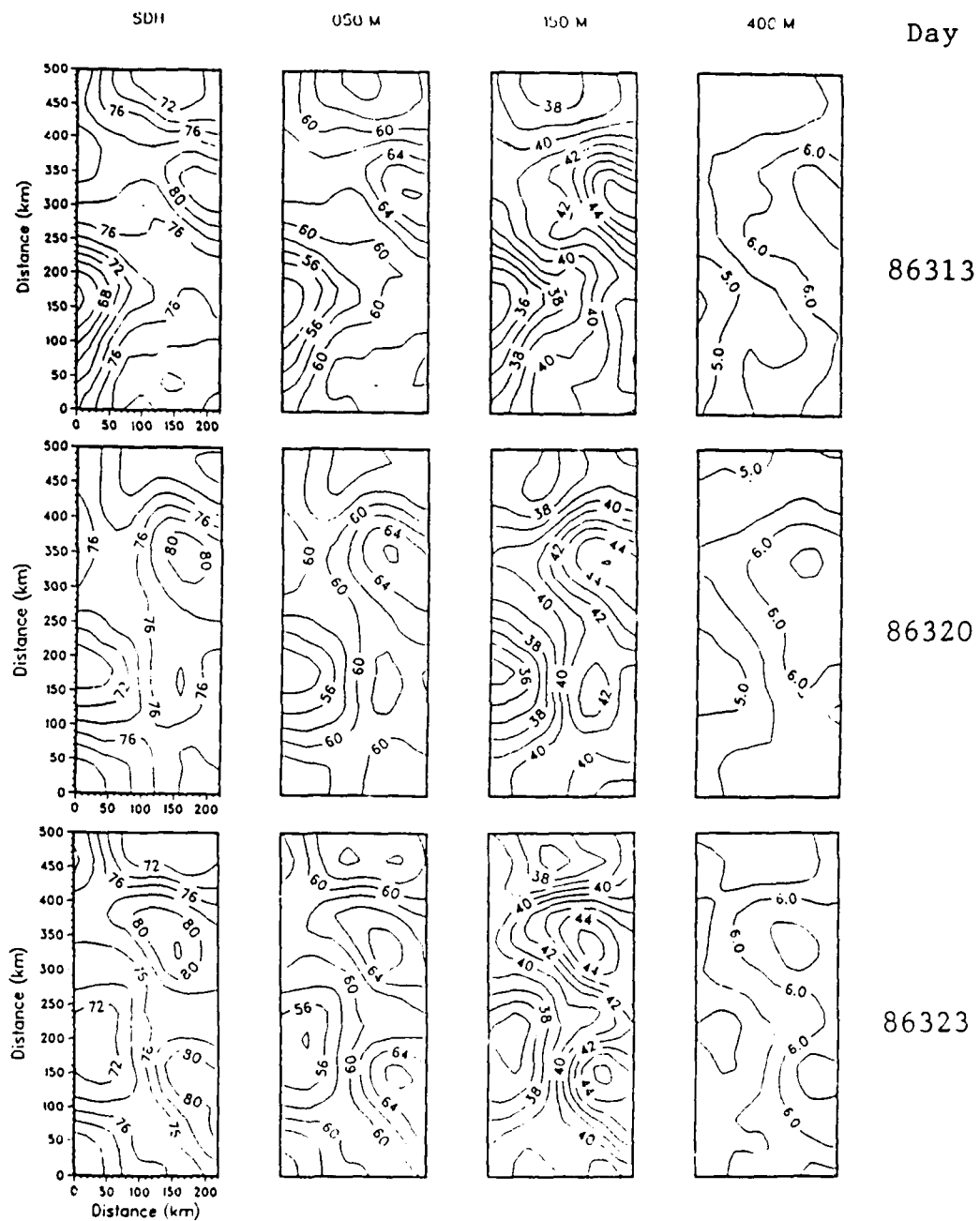


Figure 5.1 Full field SDH and dynamic height (referenced to 450 m) QG model input fields at 50, 150 and 400 m for days 86313 (top), 86320 (middle), and 86323 (bottom).

step was halved to one hour. (Table 20, Appendix G, is an example and an explanation of typical data inputs to run the model).

Hindcasts proved to be insensitive to the differences in three stratification profiles derived from: November GDEM climatology, the OPTOMA ensemble, and the observed OPTOMA 23 data. The non-dimensional stratification scale,  $\Gamma^2$ , and the normalized stratification,  $\sigma(z)$ , were calculated from the Brunt-Vaisala frequency,  $N(z)$ , for each level (Table 13). ( $N^2(z)$  was evaluated from the surface to 4000 m directly from climatology. It was fit to an exponential function with a value of  $0.227 \times 10^{-4} \text{ s}^{-2}$  at 300 m and an e-folding depth of ca. 800 m for the OPTOMA data, Rienecker and Mooers, 1989.)

## 2. Boundary Conditions

Boundary conditions for the hindcasts were provided by OA fields with a domain larger than the OG domain (they were calculated along the outer two grids). They were either persisted, in a step-wise fashion from survey-to-survey, or linearly interpolated between surveys (also called "benchmark" boundary conditions). Since the cyclonic features on the boundaries were quasi-stationary, the boundary conditions during OPTOMA 23 did not change dramatically over the course of the survey. Two hindcasts were made for each boundary condition type; one updated the boundary conditions on day 86320, the other did not.

Qualitatively, when boundary conditions were persisted, there was little change in the hindcast fields (Figure 5.2). For the first five days, there was little difference between persisted and interpolated cases (Figure 5.3). In the "interpolated" hindcast, as new boundary

TABLE 13. NON-DIMENSIONAL  $N_o / N(Z)$ ,  $\sigma(Z)$ , QG MODEL VALUES

<u>DEPTH (m)</u>	<u>NOV GDEM</u>	<u>OPTOMA ENSEMBLE</u>	<u>OPTOMA 23</u>
0	1.87	1.39	1.37
100	1.38	1.26	1.61
200	2.72	2.48	6.35
600	13.66	11.64	11.40
1530	50.58	38.08	50.50
2770	193.60	184.98	245.30
4000	1030.30	886.81	1175.90

.....

Other Parameters:

$\Gamma^2$	6.439	7.481	5.641	(note a)
$N_o$	$1.43 \times 10^{-4}$	$1.23 \times 10^{-4}$	$1.63 \times 10^{-4}$	(note b)

Notes:

- a -  $\Gamma^2 = f^2 d^2 / N_o^2 h_t^2$ , where  $f$  (coriolis) is  $0.91 \times 10^{-4} s^{-1}$  at  $3\sigma N$ ,  
 $d$  (length scale) is 50 km,, and  $h_t$  (thermocline vertical length  
scale) is 150 m
- b -  $N_o$  is the mid-thermocline (ca. 50 to 100 m) Brunt-Vaisala  
frequency; units are  $s^{-1}$

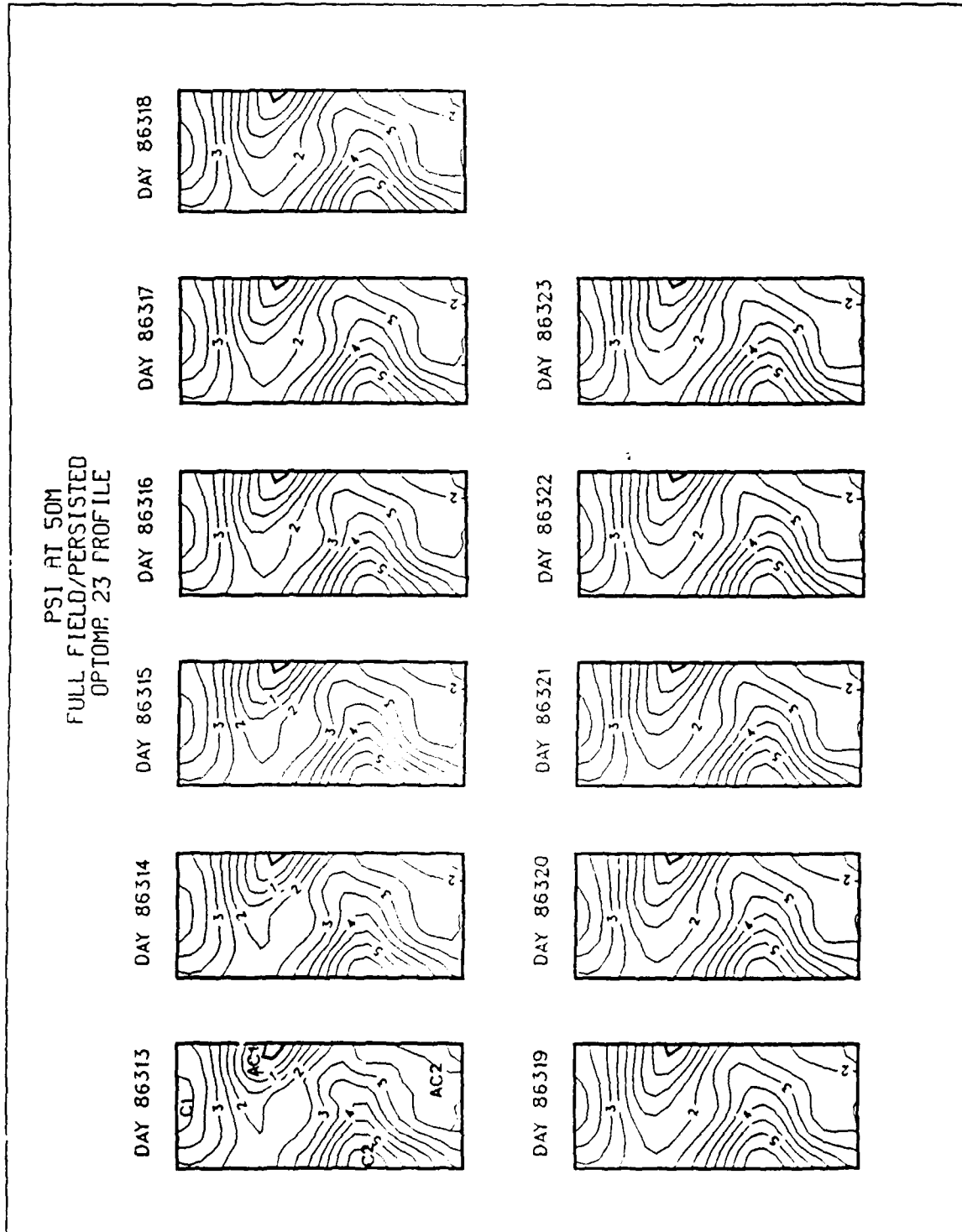


Figure 5.2 QG hindcasts with persisted boundary conditions and OPTOMA 23 stratification. Four mesoscale features, identified in OA fields, are labelled (AC1 and AC2, C1 and C2). (The hindcast plots were scaled).

11-DAY HINDCAST 86313 AND 86323  
PSI AT LVL 1; 3 LVLS; INTERPOLATED B.C.  
NO WIND STRESS/NO BOTTOM TOPO

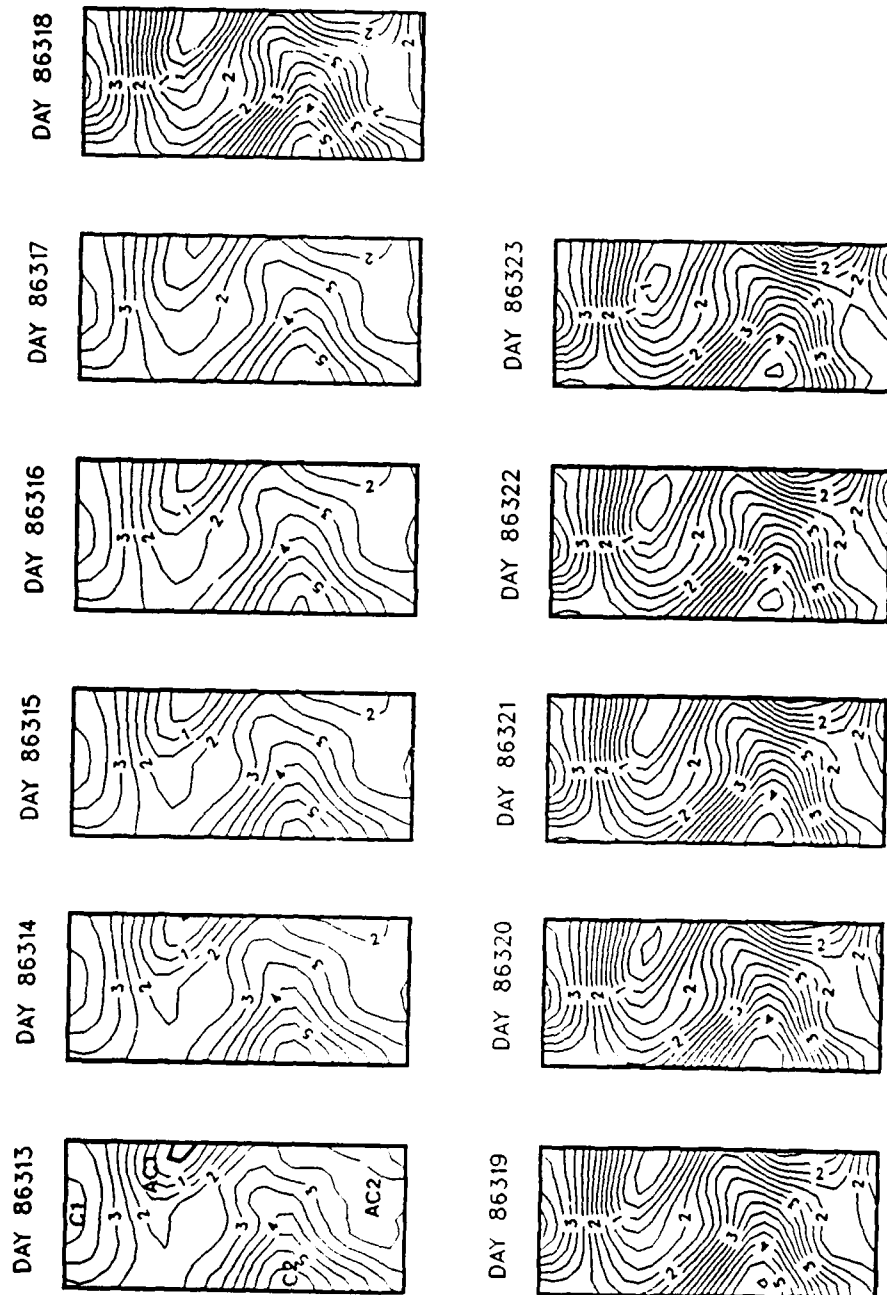


Figure 5.3 OPTOMA 23 hindcast from day 86313 to 86323; boundary conditions were interpolated and data on day 86320 were incorporated; there was no wind stress curl forcing or bottom topography. (The plots were scaled and the contour interval changed on day 86318).



conditions were inserted, AC1 moved to the northwest at ca. 5 km/day and C2 strengthened (as observed). Quantitatively, throughout the ten-day period, the interpolated boundary condition hindcasts were better than the persisted hindcasts. When compared with a verification field on day 86323, the interpolated boundary conditions resulted in ca. the same pattern correlation and RMSN (0.92 and 42%) as the persisted boundary conditions. Boundary condition updates on day 86320 improved the scores (Table 14).

### 3. Bottom Topography Effects

The QG model had a rigid lid and fixed levels. When bottom topography was incorporated in the model, it had an effect upon  $\psi$  in the lower level through vertical velocity (equation 2.7) and first-order continuity.  $\psi$  in upper levels was affected through the thermal vorticity term (equation 2.5).

Bottom topography for the QG model came from the 5' by 5' (10 km) DBDB5 NAVOCEANO data base. The sea floor is flat, with slope of order  $10^{-3}$  except for a small seamount in the southwest quadrant of the domain, which rises above the seafloor ca. 500 m with a slope of ca. 5%, and the continental slope in the northeast corner (Figure 5.4).

The QG constraint requiring no zero-order vertical velocity effectively limits bottom slope to order  $\epsilon$  (.02). The slopes, from both the unsmoothed DBDB5 data set and the OA bottom topography fields, even at their steepest in the northeast corner, were of order  $\epsilon$ . However, the vertical flow over the seamount could have had an effect upon the QG model (assuming significant horizontal flow at depth).

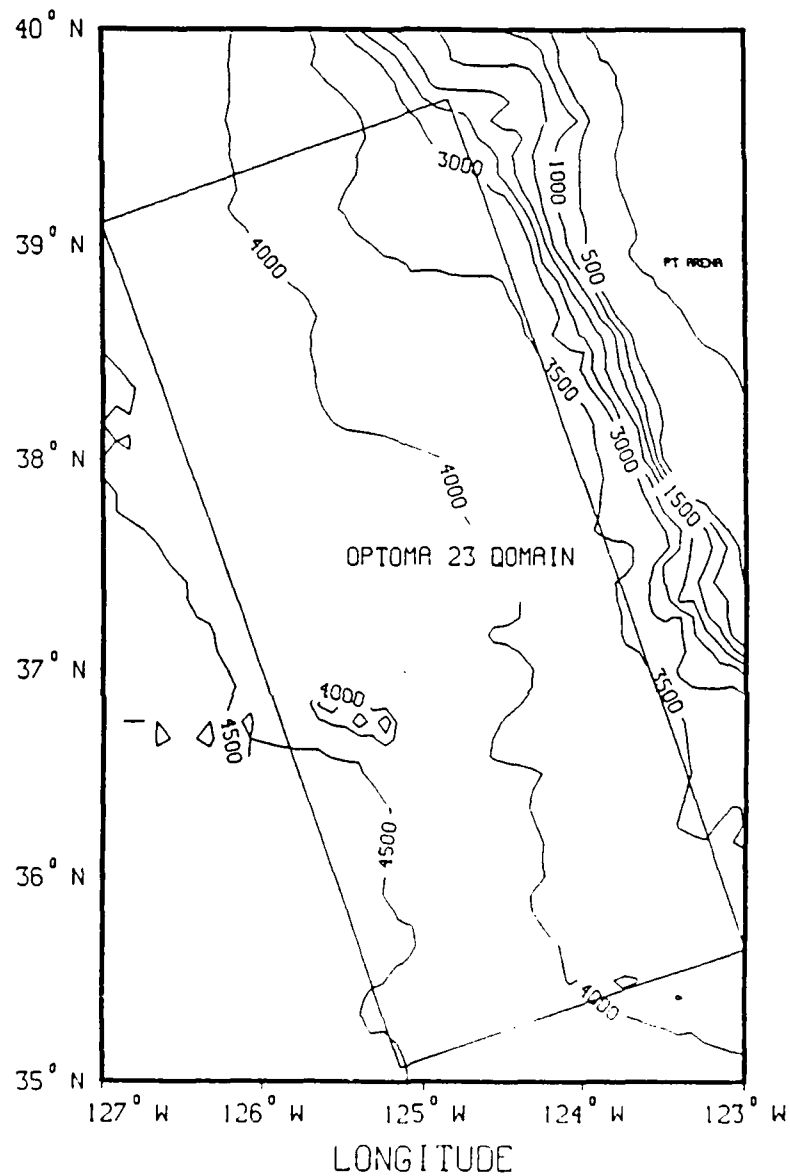


Figure 5.4 Bottom topography, contoured at 500 m intervals, from the NAVOCEANO DBDB5 data base. The bottom topography in the OPTOMA domain slopes slightly, except for a small seamount in the southwest and the continental slope to the northeast.

The topographic  $\beta$ -effect ( $\beta_t$ ) was compared to the planetary  $\beta$ -effect through:

$$\beta_t = f H / h_t d \quad (\text{equation 5.1}),$$

where  $f$  is the coriolis parameter (ca.  $10^{-4} \text{ s}^{-1}$ ),  $H$  is the bottom depth (4000 m),  $h_t$  is the thermocline vertical length scale (150 m), and  $d$  is the length scale (50 km) (Ikeda et al., 1989). Over the seamount in the southwest corner of the domain, where  $H_b$  is 2000 m,  $\beta_t$  is ca.  $10^{-8}$ , significantly greater than  $\beta$ , ca.  $10^{-11}$ .

To avoid potential problems caused by bottom topography, the DBDB5 data were smoothed and interpolated to the model grid using the OA routine (Figure 5.5). The seamount was smoothed out by the OA routine; to the northwest, bottom depths rose above 2500 m (level five in the model is at 2767 m). Topography was scaled by dividing through by the thermocline depth,  $h_t$ , and the Rossby number,  $\epsilon$ , to be consistent with the non-dimensionalization procedure followed in deriving the governing equation (equation 2.4).

Hindcasts were made using full field data inputs, OPTOMA 23 stratification, interpolated boundary conditions, and bottom topography.

OA SMOOTHED

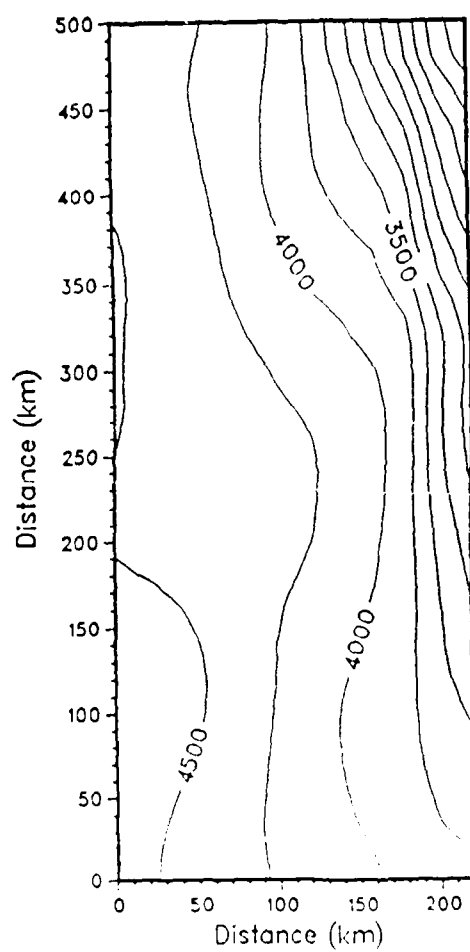


Figure 5.5 OA Bottom topography field from NAVOCEANO DBDB5 data base.  
Contour interval is 250 m.

the lower three levels were filled through the EOF data extension technique or by climatology. Qualitatively, with both EOF data extension and climatological lower levels, the surface field was markedly affected after ca. five days (Figure 5.6). The anticyclone on the eastern boundary (AC1) moved rapidly to the northwest (ca. 20 km/day), increasing the gradient between AC1 and the cyclone to the north (C1) and the cyclone on the western boundary extended to the northeast. Lower levels showed the impact of positive vertical velocity in the northeast corner of the domain: there was divergence and anticyclonic flow in level 5 (potential vorticity was conserved).

Quantitatively, incorporation of bottom topography and EOF extension resulted in a correlation of 0.85 and a RMSN of 53% in the upper level. The lower levels were also highly correlated (ca. 0.75), except for level 5 (0.34) for the reasons noted (Table 14). Truncation of the bottom topography, to depths deeper than 3400 m, had similar results. When input fields which included climatological fields at depth were used to initialize the model, the hindcasts were qualitatively and quantitatively worse (upper level correlation of 0.34 and RMSN of 188%) although the lower level was less energetic (Table 14).

#### 4. Wind Forcing

Wind stress curl forces the surface layer through Ekman pumping (equation 2.6). In past applications, wind stress curl forcing in the QG model improved pattern correlation, from 0.73 to 0.96, and reduced RMSN from 85 to 28% (Rienecker and Mooers, 1988). Since the QG model used a single value of stress over the entire domain and the Rienecker and Mooers (1988) domain was ca. one-fourth the size of the OPTOMA 23

11-DAY HINDCAST 86313 AND 86323  
PSI AT LVL 1; 3 LVL5; 3 EOF EXT  
INTERPOLATED B.C. BOTTOM TJPO

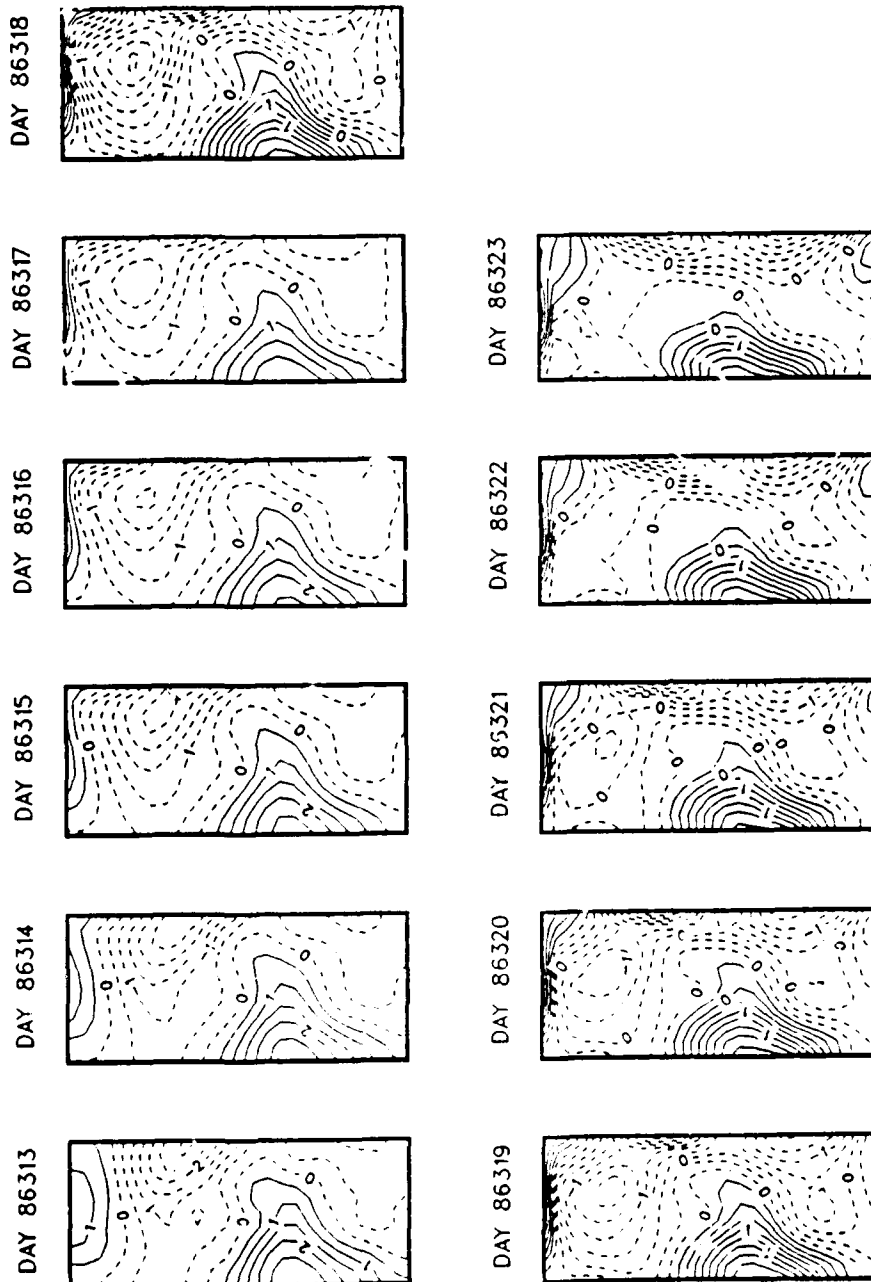


Figure 5.6 OPTOMA 23 hindcast, surface level, from day 86313 to 86323 using EOF extension, and incorporating bottom topography; boundary conditions were interpolated; there was no wind stress curl forcing. (The hindcast plots were scaled).

domain, similar results were not necessarily expected. (Whether or not differential stress curl contributed to the evolution of the mesoscale field during OPTOMA 23 was not addressed).

FNOC Marine Boundary Layer (MBL) winds were used to derive wind stress and wind stress curl on a 2.5 degree grid twice a day (Figure 5.7). The MBL winds were derived from the pressure analysis for the lowest level (19.5 m) in the Navy Operational Global Atmospheric Prediction System (NOGAPS) and wind observations, added using a Cressman over-relaxation technique.

The winds were converted to surface wind stress and the drag coefficient was corrected for stability and wind speed (equation 3.6). (The air-sea temperature difference, from NDBC buoys moored off the coast along the eastern border of the domain, averaged  $-0.5^{\circ}\text{C}$ .) Drag coefficient values ranged from 0.9 to  $1.3 \times 10^{-3}$  (Smith, 1988), a slightly larger range than other values used in the past, ca. 1.1 to  $1.2 \times 10^{-3}$  (Large and Pond, 1981, and Smith, 1980).

Wind stress curl was calculated using a centered finite difference scheme at the northern, center, and southern MBL gridpoints within the OPTOMA 23 domain. A spatial average was also calculated. Wind stress curl values during the OPTOMA 23 survey ranged from ca.  $-3.0$  to  $4.0 \times 10^{-8}$  dynes/cm<sup>3</sup> (Figure 5.8).

The MBL wind stress curl values during OPTOMA 23 were similar to those calculated during other OPTOMA winter experiments (Rienecker and Mooers, 1989). Because of the large grid spacing (300 km), estimates of wind stress curl from MBL winds were expected to be conservative (low).

# GRID POINTS FOR FNOC MBL WINDS

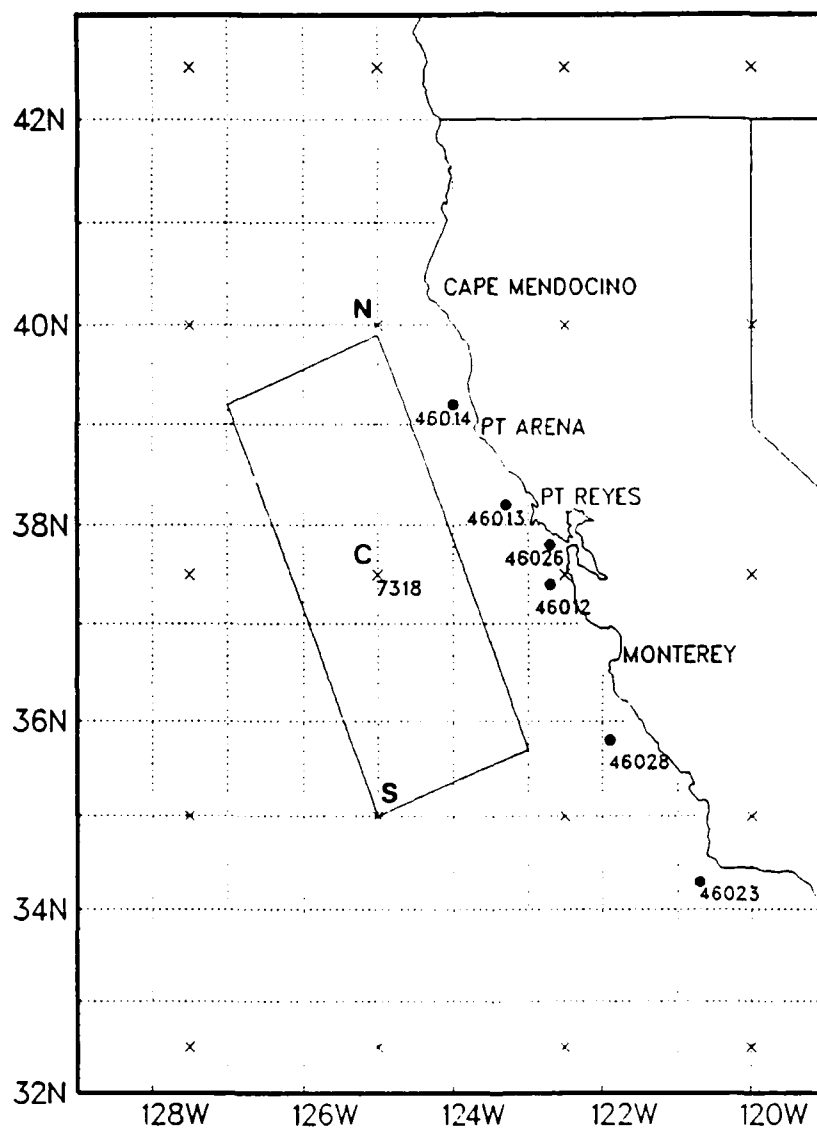


Figure 5.7 The OPTOMA 23 domain with MBL gridpoints (x), at 2.5 degree resolution, and NDBC buoy positions (dots). Wind stress curl was calculated at the northern grid point (N), the central (C), the southern (S), and area-averaged.



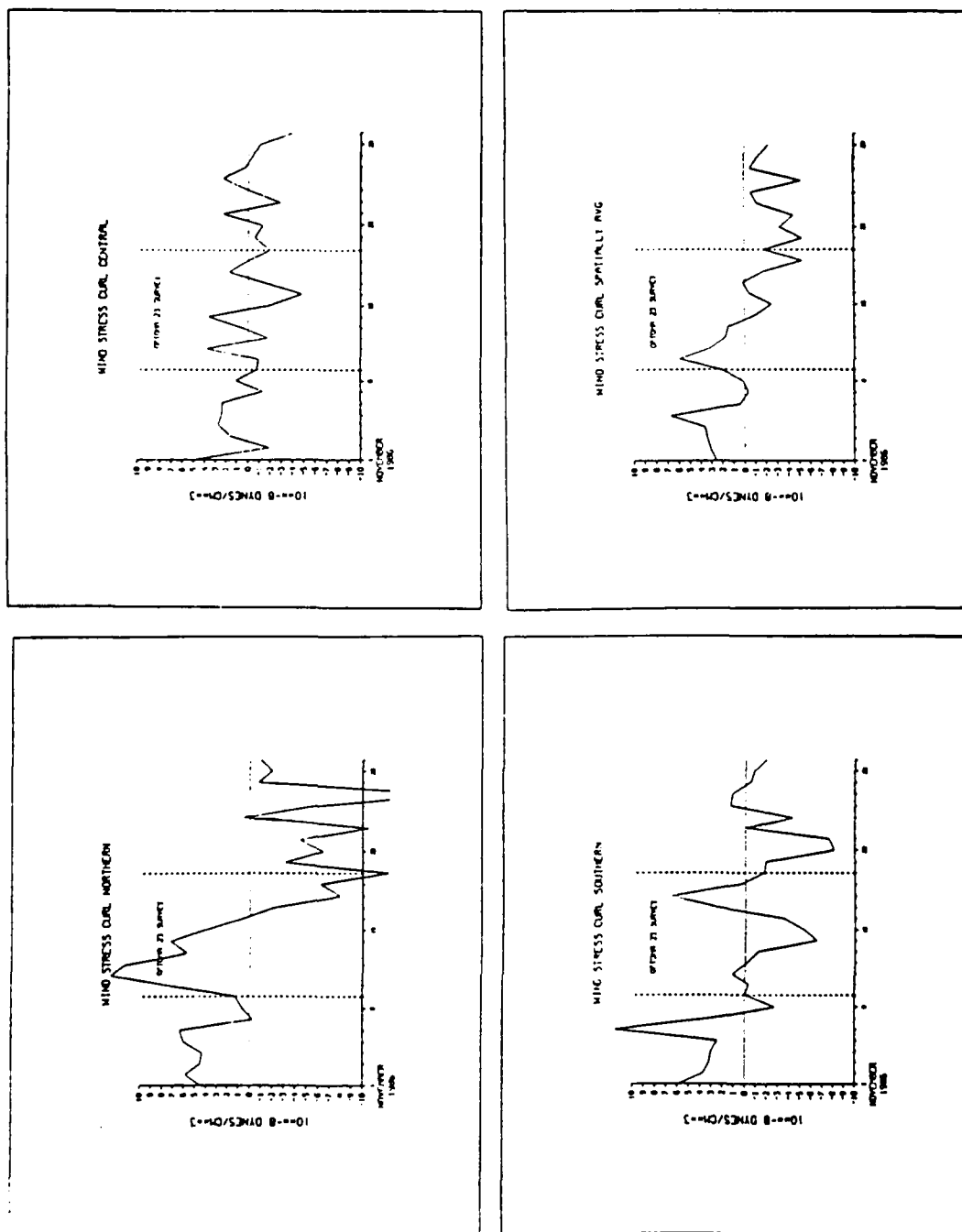


Figure 5.8 Wind stress curl in the OPTOMA 23 domain (north, southern, central and area-averaged) during the month of November 1986. The OPTOMA 23 survey took place between 9 and 19 November.

However, spot wind stress calculations using NDBC buoy data were of similar magnitude ( $\delta\tau_x/\delta y$  was calculated because the buoys were roughly aligned north-south). These buoy observations were not independent from the MBL data set, but the buoys were not spaced as far apart as the MBL grids (ca. 100 km). Aircraft wind observations at 1000 feet were closely spaced (ca. 50 km), but they were stronger (ca. 10 to 20 m/s) and the wind stress curls were much larger than at the surface. Hence, aircraft winds were not used to evaluate MBL winds.

Four hindcasts with wind stress curl forcing from the three gridpoints and the area-average were made. Qualitatively, the incorporation of wind stress curl forcing made little difference (Figure 5.9). Quantitatively, the correlation was lower (dropping to ca. 0.80) and RMSN was higher (rising to ca. 65%); the center gridpoint and averaged wind stress cases were the best of the four used. Inclusion of bottom topography with wind stress curl forcing changed the scores only slightly (Table 14).

### C. OPTIMAL CONFIGURATION HINDCASTS

#### 1. Optimal Hindcasts Fields

The optimal configuration, i.e., the configuration with the best overall comparison with the verification field, was: OPTOMA 23 stratification, three-level initialization fields (three upper level filled by OA inputs mapped from full fields on days 86313, 86320, and 86323, with the three lower levels extended by EOF), interpolated boundary conditions, no wind stress curl forcing, and no bottom

11-DAY HINDCAST 86313 AND 86323 LVL 1  
INTERPOLATED B.C. C WINDS

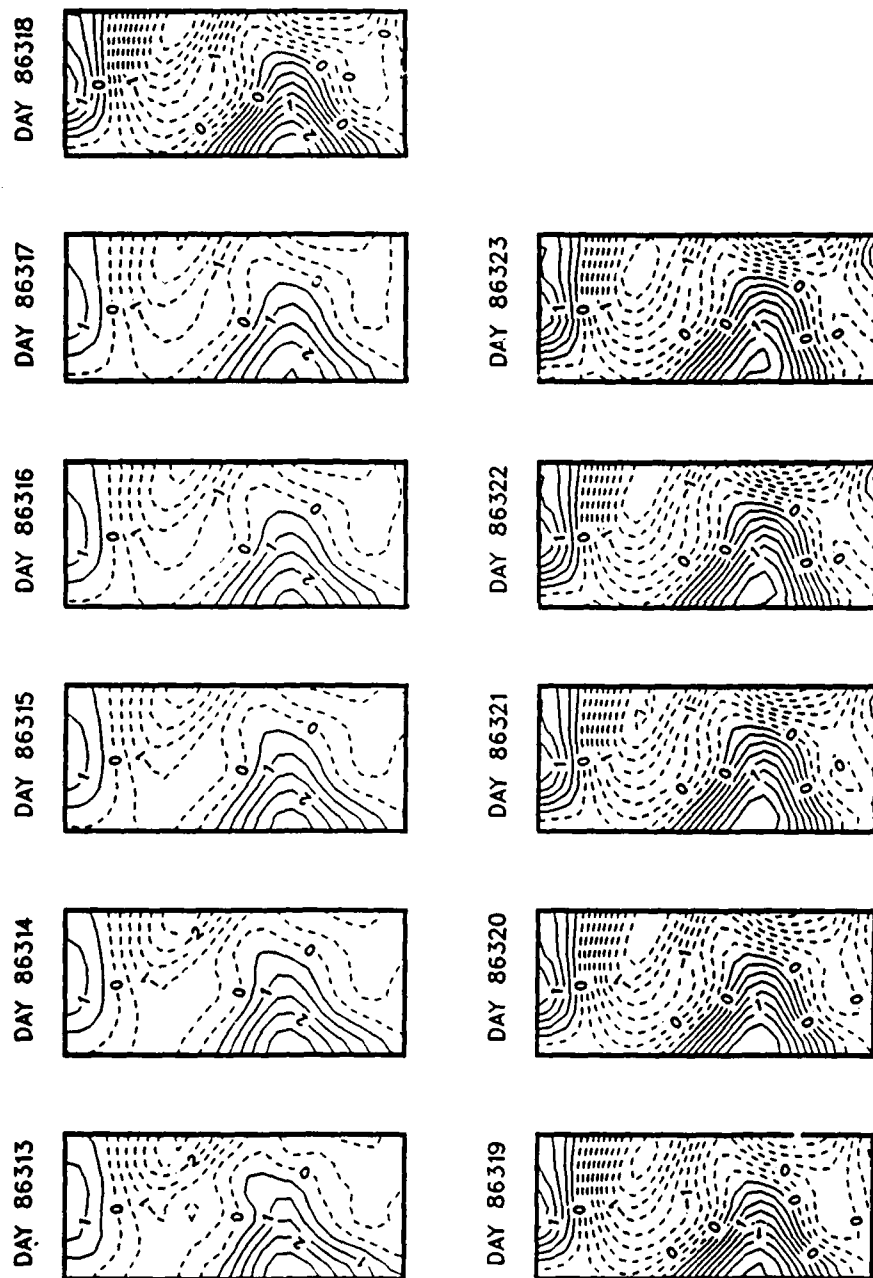


Figure 5.9 OPTOMA 23 hindcast, surface level, from day 86313 to 86323. Wind stress curl forcing was provided from values calculated at the center grid point. (The hindcast plots were scaled).

# VERIFICATION HINDCAST

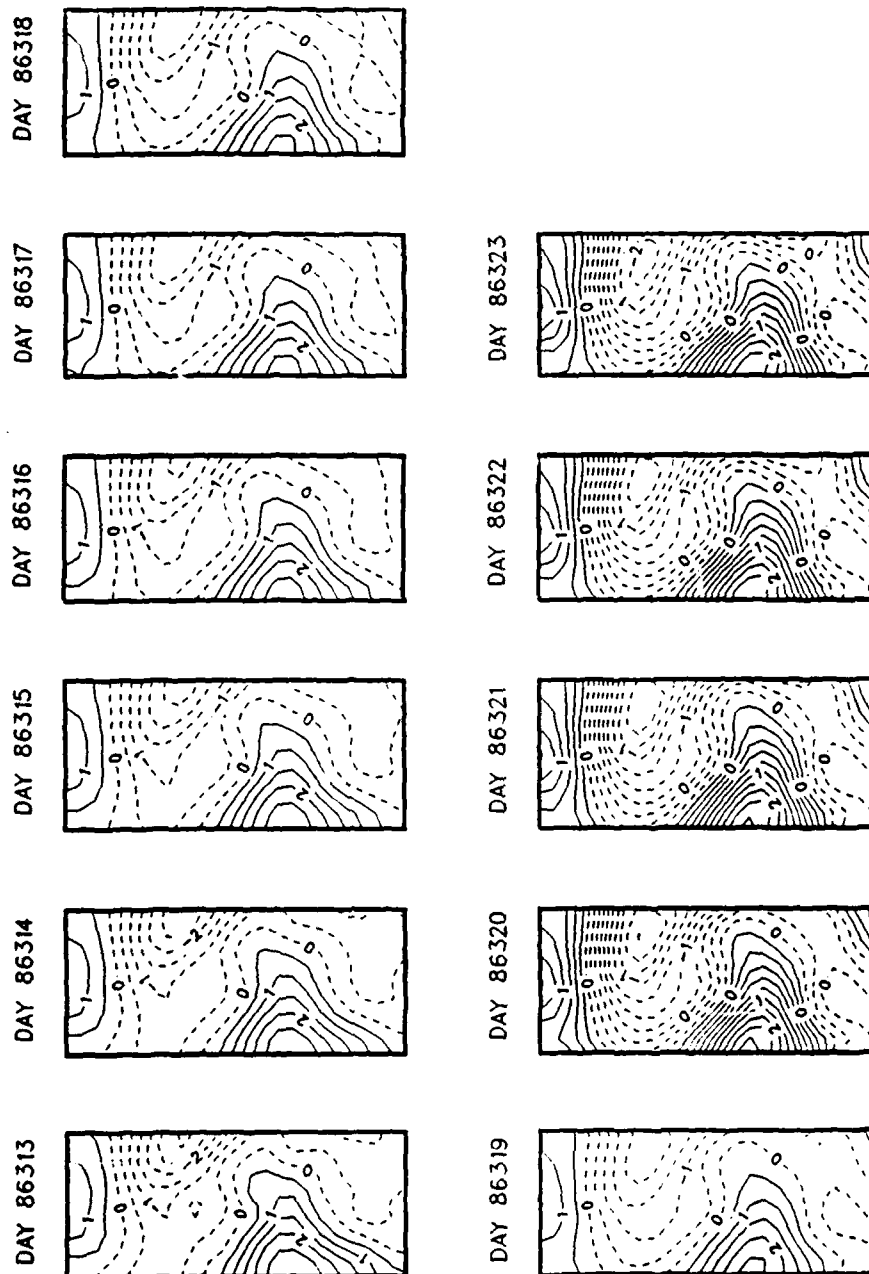


Figure 5.10 QG optimal hindcast: OPTOMA 23 stratification, initialization at three levels (extended by EOF), interpolated boundary conditions, no bottom topography, and no wind stress curl forcing. (The hindcast plots were scaled).

topography (Figure 5.10). This hindcast qualitatively and quantitatively compared the best with the verification nowcast on day 86323 and had a pattern correlation and RMSN of 0.92 and 42%, respectively. The correlations and RMSN were similar at all six levels.

The streamfunction, in the upper level, ranged from -3.01 to 2.63 with a mean of 0.03 and a standard deviation of 1.06 (non-dimensional units). The mean and standard deviation decreased with depth. Four mesoscale features (C1 to the north, C2 to the southwest, AC1 to the east, and AC2 to the southeast), identified originally in OA fields, were recognizable in the hindcasts. C1 remained on the northern border and increased in size and intensified; C2 remained quasi-stationary; AC1 moved northwest through the domain at ca. 6 km/day; and AC2 was a quasi-stationary ridge feature extending southwest.

In contrast, the nowcast persistence field, from day 86313, had a pattern correlation and RMSN of 0.78 and 88% when compared with the verification nowcast on day 86323 (Table 14). For further comparison, the model was initialized with GDEM November climatological dynamic topography, persisted boundary conditions, and no wind stress curl forcing or bottom topography (Figure 5.11). The climatological hindcast (climatological data which were dynamically balanced by the model and called "dynamic climatologies") compared poorly with the verification nowcast; the pattern correlation and RMSN were nowcast were 0.42 and 14%, respectively (Table 14). (The pattern correlations and RMSN for all variations leading to the selection of the optimal configuration are plotted in Figures 5.12, 5.13, and 5.14.)

GOEM CLIMATOLOGY INPUT  
STREAMFUNCTION AT 50M REL 450M

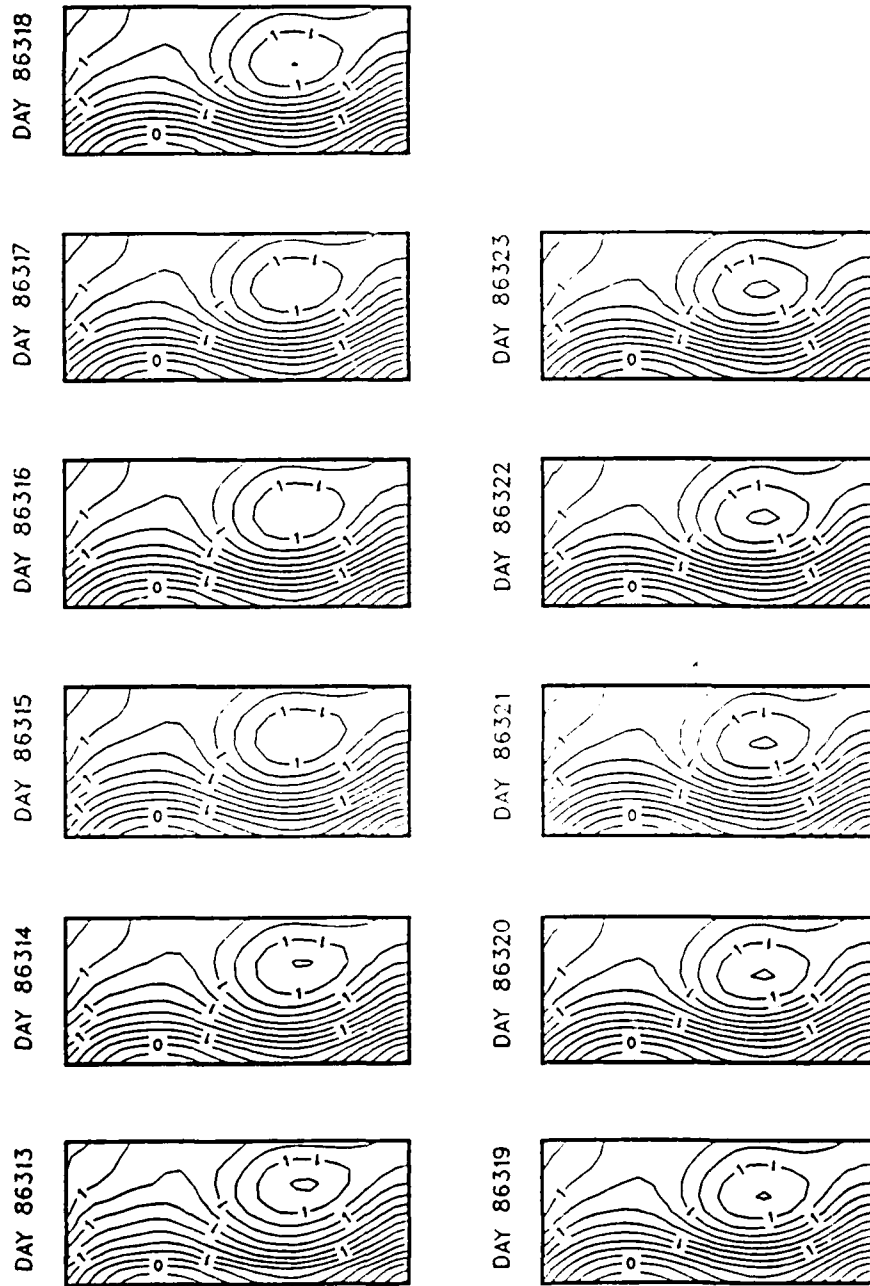


Figure 5.11 Hindcast initialized with GDEM: the upper three levels were extended to the lower three by EOF's; boundary conditions were persisted; there was no wind stress curl or bottom topography. The southern feature is cyclonic. (The hindcast plots were scaled).

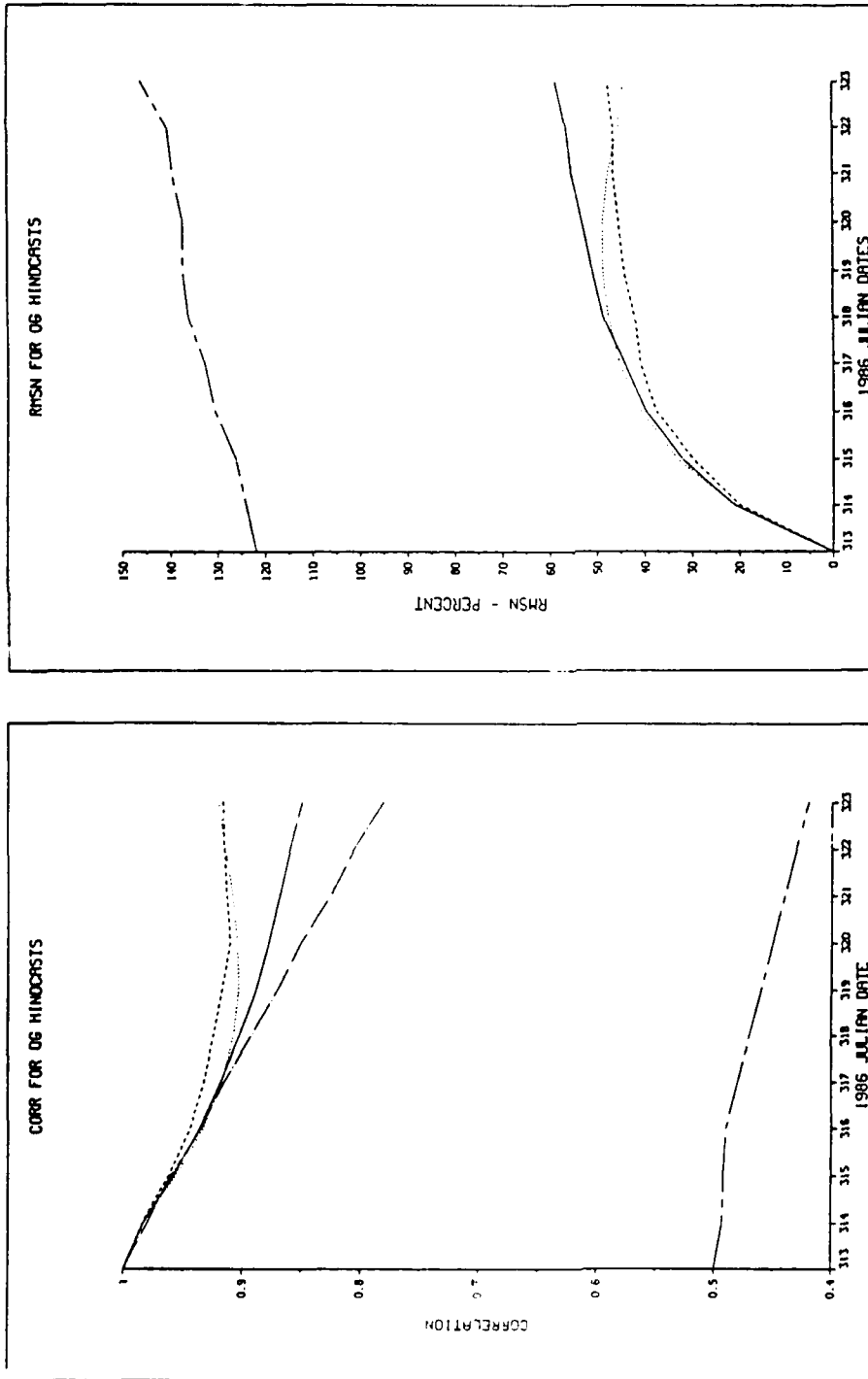


Figure 5.12 Correlation (left) and RMSN (right) for boundary condition (BC) variations: interpolated BC's between days 86313 and 86323 (solid), a BC update on day 86320 (dash), persisted BC's with data from 86313, 86320, and 86323 (dot). For comparison, persistence (chain dot), and climatology (chain dash) were added.

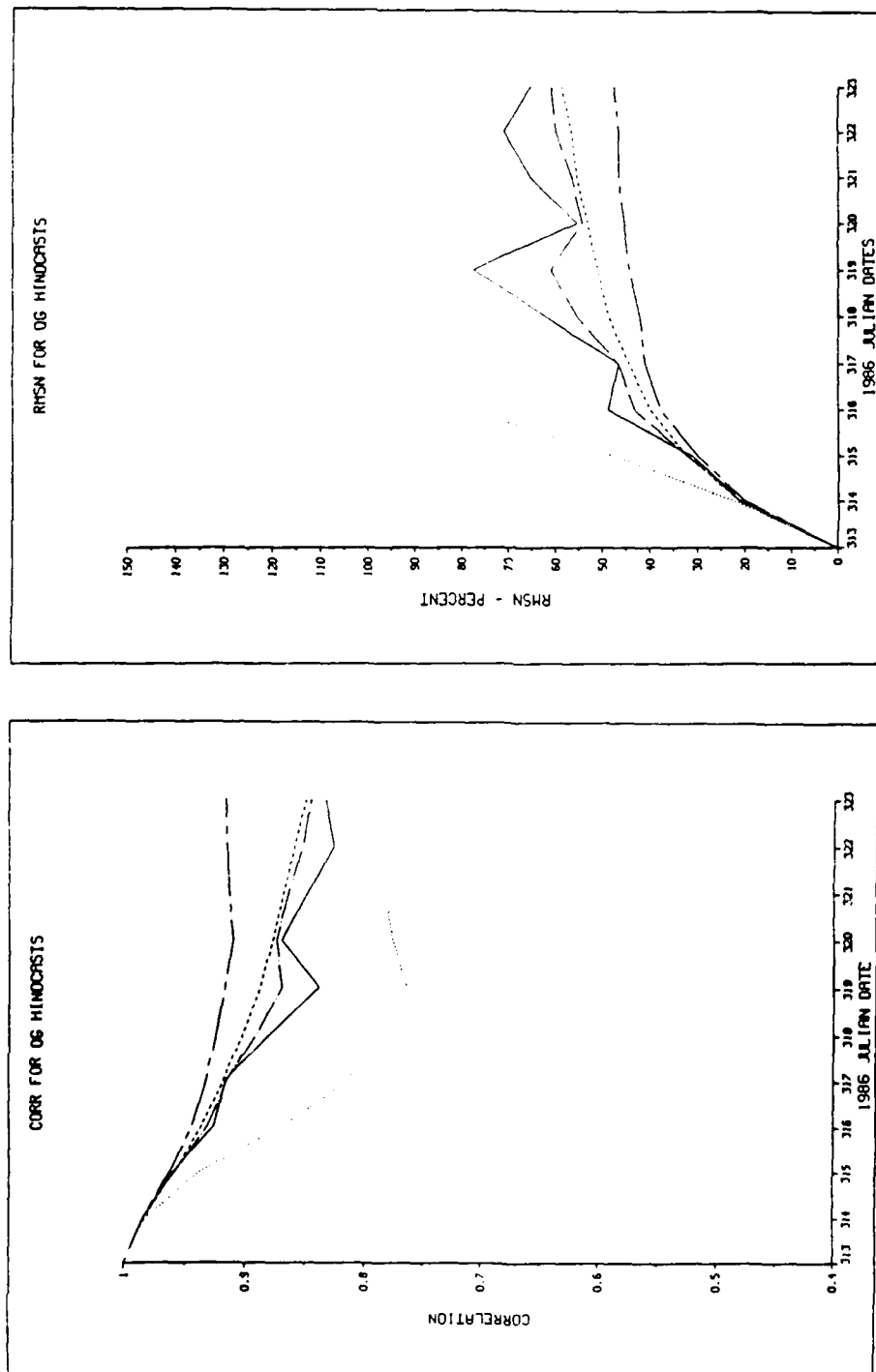


Figure 5.13 Correlation (left) and RMSN (right) for wind stress curl forcing (stress) and bottom topography (topo) variations: center grid stress (solid), no stress (dash), average stress (dot), center stress with topo (chain dot), and the optimal case of no stress and no topo (chain dash).



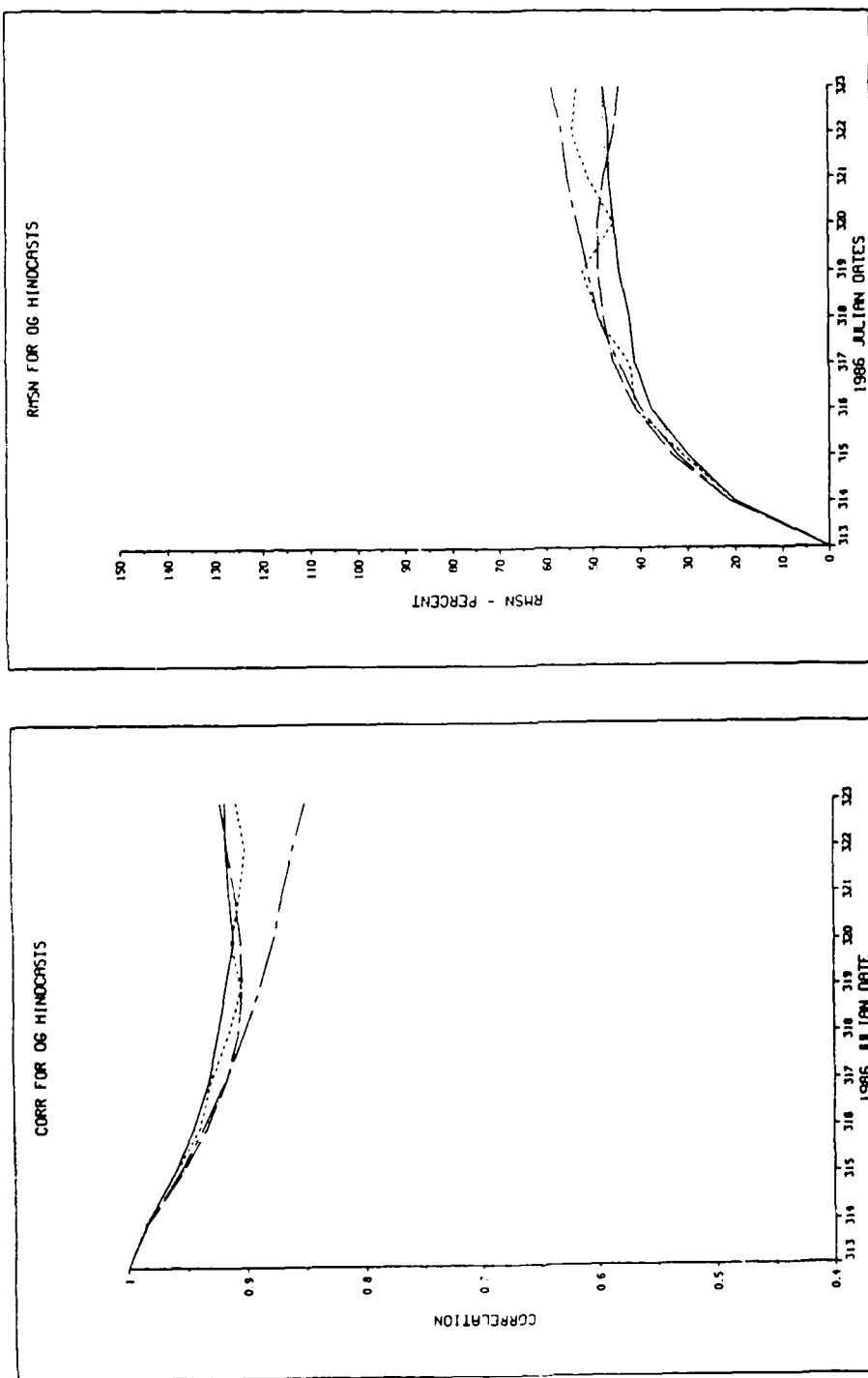


Figure 5.14 Correlation (left) and RMSN (right) for BC, stress, and topo variations: the optimal case of no stress and no topo (solid), center grid stress and topo (dash), no stress but topo included (dot), persisted BC's (chain dot), and data on days 86131 and 86323 only (chain dash).

TABLE 14. FULL FIELD QG COMPARISONS

<u>INPUT<sup>a</sup></u> <u>FIELD</u>	<u>INPUT<sup>b</sup></u> <u>LEVELS</u>	<u>BOUNDARY</u> <u>CONDITIONS</u>	<u>WIND</u> <u>STRESS</u>	<u>BOTTOM</u> <u>TOPOGRAPHY</u>	<u>LEVEL</u>	<u>CORR</u>	<u>RMSN</u>
<u>Stratification</u>							
13,20	3	PERSISTED	NO	NO	1	0.82	62%
GDEM							
13,20	3	PERSISTED	NO	NO	1	0.82	62%
OPTOMA ENSEMBLE							
13,20	3	PERSISTED	NO	NO	1	0.82	62%
OPTOMA 23							
<u>Boundary Condition Tests</u>							
13,20,23	3	INTERPOLATED	NO	NO	1	0.92	48%
13,20,23	3	PERSISTED	NO	NO	1	0.93	42%
13,23	3	PERSISTED	NO	NO	1	0.82	62%
13,23	3	INTERPOLATED	NO	NO	1	0.85	58%
<u>Bottom Topography</u>							
13,20,23	3	INTERPOLATED	NO	YES	1	0.85	53%
					5	0.34	85%
					6	0.75	67%
13,20,23	3	INTERPOLATED	NO	YES	1	0.34	18%
	3, Climatology						
<u>Wind Stress Curl Forcing</u>							
13,20,23	3	INTERPOLATED	YES C <sup>c</sup>	NO	1	0.83	65%
			YES N	NO	1	0.83	72%
			YES S	NO	1	0.81	71%
			YES A	NO	1	0.77	87%
			YES C	YES	1	0.86	58%

Notes:

a - Julian day 13 (86313); 20 (86320); or 23 (86323)

b - upper three levels are full fields; lower three are either filled by EOF extension of upper three levels or by climatology

c - C is the wind stress curl from the center grid; N, the northern grid; S, the southern grid; A, the average of all three (N, C, and S)

CORR - correlation;

RMSN - Root Mean Square, normalized by the standard deviation of the verification field on day 86323

TABLE 14. FULL FIELD QG COMPARISONS (CONTINUED)

<u>INPUT<sup>a</sup></u> <u>FIELD</u>	<u>INPUT<sup>b</sup></u> <u>LEVELS</u>	<u>BOUNDARY</u> <u>CONDITIONS</u>	<u>WIND</u> <u>STRESS</u>	<u>BOTTOM</u> <u>TOPOGRAPHY</u>	<u>LEVEL</u>	<u>CORR</u>	<u>RMSN</u>
<u>Persistence</u>							
13	3	PERSISTED	NO	NO	1	0.78	88%
<u>Dynamic Climatology</u>							
NOV GDEM	3	PERSISTED	NO	NO	1	0.42	144%
					6	0.54	110%

---

**Notes:**

a - Julian day 13 (86313); 20 (86320); or 23 (86323)

b - upper three levels are full fields; lower three are either filled by EOF extension of upper three levels or by climatology

CORR - correlation;

RMS - Root Mean Square, normalized by the standard deviation of the verification field on day 86323

## 2. Diagnostics

Daily model diagnostics were computed for each level. These diagnostics included: thermal and relative vorticity ( $Z$ ), potential vorticity ( $Q$ ), and kinetic energy ( $|\nabla\psi|^2/2$ , NRG), maximum velocity, pattern correlation (CORR), and RMS (difference between  $\psi$  fields).

The thermal and relative vorticity, potential vorticity, and kinetic energy diagnostics were area-integrated (over the full domain). In a closed basin, with no sources or sinks of heat or momentum, the model conserves potential vorticity and kinetic energy (as well as enstrophy,  $\xi^2$ ). In the OPTOMA 23 experiments, these were not constant due to the inflow/outflow of mass through open boundaries and the dissipation-like effects of filtering.

The energy and vorticity values in the upper two levels (the near surface and thermocline levels) were an order of magnitude larger than those in deeper levels (Figures 5.15, 5.16, and 5.17). Total kinetic energy, and kinetic energy in levels one and two, were fairly constant with initially high values dropping after three days. Total thermal and relative vorticity peaked near day 86321 (coincident with the new boundary conditions) and decreased steadily thereafter as the anticyclonic features propagated westward through the domain.

The vorticity values peaked on day 86321 and decreased through the end of the 30 day hindcast; potential vorticity was nearly constant through the same period. There was no evidence of "ringing" (i.e., dramatic changes in the field as the model dynamically adjusts to the initialization field).

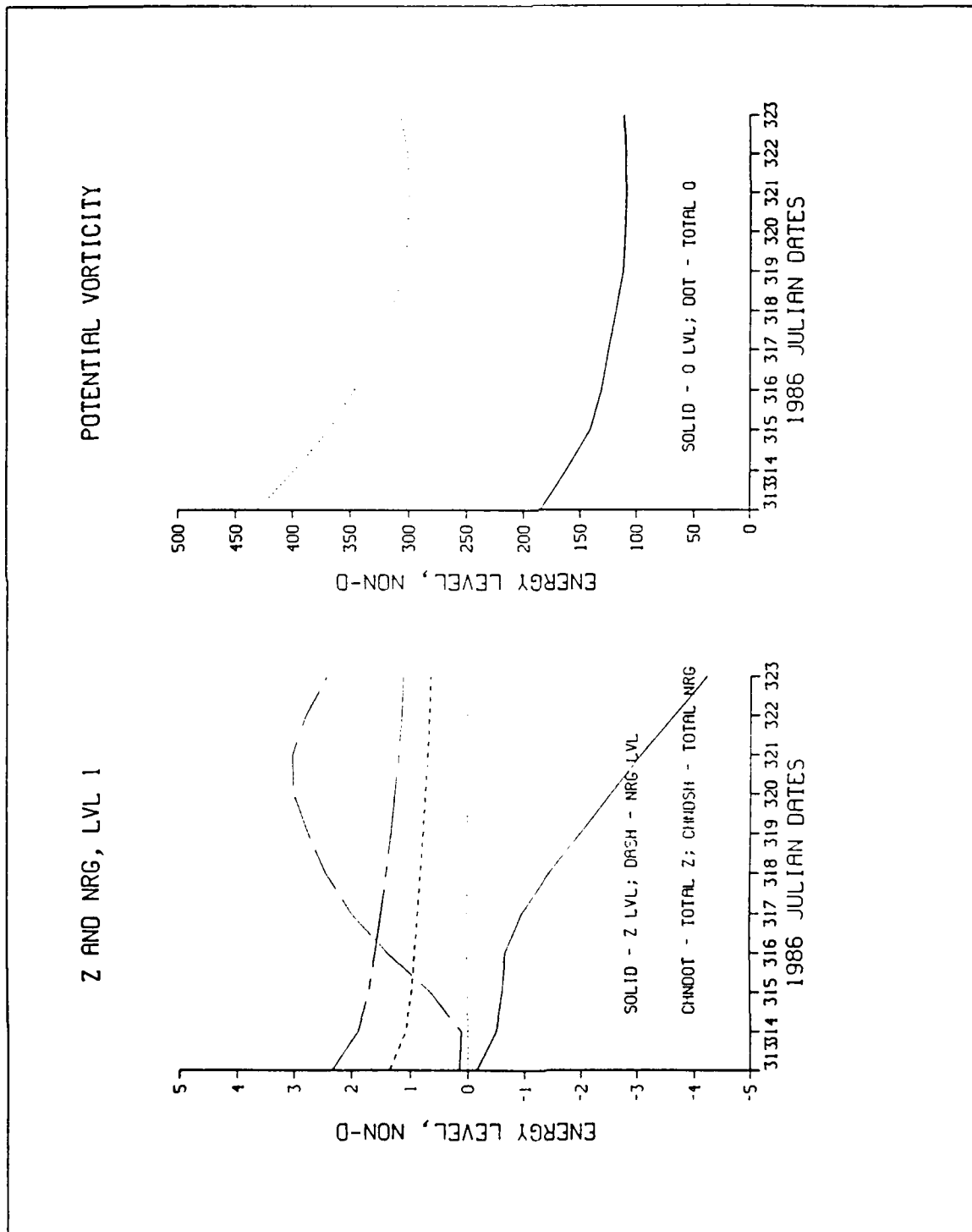


Figure 5.15 Area-integrated thermal and relative vorticity (Z) and kinetic energy (NRG) (left) and potential vorticity (O) (right). Level one values and total, over all six levels.

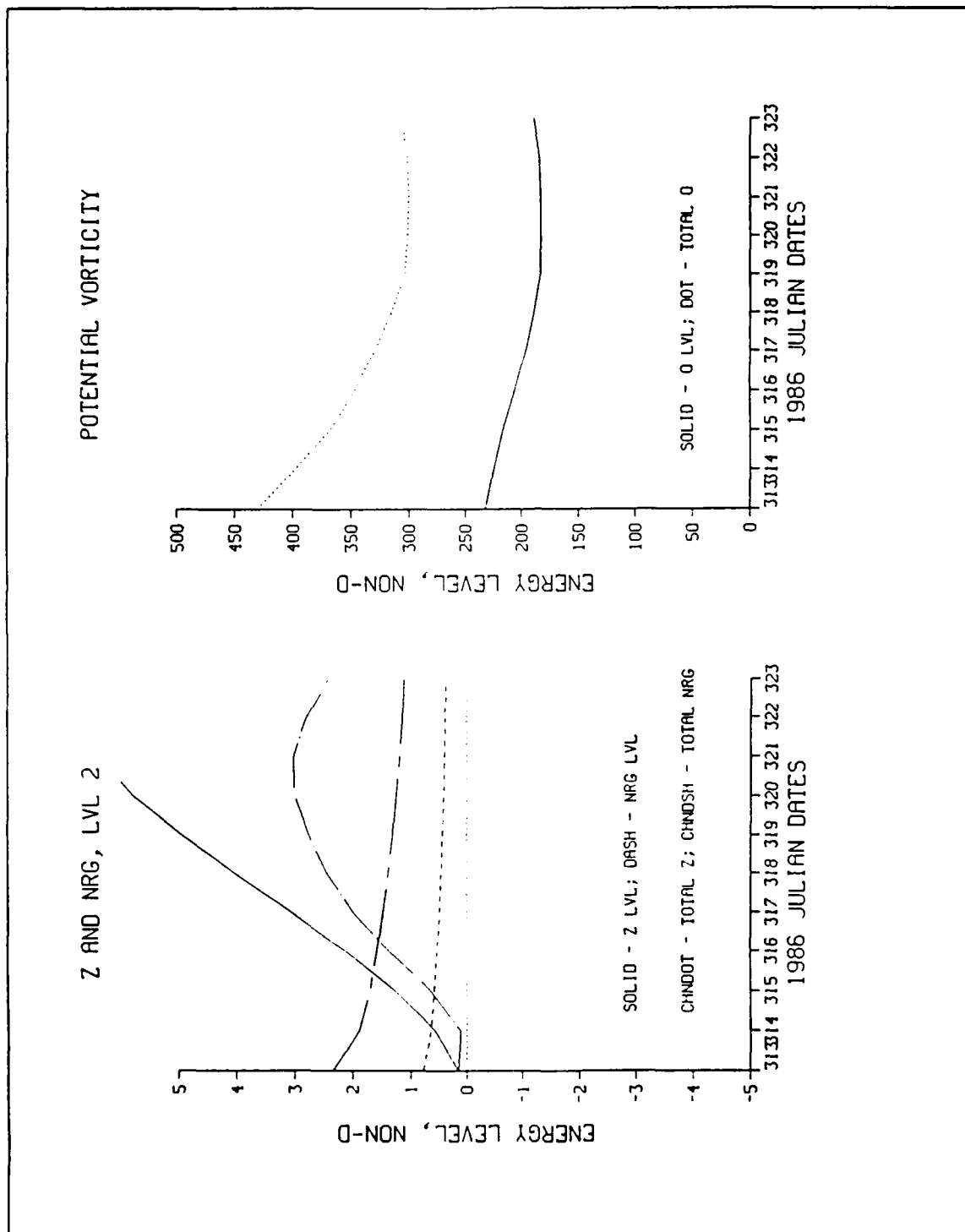


Figure 5.16 Area-integrated thermal and relative vorticity (Z) and kinetic energy (NRG) (left) and potential vorticity (Q) (right). Level two values and total, over all six levels.

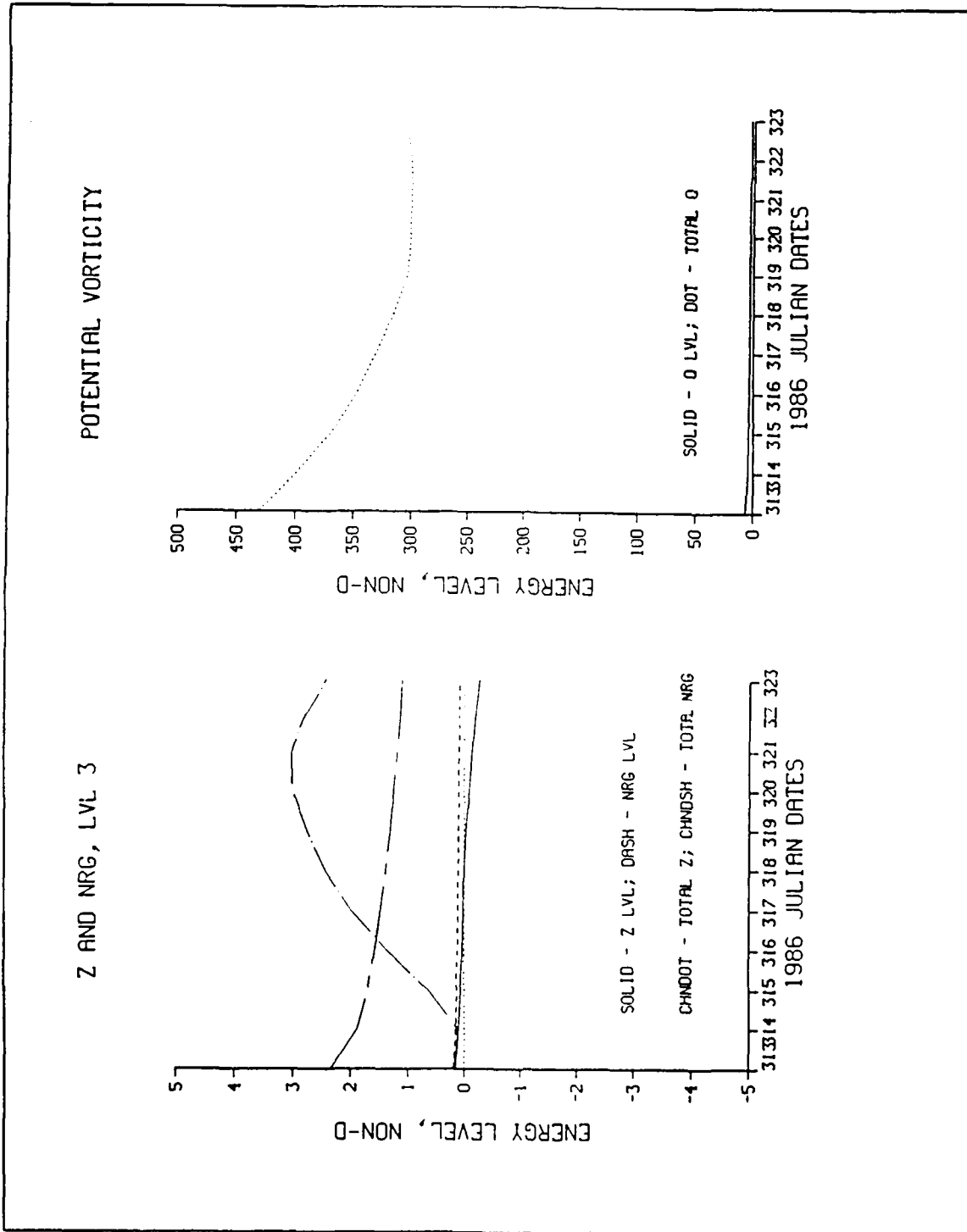


Figure 5.17 Area-integrated thermal and relative vorticity (Z) and kinetic energy (NRG) (left) and potential vorticity (Q) (right). Level three values and total, over all six levels.

The use of OA fields of dynamic topography for initialization helped ensure that the QG model started from a "realistic" state. Except for the subsampled fields, the OA fields were from full-data sets and they were smoothed by a Shapiro filter.

### 3. GEOSAT SSH Hindcast (86329)

The initialization field on day 86313 was hindcast to day 86329 to determine if QG dynamics accounted for the observed SSH field on day 86329. Boundary conditions were interpolated from day 86313 to day 86323 and persisted from then on. Wind stress curl forcing and bottom topography were not incorporated.

Although the boundary conditions on day 86323 fixed the mesoscale field in position past day 86323, the hindcast does qualitatively reproduce the major features in the SSH field on day 86329 (Figure 5.18). However, the QG hindcast propagated the anticyclonic zone further west than the observations indicate. Quantitatively, the QG forecast field had a correlation of 0.67 with the SSH field and had a maximum northward speed of ca. 37 cm/s. The SSH field had a maximum northward speed of 33 cm/s. (In comparison, the correlation between the SSH field and a 10-day OA forecast SDH field was 0.47 and the OA field had a maximum northward speed of 20 cm/s.)

### 4. Temperature Extractions

The motivation for extraction of temperatures from the QG model came from the acoustic modeling community. Of the three parameters which determine sound speed (temperature, salinity, and depth), temperature has the most pronounced effect near the surface ( $\delta C / \delta T = 2.4 \text{ m/s/}^\circ\text{C}$ );



GEOSAT HINDCAST 86329  
20-DAY HINDCAST FROM 86313 LVL 1  
INTERPOLATED NO WINDS/NO BOTTOM

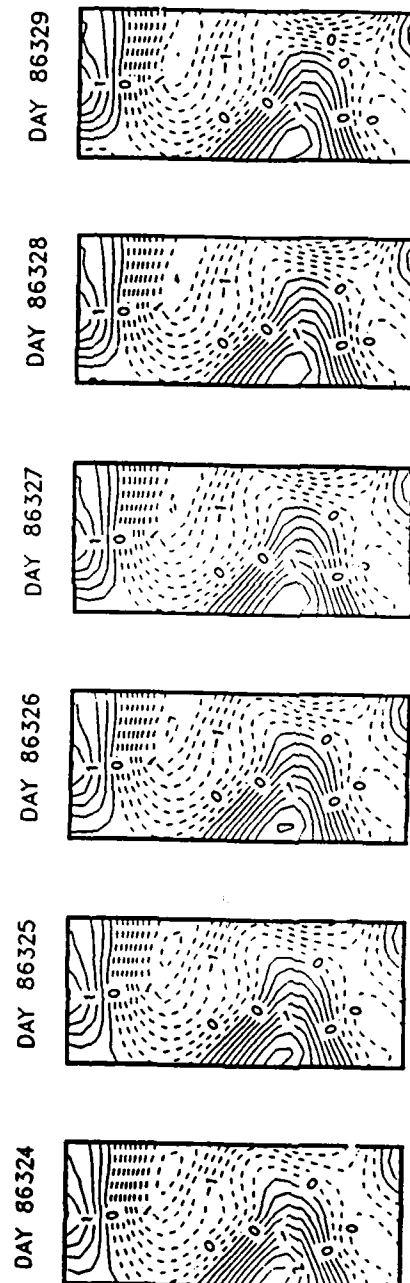


Figure 5.18 QG hindcast from day 86313 to day 86329, a GEOSAT 17-day ERM; no wind stress curl or bottom topography forcing was incorporated. (The hindcast plots were scaled).

$\delta C/\delta z$ , the gradient of sound speed with respect to  $z$ , determines the arc of the ray originating at that depth (Urick, 1982).

While MCSST or other SST estimates are accurate and readily available, temperatures at depth in most parts of the ocean are not. Unlike a primitive equations (PE) model, in a QG model, temperature ( $T$ ) must be analytically or empirically derived at the interfaces between levels. From the hydrostatic equation,  $T$  is proportional to the vertical derivative of  $\psi$ ,  $\delta\psi/\delta z$ ; however, the "analytical" approach does not produce accurate values of  $T$  because of scaling considerations and the selection of a mean temperature profile (the temperature perturbations are added to the mean). Instead, temperatures have been derived empirically from QG hindcasts in the following manner:

- (1) characteristic values for in situ  $\psi$  are identified at each model level (plus the top and bottom),
- (2) corresponding temperature profiles are obtained from in situ values or historical data bases and a value of  $T$  is assigned to the characteristic  $\psi$  at each model level, and
- (3) the appropriate  $T$  at each gridpoint is determined by linear interpolation between the two closest characteristic  $\psi$  (Glenn and Robinson, 1989).

Three methods of extracting the temperature at 100 m ( $T_{100}$ ) were compared. Two were based upon Glenn and Robinson (1989); the first used in situ observations of  $T$  and  $\psi$ , the second used climatological values. The third method empirically related  $T$  to  $\delta\psi/\delta z$ , instead of  $\psi$ .

The 'in situ', 'climatological', and 'vertical derivative' temperature equations were:

$$T = 0.43\psi + 9.3 \text{ (equation 5.2),}$$

$$T = 2.20\psi + 9.5 \text{ (equation 5.3), and}$$

$$T = 1.23\delta\psi/\delta z + 9.3 \text{ (equation 5.4).}$$

T100 fields were generated from QG hindcasts on days 86313 and 86323 and compared with T100 OA fields. Qualitatively, both the in situ and vertical derivative methods reproduced the temperature fields on days 86313 and 86323 (Figures 5.19 and 5.20). While both of these methods accurately derived the mean temperature and variance of the observed fields (ca. 9.3 °C and 0.20 °C squared), the vertical derivative was the most accurate with a pattern correlation of 0.93 and a RMSN of 61%. (The in situ scores were 0.71 and 76%, respectively.) Qualitatively and quantitatively, the climatological method was the least accurate (with a pattern correlation of 0.71, a RMSN of 88%, and a variance ca. four times that of the other methods, 4.54 °C squared).

A T100 difference field was calculated between days 86313 and 86323 for both vertical derivative and in situ methods (Figure 5.21). With both methods, warming in the southern part of the domain was observed apparently in conjunction with the fall transition. The difference field from the vertical-derivative temperature fields was more accurate (pattern correlation of 0.90 and RMSN of 11%).

# T100 OA AND QG - AVG

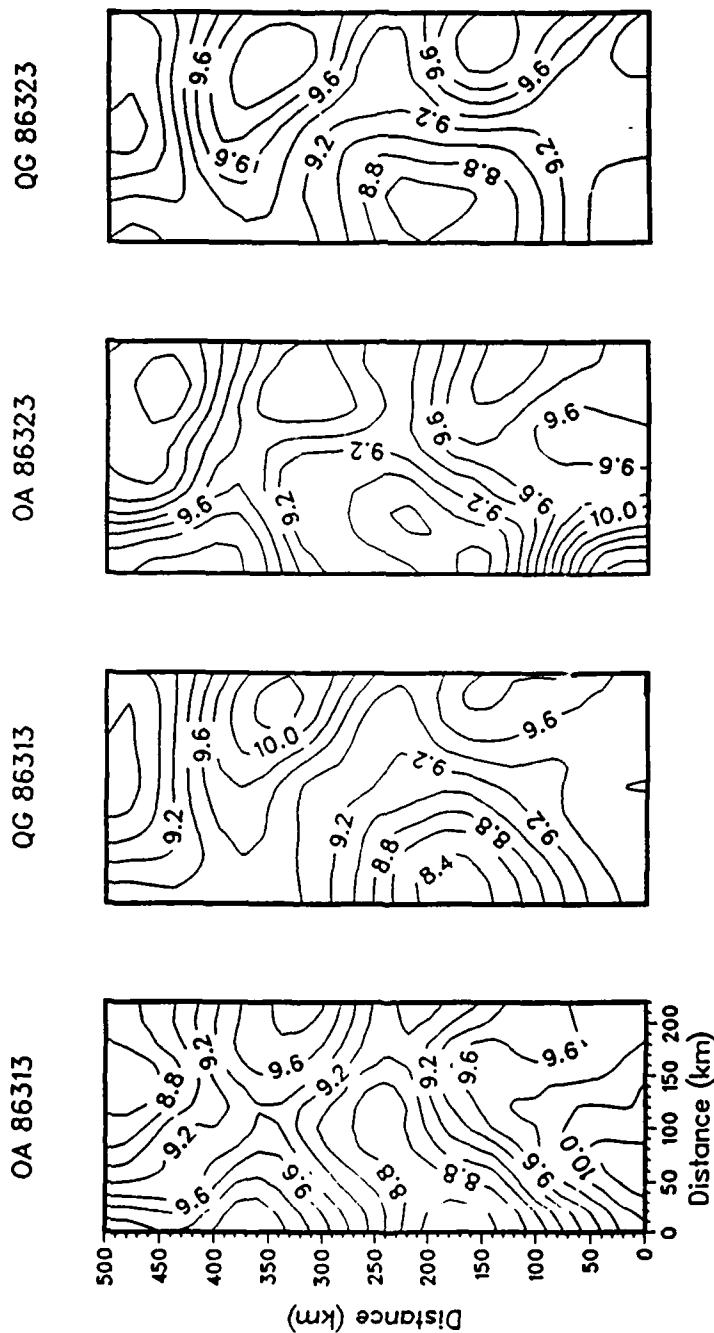


Figure 5.19 T100 OA (verification) and QG-derived fields on days 86313 and 86323. The in situ method of Glenn and Robinson (1989) was used to determine T from  $\psi$ .

# T100 OA AND QG - DIFF

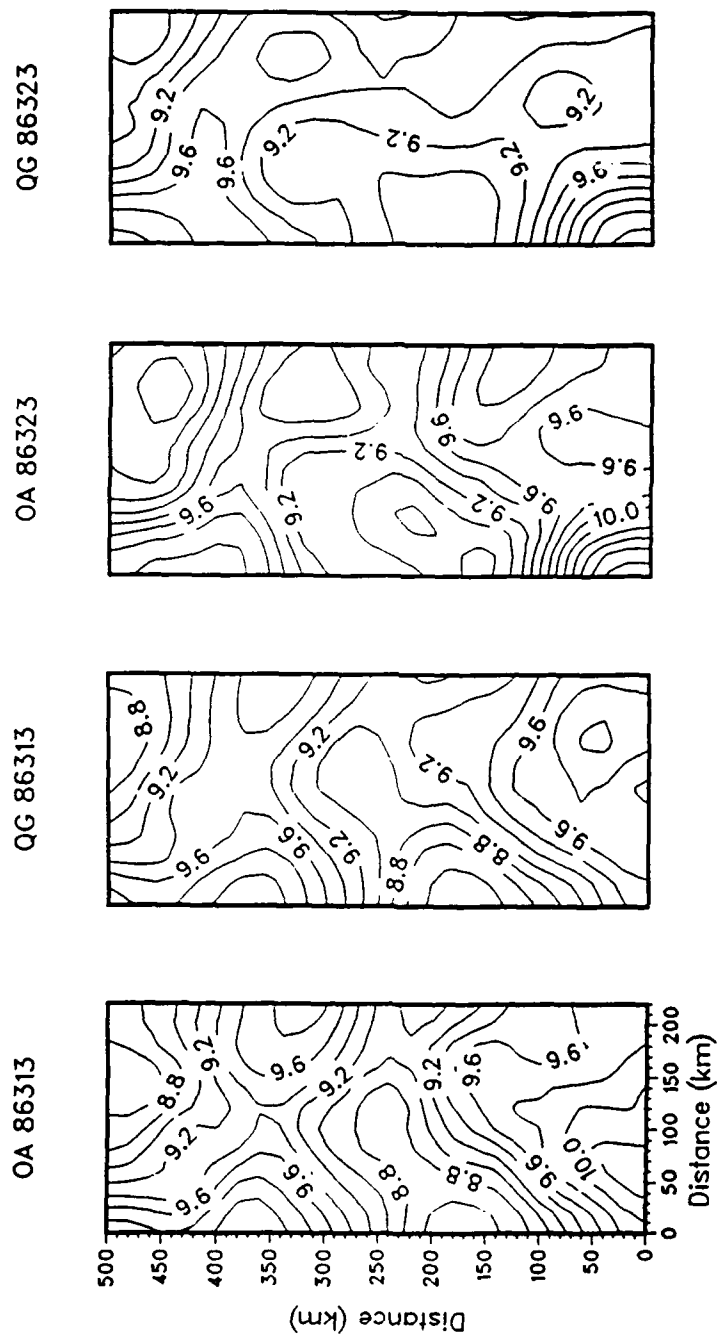


Figure 5.20 T100 OA (verification) and QG-derived fields on days 86313 and 86323. The vertical derivative method was used to determine  $T$  from  $\delta\psi/\delta z$ .

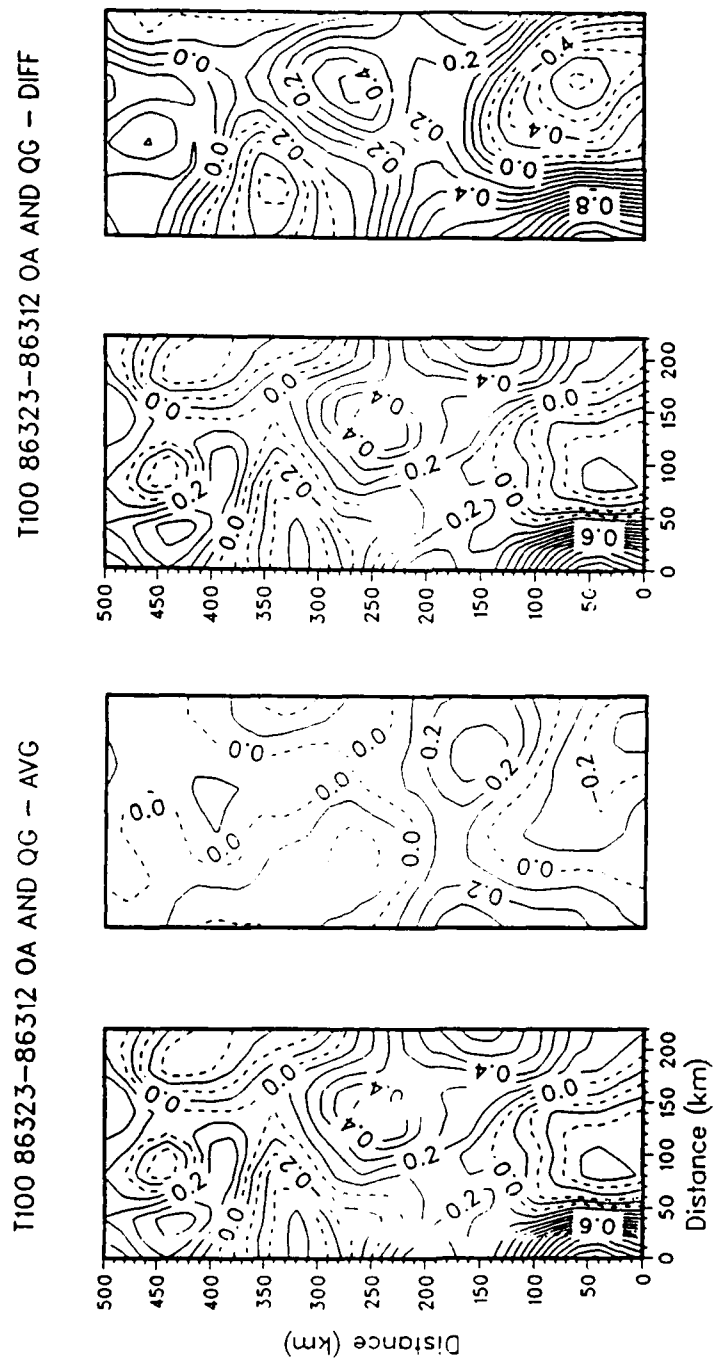


Figure 5.21 T100 86323 minus T100 86313 (verification, and QG-derived fields). The in situ method (left) does not reproduce the verification field as well as the vertical derivative method (right).

#### D. DATA SUBSAMPLING

##### 1. Subsampling Techniques

The QG model has been shown to be very sensitive to data inputs and initial conditions (Appendix H). An initial estimate of data requirements for mesoscale modeling was four hydrographic measurements per Rossby Radius per synoptic period (Walstad, 1988). This was a theoretical upper limit and equated to a station spacing of ca. 6 km and thousands of casts in the OPTOMA 23 domain. (OPTOMA 23 station spacing, based upon operational and logistical constraints, was 30 km, and ca. 550 measurements were made.)

To assess the minimum data requirements for skillfull QG nowcasts and hindcasts (pattern correlation of 0.60 or greater, Rosmond, 1989), OPTOMA 23 dynamic height data were subsampled. As with PRT-5 data (Appendix D), three subsampling techniques were utilized: alternate (selection of every other point), random, and "smart pick" (Appendix G). Data were reduced from ca. 160 observations for each field to 80 (one-half fields), 40 (one-quarter fields), and 20 (one-eighth field) (Figure 5.22).

Objective analyses of dynamic topography, at 50, 150, and 400 m, mapped using data from the three subsampling techniques produced results similar to the PRT-5 subsampling. Qualitatively, most of the one-half subsampled fields, some of the one-quarter subsampled fields, and a few of the one-eighth subsampled fields reproduced the full field analyses with skill (Figures 5.23, 5.24, and 5.25).

Quantitatively, in all cases, the basic statistics (mean and standard deviation) of the subsampled fields were representative of

# FULL AND SUBSAMPLED OBSERVATIONS AND OA GRID PLOT

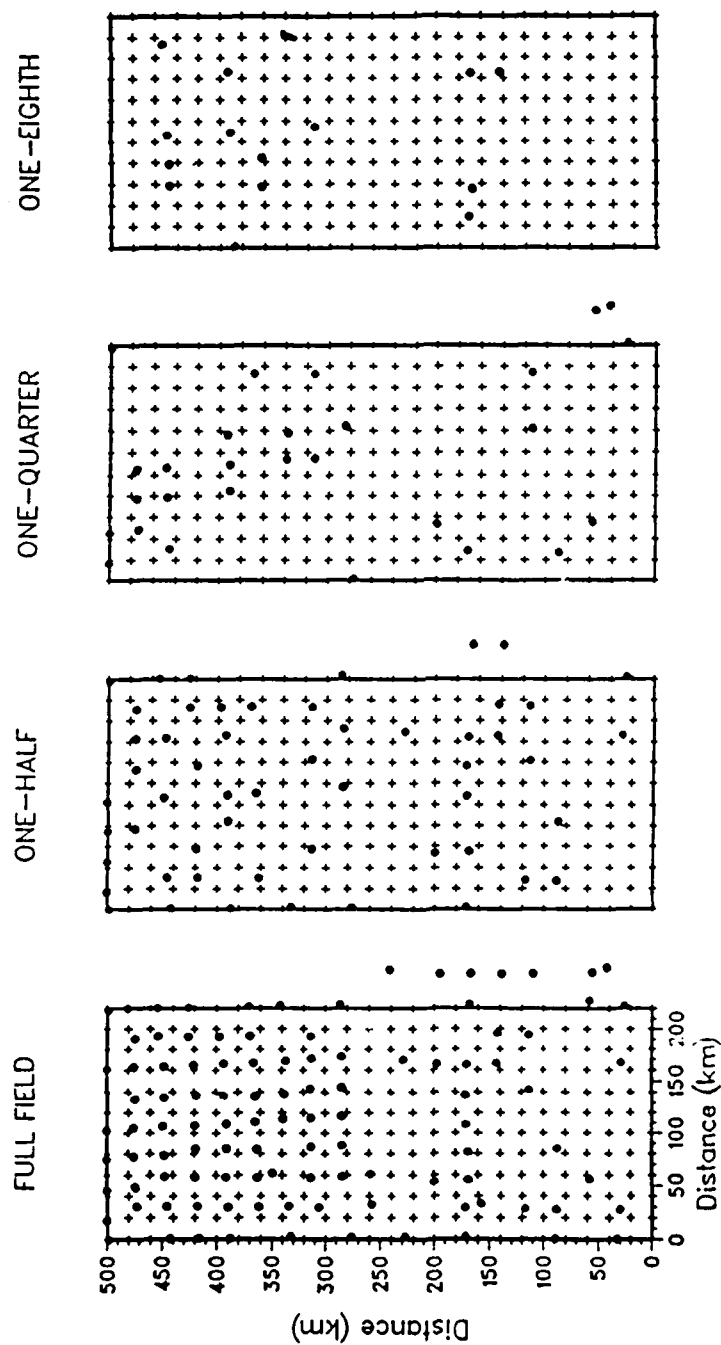


Figure 5.22 Full and randomly subsampled observations positions (dots) and grid plots (crosses) for day 86313. Full field is made up of ca. 120 observations. The other days are qualitatively similar.



those for the full fields (Table 21, Appendix G). The one-half fields compared the best: pattern correlation ranged from 0.88 to 0.97, averaged 0.93, with a standard deviation of 0.03; RMSN was the lowest, 10 to 30%. The average pattern correlation for the one-quarter and one-eighth fields were 0.72 (standard deviation of 0.09) and 0.69 (standard deviation of 0.11), respectively. The "smart pick" choices were only slightly better than the random and every other selection.

The comparisons were worse, in general, for the subsampled fields on day 86320, the boundary condition update survey. The full field consisted of 84 observations on this day, significantly fewer observations than from the initialization survey (123) or from the verification survey (154); thus, the subsampled fields were smaller.

Various combinations of full and subsampled random fields were used as input fields into the optimal QG model configuration to simulate different data quantity and sources. The subsampling experiments focused solely upon the impact of data density upon initial and boundary conditions; thus, the optimal configuration incorporated OPTOMA 23 stratification, interpolated boundary conditions, and wind stress curl forcing and bottom topography were not included.

The permutations of data inputs were combinations of full fields and subsampled fields at different levels on days 86313, 86320, and 86323. These fields were used as initial and boundary condition fields. Specific experiments were: a 'straight-forward' subsampling from full to one-eighth fields to determine minimum data requirements for the QG model (referred to as the standard subsampling); subsampled initial fields and full boundary condition updates to determine if the model

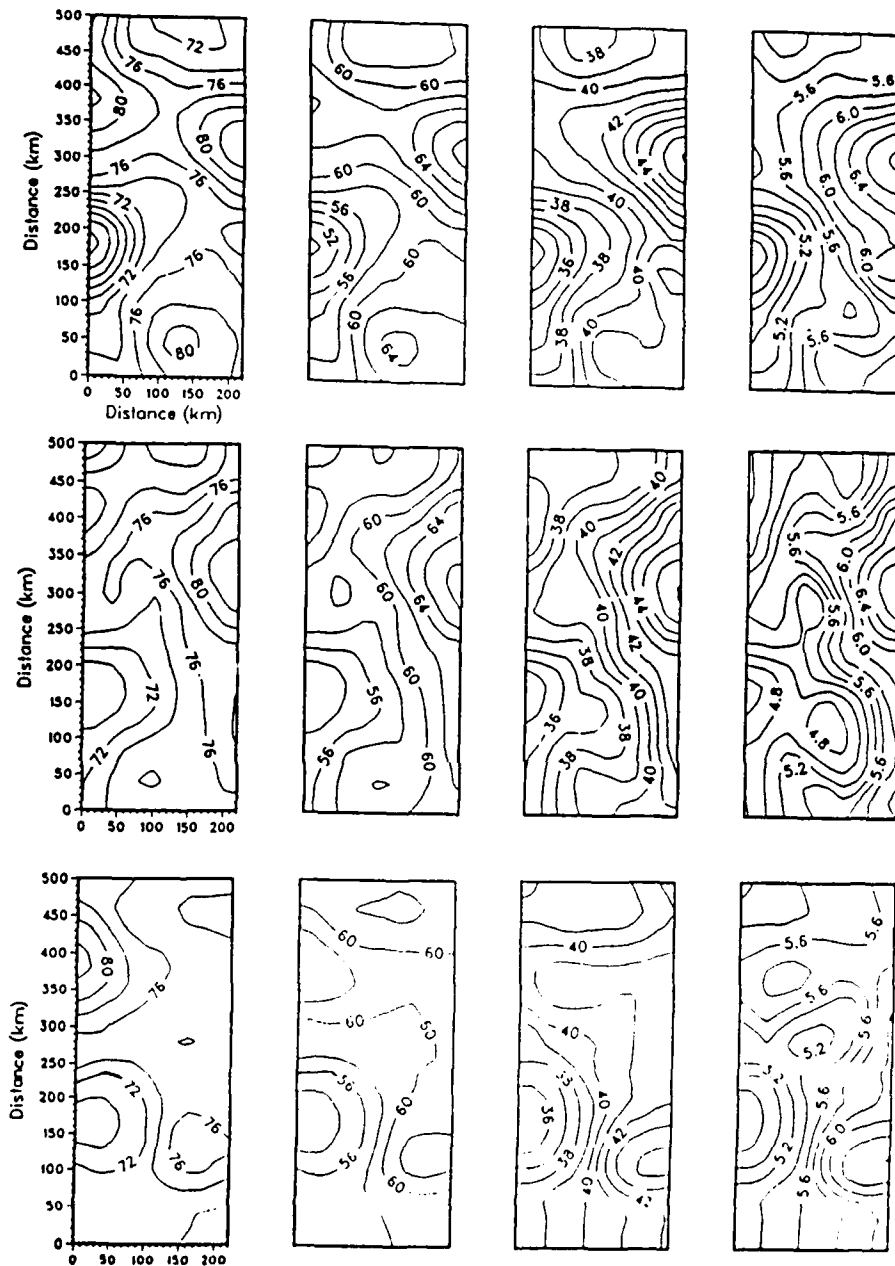


Figure 5.23 OA dynamic height fields (left to right, surface, 50, 150, and 400 m) from one-half (top), one-quarter (middle), and one-eighth (bottom) random subsamples of data on day 86313.

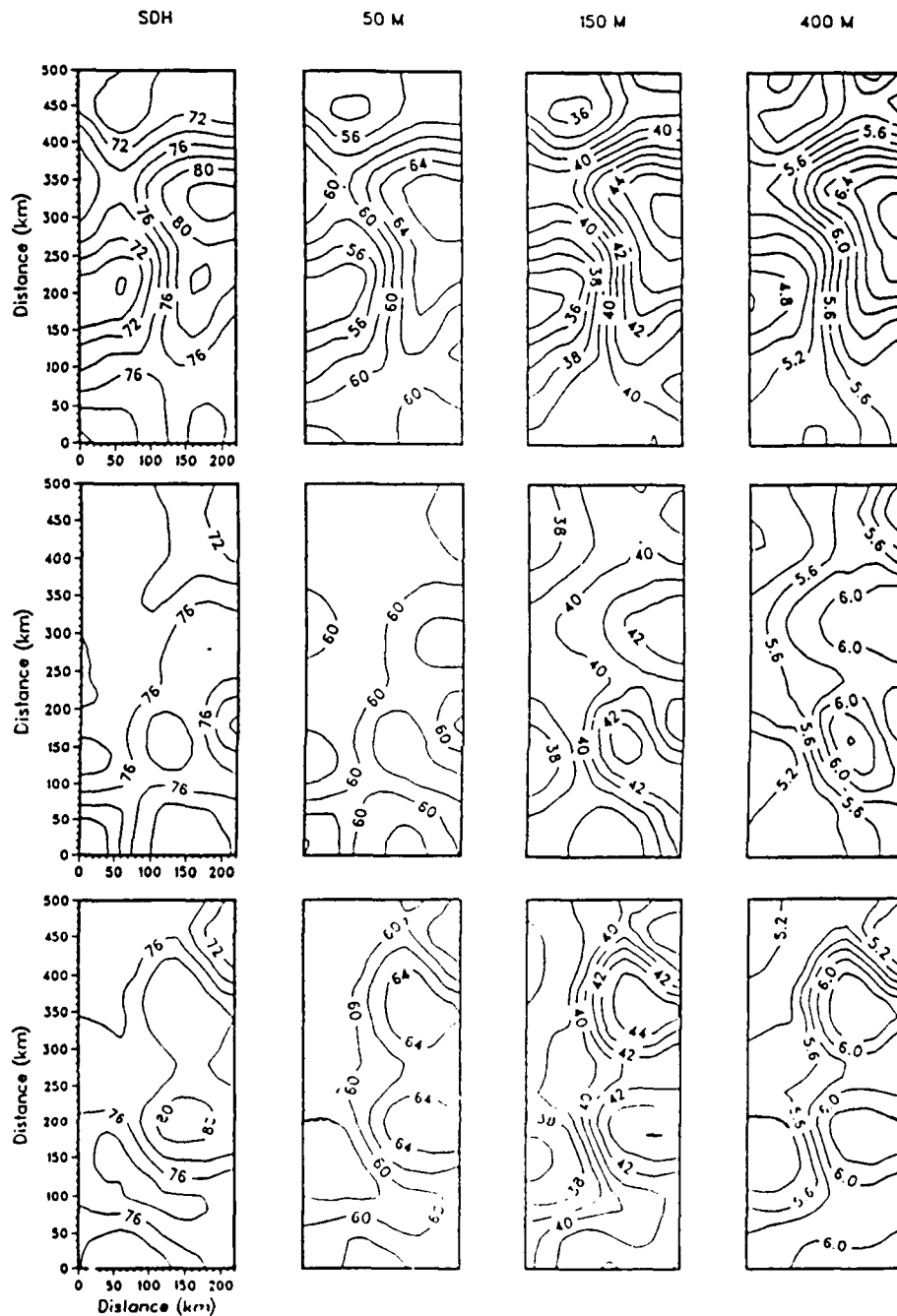


Figure 5.24 OA dynamic height fields (left to right, surface, 50, 150, and 400 m) from one-half (top), one-quarter (middle), and one-eighth (bottom) random subsamples of data on day 86320.

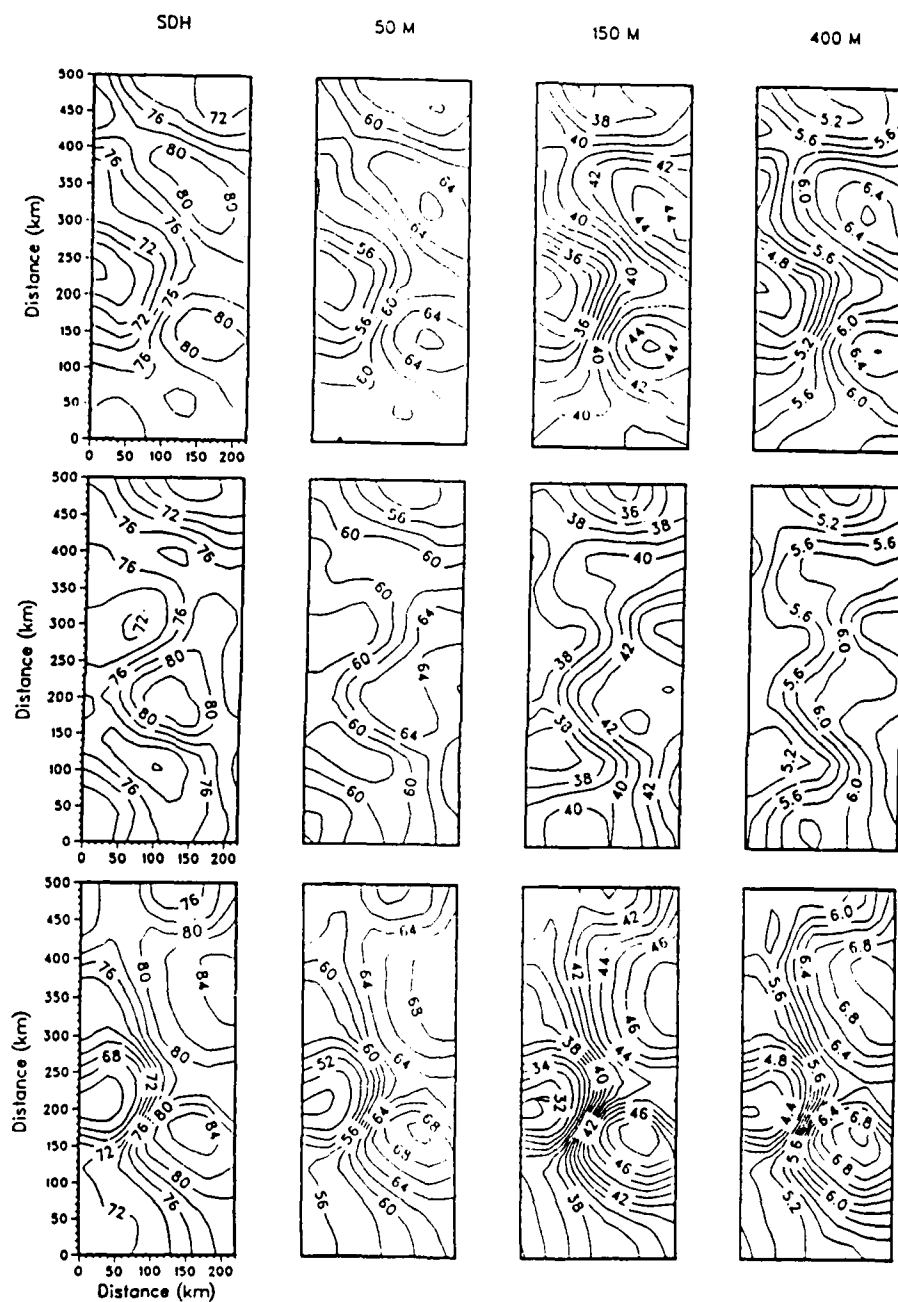


Figure 5.25 OA dynamic height fields (left to right, surface, 50, 150, and 400 m) from one-half (top), one-quarter (middle), and one-eighth (bottom) random subsamples of data on day 86323.

could improve a poor initialization (initialization and boundary condition subsampling); full fields in the upper level with climatological fields at depth to simulate GEOSAT data (GEOSAT simulations); and, fields at thermocline levels with climatology at the surface and at depth to simulate Sofar float data (Sofar simulations).

## 2. Standard Subsampling

The standard subsampling QG modeling experiments were initialized, and the boundary conditions were updated, by one-half, one-quarter, and one-eighth fields on days 86313, 86321, and 86323. Qualitatively, the one-half hindcasts reproduced the mesoscale features well (Figure 5.26). The one-quarter hindcasts also reproduced the mesoscale features, but they were noisier (Figure 5.27). The one-eighth hindcasts were poor, although the model filled data gaps and the areas of cyclonic or anticyclonic activity were accurately delineated (Figure 5.28).

Comparisons between full and subsampled OA fields of dynamic height provided initial correlation and RMSN; the QG hindcasts did not match these initial scores; but, in general, skill was maintained. Quantitatively, the half-fields performed the best, starting on day 86313 with a correlation of 0.95 and an RMSN of 32%. The correlation dropped to a low of 0.74 and the RMSN rose to 70% just before new boundary conditions were inserted on day 86321. After day 86321, the correlation rose to 0.80 and the RMSN leveled off. The one-quarter field exhibited similar behavior with the correlation dropping from 0.73 to 0.66 before rising; however, the QG model improved the initial RMSN from 142% to ca. 80%. The correlation for the one-eighth field hindcast

# STRAIGHT REDUCTION HINDCAST R2

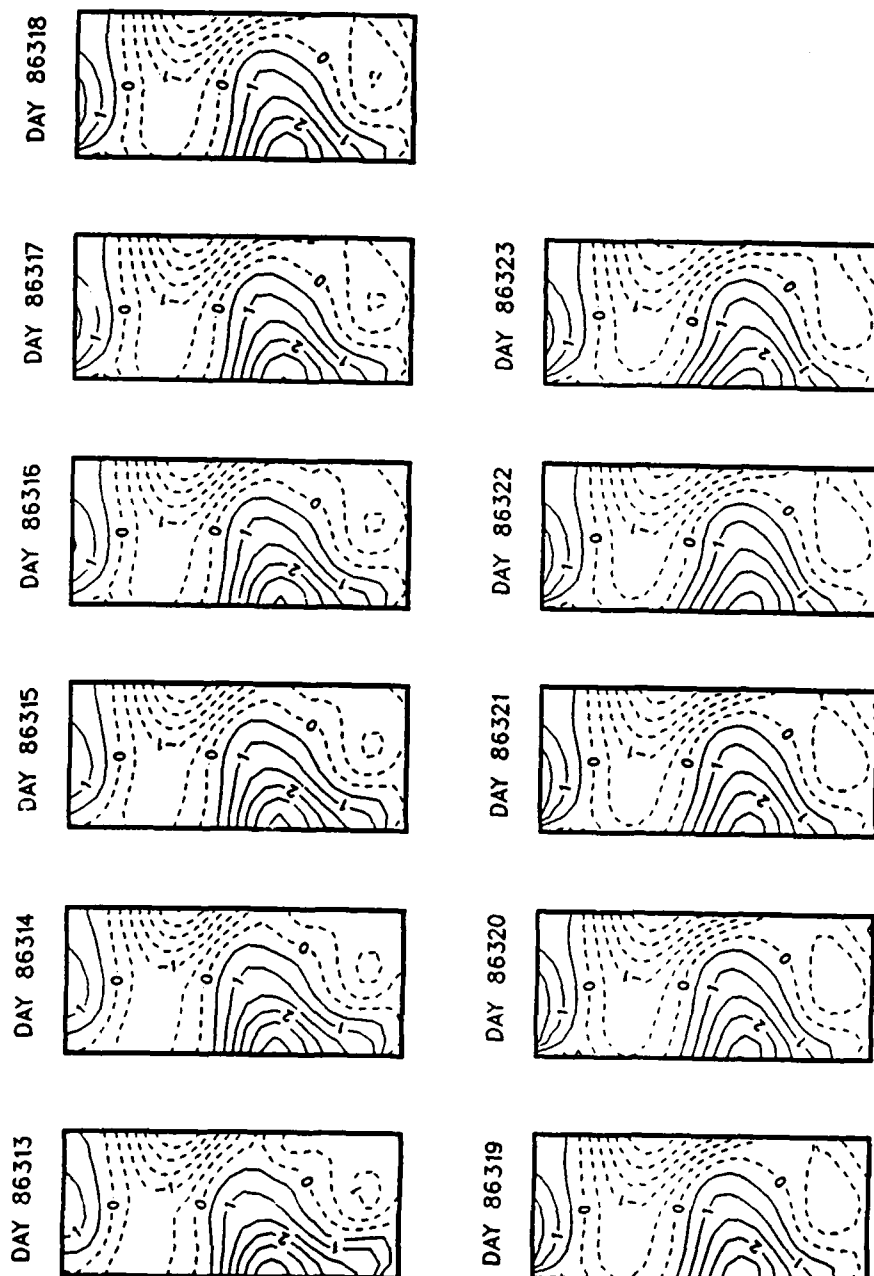


Figure 5.26 OG ten-day hindcasts using the optimal model configuration with one-half subsampled initialization (day 86313) and boundary condition updates (days 86321 and 86323). The mesoscale field was reproduced well. (The hindcasts were scaled).

STRAIGHT REDUCTION HINDCAST  
R<sub>4</sub>

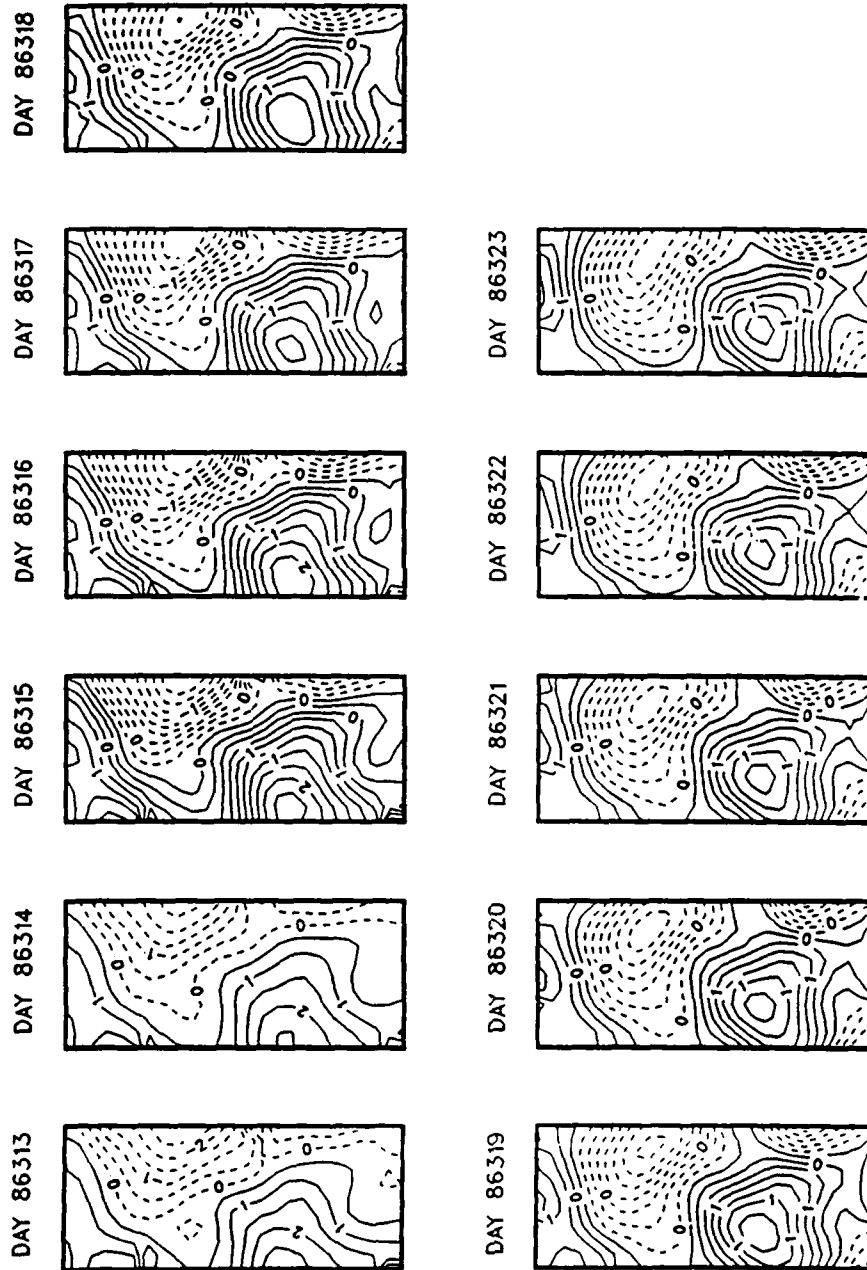


Figure 5.27 OG ten-day hindcasts using the optimal model configuration with one-quarter subsampled initialization (day 86313) and boundary condition updates (days 86321 and 86323). The mesoscale field was reproduced fairly well. (The hindcasts were scaled).

# STRAIGHT REDUCTION HINDCAST R8

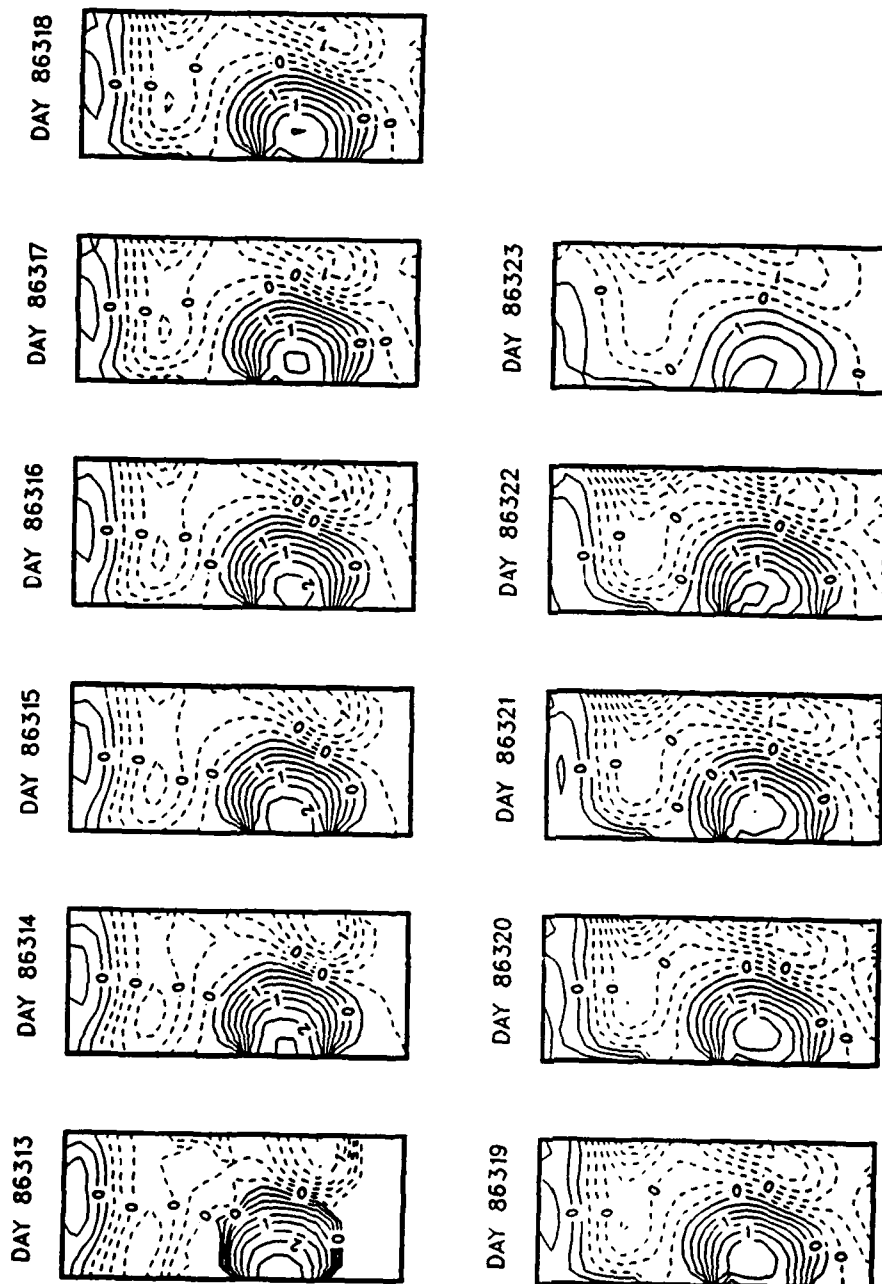


Figure 5.28 QG ten-day hindcasts using the optimal model configuration with one-eighth subsampled initialization (day 86313) and boundary condition updates (days 86321 and 86323). The mesoscale field was reproduced poorly; however, the QG model accurately delineated the cyclonic and anticyclonic zones. (The hindcasts were scaled).



dropped from 0.62 to 0.44 and skill was lost after ca. one day when the correlation dropped below 0.60. RMSN for the one-eighth hindcast remained high, ca. 115% (Figure 5.29 and Table 15).

### 3. Initialization and Boundary Condition Subsampling

QG hindcasts were run with subsampled (one-half, one-quarter, and one-eighth) initial fields and full boundary condition updates to quantify whether or not the QG model could recover a poor initialization. Qualitatively, the one-half hindcasts reproduced the mesoscale features well and there was little difference between this and earlier cases although the ridge to the south was amplified (Figure 5.30). The one-quarter hindcasts also reproduced the mesoscale features and the noisiness identified in earlier cases dissipated after three or four days (Figure 5.31). The one-eighth hindcasts were poor, although the model filled data gaps and the areas of cyclonic or anticyclonic activity were accurately delineated (Figure 5.32).

Quantitatively, correlations and RMSN values were similar to, but slightly worse than the standard subsampling cases. As with the subsampled case, most original OA scores were not matched, but skill was demonstrated. Quantitatively, the half fields performed the best, starting on day 86313 with a correlation of 0.95 and an RMSN of 32%. The correlation dropped to a low of 0.74 and the RMSN rose to 70% just before new boundary conditions were inserted on day 86321. After day 86321, the correlation rose to 0.80 and the RMSN leveled off. The one-quarter field exhibited similar behavior with the correlation dropping from 0.73 to 0.66 before rising; however, the QG model improved the initial RMSN from 142% to ca. 80%. The correlation for the one-eighth

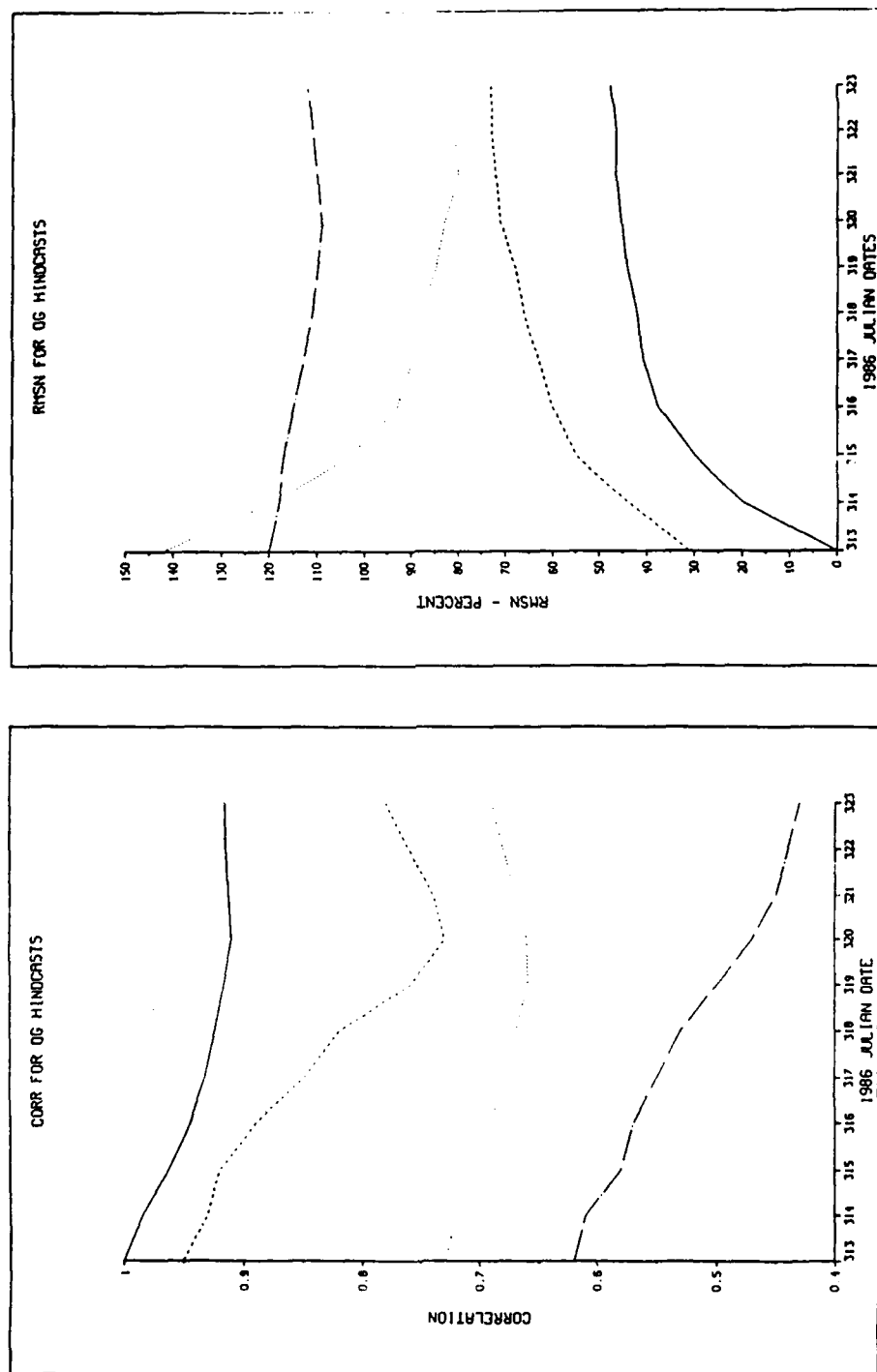


Figure 5.29 Correlation (left) and RMSN (right) for standard subsampled hindcasts. Full field (solid), one-half field (dash), one-quarter field (dot), and one-eighth field (chain dot).

POOR IC / GOOD BC HINDCAST  
R2 IC

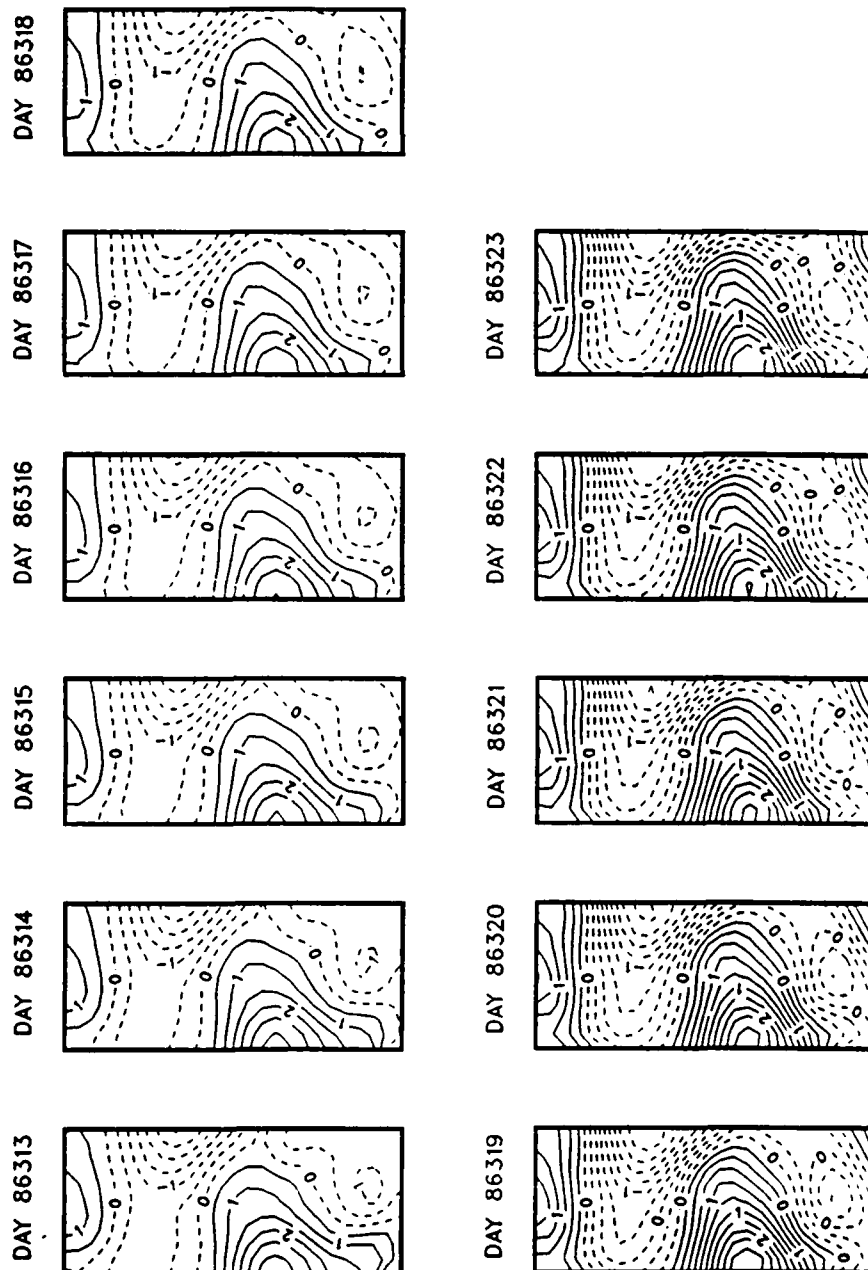


Figure 5.30 QG ten-day hindcasts using the optimal model configuration with one-half subsampled initialization (day 86313) and full boundary condition updates (days 86321 and 86323). The mesoscale field was reproduced well.

POOR IC / GOOD BC HINDCAST  
R4 IC

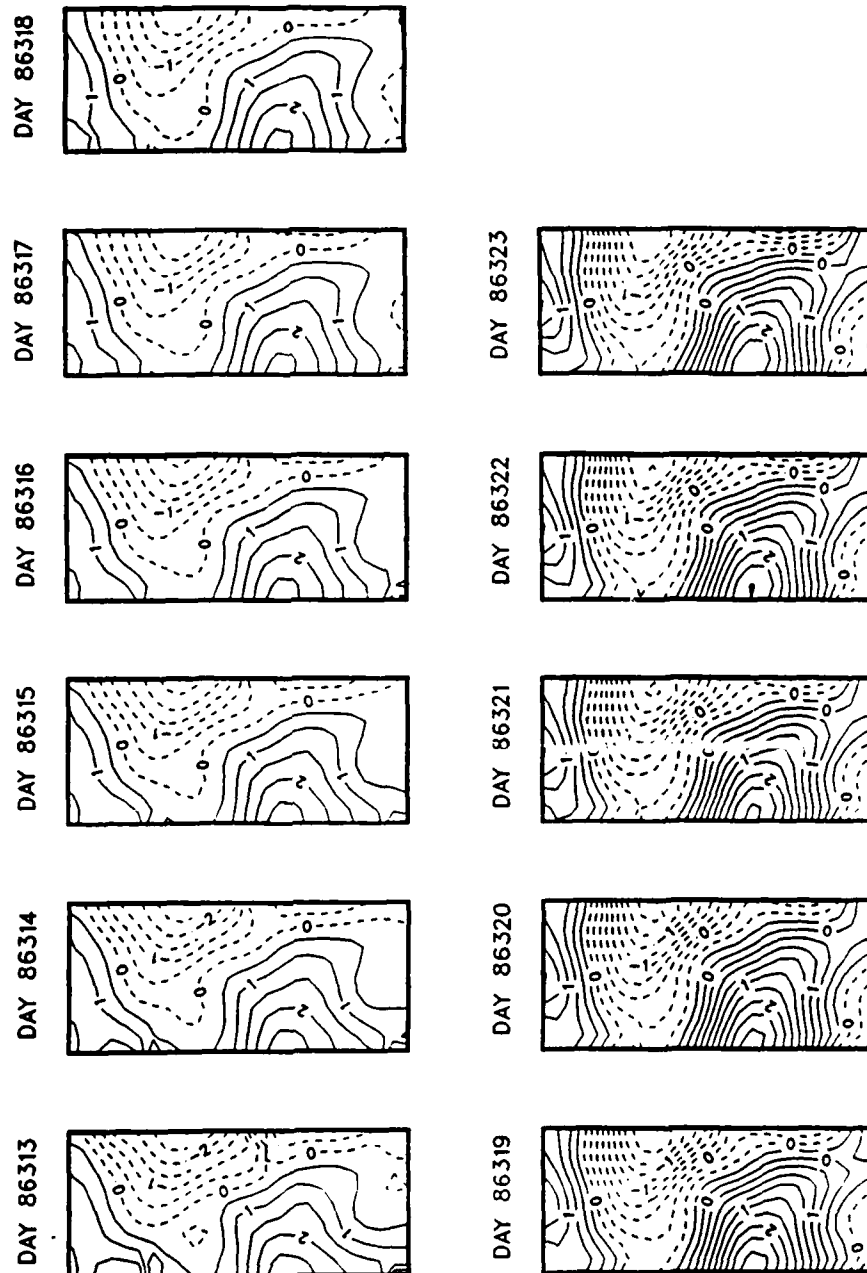


Figure 5.31 QG ten-day hindcasts using the optimal model configuration with one-quarter subsampled initialization (day 86313) and full boundary condition updates (days 86321 and 86323). The mesoscale field was reproduced fairly well.

POOR IC / GOOD BC HINDCAST  
R8 IC

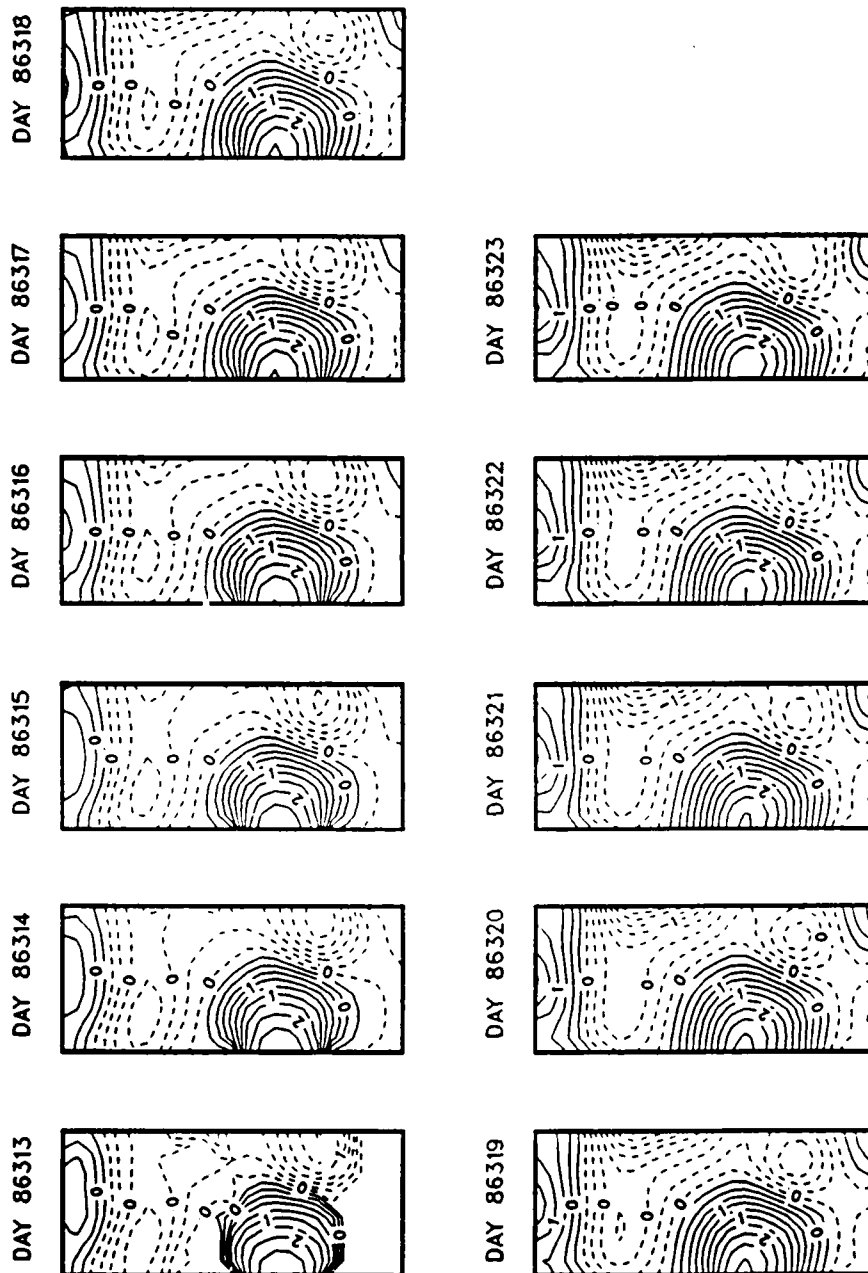


Figure 5.32 QG ten-day hindcasts using the optimal model configuration with one-eighth subsampled initialization (day 86313) and full boundary condition updates (days 86321 and 86323). The mesoscale field was reproduced poorly; however, the QG model filled data gaps and accurately delineated the cyclonic and anticyclonic zones.

for the one-eighth field hindcast dropped from 0.62 to 0.44 and skill was lost after ca. one day when the correlation dropped below 0.60. RMSN for the one-quarter hindcast remained high, ca. 115% (Figure 5.33 and Table 15).

Qualitatively, a related experiment, hindcasts for ten days with good initialization fields and poor boundary condition updates (one-half, one-quarter, and one-eighth fields on day 86321), were not much different from the optimal hindcast and showed no significant impact on the mesoscale features. Qualitatively, correlations and RMSN values were slightly worse than the optimal hindcasts (Table 15). However, these were ten-day hindcasts and the poor boundary conditions were inserted near the end of the period. If these were persisted past ten days, the mesoscale fields would be poorly reproduced.

#### 4. GEOSAT and Sofar Simulations

Simulated GEOSAT and Sofar initialization and boundary condition update fields were created by combining upper level OA dynamic height fields with lower level climatology (GEOSAT) and mid-level (150 and 400 m) OA dynamic height fields with upper and lower level climatology (Sofar). Hindcast experiments included GEOSAT or Sofar initialization and combinations of GEOSAT, Sofar, or full data boundary condition updates.

Qualitatively, GEOSAT initialization did locate mesoscale features accurately; however, in all cases, the range of values was lower than the verification field and the fields appeared noisier, especially when GEOSAT boundary conditions were used (Figure 5.34). Quantitatively, all simulations showed skill in pattern correlation, and

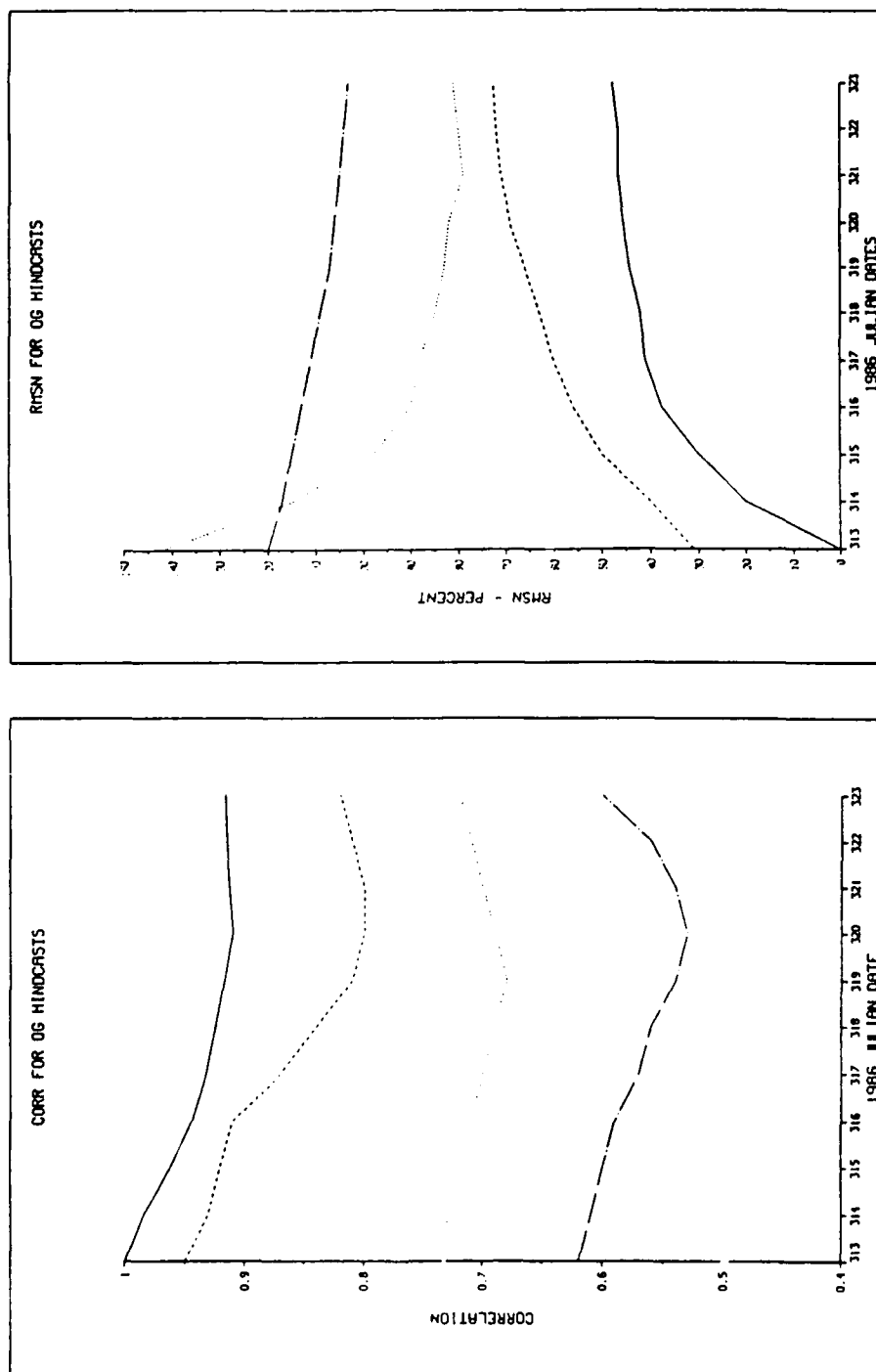


Figure 5.33 Correlation (left) and RMSN (right) for poor initialization and full boundary condition subsampled hindcasts. Full field (solid), one-half field (dash), one-quarter field (dot), and one-eighth field (chain dot).

the simulation with full boundary conditions updated scored best with a pattern correlation on day 86323 of 0.80, and a RMSN of 75%. (Figure 5.35, Table 15).

Qualitatively, the QG model rapidly filled in the initial climatological upper level and all of the Sofar initialization hindcasts located the mesoscale features accurately. As in the GEOSAT simulation, the range of values in the Sofar hindcasts was less than that observed in the verification field and the fields appeared noisier (Figure 5.36). Quantitatively, insertion of data at two levels (2 and 3) did not improve the single level initialization much (correlation changed from 0.73 to 0.74, and RMSN dropped from 93 to 75%). Boundary condition updates improved the scores more so; full boundary condition updates on day 86323 increased the pattern correlation to 0.82 and reduced RMSN to 62% (Figure 5.37, Table 15).

#### 5. Temperature Extractions from Subsampled Hindcasts

Temperature extractions were calculated for the standard subsampling cases (subsampling of one-half, one-quarter, and one-eighth) using the vertical derivative method (equation 5.4) (Figure 5.38). Qualitatively, on day 86313, the one-half field reproduced the T100 observed field well with a pattern correlation of 0.95 and RMSN of 31%. The one-quarter field also showed statistical skill, but it reproduced only a few of the features. It had a pattern correlation of 0.73 and a RMSN of 142%. The one-eighth field also was poor (0.62 and 119%). The quality of the extracted T100 field deteriorated with forecast time with pattern correlations dropping and RMSN rising in all but one case, the one-quarter subsampling (Figure 5.39).



TABLE 15. QG SUBSAMPLED COMPARISONS

<u>INPUT<sup>a</sup></u> <u>FIELD</u>	<u>INPUT<sup>b</sup></u> <u>LEVELS</u>	<u>BOUNDARY</u> <u>CONDITIONS</u>	<u>WIND</u> <u>STRESS</u>	<u>BOTTOM</u> <u>TOPOGRAPHY</u>	<u>LEVEL</u>	<u>CORR</u>	<u>RMSN</u>
<u>Optimal Configuration</u>							
13,20,23	3	INTERPOLATED	NO	NO	1	0.92	42%
<u>Standard Subsampling</u>							
13,20,23	1/2	INTERPOLATED	NO	NO	1	0.77	72%
	1/4				1	0.71	82%
	1/8				1	0.44	115%
<u>Poor Initialization; Good Boundary Conditions Subsampling</u>							
13,20,23	1/2	INTERPOLATED	NO	NO	1	0.82	73%
	1/4				1	0.72	81%
	1/8				1	0.62	105%
<u>Good Initialization; Poor Boundary Conditions Subsampling</u>							
13,20,23	1/2	INTERPOLATED	NO	NO	1	0.89	46%
	1/4				1	0.83	53%
	1/8				1	0.72	61%
<u>GEOSAT Simulation</u>							
13,23	SFC	INTERPOLATED TO FULL FIELD	NO	NO	1	0.80	77%
<u>Sofar Simulation</u>							
13	150 M	PERSISTED	NO	NO	1	0.73	93%
13	150 M	PERSISTED			1	0.74	75%
	450 M						
13,23	150 M	INTERPOLATED			1	0.82	62%
	450 M	TO FULL FIELD					

**Notes:**

a - Julian day 13 (86313); 20 (86320); or 23 (86323)

b - upper three levels are full fields; lower three are either filled by EOF extension or by climatology

CORR - correlation;

RMSN - Root Mean Square, Normalized by the standard deviation of the verification field on day 86323

GEOSAT HINDCAST  
13 LVL1 23 LVL1

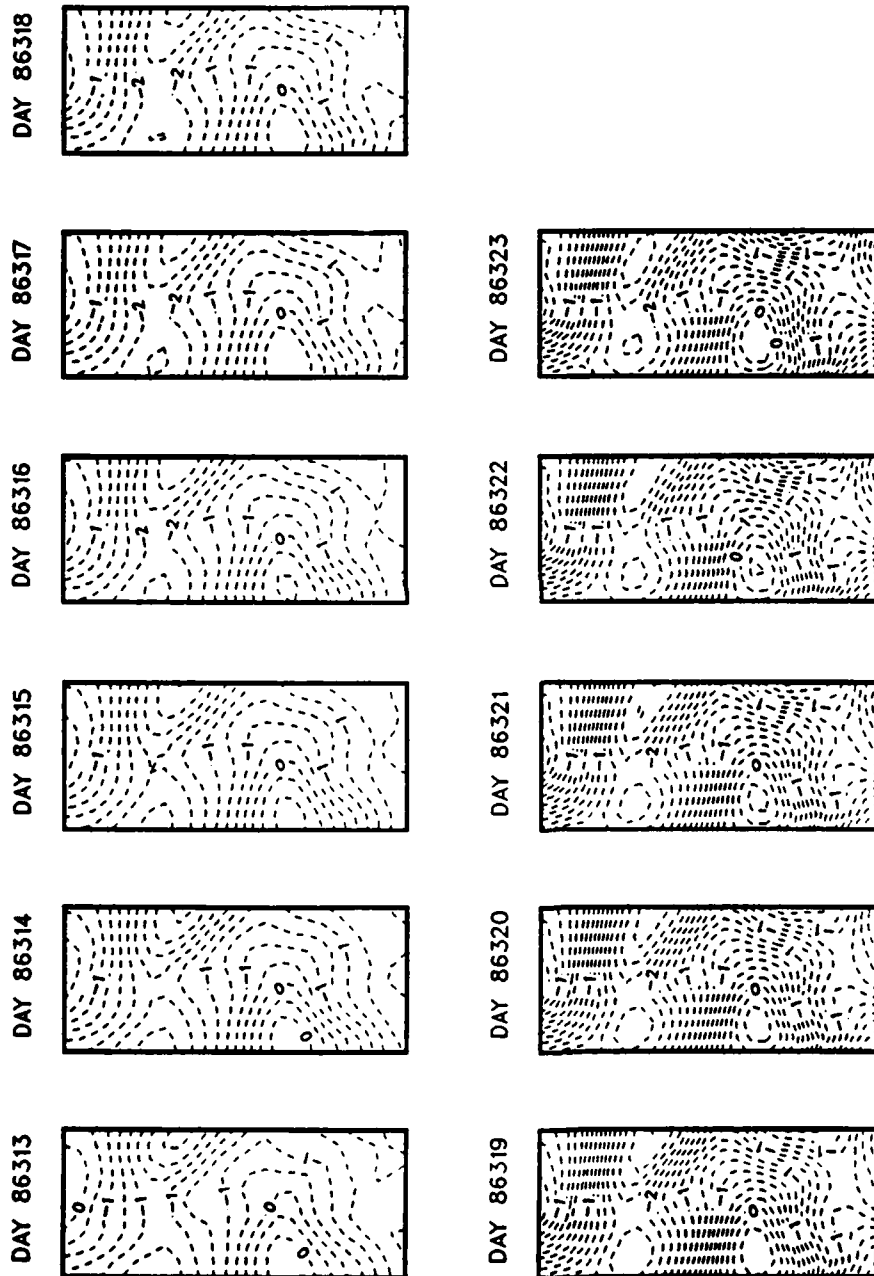


Figure 5.34 QG ten-day hindcasts using the optimal model configuration initialized with level one data and climatology at depth (day 86313) to simulate GEOSAT data. Boundary conditions were interpolated to GEOSAT simulated data on day 86323. Features in the mesoscale field are well located; the range of values was reduced and the fields were noisier.

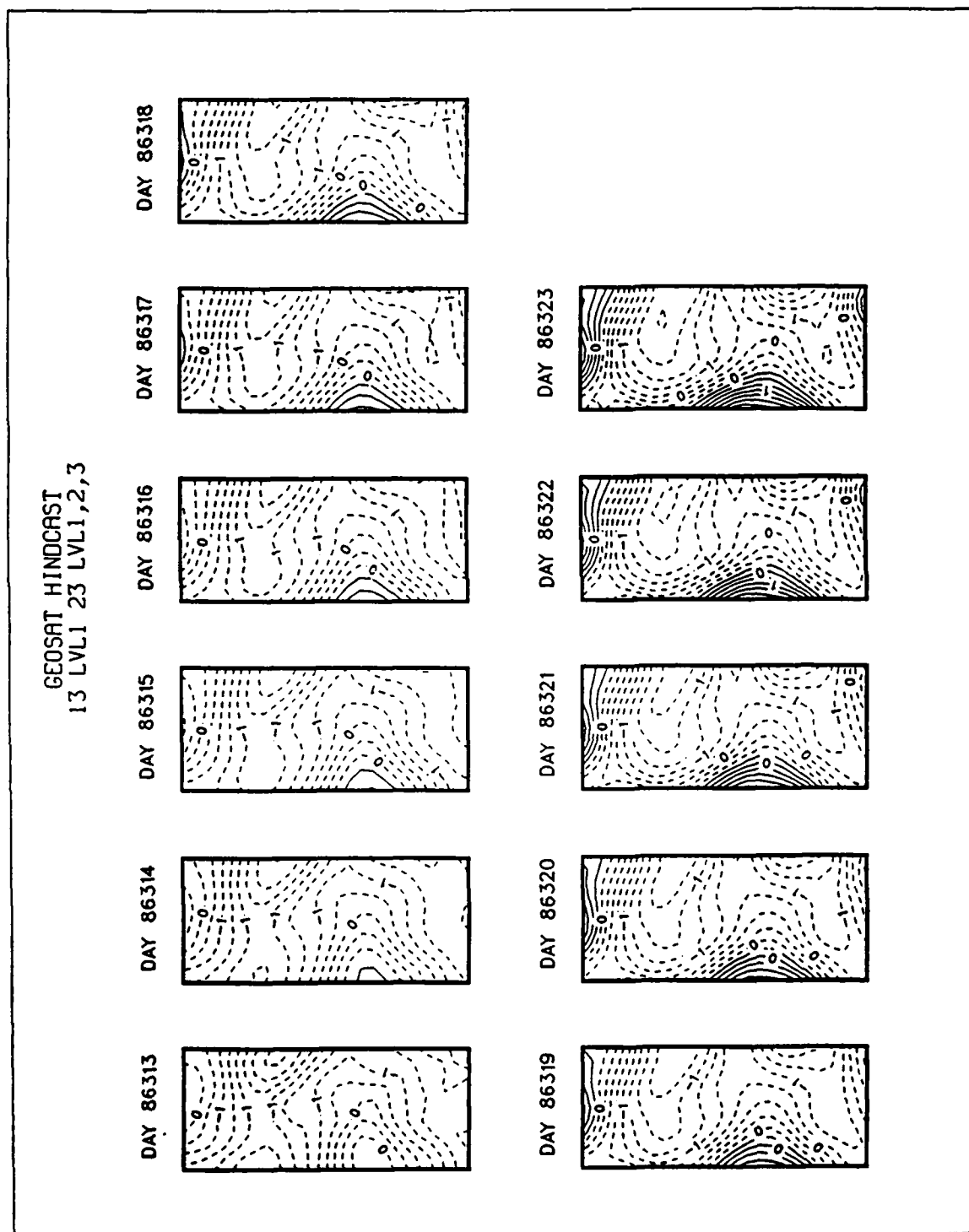


Figure 5.35 QG ten-day hindcasts using the optimal model configuration initialized with level one data and climatology at depth (day 86313) to simulate GEOSAT data. Boundary conditions were interpolated to full fields on day 86323.

SOFAR HINDCAST  
13 LVL 2

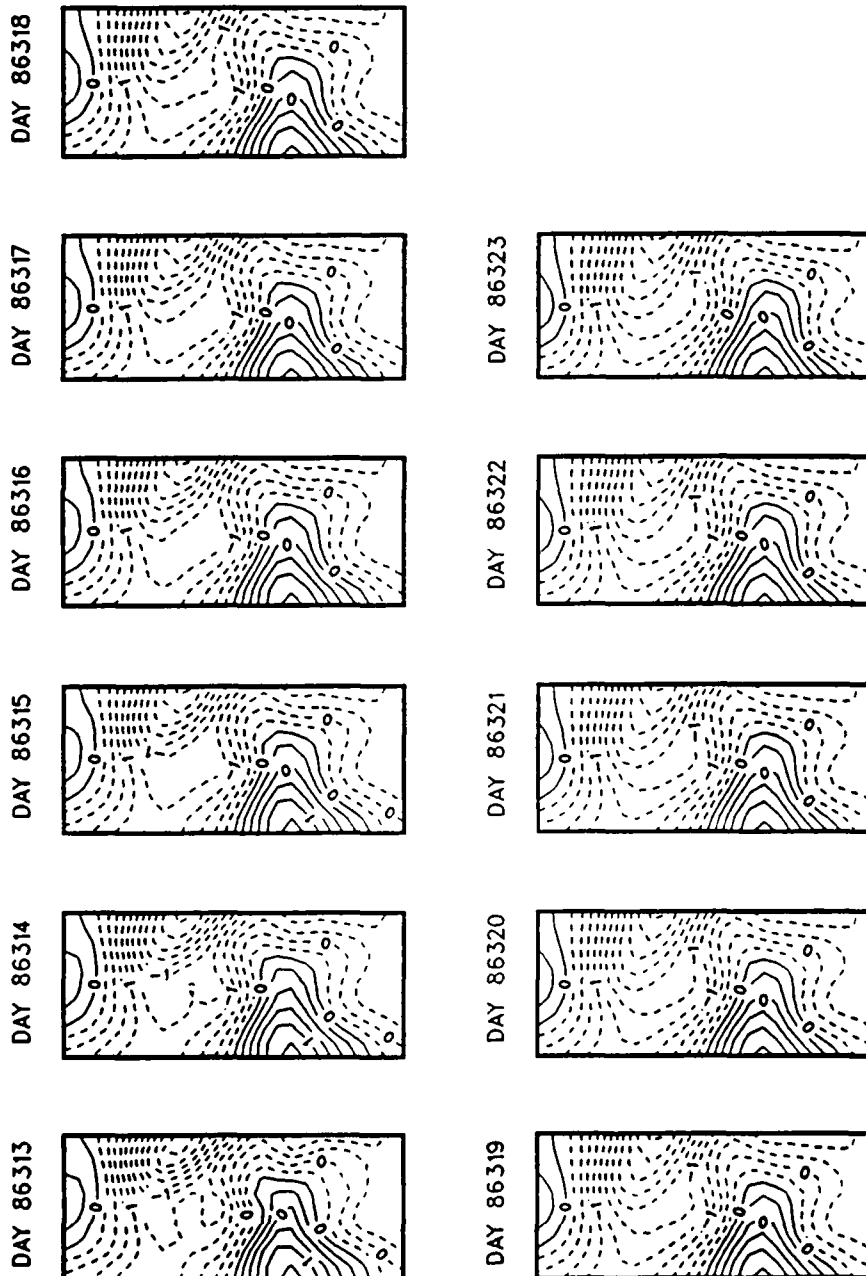


Figure 5.36 QG ten-day hindcasts simulating Sofar data using the optimal model configuration initialized with level two data (day 86313) and climatology in the upper and lower levels.

SOFAR HINDCAST  
13 LVL 2,3; 23 LVL 1,2,3

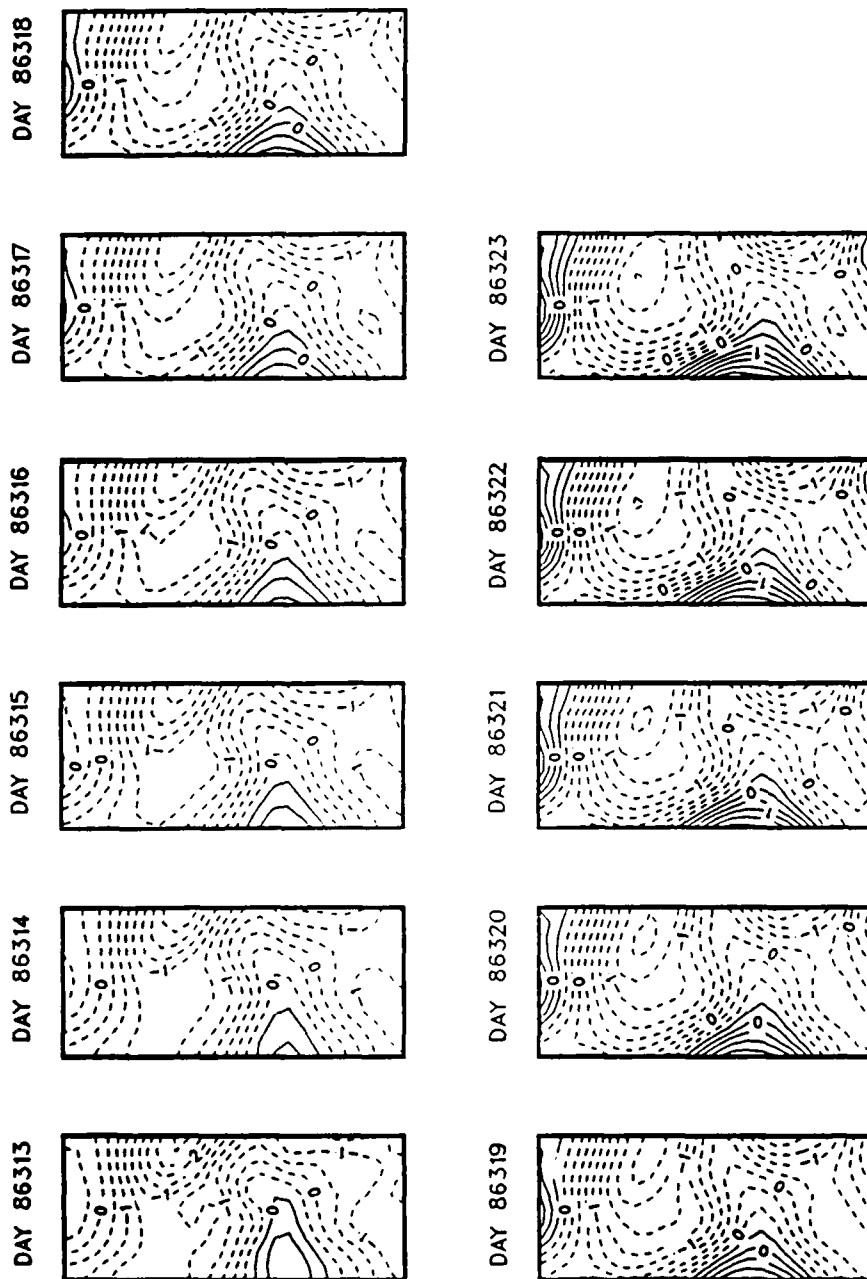


Figure 5.37 QG ten-day hindcasts simulating Sofar data using the optimal model configuration initialized with level two data (day 86313) and climatology in the upper and lower levels and boundary conditions updated by full fields (day 86323).

# T100 DIFF - R2

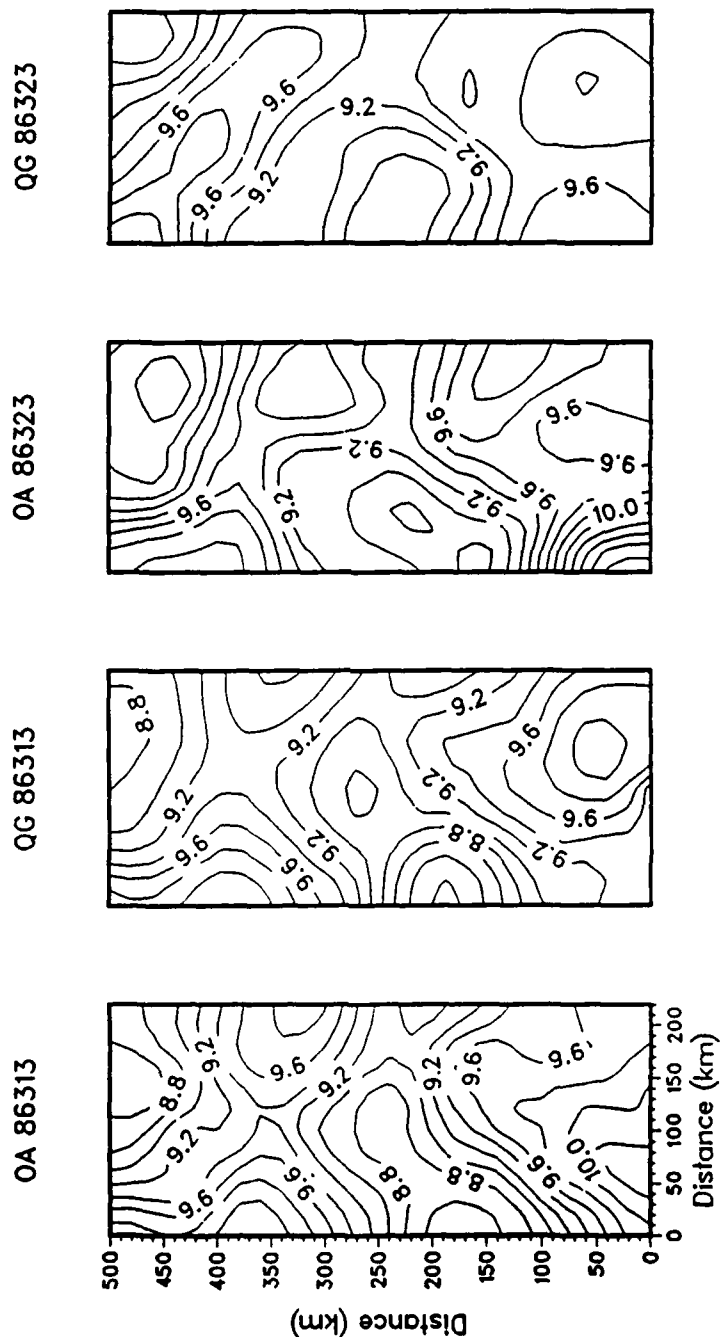


Figure 5.38 T100 OA (verification) and QG-derived fields on days 86313 and 86323 using one-half subsampled fields. The vertical derivative method was used to determine T from  $\delta\psi/\delta z$ .

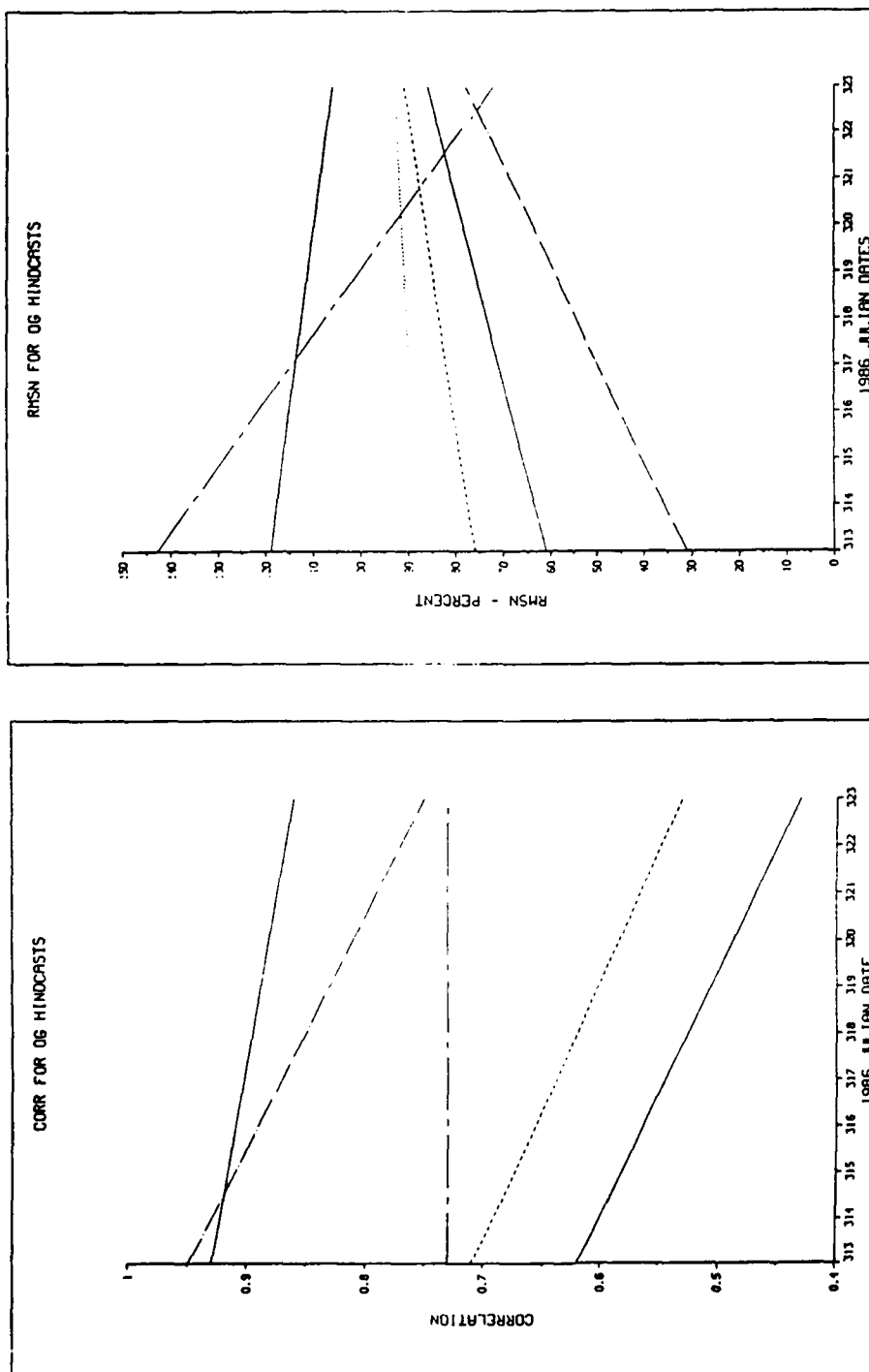


Figure 5.39 Correlation (left) and RMSN (right) for T100 extractions on days 86313 and 86323 from standard subsampled hindcasts. Full field (solid), one-half field (dash), one-quarter field (dot), and one-eighth field (chain dot).

## E. SUMMARY AND DISCUSSION OF QG MODELING

There was not much change in the ocean field over the ten day OPTOMA survey period. Most QG nowcasts and hindcasts located the mesoscale features accurately, but RMSN varied greatly with data inputs. The significance of the individual hindcast scores lies in how well the hindcasts did with respect to persistence and climatology. Persistence scores were good (0.78 and 88%, pattern correlation and RMSN, respectively) and proved hard to beat without full data inputs (if there had been more change in the mesoscale fields, persistence scores would be worse). As expected, climatology represented the mesoscale activity poorly (0.42 and 144%).

With the cyclonic features on the north (C1) and southwest (C2) boundaries being quasi-stationary, the principal dynamic event was the movement of an anticyclonic feature (AC1), from the eastern boundary of the domain off Point Arena, to the northwest at ca. 5-to-6 km/day. A secondary event, the apparent movement of an anticyclone (AC2) from the southeastern boundary north (as seen in the Z08 field, Figure 4.19), was not resolved by the QG model. Instead, a persistent ridge extended southwest through the domain from the initialized position.

The optimal QG model configuration for OPTOMA 23 utilized OPTOMA 23 stratification, interpolated boundary conditions, no wind stress curl forcing, no bottom topography, and full data fields extended from the upper three levels to the lower three by EOF's. Although the optimal configuration used OPTOMA 23 data for stratification, the hindcasts were robust to stratification scales. Interpolated boundary conditions allowed the model to adjust to the insertion of new data over time (in a



linearly interpolated fashion). Persisted boundary conditions were abruptly introduced and forced the model to adjust to an instantaneous change in boundary conditions. The inclusion of wind stress curl forcing and bottom topography both had a detrimental effect upon the quality of the hindcasts; the single value of wind stress curl used over the entire domain may not have been representative of actual forcing and the steep bottom topography in the northeast made the QG approximation invalid.

The QG hindcasts were most sensitive to initialization and boundary conditions. A decrease in data quantity was seen to directly impact hindcast skill; however, skill was still shown at a one-quarter subsampling (with pattern correlation greater than 0.60). Initialization of deep fields was crucial to overall mesoscale development as was observed by the use of climatology in the upper and lower levels in GEOSAT and Sofar hindcast experiments. In these initializations, the QG model located features accurately and the pattern correlations were high, but RMSN values were high due to the low range of  $\psi$  values (with respect to observations) in the upper level of the hindcast. These simulations improved as more data were added through boundary condition updates.

In other experiments, the QG model was able to forecast the features in the mesoscale field observed in GEOSAT SSH on day 86329, six days after the conclusion of the OPTOMA 23 survey, and T100 fields, derived from an empirical relationship between T100 and  $\delta\psi/\delta z$ , were accurate. The QG hindcasts showed a warming trend, also observed in OA fields, in the southern part of the domain which occurred between the start and finish of OPTOMA 23.

## VI. THE FALL TRANSITION OF 1986

### A. GENERAL

Fall transitions, the change in the CCS from southward surface flow and northward subsurface flow to northward flow over the continental slope and shelf, have been observed in coastal sea level (SL) and SST data, and in nearshore moored-buoy and current meter records (Chapter II). There have not been associated analyses of the offshore mesoscale field during the fall transition (nor during the spring transitions).

In the OPTOMA domain, the summer atmospheric and oceanic conditions are characteristic of an upwelling regime with persistent equatorward winds, relatively cool water over the continental shelf, and low coastal SL. Near capes, the cool water is often advected offshore in cool filaments tens of km wide and hundreds of km long by strong mesoscale features (Rienecker et al., 1985, and Flament et al., 1985). During the winter, the winds are variable (occasionally equatorward), there is relatively warm water over the continental shelf, and the coastal SL are high. Some mesoscale features exist, but they are weaker and less densely packed than those in the summer.

The spring transition between the two regimes typically occurs over a period of a few days or a week in March or early April. Fall transitions, starting in November or early December, are not as pronounced as spring transitions and sporadic upwelling may continue through the winter. A cessation of winds favorable for upwelling (the Aleutian Low deepens near 40 N and 150 W and the 500 mb flow becomes zonal), an increase in coastal temperatures, and a rise in coastal SL

(as the southward flowing California Current is "displaced" in upper ocean, coastal waters by the northward flowing Davidson Current) are expected with fall transition (Strub and James, 1988).

#### B. COASTAL DATA PROCESSING

Atmospheric and oceanic conditions along the California coast were examined over a six-month period from July through December 1986 (the OPTOMA 23 survey was between 9 and 19 November 1986). SL data from NOAA/NOS tide gauges at six coastal stations, data from nine National Data Buoy Center (NDBC) moored buoys (SST, 10 m winds, and sea level pressure), SST data from Granite Canyon (40 km south of Point Sur), analyses from FNOC (Marine Boundary Layer (MBL) winds, surface and 500 mb analyses), and Bakun upwelling indices at four positions were analyzed to determine when the Fall Transition of 1986 started. Additionally, satellite-derived surface velocity vectors (near the coast), offshore observations (CTD's and XBT's), and GEOSAT data (a 17-day ERM SSH OA field) were used to confirm and expand upon the coastal observations.

Hourly data (coastal SL and NDBC buoy data) were filtered using a Godin filter, which has a low pass of 0.0 to 0.8 cpd (30 hours) and a half amplitude of 0.4 cpd (66 hours); this filter effectively reduces diurnal and semi-diurnal components of the original data to zero (Godin, 1972). The SL deviations were hydrostatically corrected for atmospheric pressure (equation 3.9) and demeaned.

Granite Canyon is a coastal site 15 km south of Monterey (ca. 50 km north of NDBC buoy 46028 and 150 km southwest of NDBC buoy 46012)

included in this analysis to provide a coastal "benchmark" for comparison with SST measured offshore by the NDBC buoys. It is representative of open ocean measurements; the site has excellent exposure to the deep ocean with the continental shelf break less than 10 km offshore. Bucket SST's were measured to the nearest 0.1 °C at ca. 0800 local daily (thus, the possibility of aliasing by the predominately semi-diurnal tide, Breaker and Mooers, 1986).

The SST range at Granite Canyon during 1986 was ca. 3.5 °C with a minimum in April and May due to coastal upwelling and a maximum in September and October. In the fall, the mean temperature dropped from 13.0 °C in early October to 12.5 °C in early November. There was a 0.5 °C rise in the middle of November followed by a drop to 12.4 °C in early December.

Six-month time series of winds were generated from MBL winds (on a 2.5 degree grid and at a level of 19.5 m) and winds from six NDBC buoys (these are not independent data sets). Both wind sets were decomposed into alongshore and cross-shore components using a counter-clockwise rotation of 20 degrees. Wind stress was computed from the winds using the drag law (equation 3.7) at five points along the coast (Figure 6.1).

Bakun upwelling indices were computed by the NOAA/NMFS Pacific Environmental Group. These indices describe offshore Ekman transport in cubic meters per second per 100 m of shoreline; the larger the number, the more transport offshore. Values were calculated from FNOC 6-hourly objectively analyzed synoptic wind/pressure analyses (Mason and Bakun, 1986).

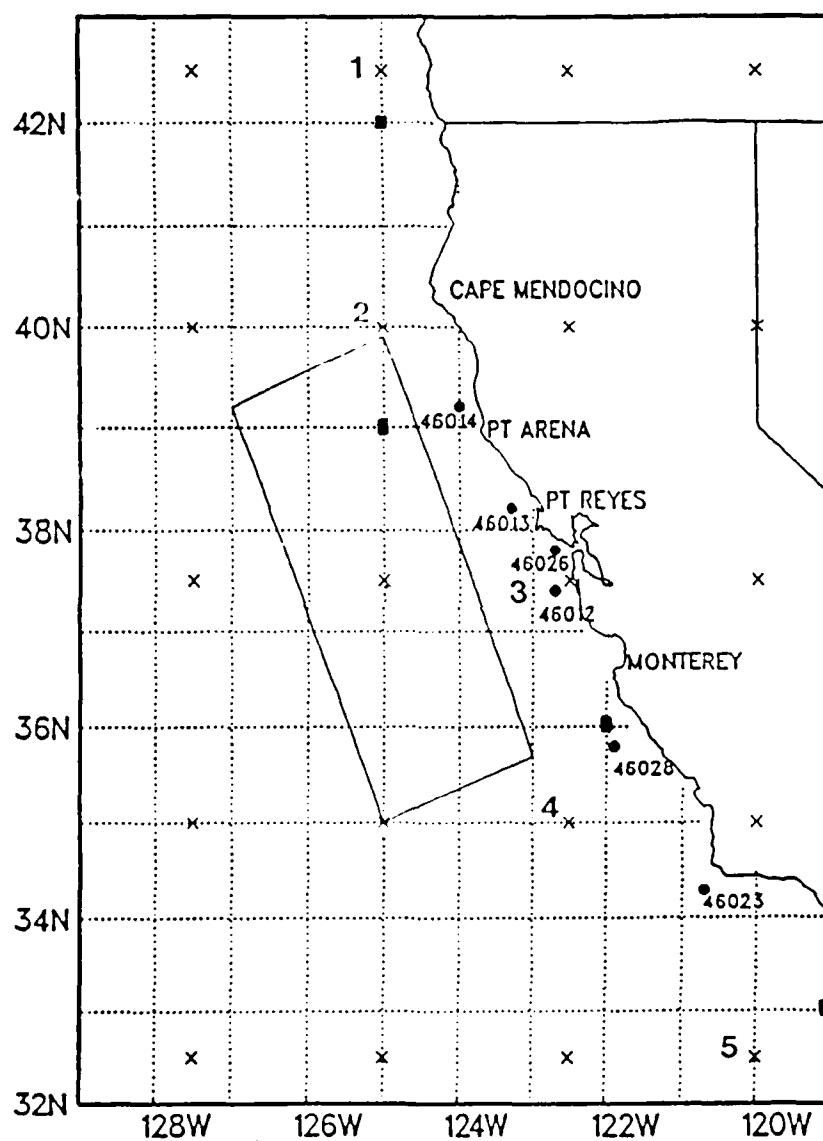


Figure 6.1 Gridpoints for MBL winds (X) and the positions of the six NDBC moored buoys (circles). Time series of winds were analyzed at grids labelled 1 through 5. Bakun indices were calculated at 33, 36, 39, and 42 N (squares).

### C. DESCRIPTION OF THE TRANSITION

The 1986 time series of daily and weekly averaged Bakun upwelling indices at 36 and 39 N depicted typical summer and winter periods (Figure 6.2). A persistent positive (i.e., winds favorable for upwelling) signal commenced at both latitudes in late March; the signal was inconsistent in November and negative in early December. In early November, the North Pacific High was near 40 N 140 W and there was a 500 mb trough over the southwestern United States; on 17 November, the Aleutian Low, near 50 N 140 W, had deepened and the 500 mb flow was zonal. This change was typical of a fall transition (Strub and James). Hence, from consideration of the atmospheric forcing alone, the start of the fall transition was expected in November or early December.

Upon closer review of the Bakun upwelling indices from 33 to 42 N in the fall (Figure 6.3), there were four episodes of winds favorable to coastal upwelling near the expected time of the fall transition: 4 to 9 November, 21 to 27 November, 29 November to 1 December, and 6 to 10 December.

The wind vectors, and the sea level pressures, from the six NDBC data buoys nearest the OPTOMA 23 domain showed episodic atmospheric events typically every five-to-seven days throughout the fall (Figure 6.4). Those episodes in November and early December were consistent with the Bakun upwelling indices. The atmospheric events occurred simultaneously or within a day along the entire coast. However, there was a distinction between atmospheric regimes; the winds in the south were predominantly southeastward while winds in the north were predominantly northward. Variances in SLP and winds were less at the two

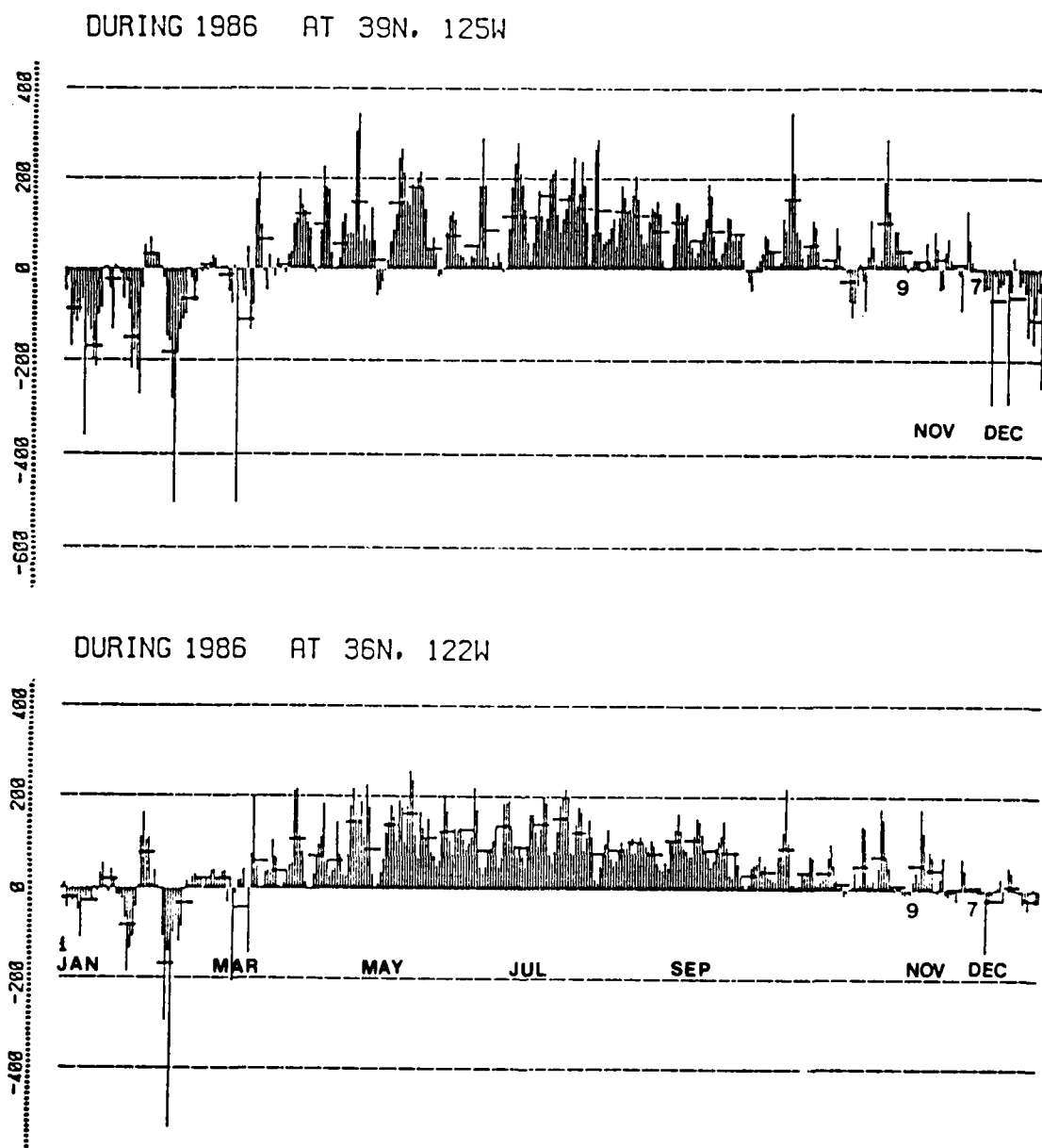


Figure 6.2 1986 daily (vertical bars) and weekly average (short horizontal bars) Bakun upwelling indices at 39 N (top) and 36 N (bottom). Positive values indicate offshore transport.

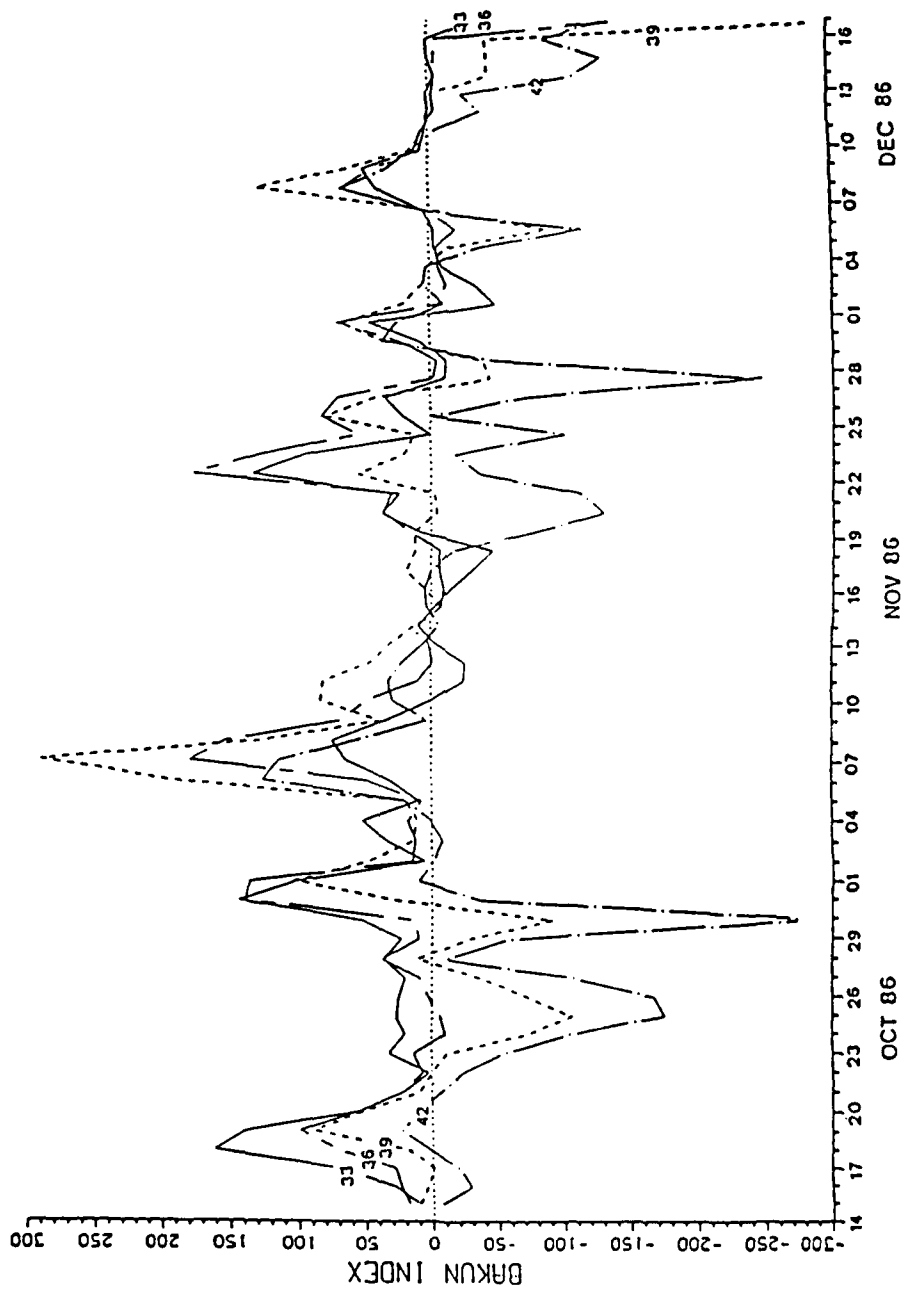


Figure 6.3 Daily Bakun upwelling indices at 33 N (solid), 36 N (chain dash), 39 N (dash), and 42 N (chain dot) from 14 October to 14 December 1986. Four strong upwelling episodes occur near the time of transition: November 7th, November 23rd, December 1st, and December 9th.



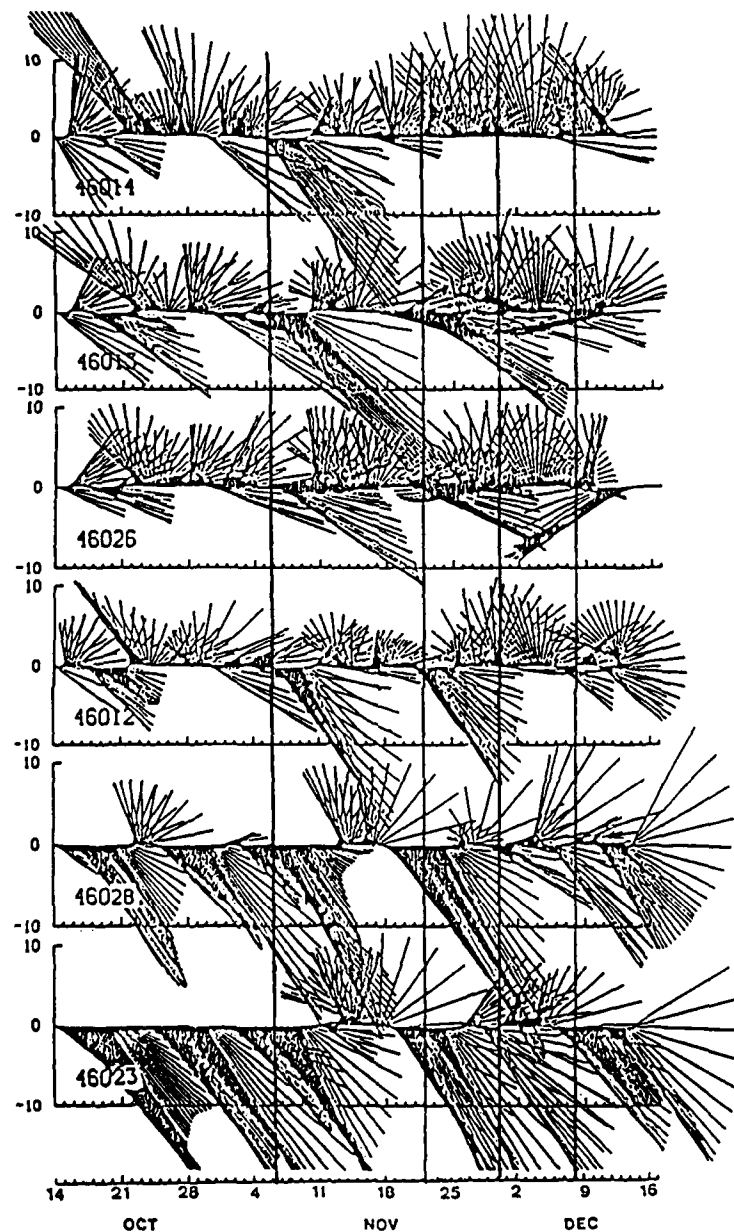


Figure 6.4 Low pass filtered wind vectors from 14 October to 14 December 1986. The scale is in m/s and the vector is towards the direction the wind is blowing; direction has not been rotated. The vertical lines identify the four episodes of winds favorable for upwelling.

southern buoys than at the four northern buoys. The alongshore and cross-shore wind stresses from the four northern buoys confirmed that winds favorable to coastal upwelling ceased in the north except for the four events noted (Figure 6.5). The intervening periods between the episodes had light and mostly onshore wind stress.

The first episode, which peaked on 7 November, included strongly positive Bakun indices at all latitudes with a maximum at 39 N of ca. 300 (units are cubic meters per second per 100 m of coastline), the largest signal during the three month period. For this episode, the alongshore stress was as high as  $10 \text{ dynes/cm}^2$  and cross-shore stress was as high as  $6 \text{ dynes/cm}^2$ . The hydrostatically-adjusted SL deviations along the coast showed a dramatic drop (ca. 30 cm at Crescent City) from 3 to 9 November, followed by a larger rise (ca. 40 cm at Crescent City) from 10 to 19 November (Figure 6.6). This drop and rise cycle was coincident with the onset and demise of the week-long period of strong winds. This SL signal occurred first at Crescent City and progressed southward, apparently covering 900 km over a two-to-three day period, about the same time as an atmospheric wind event passed southward along the coast. The winds favorable for upwelling ceased in the south first, and the subsequent rise in SL took the same amount of time to progress northward along the coast.

There was a  $2.5^\circ\text{C}$  drop in SST over a two-day period at offshore buoys first observed at the northernmost buoy (46014) on 7 November coincident with the wind event favorable for upwelling and lower SL (Figure 6.7). This SST signal also progressed southward as far as the

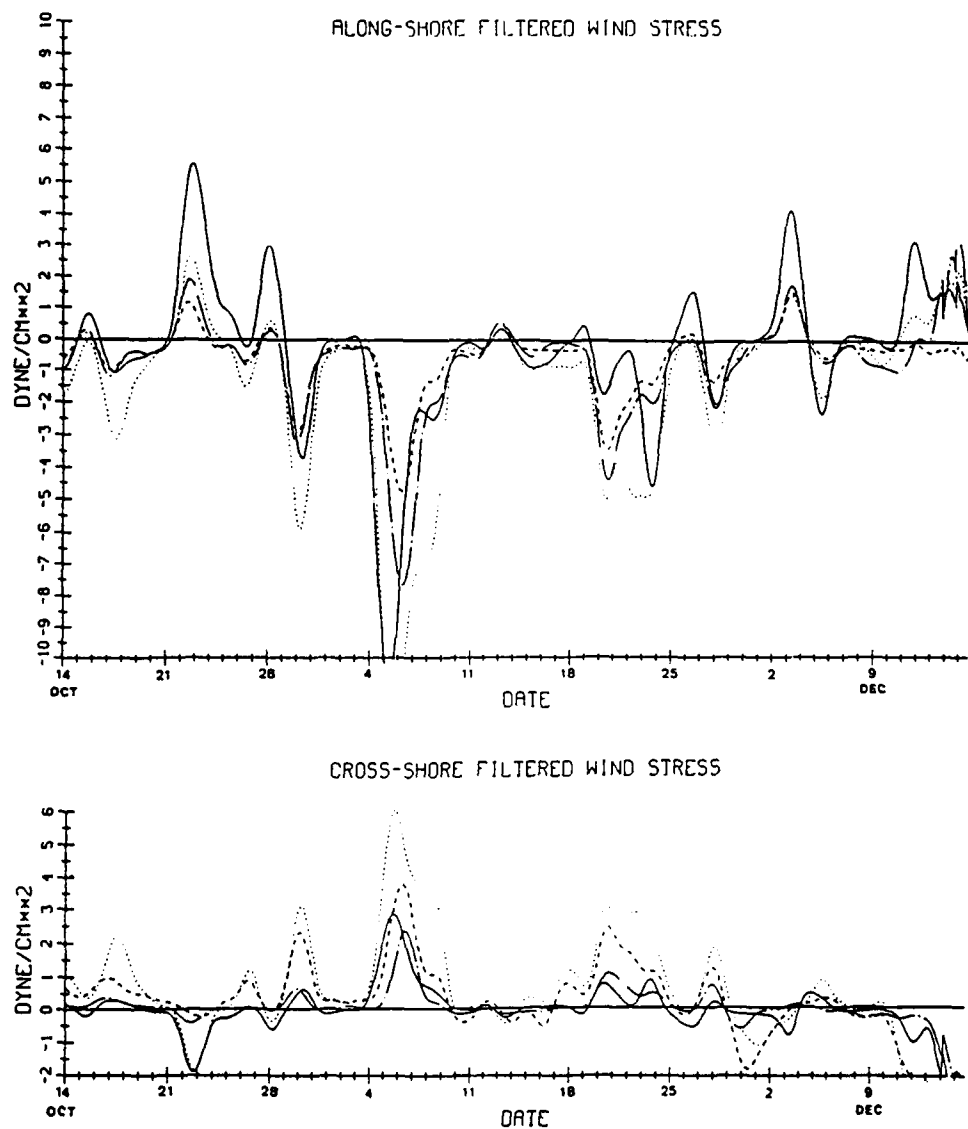


Figure 6.5 Low pass filtered hourly alongshore wind stress (dynes/cm<sup>2</sup>), top, and low pass filtered hourly cross-shore wind stress, bottom, calculated from NDBC 10 m winds at the four northern buoys from 14 October to 14 December 1986. Buoy 46014 is the solid line; 46013, dotted; 46026 dashed; and, 46012, chain.

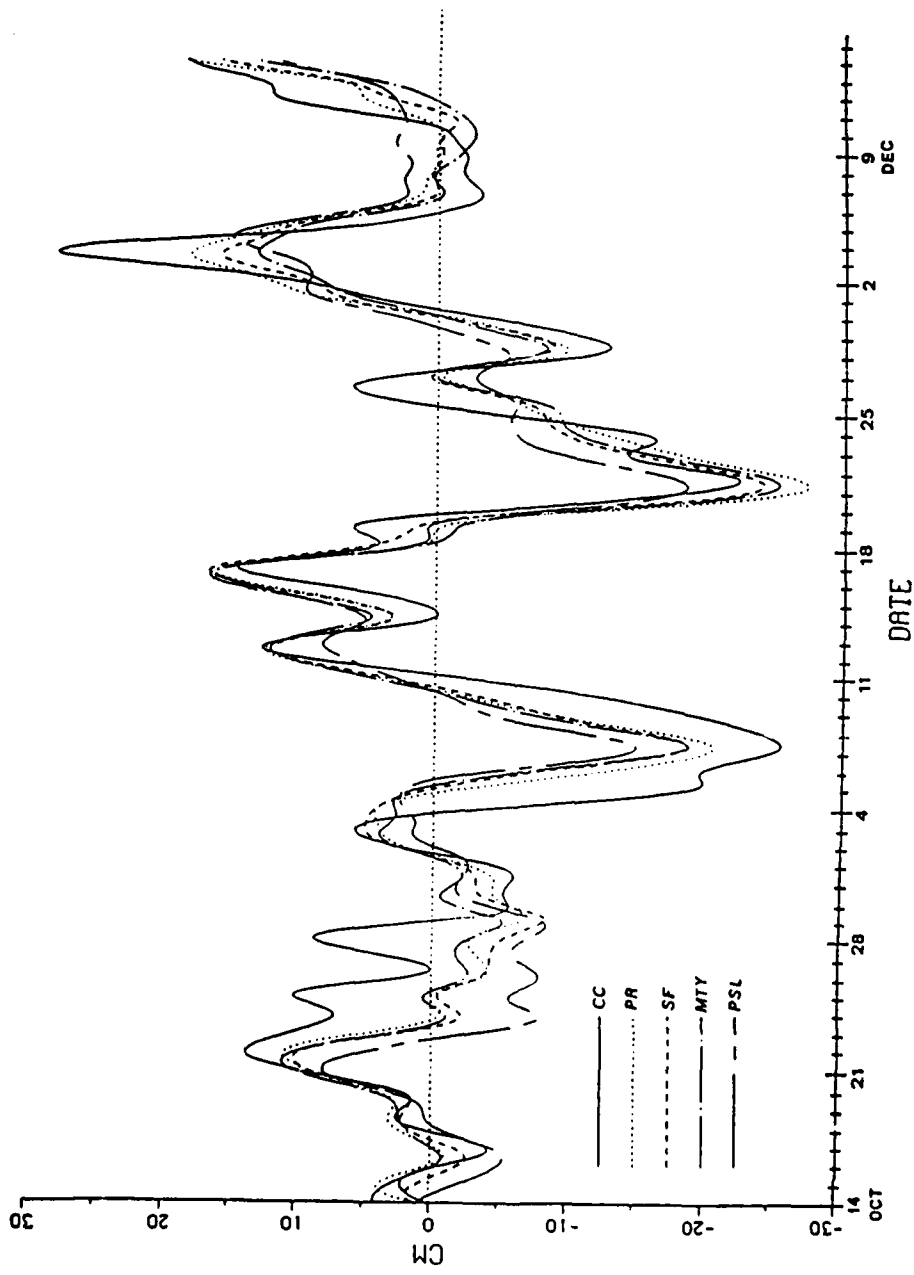


Figure 6.6 Hydrostatically adjusted low pass filtered hourly sea level deviations from 14 October to 14 December 1986. The solid line is the northern-most station, Crescent City; the dotted line, Point Reyes; the dashed line, San Francisco; the chain-dot, Monterey; and the chain-dash is Port San Luis.

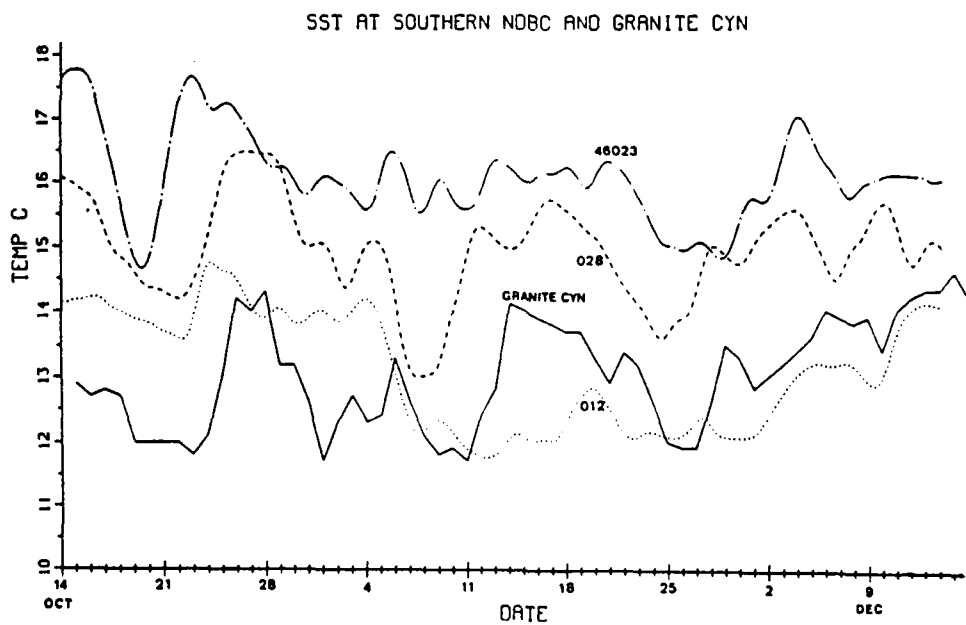
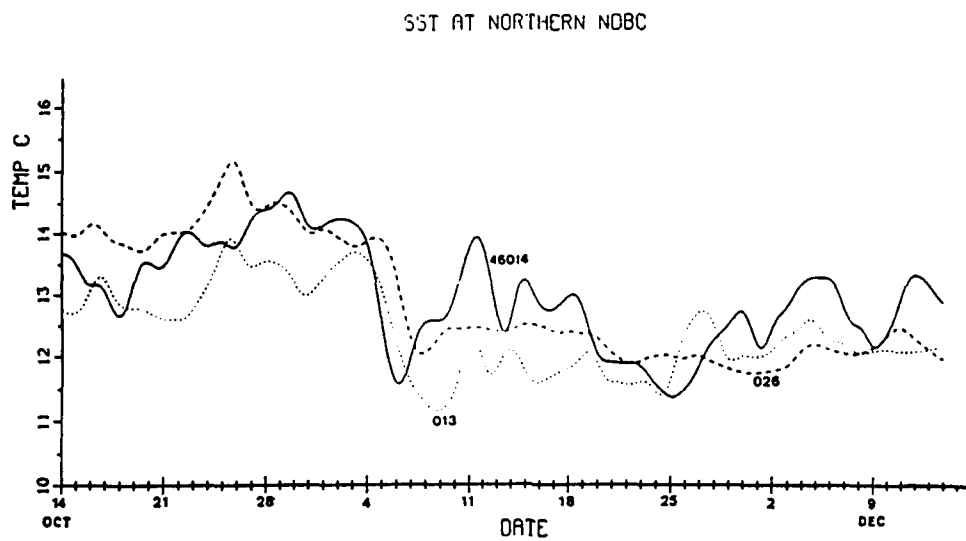


Figure 6.7 Low pass filtered hourly SST from the northern three NDBC buoys (top) and the southern three NDBC buoys plus Granite Canyon daily SST (bottom) from 14 October to 14 December 1986.

buoy south of Point Sur (46028); but did not reach the buoy off Point Conception (46023) which only cooled to 16 °C. With the cessation of the wind event and the rise in SL, the SST rose ca. 2 °C over a three-to-five day period at the two northern buoys, at Granite Canyon, and at the buoy offshore between Monterey and Port San Luis, 46028. The SST at the other three buoys remained cooler (46023 got no cooler than 16.0 °C; 46026, 12.0 °C; and 46012, 12.5 °C) throughout the analyzed period in a manner similar to the response reported by Breaker and Bratkovich (1988). These buoys were all located near points or capes; i.e., sites of coastal upwelling centers and positions of cool filaments.

The second episode, which peaked ca. 22 November, had moderately positive Bakun indices south of 39 N with a maximum of ca. 175 at 36 N. This event was less than half as intense as the first with an average wind stress of ca. 5 dynes/cm<sup>2</sup>. Between 19 and 22 November, a second (larger) drop (ca. 40 cm at Crescent City), coincident with winds favorable for upwelling, was followed by a second (smaller) rise from 22 to 28 November. The SL drops occurred more or less simultaneously along the coast and, again, recovery progressed from south to north.

The second upwelling event started with winds favorable for upwelling on 18 November and resulted in a uniform drop in SL and SST at some sites a few days later. Again, the buoys off capes or points generally did not react. However, the SST at the buoy off Point Conception dropped ca. 1.5 °C from its earlier "floor" and the SST off Point Arena, at buoy 46013, was constant at 12.0 °C. The drop in SST at Granite Canyon was similar to the drops at the two closest offshore

buoys, and it apparently occurred slightly after the drop at buoy 46012 to the north and slightly before the drop at buoy 46028.

The third episode, which peaked on 30 November, had weakly positive Bakun indices at all latitudes with a maximum of 50 at 36 and 39 N. A third smaller two-day drop in SL, which started on the 29 November occurred more or less simultaneously along the coast. Qualitatively, there was good correlation between the sea level and atmospheric signals with the ocean responding in a manner typical to upwelling; i.e., there were slight and temporary decreases in SST during this short period.

The final (fourth) episode, which peaked on 8 December, was moderately positive at all latitudes with a maximum Bakun index of 125 at 39 N. There was a large increase (e.g., ca. 40 cm at Crescent City and ca. 30 cm elsewhere) in SL, which peaked on 3 December. This episode occurred during upwelling favorable conditions. The increase was first observed at Port San Luis to the south and last observed at Crescent City to the north two days later yielding an apparent propagation speed of ca.  $400 \text{ km day}^{-1}$ . The following drop in the SL anomaly to nearly zero occurred during southward and onshore winds.

The final (fourth) upwelling event differed in that the sea level pressure was high, the Bakun index was high, the sea level dropped, but SST did not change for most of the buoys. To the contrary, for most buoys and Granite Canyon, the low SST on 25 November was followed by an increase which continued through the first two weeks in December, raising temperature ca.  $0.1 \text{ }^{\circ}\text{C/day}$  for two-to-three weeks. The rise

started in the south and traveled north at ca. 150 km/day to Monterey. From Monterey north, the change was almost simultaneous.

#### D. CHANGES IN MESOSCALE FIELDS

Offshore, mostly in the OPTOMA 23 domain, a total of six OPTOMA survey flights were flown between 9 and 19 November (Julian dates 86313 and 86323), deploying ca. 350 shallow AXBTs. During OPTOMA 23P3, ca. 20 AXBT's were deployed near Monterey Bay on 11 November (Julian Day 86315). From 15 to 19 November, the R/V POINT SUR was at sea making ca. 80 CTD and XBT observations during two quasi-synoptic surveys off Monterey and Point Sur near a cool filament identified in satellite imagery and in objectively-analyzed data fields from earlier survey flights (Chapters III and IV).

The CTD's and XBT's acquired by the R/V POINT SUR were an independent in situ data set (except for the use of the CTD's in providing an average T-S relationship to use with the AXBT's in the CENCAL domain) linking the coastal and offshore observations. The CTD observations were acquired along two roughly parallel lines extending ca. 250 km offshore from Monterey and Point Sur 50 km to the south (Figure 6.8).

These data were analyzed in two ways: SDH, SST, T200, and S200 were objectively analyzed on 16 November (Julian date 86320); and, differences throughout the water column from the surface to 450 m were calculated at positions common to the two ship surveys. These were usually within two to three km and ca. 96 hours apart. Differences were calculated by subtracting leg 1 data from leg 2 data in the vertical



# CTD AND XBT POSITS

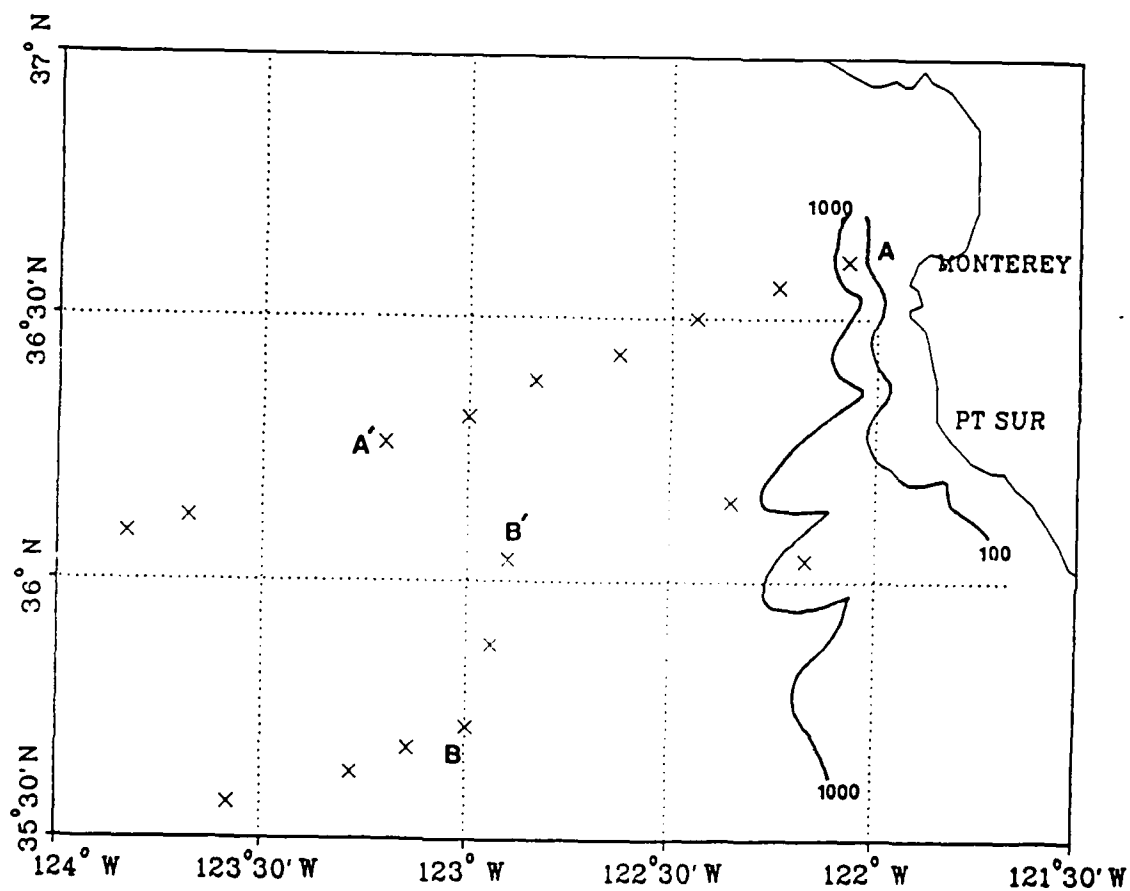


Figure 6.8 CTD and XBT positions during the two R/V POINT SUR surveys in November 1986. A-A' identifies the seven XBT's in the offshore group; B-B', the three CTD's in the "off-filament" group.

from the surface to 450 m at 17 positions. About half of the comparisons were CTD measurements which provided an estimate of change in both temperature and salinity fields. The remainder were XBT measurements or a mix which provided only temperature changes.

The OPTOMA 23 domain was active with mesoscale variability (Figure 6.9). There were two cool filaments, one off Point Reyes and one off Point Sur, which extended westward through the domain and were readily identified in satellite IR images. There were two anticyclones (200 km diameter) extending from the surface to depth which propagated westward (ca. 5 km/day) over the course of ten days from the eastern boundary to the center of the domain north of the cool filament axes. There were also two quasi-stationary cyclones; one to the north and one to the southwest. Z08 generally deepened towards the coast. Correspondingly, temperatures at depth, e.g. T50, generally decreased towards the coast. Mixed layer depths averaged 30 m and ranged from the zero to 40 m.

On 9 November, the jet appeared to enter the domain in the northwest corner ca. 300 km offshore and turn towards Point Reyes where it recurved seaward and joined flow from the south circulating around a cyclone. It was at most 90 km wide and had a maximum speed of ca. 15 cm/s. The jet was similar ten days later although there was circulation around the anticyclone off Point Reyes.

There was an anticyclonic feature near Monterey Bay on 16 November, evident in the SDH field, but not in the SST field (Figure 6.10). The northward geostrophic flow around this feature was ca. 10 cm/s. At 200 m, the feature was warm and less saline than the surrounding water (Figure 6.11). These OA fields were generated from R/V POINT SUR, OPTOMA

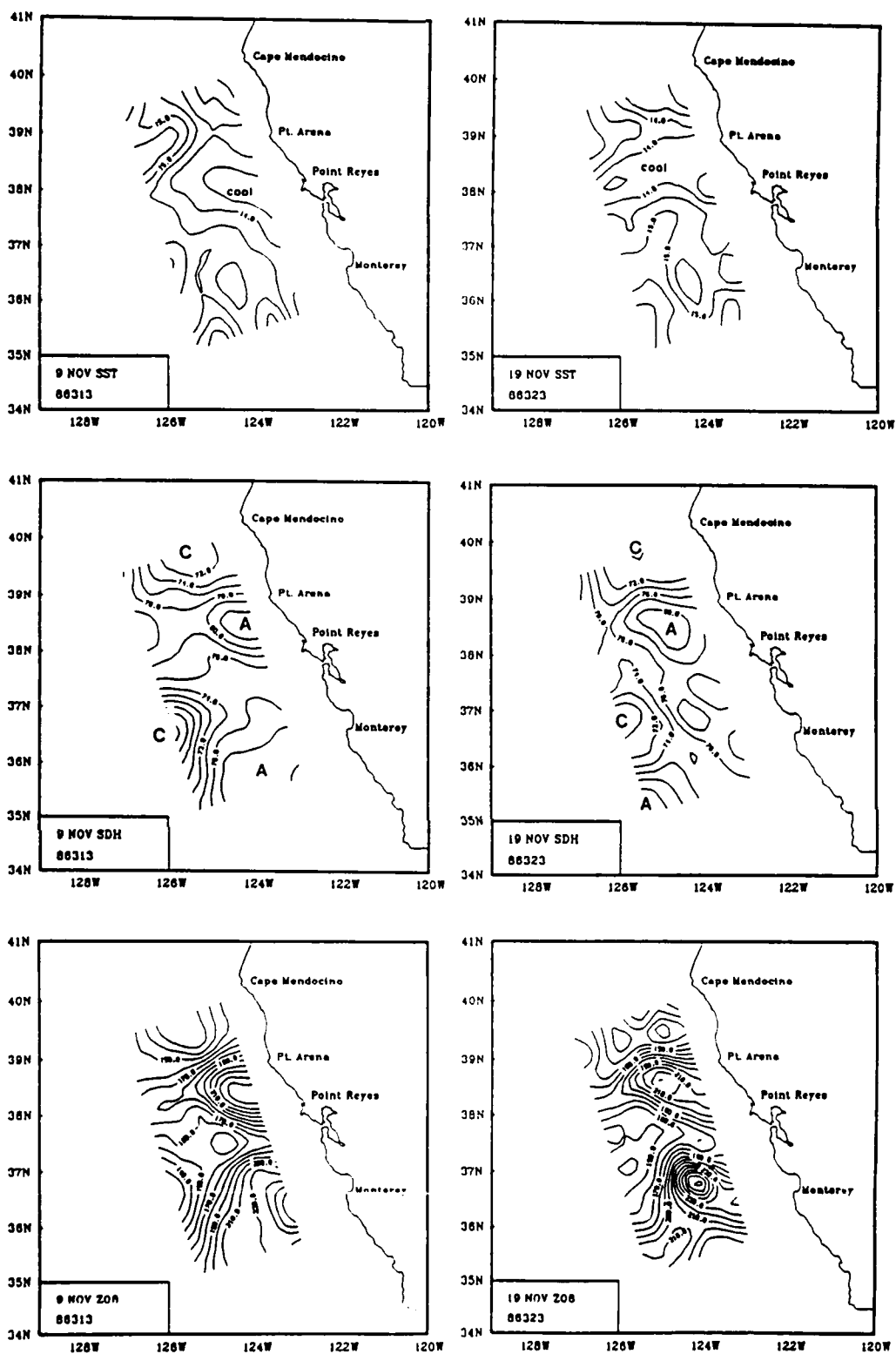


Figure 6.9 OPTOMA 23 fields at the beginning of the survey, 9 November (left), and at the end of the survey, 19 November (right). Surface dynamic height, referenced to 450 m, is contoured at 2 dyn cm intervals.

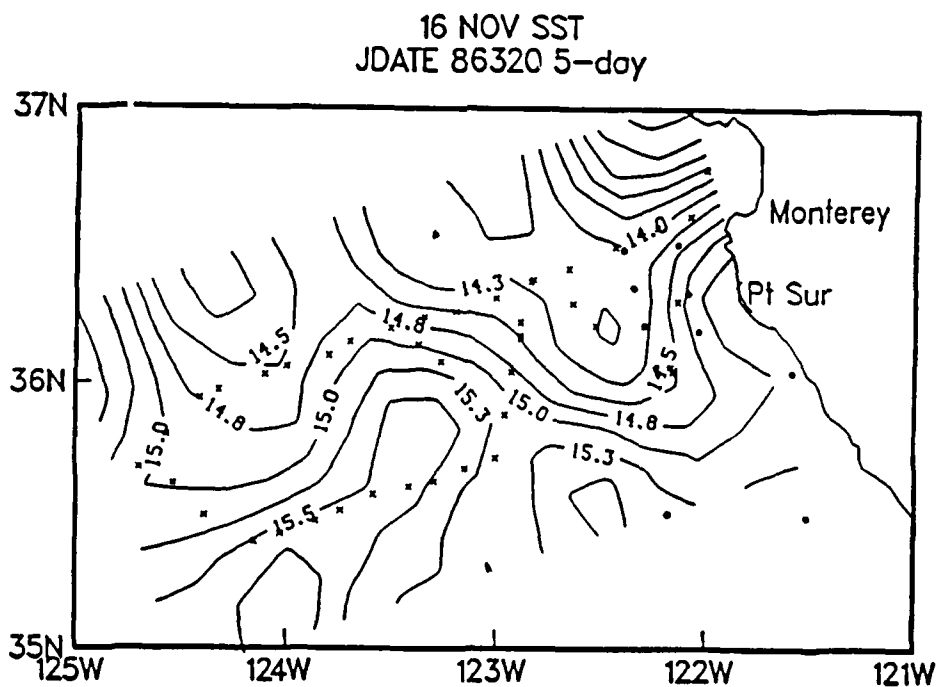
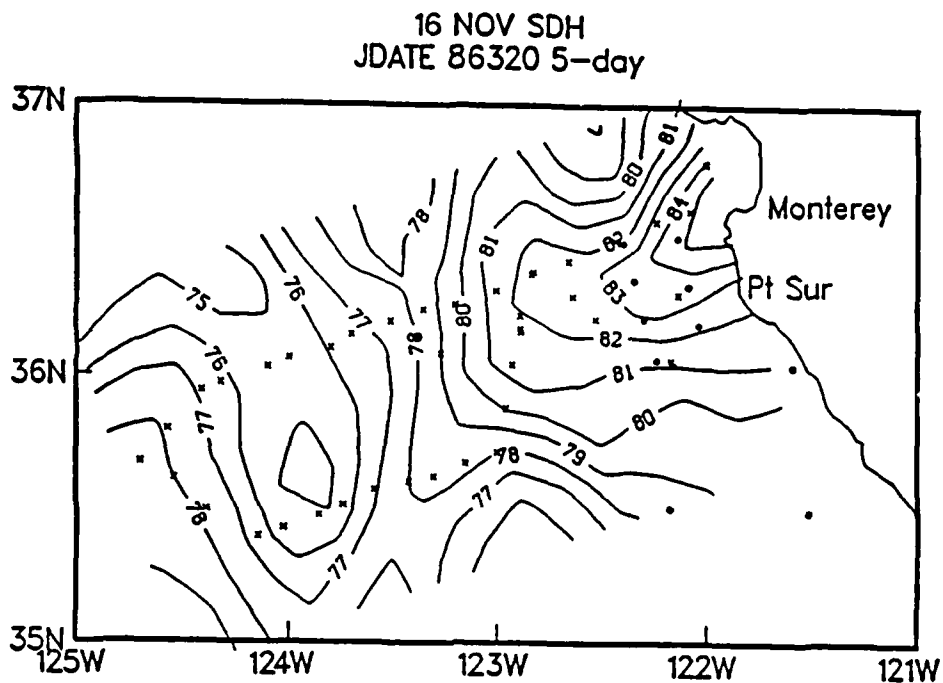


Figure 6.10 OA fields off Monterey Bay on 16 November 1986. SDH (top) is referenced to 450 m and contoured at one dyn cm. SST (bottom) is contoured at 0.25 °C. The crosses are data from the R/V Point Sur; the dots are data from OPTOMA 23P3. OPTOMA 23P4 data was also used.

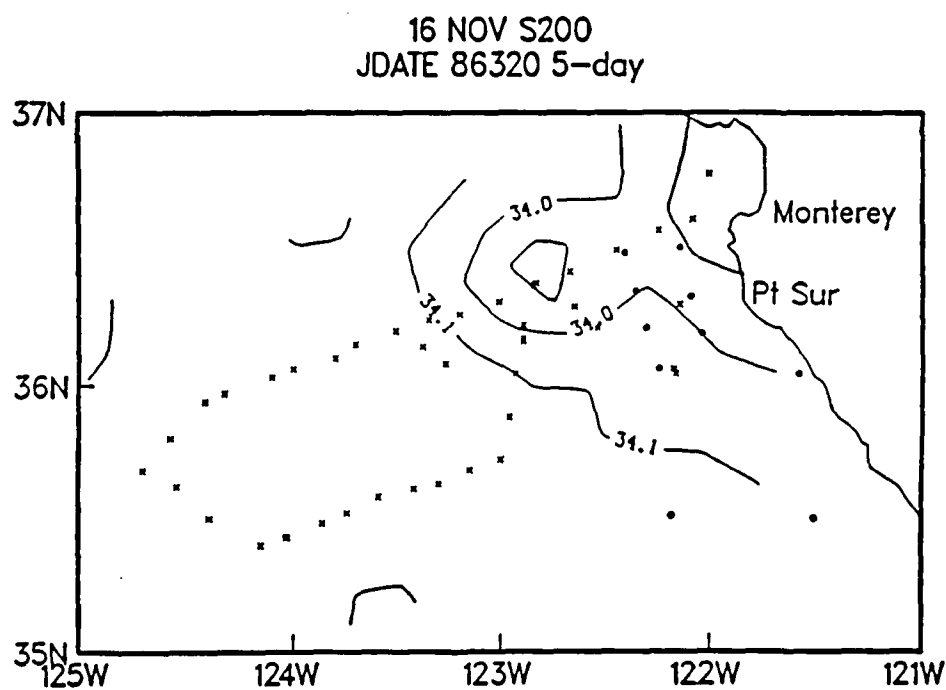
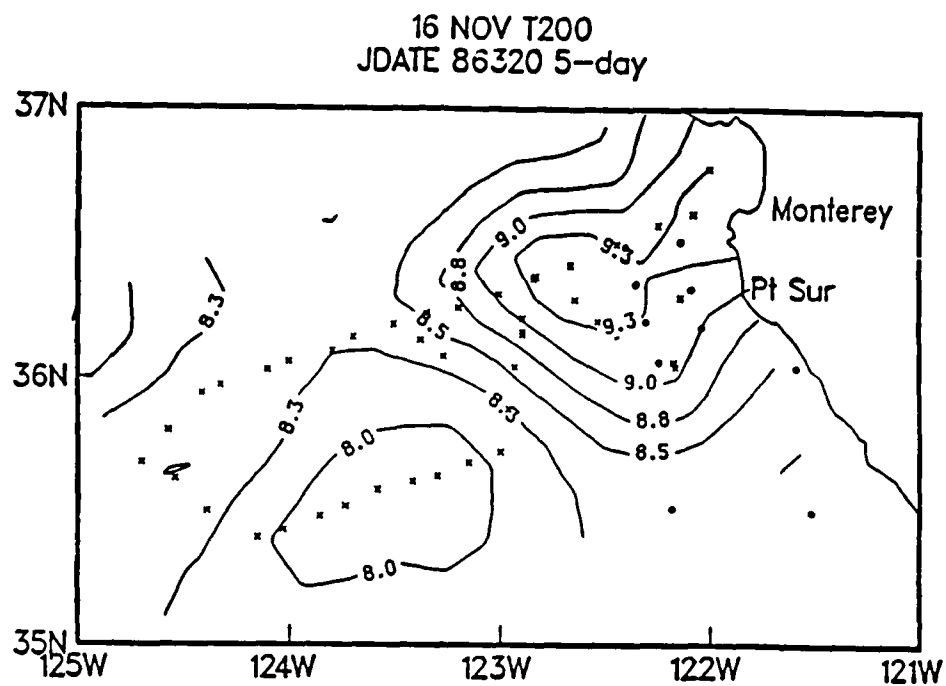


Figure 6.11 OA fields off Monterey Bay on 16 November 1986. T200 (top) is contoured at 0.25 °C. Salinity at 200 m (bottom) is contoured at one PPT. The crosses are data from the R/V Point Sur; the dots are data from OPTOMA 23P3. OPTOMA 23P4 data was also used.

23P3, and OPTOMA 23P4 data using a five-day temporal window and were consistent with the fields in the OPTOMA 23 domain.

Satellite-derived surface velocity vectors from images on 11 and 12 November (Julian dates 86314 and 86315) showed the broad southward flow associated with the California Current, its interaction with the cool filament off Point Reyes, and the nearshore coastal jet flowing northward at 10 to 20 cm/s (Figure E.9). The nearshore coastal jet was present from the southern limit of the imagery (near Point Sur) to Point Reyes where it appeared to be truncated by the cool filament "anchored" there. North of Point Reyes, mesoscale features dominated the flow field from the OPTOMA domain to the coast and there was no evidence of a coastal jet. These conditions persisted a week later in satellite imagery on 19 November (Julian date 86323, Figures E.10, E.11, and E.12).

Difference fields of SST, temperatures throughout the water column to 300 m, and the Z08 were calculated by subtracting the 9 November fields from the 19 November fields (Figure 6.12). The SST difference field showed a warming trend from the southern border of the domain to as far north as Point Arena with an increase in SST as great as 1.2 °C. The T50 field had also warmed, an average of 0.3 °C with a standard deviation of 1.1 °C, in the same region except for a cool area associated with the southern anticyclone. The cool filament off Point Reyes was the northern boundary of the warming trend in both the surface and T50 fields. The T100, T200, and T300 fields also warmed, about half as much as the T50 field, mostly to the south.

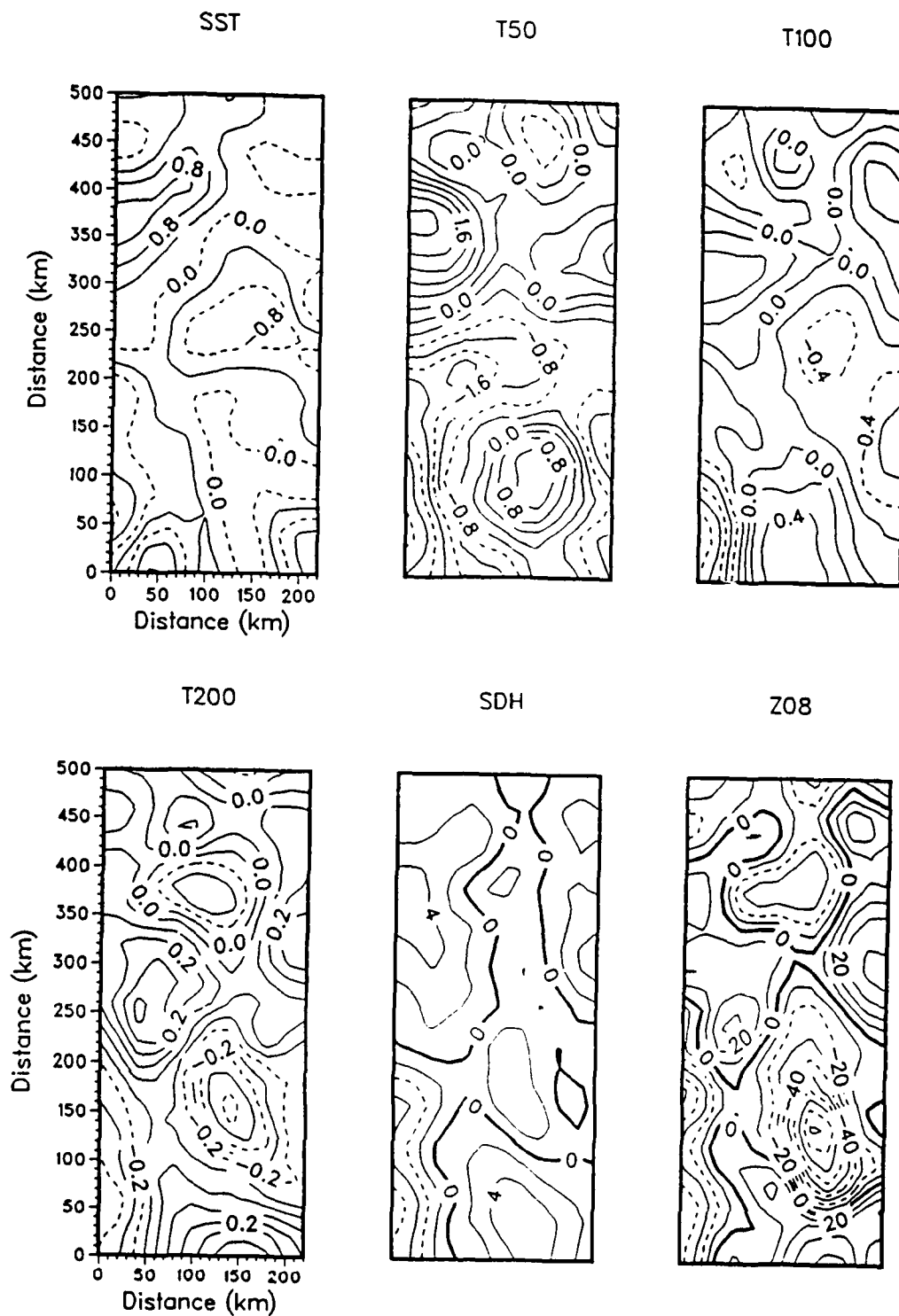


Figure 6.12 OPTOMA 23 difference fields calculated by subtracting fields on 9 November from the same fields observed on 19 November. SST and T50 are contoured at 0.2 °C intervals. T200 at 0.05 °C and Z08 at 10 m.

During the winter, the isotherms in the mid-thermocline were expected to be level; during active upwelling, they were expected to slope upward towards the coast (Lentz, 1987). Mesoscale features superimpose variation upon a "smooth plane". During OPTOMA 23, Z08 ranged from 130 to 270 m and it was difficult to determine a trend. The difference field indicated shoaling of Z08 in the southern part of the domain and off Point Reyes, and deepening near the anticyclone to the south and offshore.

The difference between observed temperature and salinity profiles, CTD's and XBT's from the R/V POINT SUR on 15 and 19 November were used to verify change in the water mass indicative of the transition. To avoid the effects of mixed layer dynamics, difference calculations were between 50 and 300 m. The average MLD was 24.5 m (standard deviation; 12.2 m; range, from zero to 40 m) on 15 November and it was deeper, 27.2 m (standard deviation, 8.8 m; range, 10 to 40 m), on 19 November. Diurnal biases and effects of internal waves were not estimated.

The average temperature increased with the major warming occurring between 50 and 150 m. At 50 m the average increase was 0.7 °C and the standard deviation was the largest, 1.3 °C. This was an increase of ca. 0.2 °C per day. The average salinity change decreased, particularly between 50 and 150 m (Figure 6.13).

To isolate the bias of observations in the filament and to distinguish between observations on the shelf and those offshore in the mesoscale field, the differenced pairs of CTD's and XBT's were placed into four groups: shelf, offshore, filament, and nearshore. Two of these groups, offshore and filament, showed changes expected during the



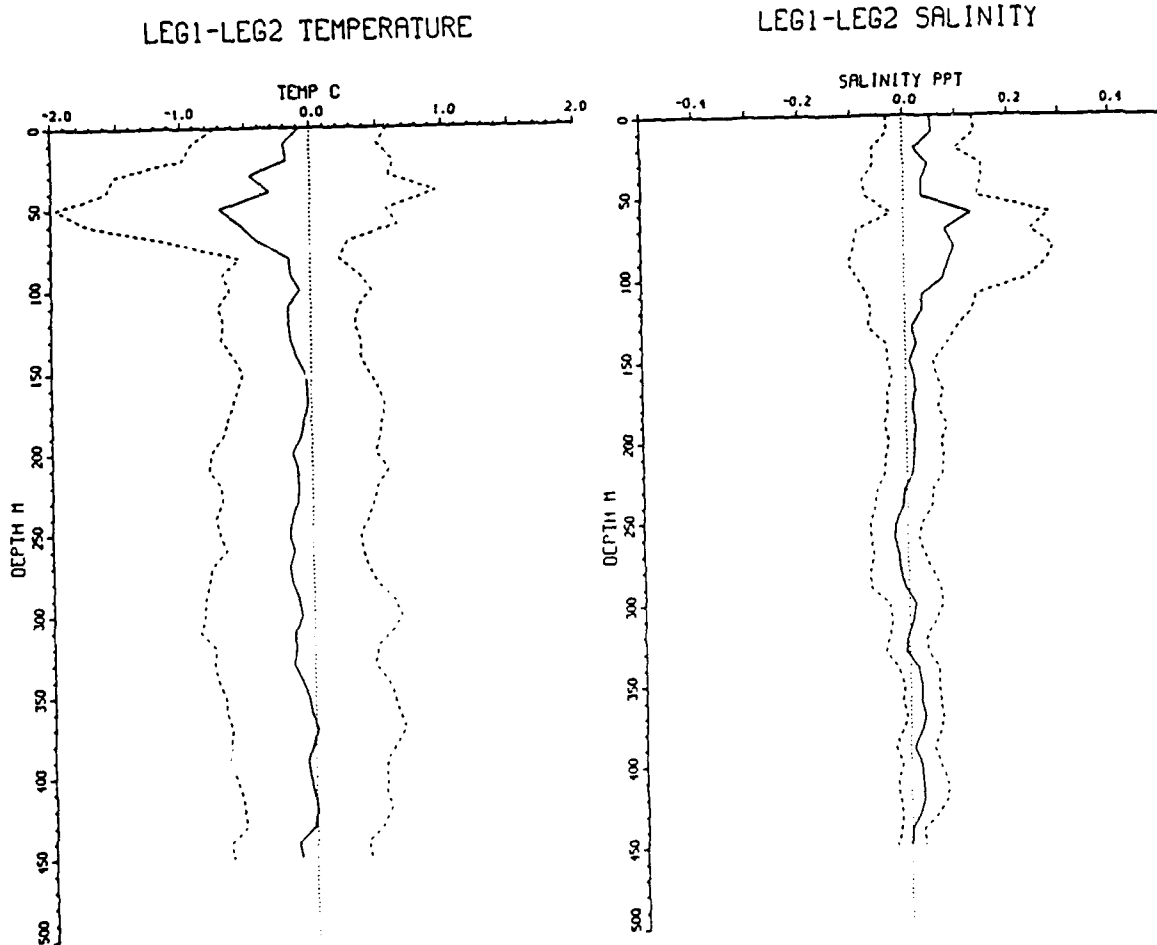


Figure 6.13 R/V POINT SUR CTD and XBT temperature (left) and salinity (right) average differences (solid lines) and one standard deviation (dashed lines) calculated from positions (17) common to the surveys.

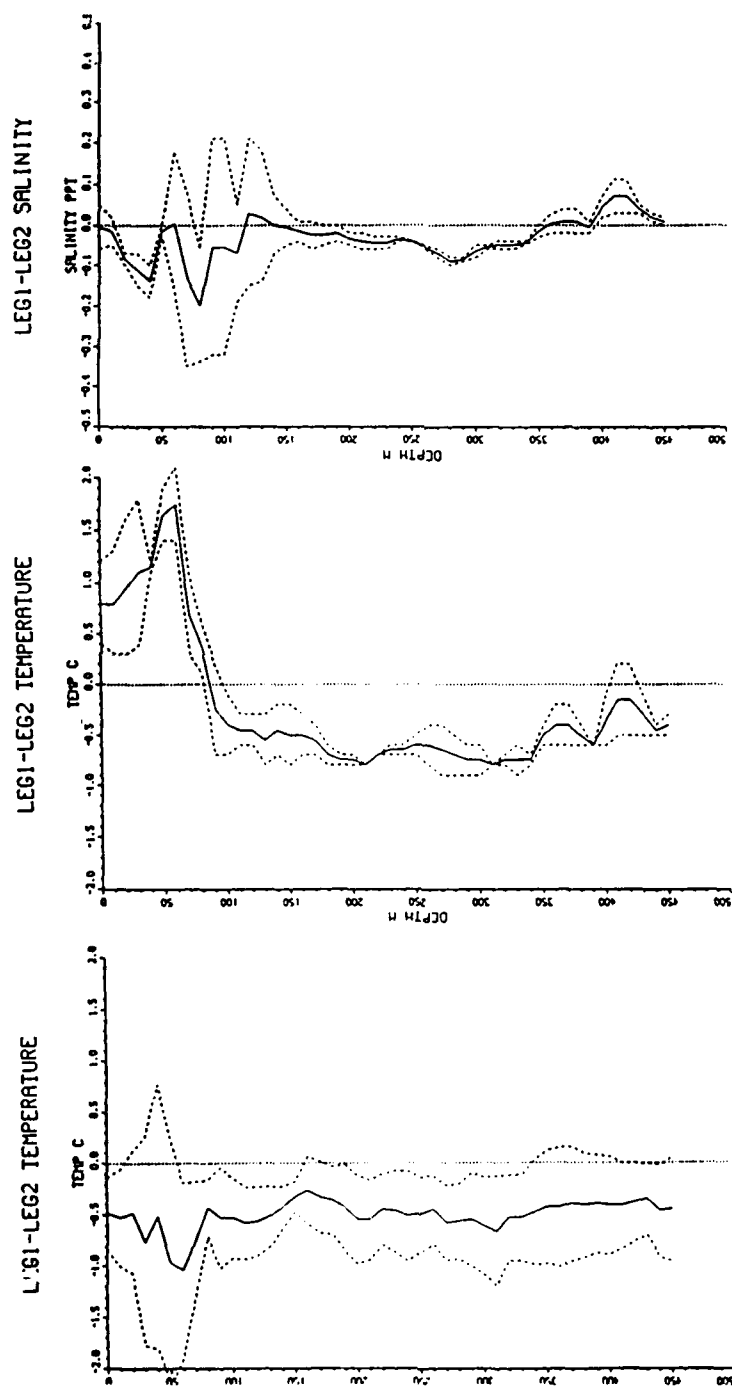


Figure 6.14  $\Delta T$  from the northern line perpendicular to the coast at Monterey, group A XBT's (left), and  $\Delta T$  and salinity difference (right) from the observations off the cool filament, group B CTD's.

transition, i.e., increases in salinity and temperature (Figure 6.14). The northern offshore line was made up of XBT's only; their temperature increase averaged 0.5° C with the highest values again at 50 m. The CTD's off the filament cooled above 80 m and warmed below. The warming at depth was greater than 0.5 °C. Salinity increased an average of .04 PPT, with the largest increase also above 80 m.

There were no in situ surveys later than 21 November (Julian date 86323). However, OA SSH fields on days 86312 and 86329, the two 17-day ERM orbits which bracketed the OPTOMA 23 survey, indicated a change in the mesoscale flow pattern (Figure 6.15). Prior to and during the OPTOMA 23 survey, the domain was filled with mesoscale features; after the survey, a large meridional nearshore ridge and an offshore trough were the predominant features in SSH. These would be expected after the fall transition. The northward geostrophic flow between the two features was ca. 20 cm/s.

## E. DISCUSSION OF THE FALL TRANSITION OF 1986

### 1. General

Regarding the sea surface as an externally prescribed forcing function, and neglecting bottom friction and non-linear effects, the local velocity profile can be uniquely determined by wind stress and sea surface slope:

$$\partial \bar{v} / \partial t + f \bar{u} = -g \partial \zeta / \partial y + (\tau_{y0}) / H \quad (\text{equation 6.1})$$

where  $\bar{u}$  and  $\bar{v}$  are depth-averaged velocities,  $f$  is the coriolis parameter,  $g$  is gravity,  $\zeta$  is the free surface elevation (above the undisturbed surface),  $\tau_{y0}$  is the average wind stress in the north-south direction at the surface, and  $H$  is the depth (Welander, 1957 and Werner and Hickey, 1983).  $H$  is typically 100 m (Enfield and Allen, 1980).

The balance is between the alongshore pressure gradient force (PGF),  $-g\partial\zeta/\partial y$ , and the surface wind stress,  $\tau_{y0}/H$ , assuming no offshore flow and no local acceleration term. At a position on the coast, local forcing is due to wind stress; remote forcing is due to a change in SL at a neighboring position which changes the SL slope between the two. The remote forcing contribution decreases southward along the west coast; it is ca. 25% at Crescent City, 12% at San Francisco, and 10% at Avila Beach. Additionally, seasonal heating or cooling and freshwater contributions to large scale elevation slope are insignificant (less than 10 % at Monterey) (Hickey and Pola, 1983).

In the CCS (off Washington and Oregon), a northward PGF develops in the summer, opposing the southward local wind stress. During winter, the PGF is southward, opposing the northward local wind stress (Werner and Hickey, 1983). In November, between 35 and 38 N in the CCS (a Northern Hemisphere minimum in SL and SST anomaly variances, Enfield and Allen, 1980), the PGF is usually northward (Hickey and Pola, 1983). Northward flow is expected at a coastal position when the SL to the south is higher than the SL to the north. This may occur when winds were not favorable for upwelling to the south and favorable to the north.

SDH AND SSH OA FIELDS (GLOSAT 17-day ERM)

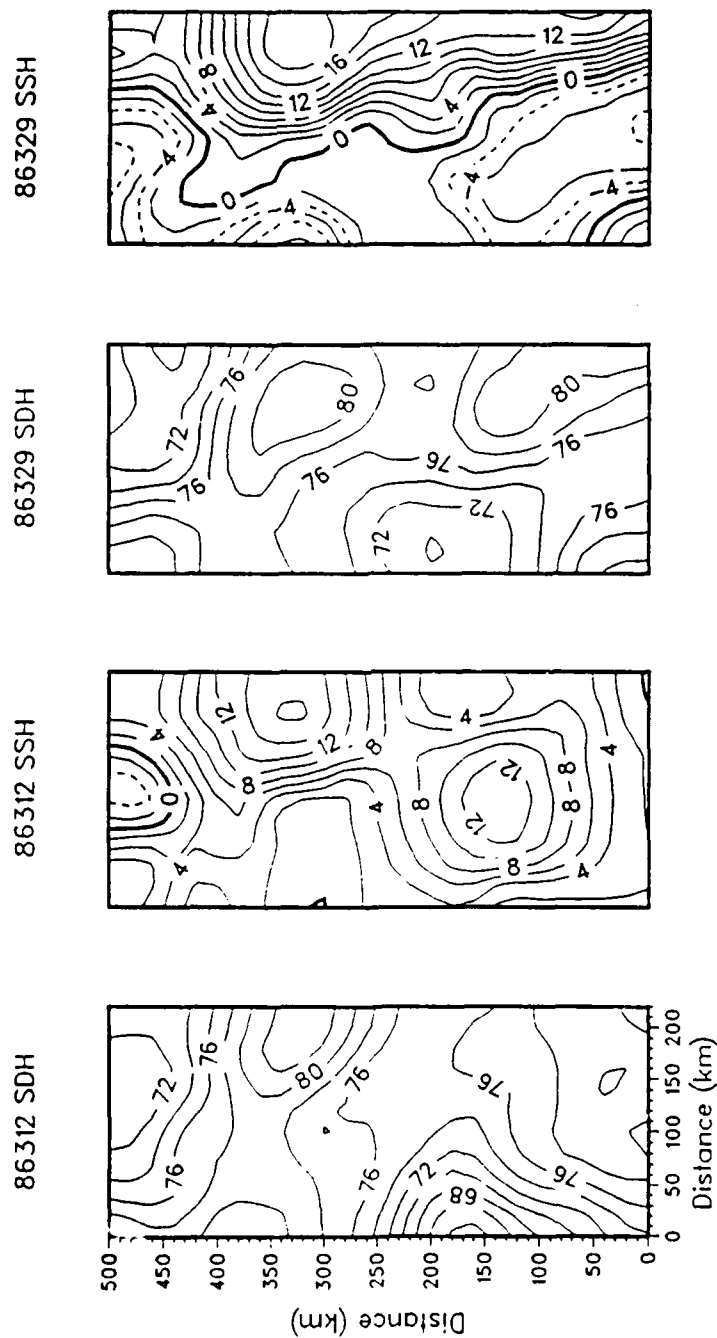


Figure 6.15 SDH and SSH OA fields from Julian dates 86312 and 86329 (8 and 25 November 1986). The SDH field on day 86329 is generated from data on days 86321 and 86323. The contour interval is 2 dyn cm (or cm).

Calculation of the SL slope between two stations is not straight forward due to difficulties in geodetic leveling and the effects of deep ocean currents on coastal SL. Geodetic leveling indicates that the SL rises 7 cm between 32 N and 48 N. South of San Francisco, empirical evidence suggests that deep ocean currents contribute significantly to coastal elevation slope, where shelf is narrow (the offshore scale is ca. 20 to 30 km), in the summer and fall. A steric height leveling, referenced to 500 m, is opposite to the geodetic correction and decreases from south to north; the correction to "quasi-absolute" SL is 82.0 cm at Port San Luis, 78.5 cm at San Francisco, and 77.8 cm at Crescent City (Reid and Mantyla, 1976).

The changes in the offshore fields may have been related to the transition in the coastal zone because of a combination of offshore mesoscale advection and coastal wave activity. A similar effect was noticeable in IR imagery when mesoscale features advected cool filaments of upwelled water hundreds of kilometers offshore. In this situation, the mesoscale feature bordered the upwelling zone. With the cessation of upwelling and the persistence of the mesoscale feature within the coastal zone of influence, warm water could be advected offshore.

In a coastal topographic wave, the pressure field is trapped in a nearshore band, the scale width of which is:

$$L = (2r / fks)^{1/2} \quad \text{(equation 6.1),}$$

where  $r$  is the bottom resistance coefficient,  $f$  is coriolis,  $k$  is the alongshore wavenumber of the wind stress, and  $s$  is the bottom slope (Csanady, 1978).

Using values appropriate for the Central California coast ( $r = 0.1 \text{ cm s}^{-1}$ ,  $f = 10^{-4} \text{ s}^{-1}$ ,  $k = 10^{-8} \text{ cm}^{-1}$ , and  $s = 10^{-2}$ ),  $L = 45 \text{ km}$  (compared to  $141 \text{ km}$  off the east coast, where  $s$  is an order of magnitude smaller). With a stress amplitude,  $F$ , of  $1 \text{ cm}^2 \text{ s}^{-2} (\tau/\rho)$ , the velocity amplitude,  $V = F/r$ , is  $10 \text{ cm s}^{-1}$ , and the elevation amplitude,  $2F/kLg$ , is ca.  $40 \text{ cm}$  (Csanady, 1978). These values are similar to observed changes in SL and the nearshore surface velocities and mesoscale features with offshore circulation (e.g., the anticyclone near Monterey Bay) were within  $45 \text{ km}$  of the coast.

The results are sensitive to the bottom friction component; a value of  $0.01 \text{ cm s}^{-1}$  results in a smaller width scale of  $14 \text{ km}$ , a higher velocity of ca.  $100 \text{ cm s}^{-1}$ , and a smaller elevation amplitude of ca.  $14 \text{ cm}$  (Hickey and Pola, 1983). A higher wavenumber (e.g.,  $10^{-7} \text{ cm}^{-1}$ ) results in a larger width scale ( $141 \text{ km}$ ) and a negligible elevation amplitude.

## 2. CCS, November 1986

Autumn climatological ocean and weather conditions along the Northern and Central California Coast consist of northward winds, warm, saline water near the coast, and a flat thermocline offshore. The actual conditions differ from climatology for a variety of reasons (e.g., sporadic southward winds due to passing storms, large scale oceanic

warming due to El Nino events, and perturbations due to mesoscale activity from the continental shelf to at least the continental rise).

By early November 1986, persistent winds favorable for upwelling had ceased along most of the coast and upwelling became a sporadic event (as opposed to an almost continuous condition during the summer months). The upwelled water (Undercurrent) during early November was different from the local surface water (California Current). The transition had not yet started. Later in the month, the upwelled water was indistinguishable from surface water, and in many locations, SST started to rise, as is typical during the winter season. The Davidson Current had displaced the California Current off Central California and Fall Transition of 1986 had started. During this period, a warming trend in the upper 200 m in the mesoscale field hundreds of kilometers offshore apparently accompanied the coastal transition.

Three upwelling events (4 to 11 November, 18 to 25 November, and 2 to 5 December) and the intermediate periods were of interest (Table 16). The first two events were consistent with summer regime upwelling as there were higher sea level pressures, stronger equatorward winds (and thus higher upwelling indices), lower sea levels, and lower SST. The last episode included higher SST and was not consistent with summer upwelling; it appeared that the Davidson Current was established off Northern and Central California near 25 November while there were intermittent winds which were occasionally favorable for upwelling.

Unlike conditions described by Breaker and Mooers (1986), there was inconclusive evidence in 1986 for a wave-like disturbance propagating along the coast accounting for the transition. During the



TABLE 16. QUALITATIVE SUMMARY OF COASTAL SIGNALS

	1	2	3	4	5
Time Period:	4 to 11 NOV	12 to 17 NOV	18 to 25 NOV	26 NOV to 1 DEC	2 to 5 DEC
Sea Level Pressure:	High	Avg	High	Avg	Avg
Winds:	Onshore Southward Strong	Nil	Onshore Southward Moderate	Light	Onshore Southward Light
Bakun Index: <sup>1</sup>	++ 150	Nil	++ 150	Nil	Nil but rising to 50
SST: <sup>2</sup>	Large drop	Large rise			Moderate rise
DT/Dt <sup>3</sup> :	-0.8	+0.5 to +0.8			
Sea Level:	Big drop 16 to 32	Big rise 17 to 39	Big drop 23 to 37		Big rise 24 to 32
Remarks:	Upwelling		Upwelling	Transition	Transition

## Notes:

1. Positive implies upwelling favorable
2. Includes Granite Canyon
3. degrees C per day

upwelling events, the northern and central coast SST's reacted simultaneously; during the warming transition event, there was apparent propagation along the southern part of the coast, suggesting that two or more regimes may exist. On the otherhand, similar to the spring conditions described by Huyer et al. (1979), the coastal waters responded to rapidly moving wind events.

The balance of forces, between the alongshore PGF,  $(-g\partial\zeta/\partial y)$  and the surface wind stress  $(\tau_{yo}/H)$ , were calculated at four of the six coastal SL sites (Port San Luis, Monterey, Point Reyes, and Crescent City), from 1 July 1986 through 31 December 1986. The alongshore PGF was calculated from the slope of SL between the site and its southern neighbor. The wind stress was calculated at the nearest MBL grid point, except for Monterey where the wind stress was linearly interpolated between grid points. The analysis was not sensitive to depth (H was varied from 25 to 100 m) or to the steric and geodetic corrections. Changes mostly affected the time of the zero crossing; a reduced H and no corrections resulted in a delay of one or two days.

The balance at Monterey best depicted the start of the fall transition, in late November and early December, and its nature; i.e., the balance fluctuated throughout the winter as the PGF and wind stress varied (Figure 6.16). Although the start of the transition was not evident elsewhere, its fluctuating nature was universal:

- (1) the PGF at Crescent City was strongly northward, and increasing, throughout the six-month period; wind stress was predominantly southward until late October when it became mostly northward (exceptions noted in Table 16),

# U MTY, FROM BAL OF PGF/WIND STRESS

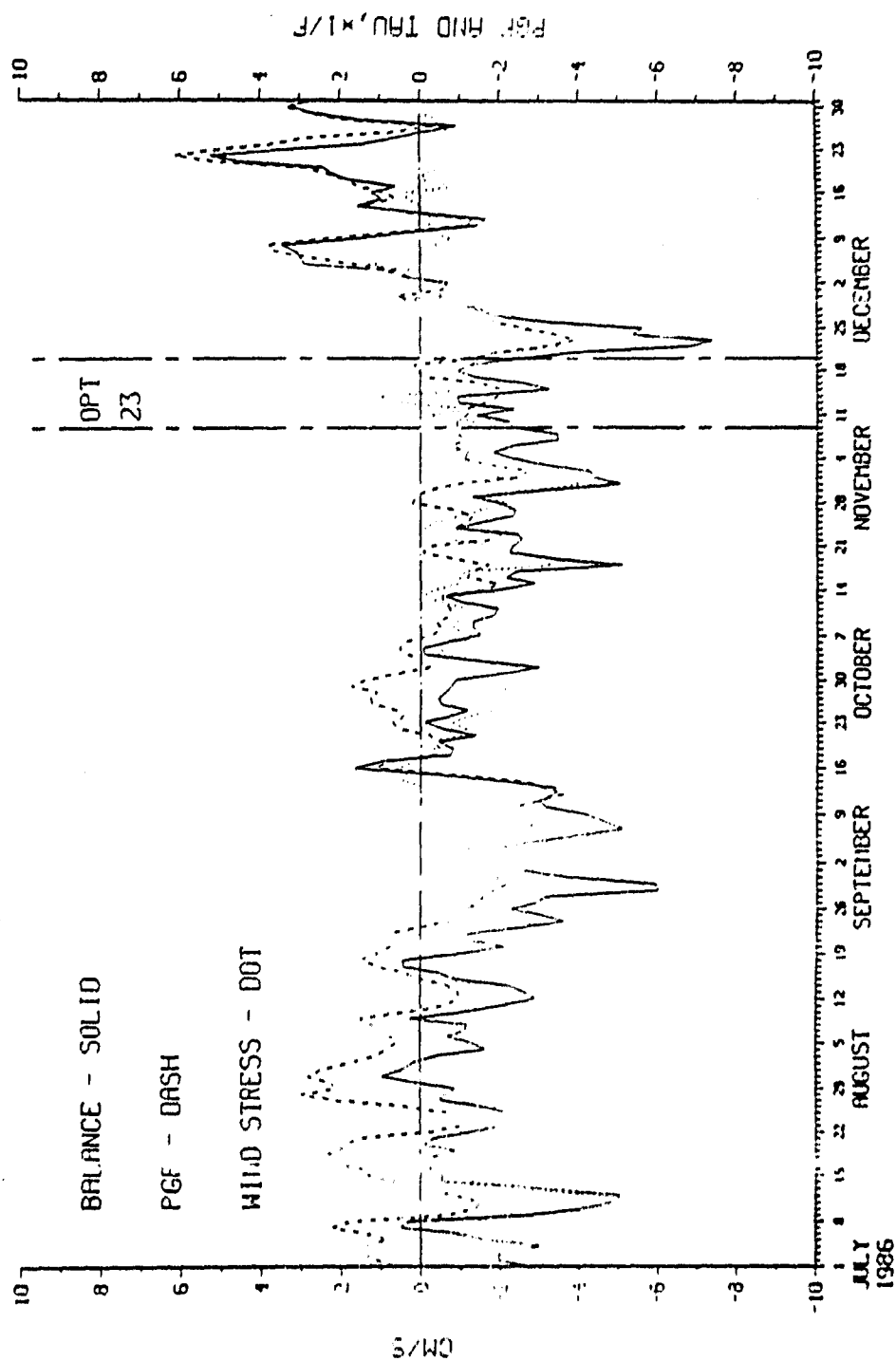


Figure 6.16 The balance of alongshore PGF and wind stress forces at Monterey Bay, from 1 July to 31 December 1986. In October and November, the both were southward. Near 2 December, the PGF became northward.

(2) before the start of the transition, the PGF and wind stress at Point Reyes were generally southward; in November, both forces were near zero, and

(3) generally, the PGF at Port San Luis was strongly northward and the wind stress was weakly southward.

Minima in the balances near the start of the transition, progressed poleward from Port San Luis on 25 November to Crescent City on 7 December (800 km in 12 days, ca. 70 km/day).

The onset of the Fall Transition of 1986 was easily distinguished at Monterey as the balance changed from an extreme minimum on 20 November (Julian date 86324, a day after OPTOMA 23 concluded), when both PGF and wind stress were southward, to a zero crossing on 3 December, and a maximum on 8 December, when PGF was strongly northward and the wind stress was near zero. Although the wind stress remained slightly southward for the rest of the year, the balance did not remain strongly positive; the PGF was southward for a few days on 13 December and 27 December. This reinforced the impression that the fall transition was not abrupt (as is the spring transition).

That the balance of forces was not expected to be zero; the wind stress and SL along the west coast are not always correlated. In an analysis of monthly sea level anomalies along the North and South American West Coast from 1950 to 1974 (which focused on El Nino events), there was high correlation between wind stress and SL north of San Francisco and low correlation south (however, the study only had two SL sites south of San Francisco in the Northern Hemisphere and wind stress in those areas may have been an overestimation due to the effects of the coastal mountain range), the anomaly variances for SL and SST were

minimum in the Northern Hemisphere between 35 and 38 N, and there was poleward propagation of events at a speed of 60 to 100 km/day (Enfield and Allen, 1980).

Identification of either the spring or fall transition, as discussed, may come from identification of the subsurface water mass, either with subsurface measurements using CTD's or inferences of water mass origin using current meters, by analysis of upwelled surface water, or from the cessation of winds favorable for upwelling (and the subsequent balance of forces). Sporadic winds favorable for upwelling may occur anytime during the year, but the upwelled water is similar to the surrounding surface waters only after the fall transition and before the spring transition. The time of the spring transition, because of the quick onset of strong upwelling favorable winds, is easier to determine than the time of the fall transition when the winds favorable for upwelling gradually and erratically cease.

SST was a good indicator of the transition. Upwelling along the Northern and Central California Coast during the summer generally results in lower SST and SL. Offshore measurements reflected the upwelling when acquired within the upwelled water mass (i.e., between the upwelling front and the shore or within a cool filament of entrained upwelled water). When upwelling occurred after the fall transition and before the spring transition, there was no drop in SST since the underlying water mass was the same temperature as the offshore surface water mass.

## VII. SUMMARY, CONCLUSIONS, AND RECOMMENDATIONS

### A. SUMMARY

#### 1. General

A mesoscale model selected for operational use must be thoroughly tested to understand its strengths and weaknesses and how it reacts to different data inputs. Such testing has high priority within the Navy, and it generally has not been done (Pittenger, 1989). The purpose of this case study was to determine the sensitivity of OA and QG models to the spatial resolution of input surface and subsurface data.

This case study is one of a limited number of evaluations of an end-to-end ocean mesoscale nowcast system. Although it is a study in the CCS, the overall Navy objective is to acquire a model which is 'transportable' and the geographic focus of Navy modeling efforts is being de-emphasized (Peloquin, 1988).

Elements of the study were ODPS (OA and QG models) and data collected during OPTOMA 23, a survey (principally airborne) planned and executed as a fundamental part of this study. Six aircraft flights, conducted by a research RP-3D aircraft between 9 and 19 November 1986, surveyed a 250 km by 550 km domain in the CCS off Central California and dropped a total of ca. 550 AXBT's. This was one of the first uses of the NAVOCEANO RP-3D in which local scientists had absolute control over planning the mission.

Data from many other sources were also incorporated: ship data, drifting and moored buoy data, satellite data (AVHRR and GEOSAT),

modeled fields (MBL winds), climatology (GDEM and CalCOFI), and coastal data. Some of these were unique (e.g., GEOSAT descending orbits were used for the first time in OPTOMA). Coincidentally, the survey period, 9 through 19 November 1986 (Julian Dates 86313 through 86323) included the beginning of the Fall Transition of 1986, the change in the CCS from southward surface flow and northward subsurface flow to northward flow throughout the water column over the continental shelf and slope as equatorward wind stress ceases.

The OPTOMA program has provided one of the richest data sets for ocean mesoscale analysis anywhere in the world; it surveyed the CCS off Central California over a period of four years and revisited the domain every few months. The surveys all made extensive use of AVHRR imagery in planning and to observe ocean conditions, in particular, the mesoscale activity, jets, and coastal upwelling. The data have led to better descriptions of mesoscale activity in the CCS, both during normal and anomalous (e.g., El Nino) periods, and the modeling of jets and mesoscale features. OPTOMA 23 was the last survey in this extensive series and it extended the modeling domain.

## 2. Synopsis

The California Current is a broad and shallow southward flowing eastern boundary current; the system exhibits year-round mesoscale activity such as complex meanders with wavelengths of 300 to 500 km, eddies with diameters of ca. 100 km, and jets with speeds of ca. 20 to 50 cm/s (or greater).

OA was used to map features, to test the sensitivity of mapping accuracy to data sampling and other parameters, and to provide inputs

for the QG model. SDH, SSH, SST (from AXBT and PRT-5 measurements), MCSST, MLD, T50, and Z08 were mapped for the initialization surveys (OPT23P1 and P2, day 86313, 9 November), the boundary condition update survey (OPT23P4, day 86321, 17 November), and the verification survey (OPT23P5 and P6, day 86323, 19 November). OA time series of SDH, SST, and Z08 from day 86313 through day 86323 were also generated from OA maps. OA observation experiments with different data sources and subsampling schemes were also conducted and intercomparisons were made: PRT-5 SST data (the most dense data set) were subsampled from full to one-eighth fields; GDEM climatology, analyzed for the first time in the CCS, was compared to observations; a 10-day forecast of SDH, SST, and Z08 was generated; and, the GEOSAT survey pattern was analyzed. Finally, for each QG model run, the OA provided dynamic heights for the upper three model levels (50, 150, and 400 m).

To calculate dynamic heights, a salinity profile was estimated for each AXBT (or XBT) from a T-S relationship, a reliable technique in the CCS where the T-S relationship is "tight" in the main thermocline. Where possible, an observed T-S relationship was used. To the south of Monterey Bay, this came from a concurrent survey by the R/V POINT SUR (ca. 40 CTD's); to the north, historical data from OPTOMA 13 was used. Both of these T-S relationships were similar to the corresponding T-S relationship from CalCOFI data.

In general, during all of the OPTOMA surveys, there were many useful AVHRR images (Table 2). Most of the surveys were predicated upon the availability of good imagery to guide the ship or aircraft survey.



Whenever possible, visual and IR images were used side by side to help discern low level clouds. There were 12 useful images during OPTOMA 23. Eight pairs of AVHRR images were processed, manually, with OCEANTRAK.

This study included the first use of GEOSAT data from descending passes and, consequently, the first mesoscale OA mapping of SSH in the CCS. The raw GEOSAT data were processed in a colinear fashion, i.e., a long term mean was removed from each ERM orbit, and the tides were removed. No moisture correction was applied. The SSH data were then processed in a manner similar to SDH; autocorrelations were performed and the data were objectively analyzed.

The weather was generally benign, there were some cloud-free days (IR images were available), and winds favorable for coastal upwelling had ceased, except for short events. There was one frontal passage, on 14 and 15 November (in the middle of the survey), during which the light winds shifted to the north.

In the OPTOMA 23 domain, there were two anticyclones, one off Point Arena and one off Monterey, and two cyclonic features, both on the boundaries, one to the northeast and one to the southwest. The cyclonic features were quasi-stationary throughout the survey, while the northern anticyclone moved westward at 5 km/day and the southern anticyclone moved northwestward at roughly the same speed. The mesoscale features were not as tightly packed as during the summer; the maximum speed in the jet was ca. 20 cm/s. Although only part of an eddy cycle, the 10-day OA time series showed the evolution, persistence and stability of the features adequately. The features changed strength slightly, deepening or filling ca. 2 dyn cm over the survey period.

There were two cool filaments, narrow (ca. 30 km) and long (ca. 200 km) in IR images, one off Point Reyes and the other off Point Sur. The IR imagery also showed that the filaments were embedded in a wide, cool body of water. In the OA SST maps, they were spread over many grid cells and appeared to be 100 km wide. The cool filaments were persistent in the OA SST time series and moved through the domain westward at ca. 10 km/day. About 10% of the AXBT's had acoustically significant inversions, with strengths of at least 0.2 °C and widths of at least 5 m, between 50 and 200 m. These were clustered about the filaments and were deepest towards shore.

At the beginning of survey, the upwelling front was 25 to 75 km offshore; at the end, it was 10 to 40 km offshore and the cool filaments had lost their integrity. This was consistent with the weakening and cessation of winds favorable for upwelling (Table 7).

The activity surveyed during OPTOMA 23 was typical of that surveyed during other OPTOMA surveys in autumn. The SDH values (the lowest in the entire OPTOMA ensemble), range of values (20 dyn cm), and standard deviation were lower than summer values. SST averages were typical of autumn averages and SST did not correlate with SDH (0.06) nor fields at depth. (The OPTOMA ensemble mean correlation between SST and SDH was 0.65 with a standard deviation of 0.11.) SDH and Z08 were highly correlated (0.80), close to the OPTOMA ensemble mean, 0.83 (with a standard deviation of 0.17).

The OPTOMA 23 fields were qualitatively similar to those of the previous year, during OPTOMA 18, although the positions of the cyclonic features and anticyclonic features were reversed (i.e., during OPTOMA

18, the cyclones were nearshore). OPTOMA 23 fields were quite different from OPTOMA 22 fields, a summer 1986 survey during a period of relaxed equatorward winds.

The optimal QG model hindcast configuration was OPTOMA 23 stratification, full data fields in the upper three levels (extended to the lower three levels by EOF's), interpolated boundary conditions, no wind stress curl forcing, and no bottom topography. These hindcasts scored well over the ten day OPTOMA 23 period (pattern correlation of 0.92 and RMSN of 42%). T100 fields, extracted from the optimal configuration and derived from an empirical relationship between T100 and the vertical derivative of the stream function, were accurate.

The optimal hindcasts depicted the principal dynamic event in the domain, the movement of an anticyclonic feature (AC1) from the eastern boundary to the northwest at ca. 5 or 6 km/day, as was observed. A secondary event, the apparent movement of an anticyclone (AC2) from the southeastern boundary north, was not resolved by the QG model. Instead, the QG dynamics extended a persistent ridge southwest through the domain from the initialized state.

The QG hindcasts were most sensitive to initialization and boundary conditions. A decrease in data quantity was seen to directly impact hindcast skill; however, skill was still shown at a one-quarter subsampling (with pattern correlation greater than 0.60). With subsampled inputs, most nowcasts and hindcasts located the mesoscale features accurately, but RMSN varied greatly with data inputs. Persistence scores were good (0.78 and 88%, pattern correlation and RMSN, respectively) and climatology scores were poor (0.42 and 144%).

GEOSAT and Sofar simulation hindcasts showed skill in pattern correlation and improved overall with the addition of in situ data through boundary conditions.

The Fall Transition of 1986 started immediately after the OPTOMA 23 survey, near 25 November and was most apparent in a balance of PGF and wind stress forces at Monterey and in Granite Canyon SST. The transition influenced the coastal waters (coastal sea levels were lower and temperatures were higher) and the OPTOMA domain (temperatures were higher). By early November, persistent winds favorable for upwelling, characteristic of the summer, had ceased along most of the coast as the Aleutian Low deepened, although there were sporadic upwelling events throughout the rest of the year. During the first of these sporadic events, the upwelled water was cool; later in the month, the upwelled water was indistinguishable from surface water and SST along the coast started to rise, indicating that the transition had occurred.

This was the first look at the offshore mesoscale field during a fall transition (spring transitions have not been analyzed either with such a focus). From the beginning to the end of the survey (9 to 20 November), the southern half of the OPTOMA 23 domain warmed  $1.2^{\circ}\text{C}$  at the surface and  $0.3^{\circ}\text{C}$  at 50 m. This warming was also noted in the QG hindcasts. While the aircraft surveys did not continue through the transition, northward flow was indicated in satellite-derived surface velocity vectors, in the GEOSAT SSH field on 25 November (day 86329), in SDH OA 'forecasts', and in a QG model forecast. This was consistent with the conjectured presence of the Davidson (Inshore) Current.

## B. CONCLUSIONS

### 1. General

The CCS is representative of other eastern boundary currents and coastal upwelling regimes; hence an operational ability to nowcast the ocean mesoscale in the CCS implies an ability to nowcast elsewhere. In situ data requirements for an accurate OA or QG representation of the CCS were shown to be high.

### 2. Observations

The utility of an aircraft AXBT survey for a large domain in the CCS was demonstrated to be practical. The inherent weaknesses of aircraft surveys to describe the mesoscale fields and to provide inputs to ODPS (e.g., grid spacing which is about the Rossby radius of deformation, shallow AXBT's whose profiles must be extrapolated to depth, the lack of salinity measurements, and data gaps) are overcome by prudent selection of methods and the use of other data sources.

The use of historical and observed T-S relationships to generate salinity profiles from temperature profiles was appropriate; extreme cases differed uniformly across the domain by less than 3 dyn cm. The extension of shallow data, from 300 to 450 m, produced an average difference in SDH of 16.7 dyn cm, between the reference levels of 300 and 450 m. (This compared to 19.0 dyn cm for the OPTOMA ensemble and for GDEM climatological data).

Although the range of values and means were accurate in the CCS for the month of November, GDEM climatology, at 30' resolution, was, of course, of limited value in describing mesoscale activity. (GDEM provides a monthly climatology which presumably averages out mesoscale

variability.) However, OA fields from GDEM data reproduced the large scale features of flow in the CCS, i.e., the California Current and the California Undercurrent (Table 5), and the vertical profile of the Brunt-Vaisala frequency obtained from GDEM was good enough for use in the QG model. GDEM also provided reasonable T-S and T- $\psi$  relationships for calculations of dynamic topography and T100, respectively.

November 1986 was a good period for observing the CCS with AVHRR imagery, as suggested by Fiedler et al. (1985). A single, enhanced IR image, although rich with small scale detail such as cool filaments and the coastal upwelling front, could not be used to pinpoint the location of mesoscale features in the CCS. Flickering between pairs of images, or an analysis of the satellite-derived surface vector field did highlight mesoscale features.

The satellite surface vector analysis produced vectors which were repeatable and consistent over 6-to-48 hours (compared with the 20 to 24 hour time difference used previously in the CCS by Svejksky, 1988). There was a bias away from low speeds due to the technique; the lowest detectable speed was estimated to be 2-to-3 cm/s. The speeds from satellite surface vector analysis averaged 17-to-28 cm/s, which was higher than the average geostrophic speeds from SDH. This was expected since the resolution of the satellite image was higher than the resolution of the OPTOMA AXBT grid. A correction for Ekman drift, about 3-to-4 cm/s, improved the comparison.

MCSST fields compared well with SST fields on cloud-free days; e.g., RMSE 0.7 °C and a pattern correlation of 0.9, with the MCSST colder than SST. These values agree with the performance figure

predicted by Minnett (1986). However, on partially cloudy days, even with cloud screening, MCSST and SST did not compare well; e.g., RMSE increased to as high as 1.4 °C and the pattern correlation dropped to as low as 0.22. These inferior results indicated contamination of the retrieved temperature by sub-pixel size clouds or low stratus clouds which were not screened. An automated MCSST system in the CCS during the fall could include a first guess field, but it may still require manual quality control, using visual and IR images side by side, to properly distinguish low level stratus and fog from the sea surface.

GEOSAT altimetry was a useful data source for analysis of the mesoscale field in the CCS. The GEOSAT ascending orbits were most reliable and had few data gaps while the descending orbits suffered from data drop-off (i.e., the altimeter was off-line as the satellite passed overhead from land to sea). However, the descending orbits were crucial in mapping the mesoscale field; simulations of data subsampling using GEOSAT suborbital tracks showed that the accuracy of the GEOSAT altimeter in reproducing a mesoscale field, as reflected in pattern correlation, increased significantly as the number of available subtracks increased, from 0.73 with three subtracks to 0.97 with seven subtracks (Table 10). Simulations also indicated that the absence of a moisture correction to the altimetric measurements had no apparent impact upon the accuracy of the SSH fields during OPTOMA 23. With these results, it was apparent that the ERM 17-day repeat orbit survey pattern was adequate for a description of mesoscale ocean variability in the CCS as long as data were available from all orbits.

The PRT-5 provided high resolution, stable, and continuous SST measurements over a narrow swath (Appendix B). There was one exact repeat track which reproduced SST measurements within 0.1 °C of the previous track, and the SST OA maps from PRT-5 data were highly correlated with the SST OA maps from AXBT data, but ca. 0.7 °C cooler, with a standard deviation of 0.5 °C (similar to MCSST from IR imagery). The PRT-5 measured SST gradients as high as 0.5 °C/km (about twice as high as IR imagery and many times higher than OA maps indicated), and it indicated surface cooling of ca. 1.0 °C between 9 and 19 November.

The drifter was of little value in analyzing the mesoscale fields, principally because it was deployed late in the survey in the jet off Point Sur, at the southern boundary of the domain. It was advected 40 cm/s to the west until it was ca. 250 km offshore (at the seaward extent of the Point Sur cool filament) when it turned and progressed southward at 80 cm/s. This speed was greater than expected (an order of magnitude greater than the Ekman drift) and the southward movement may have been associated with the loss of the drogue. Overall, the drifter speeds were about twice as high as the maximum geostrophic speeds; the latter may have been underestimated due to coarse grid spacing or a reference level which was too shallow (the drifter speeds were somewhat higher than satellite surface vectors).

SST did not correlate with any field at depth during OPTOMA 23. This may be due to the broad areas of warm water offshore and cool water inshore which were over anticyclonic and cyclonic features alike and the numerous inversions near the filaments. SDH and Z08 did correlate well; Z08 was indicative of the mean thermocline.



### 3. Modeling

Even though there were gaps in the observations (due to AXBT failures), the Gandin OA technique worked well for all fields (SDH, SSH, SST, MCSST, MLD, T50, Z08) and produced gridded maps with low error estimates (e.g., typically 10% and no greater than 30%). When data were dense (i.e., observations spaced 20 to 30 km), the OA fields proved to be robust and insensitive to variations in model parameters and technique. Also, since the autocorrelation scales and noise estimates at zero lag were roughly similar for all fields, and when the data were dense, a single zero-crossing and error estimate (ca. 100 km and 0.95, respectively) could be used for all fields with minimal impact. An alternative OA technique, inverse distance, provided maps which were virtually identical to those from the Gandin method, although it did not provide error estimates. OA time series of SDH, SST, and Z08 were consistent with observations. These used a 5 km/day westward phase velocity, the standard phase propagation used for all fields during OPTOMA 23, for maps between the surveys.

For some fields, the OA showed that some skill as a "forecasting" scheme over persistence and climatology. An OA 10-day forecast experiment qualitatively reproduced estimates of the SDH field, but only good estimates of the Z08 field and poor estimates of the SST field. Quantitatively, the SDH and Z08 forecasts were slightly better than persistence and much better than climatology, but SST climatology was better than either the forecast or persistence (Table 6). The same experimental technique was used to produce a SDH field on day 86329 from data observed on day 86323. This field was very similar to that observed

in GEOSAT data, SSH, on day 86329 and verified the presence of northward flow near the coast.

The OA acted as a low-pass filter; the technique spread data over too large an area (the radius of influence), smoothed small scale features, decreased gradients, lowered variance, and persisted features which had dissipated. For example, the OA MCSST fields did not reproduce the smaller mesoscale eddies (ca. 10 km in diameter), the sharp gradients, or the narrow width of the cool filaments as they were observed in IR imagery. The imagery showed the breakup of the filament as upwelling ceased; the OA persisted the filament throughout the survey.

Also, the OA required a large amount of data to provide maps which had skill over persistence and climatology. PRT-5 SST data, the densest data set of the OPTOMA 23 survey, were subsampled and reduced from full fields to one-eighth fields by random selection, alternate selection (selection of every other point), and by "smart pick". Both Gandin and Inverse OA techniques were used for comparison. At one extreme, the one-half fields correlated higher than 0.80 with an RMS of ca. 1.0 °C; at the other extreme, the one-eighth fields did not correlate and had high errors, 2.0 to 3.0 °C. The "smart pick" selections did the best, but with little appreciable difference over the other two methods.

In the OPTOMA 23 domain, the lowest number of observations needed to demonstrate skill (i.e., correlation of 0.60 or higher) was ca. 40 (the one-quarter subsampled field); on a rectangular grid covering the domain, these would need to be spaced 50 km or less. OA maps of

mesoscale features during OPTOMA 23 are fairly insensitive to the spatial sampling scheme and a feature-oriented scheme is slightly better than a regular spaced grid (these results are consistent with Rienecker et al., 1987, and Batteen et al., 1988a).

The QG model was capable of producing accurate nowcasts, ten-day hindcasts, and in one case, an accurate forecast (with persisted boundary conditions) of the SSH field. The advantages of the QG model were: it produced accurate results for medium range forecasts (i.e., three to five days) with good initial conditions, it could be initialized with various data types, accurate temperatures were extracted from it (using the vertical derivative method), and it could be run quickly and cheaply (allowing numerous sensitivity analyses). The disadvantages were that it took careful fine-tuning and manual intervention to produce the best forecast (prohibiting a "stand alone" system), temperature could not be extracted directly, and the results were very dependent upon data density.

The QG model was resource intensive and sensitive to boundary conditions. Initialization with full OA fields from all three survey dates (days 86313, 86321, and 86323) produced accurate hindcasts with both persisted and forecast boundary conditions. The westward advection of the anticyclonic features and the stationary cyclonic features (fixed in position by the boundary conditions) were accurately hindcast. Wind forcing was of little impact; FNOC MBL winds on a 2.5 degree grid may be too coarse to be effective in forcing mesoscale ocean models, and their curl may be a serious underestimate. Except for the continental slope in

the northeast corner of the domain where the bottom shoaled, the inclusion of bottom topography had no effect upon the model SSH.

With relative comparisons between climatology, persistence, model output, and verification (observed) fields, quantitative measures (i.e., pattern correlation and RMSN) gave a good evaluation of model accuracy. A qualitative comparison, with historical or climatological fields, also had merit in giving a general sense of how well a model represented the mesoscale field and would be particularly useful in identifying anomalous ocean conditions (e.g., El Nino).

#### 4. Fall Transition

The Fall Transition of 1986 started about a week after the end of the OPTOMA 23 survey, around 25 November. The transition influenced the coastal waters and the OPTOMA domain. The transition was expected after the cessation of winds favorable for upwelling, but in November and December, there was no abrupt cessation of these winds. The transition was identified through an analysis of many data records: wind (offshore and MBL fields), temperature (offshore and coastal), and coastal SL. A change in the balance of forces, between alongshore pressure gradient and wind stress, at Monterey indicated the start of the transition most clearly. In addition, AVHRR imagery showed nearshore northward flow as did GEOSAT SSH OA fields on 25 November, when there was no in situ data. A warming trend in the mesoscale field, hundreds of kilometers offshore, suggested a link between the coastal transition and the mesoscale field.

Although the boundary conditions may have been inadequate, the QG model did confirm two important changes associated with the transition,

the northward flow throughout the eastern half of the OPTOMA domain, seen in the SDH and SSH OA fields, and the warming trend. SST, specifically from NDBC buoys which were ca. 30 km offshore and within the coastal upwelling zone or near filaments, was not a good indicator of the transition because the temperatures measured at these buoys was relatively constant for some time after its onset.

Unlike conditions described by Breaker and Mooers (1986), there was inconclusive evidence for a wave-like disturbance propagating along the coast. Instead, the coastal waters responded to rapidly moving wind events, similar to the spring conditions described by Huyer et al. (1979). During the upwelling events, the northern and central coast SST's reacted simultaneously; during the warming transition event, there was apparent northward propagation along the southern part of the coast, suggesting that two or more regimes may exist.

## C. RECOMMENDATIONS

### 1. General

With focus on the operational use of a dynamical model, the importance of a good initial estimate of the state of the ocean cannot be over emphasized. Some poor initializations may be improved by accurate boundary condition updates; however, a priori knowledge of the quality of initialization is unavailable in a real-time operational run. Emphasis in modeling should be on providing the best possible nowcast from available data, knowledge of the statistics of mesoscale fields, and understanding the dynamics influencing a domain.

This modeling effort, involving data processing, OA for initialization and boundary condition updating, and the QG model, requires dense in situ observations (e.g., 40 AXBT's every two weeks), full satellite coverage (e.g., cloud-free AVHRR images and GEOSAT orbits with no data gaps), and intensive manual interaction to produce hindcasts with skill (i.e., a pattern correlation of at least 0.60). If similar systems are expected to be used correctly and accurately, then they must be utilized at large "centers" (e.g., FNOC and NAVOCEANO) where human expertise and data resources, unavailable elsewhere, can be pooled and tapped.

Model evaluation, in the research or operational sense, requires access to research quality data, quasi-operational data streams, climatology, gridding (interpolating and extrapolating) routines, and statistical routines. Acquiring data and processing it for model evaluation is a time-consuming and expensive process; for a single researcher, the process is difficult. Community-wide acceptance of procedures and standards of performance and an objective facility providing access to research-quality data bases and evaluation software are needed.

With the predominant Navy interest on the effects of mesoscale activity upon acoustic propagation, all mesoscale models should be evaluated on their impact upon acoustic propagation loss profiles and their ability to couple with an acoustic model, such as the Limited Finite Difference Parabolic Equations (LFDPE) model. The limited number of vertical levels in the QG model cannot represent all of the areas

critical to an accurate acoustic propagation forecast: SST, the mixed layer depth, the shallow sound channels, and the deep sound channel axis.

## 2. Observations

This survey measured the mesoscale field in the CCS over a ten-day period during a period of weak mesoscale activity. This was an inadequate duration and inappropriate season to observe substantial temporal changes in the mesoscale field (note: it had been originally scheduled for a month). A month-long survey, perhaps in the summer, would capture much of the life cycle of a mesoscale feature. With adequate planning, such a survey could be completed with no increase of in situ resources; the aircraft would be scheduled to do the initialization survey, a boundary condition update flight one-to-two weeks later, and a verification survey one-to-two weeks after that. Additional IR images and GEOSAT orbits would be processed at minimal expense. This would provide a more comprehensive assessment of the ODPS.

To better observe a fall, or spring, transition with in situ data, an array of drifters should be deployed nearshore. Since the drifters advect offshore rapidly, deployment would have to be quick and timed carefully from coastal SL and SST indications.

The AVHRR IR, PRT-5 SST, and GEOSAT altimetry processing or analyses from OPTOMA 23 should be expanded to:

- (1) Provide a time series of SST and satellite (AVHRR) surface vectors in the CCS which could provide insight into the seasonal transitions, and other phenomena,
- (2) Run the automated satellite surface vector technique on the same images used manually and compare results,

- (3) Generate a dynamic height field from the satellite surface vectors for comparison with in situ fields and altimetric SSH for possible use as an initialization field,
- (4) Investigate the dynamic processes involved with the formation of inversions to determine if they are present in conjunction with identifiable surface features,
- (5) Follow the track of the drifting buoy south of the OPTOMA 23 domain through December 1986 and compare buoy velocities and temperatures with satellite surface vectors and MCSST, and
- (6) Process another GEOSAT ascending orbit, preferably to the west, and incorporate it into OA SSH fields.

### 3. Modeling

The present OA used in ODPS is a rudimentary data assimilation scheme which does not provide a full 4-D assimilation capability. The relative merits of an improved scheme can be evaluated by reworking OPTOMA data and comparing results. The OA can be improved in a number of ways:

- (1) Data which influence a gridpoint can be filtered to ensure that they come from similar water masses (thus eliminating "smearing" across fronts),
- (2) The selection of phase speeds to provide advection of observations can be improved by having differing phase speeds at various gridpoints to account for differential advection, and
- (3) A 3-D OA could account for vertical tilt, incorporate stability constraints, and simplify the mapping of fields at different levels for entry into the QG model (i.e., a single OA model run instead of one run for each level and a merging routine, as is presently done).

The physics of the dynamic model in ODPS could be improved by replacing the QG model with a primitive equation (PE) model, and the PE



model nowcasts/hindcasts could be compared with existing QG nowcasts/hindcasts. Until then, the QG model may be improved by:

- (1) Providing wind stress at all gridpoints (investigate the impact of differential wind stress curl forcing),
- (2) Developing feature models for CCS, and
- (3) more fully investigating the temperature extraction process (specifically adding the temperature perturbations related to the vertical derivative of the stream function to the mean temperature profile from climatology).

## APPENDIX A: LITERATURE REVIEW ON SATELLITE REMOTELY SENSED DATA

Cloud cover presents the most difficult problem for viewing the sea surface off the West Coast. Fiedler et al. (1985) determined that between 30 and 38 N the most favorable conditions for remote sensing of the CCS exist from October through April and that low stratus interferes otherwise. However, Kelly (1983) and Rienecker et al. (1985) have had limited success at other times of the year (e.g., summer).

The masking of the sea surface by cloud cover has biased the estimated oceanic front location to the cloud-free areas. Additionally, Legeckis (1978) noted that it was difficult to distinguish between low clouds and upwelled water in IR images due to the similarity of their temperatures. Viewing both visible and IR channels eliminates areas of confusion.

Although the AVHRR does not view through clouds, its high resolution allows use in partly cloudy areas although sub-grid scale clouds will always contaminate the retrieved temperatures. Many algorithms using threshold tests, uniformity of temperature tests and comparison of two channels have been developed to detect cloudiness (Kelly, 1985); still, most investigators use composites of partially clear IR images to construct an image "averaged" over a few days (e.g., Stramma et al., 1986).

Although the measurements are done in an atmospheric window, atmospheric absorption and emission are not negligible. The net effect of the atmosphere is to make the retrieved SST lower than the actual

SST. The relevant absorbing and emitting constituents are carbon dioxide, nitrogen and water vapor. The first two are well-mixed gases with negligible effects. Water vapor is not well mixed and the vertical distribution of temperature and moisture are usually not known.

Atmospheric transmissivity can vary from about 90% for dry atmospheres with 1.0 cm precipitable water to 30% for moist atmospheres with 5.5 cm precipitable water (Deschamps and Phulpin, 1980). The effects of atmospheric state, nadir angle, cloud height, and cloud amount upon the accuracy of retrieved SST were theoretically estimated to account for a 2.0° C error (Maul and Sidran, 1973). Algorithms have since improved and the rms difference between corrected SST from AVHRR and in situ measurements is about 0.7° C (Minnett, 1986).

The remote sensing of SST measures the skin temperature of the ocean surface. The skin temperature is usually different from the temperature measured at 1 m (bucket or shallow ports) by thermometers. Bulk measurement accuracies are estimated to be about 0.2 to 1.0° C (Tabata, 1982) and differences between the skin temperature sensed by the satellite and the bulk temperature is between 0.1 and 0.5° C, with the skin temperature usually less than the bulk temperature due to upward heat flux (Paulson and Simpson, 1981). Additionally, spatial variability is greater in the satellite SST field than in the in situ 1 m temperature field due to diurnal heating and cooling, air-sea interactions, and "patchiness" within a satellite footprint (fronts, differential heating, mixing and varying surface emissivity).

SST derived from AVHRR data have been compared with bucket, ship injection, drifting and fixed buoys and XBT measurements. In the North

Pacific, there was a bias of  $-0.2^{\circ}$  C with a standard deviation ( $\sigma$ ) of  $1.0^{\circ}$  C between AVHRR and XBT's using a point comparison with a 12 hour and 100 km window (Njoku, 1985). A rms difference of  $0.6^{\circ}$  C has been calculated between AVHRR and drifting buoys (Strong and McClain, 1984).

Navigation error is inherent to the problem of comparing accuracies. The process of earth-locating an image and correcting for geometric distortion has an error of two to five km (Kelly, 1983). The navigation systems of the ships, aircraft, and buoys also have errors (LORAN-C fixes are accurate to 0.1 km). As an example of the cumulative effect of these errors, the Ships of Opportunity Program (SOOP) verified frontal locations derived by satellite only to within 10 km for months with well-defined fronts (Stage and Weller, 1985).

Algorithms using two or more channels provide a relatively accurate correction for each pixel regardless of the scale of the moisture field in the atmosphere. These algorithms assume that the surface is a uniform, perfect black body. Three channel algorithms minimize the non-linear effects due to the first order Taylor series expansion and variable absorption coefficients, but they utilize the near IR channel. While this channel is least affected by water vapor, it has been a noisy channel due to sensor problems and sunglint. In practice then, the three channel algorithms are used at night while the two channel algorithms are used during the day.

The coefficients for the algorithms may be calculated from knowing the specific absorption coefficient of water vapor for the different channels, but in practice, these coefficients are determined through regression analysis. Often, these analyses are performed over large

areas and under a wide variety of conditions in order to provide a meaningful number of comparisons. The moisture correction, skin-bulk temperature differences, and other factors are included in the analysis.

Other factors add noise and uncertainty to what is measured by the AVHRR. Robinson et al. (1983) measured a diurnal thermocline in the top meter of the water column with a  $\Delta$ SST as much as 1.5° C. Deschamps and Frouin (1984) fit the diurnal change in SST to the inverse of the wind speed. They noted a mean change of 1.0° C and the highest, 5.0° C, was under no-wind conditions. They recommended restricting the use of satellite SST measurements to night or when the wind was greater than 5 m/s to avoid biases from diurnal changes. In a study of surface cooling by Atlantic hurricanes, Stramma et al. (1986) note diurnal biases in areas of high pressure (light winds).

The AVHRR sensor field of view acts much like a low pass filter and for a 1 km square footprint, SST variations are low (less than 0.1° C) except near fronts, and with larger footprints (25 km square), the variations are 1.0 to 3.0° C. Surface and bulk temperature differences and instrument noise make a point-to-point comparison of less than 0.5° C difference unlikely even when the satellite image is centered upon the in situ device (Gasparovic, 1983). Also, due to the spatial averaging, noise introduced by factors such as the thinning of the surface viscous layer due to surface gravity waves is negligible (Simpson and Paulson, 1980).

The interaction of a radar pulse with the sea surface is well understood. Simply put, the returning wave shape increases linearly to a plateau, then decreases, due to a finite antenna beamwidth and the lower

number of sea surface elements having the proper geometry for specular reflection. Each return pulse is divided into range gates and the time associated with the center of the returning rise area determines the range to the ocean surface. The shape of the return is analyzed to determine other ocean properties: the stretching of the pulse by ocean waves has been modeled with the probability density functions of various significant wave heights, and the backscatter has been modeled with the mean square slope of the sea surface and wind (Barrick and Swift, 1980).

An accurate measurement of the height of the satellite above the instantaneous ocean surface,  $H_a$ , is obtained only after numerous corrections are applied to the raw signal. "Housekeeping" eliminates much data. Due to the wobble of the satellite as it passes over the poles, data from many descending passes in the northern hemisphere are lost until the satellite stabilizes. Also, the sensor takes about six seconds to recover after passing from land to water (ca. 42 km of track), although some tracks have lost data for hundreds of kilometers.

Atmospheric corrections are well-modeled. An ionospheric correction of 2 to 20 cm is required to account for free electrons in the ionosphere which change the index of refraction for EM propagation (Lorell, 1982).

Atmospheric moisture algorithms are more controversial: a wet troposphere correction of 10 to 50 cm can be provided from Fleet Numerical Oceanography Center (FNOC) fields, or measured by the Scanning Multi-spectral Microwave Radiometer (SMMR), an experimental sensor on

NIMBUS-7. Most corrections have used the FNOC fields which have a 5.73 cm rms error compared to radiosonde data and are on a coarse grid of 2.5 degrees; the SMMR fields have a 2.79 cm rms error and higher spatial resolution of ca. 30 km (Tapley, 1982). In some parts of the world, a weak oceanic signal can be masked by moisture in the atmosphere unless high resolution SSMR data are used (Hawkins, 1989). Many investigators use no moisture correction since the algorithms are uncertain (Sirkes, 1989).

The resulting signal,  $H_a$ , is a combination of various geophysical signals and instrument error (Figure A.1). The sea height,  $\eta$ , is the difference of two large numbers, the orbit height above the reference geoid,  $H_o$ , and  $H_a$ :

$$\eta = H_o - H_a - H_g + E \quad (\text{equation A.1}),$$

where  $\eta$  is the sea surface height (SSH),  $H_o$  is the orbit height above the reference geoid,  $H_a$  is the range to the instantaneous ocean surface,  $H_g$  is the geoid, and  $E$  is instrument error.

The geoid is the dominant signal competing with SSH. An independent determination of the geoid by means other than altimetry would be ideal (e.g., a single track minus an accurate geoid). The alternative is to difference data from repeat orbits or cross-over tracks to remove the signal from time-independent sources. This not only removes the geoid and orbital errors, but also mean currents. Satellite orbit

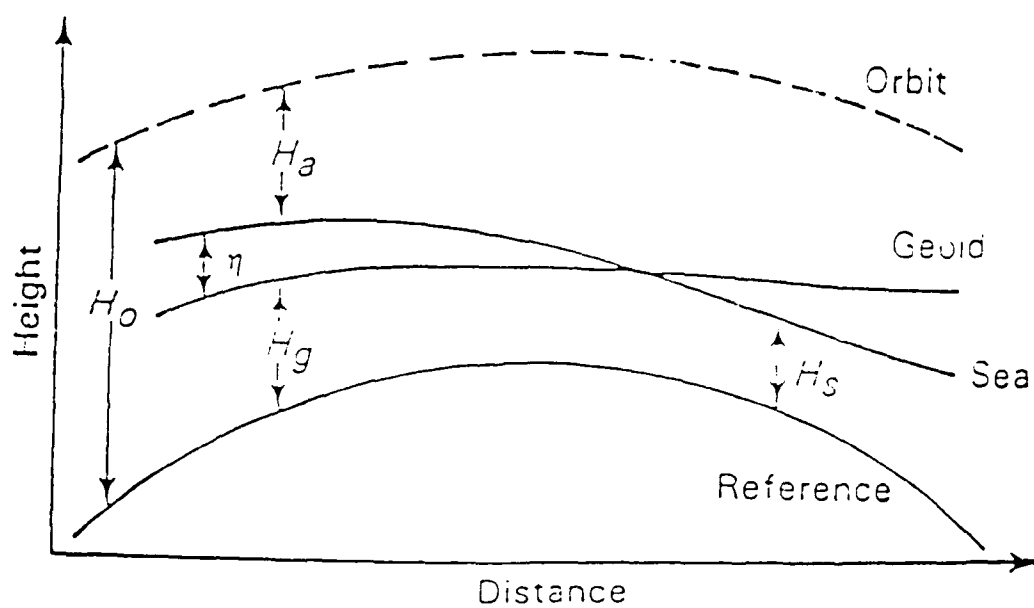


Figure A.1 A definition sketch for the altimetric measurement of sea height (Calman, 1987).



uncertainties exist due to incomplete modeling of the dynamic forces upon the satellite (e.g., gravity, atmospheric drag, and solar radiation pressure). The orbit height is obtained from orbit models or from a world-wide ground based tracking network which provides a best fit to an ellipse or an ephemeris. The rms instrument noise error for the GEOSAT altimeter is estimated to be 3 cm (Sailor and LeShack, 1987).

$\eta$  is further broken down into contributions from various oceanic components (Calman, 1987):

$$\eta = \eta_{\text{mean}} + \eta_{\text{meso}} + \eta_{\text{tide}} + \eta_{\text{wave}} + \eta_{\text{bar}} + \eta' \quad (\text{equation A.2}),$$

where  $\eta$  is the ocean surface,  $\eta_{\text{mean}}$  is due to mean currents,  $\eta_{\text{meso}}$  is due to mesoscale features,  $\eta_{\text{tide}}$  is due to tides,  $\eta_{\text{wave}}$  is due to the significant wave height,  $\eta_{\text{bar}}$  is the inverse barometer correction, and  $\eta'$  is due to other time-dependent contributions (e.g., wind).

Tides are modeled using the Schwiderski tidal model. Surface waves cause an EM bias that is not well-accounted for. Shorter waves are more predominant on the crests of larger waves than in the trough. This results in a more intense return from the trough thus biasing the measured range towards the trough. For this problem, a constant 2% correction is used. The inverse barometer effect is accounted for with a ratio of 1.005 mb to 1.0 cm sea height.

## APPENDIX B: PRT-5 DATA

The PRT-5 data provide another independent estimate of SST (the others are AXBT, AVHRR, and buoy measurements). The PRT-5 measures skin temperatures accurate to 0.1 °C in a swath approximately 10 m wide from an altitude of 1000 feet (Athey, 1986). A PRT-5 recorded skin SST continuously throughout each OPTOMA 23 flight except when the aircraft passed over or through low clouds, fog, or areas of precipitation (defined as "undercast") and when calibrations were made. Another PRT-5 scanned upward and recorded the presence of overcast. Calibrations were done about every 30 minutes by manually placing the instrument over a 13 °C water bath. The PRT-5 readings were then corrected by assuming a linear drift between calibrations. For the most part, corrections were about +1.0 °C. On one flight, the instrument was stable throughout with a constant correction of +1.3 °C and on two flights, corrections were as high as +2.5 °C.

Only "reliable" data were digitized (i.e., cloud free); these consisted of measurements colocated with AXBT drops and of measurements near features of interest (e.g., fronts) between AXBT drops. The PRT-5 record provided a continuous and annotated time line of events with time accurate to about 6 seconds (0.8 km of travel at 240 knots). The intermediate positions had to be calculated assuming a direct flight path and constant airspeed between AXBT drops. The routine used to position these intermediate points was tested on about 10 "known" points for each survey (i.e., known to within the accuracy of the onboard

# SST DERIVED FROM PRT-5

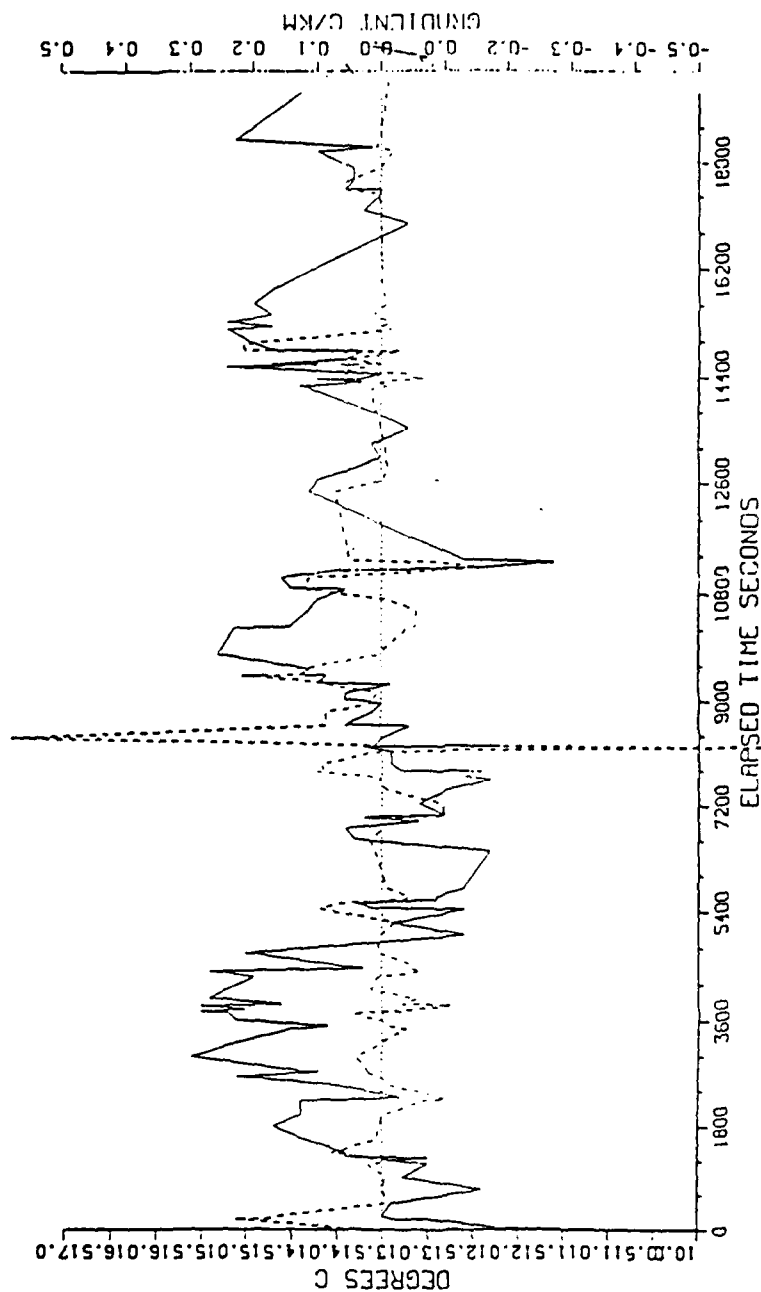


Figure B.1 PRT-5 (solid) and gradient (dash) versus elapsed time of flight for OPT 23P1 survey. This plot is similar to that from other surveys.

navigation system). For all flights, the rms error in plotting these points was 1.2 to 1.6 km.

Of interest are the rapid changes in SST as recorded by the PRT-5 and the large gradients encountered (Figure B.1). These gradients are as large as  $0.5^{\circ}\text{C}/\text{km}$ . All OPTOMA survey flights recorded similar PRT-5 measurements although there was cooling of the average PRT-5 SST of ca.  $1^{\circ}\text{C}$  from the first two flights to the last two flights. None of the SST gradients were correlated with changes in the air temperature or dew point at altitude suggesting that they were not caused by atmospheric phenomena.

The objectives of this survey did not include repeated sampling of the same track; however, in reseeded a critically-positioned failed buoy on day 86321, the aircraft repeated, within navigation limits, ca. 40 km of track (equating to ca. 5 minutes travel time) which included a frontal zone. The track was first flown at approximately 0000 GMT and repeated about one hour later. The records fit within  $0.1^{\circ}\text{C}$  over the entire 5 minute period except at the front. Although the relative temperature change across the front is the same for both transits, the gradient measured later is twice that of the earlier measurement ( $0.8^{\circ}\text{C}/\text{km}$  versus  $0.4^{\circ}\text{C}/\text{km}$ ). This may be caused by the aircraft crossing the front at a different angle.

Objective analyses of SST derived from the PRT-5 measurements were generated from measurements on the survey day only using the same grid and procedures described earlier with ensemble PRT-5 statistics (Figure B.2). These are qualitatively similar to the AXBT SST fields. Higher resolution PRT-5 objective analyses with grid spacing of 6 km have

finer scale structure than the coarse 20 km grid spacing set, but the major features in both are similar.

There were 327 intercomparisons of PRT-5 and AXBT SST (cloud free and reliable AXBT drops). This was 81% of the total possible. The difference, PRT-AXBT, for the entire ensemble ranged from -2.2 to 0.4 °C. The mean difference was - 0.7 °C with a  $\sigma$  of 0.5 °C. In individual data sets, the differences varied and there was cooling of the average PRT-5 SST from 13.0 to 11.8 °C throughout the period while the AXBT SST cooled from 14.0 to 13.7 °C (one-third the PRT change). Since the time of day was relatively constant survey-to-survey, it is assumed that the passage of the cold front on the 14th and 15th accounted for the skin surface cooling. OA difference fields were generated for days 86313, 86320, and 86323 (Figure B.3). These fields are inversely correlated with the mixed layer fields (correlations range from -0.95 to -0.89).



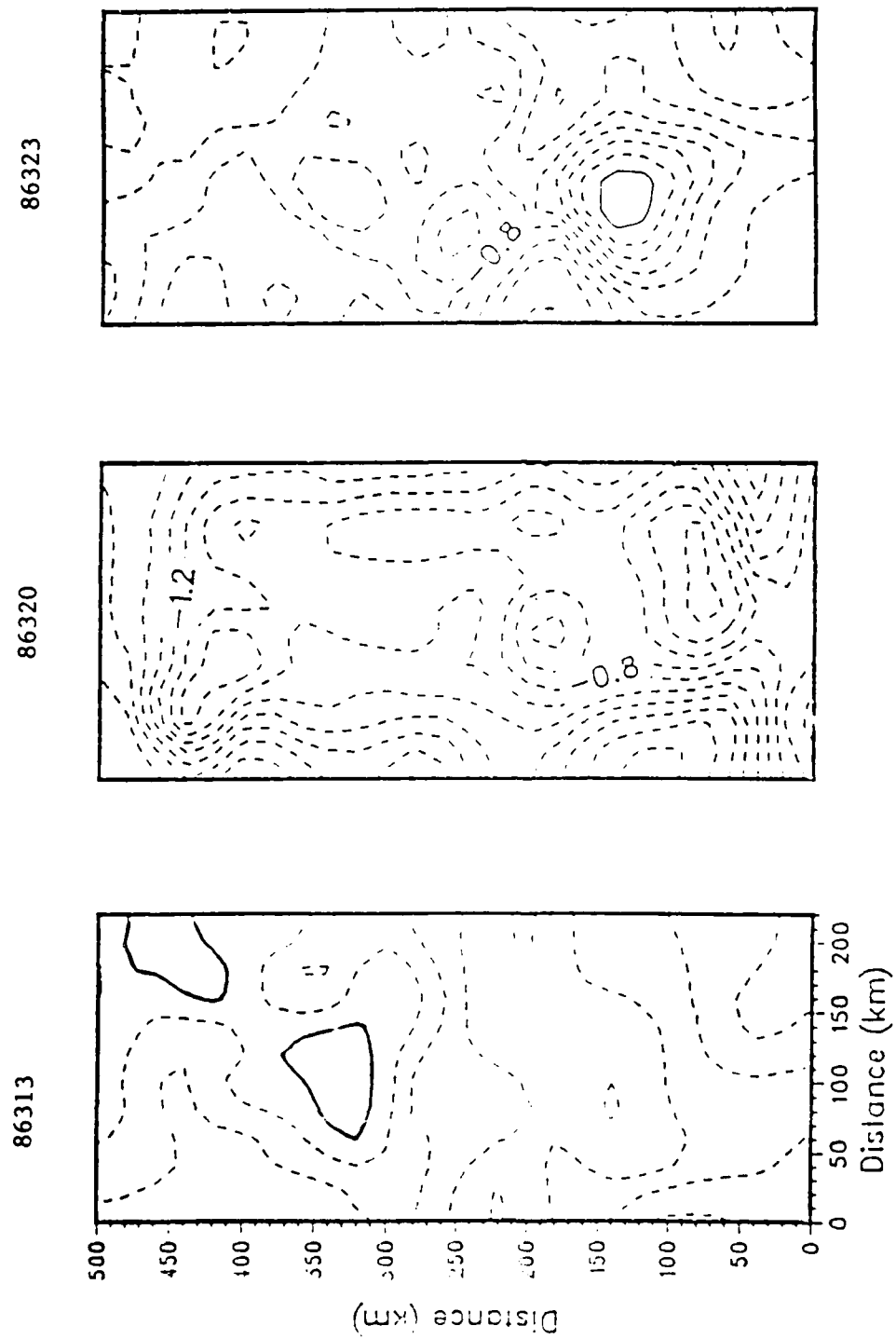


Fig. re B.3 OA of difference field (PRT-AXBT) 86313, 86320, and 86323.

## APPENDIX C: DRIFTING BUOY

A drifting buoy was deployed by R/V POINT SUR on 18 November 1986 (Julian Date 86322) 120 km due west of Monterey. The buoy was a standard Polar Research Laboratory hull and sensor package. It was equipped with a SST sensor which provided near instantaneous measurements, a 20 m wide windowshade drogue at 65 m, and an Argos satellite transmitter. The buoy was deployed in an offshore jet which was identified in preliminary objective analyses of SST and Z10; there were no plans for recovery.

A Local User's Terminal (LUT) was used to receive the satellite transmissions. Five satellite-derived fixes were received prior to deployment; these fixes were 1.2 to 9.2 km from the actual buoy position. The SST measurements were not given an *situ* test; the manufacturer's specification for temperature accuracy is 0.2° C.

SST and position information were transmitted and received by the LUT several times a day through NOAA 6 and 9 (Table 17). The buoy advected to the west at ca. 40 cm/s until 29 November when it turned south and accelerated to ca. 80 cm/s. It is possible that the drogue fell off at this time, and that the turn and increase in speed were due to surface winds or that the buoy left the influence of the cool filament and was caught up by the mean southward flow of the CCS.

The buoy positions from time of deployment to 1400 06 December 1986 were plotted along with SST and SDH objective analyses for 18 November (Figure C.1). The SST from the buoy agrees well with the synoptic shipboard and aircraft measurements. Qualitatively, there is some agreement between the path of the buoy and the expected influence of the



synoptic features identified on 18 November. The track starts in an apparent offshore jet and turns south under the influence of an anticyclone to the west. The track is not perfectly matched with the features in the analyses and many factors may account for the difference: the current affecting the buoy may be made up of ageostrophic components not reflected in this analysis, the OA fields are generated from data measured on the first day of drift only, the OA technique spreads features out (with grids of 20 km), and navigation error in both platforms (buoy and ship/aircraft) could be as large as 10 km.

TABLE 17. DRIFTING BUOY DATA

Point	Time	Date	Lat	Long	SST
A	0112	19 Nov	36.16	123.19	N/A
B	2208	19 Nov	36.13	123.27	N/A
C	2157	20 Nov	36.17	123.34	15.3
D	0162	21 Nov	36.17	123.43	14.9
E	0052	22 Nov	36.18	123.55	14.1
F	1141	22 Nov	36.17	124.03	14.0
G	0019	25 Nov	36.12	124.22	15.1
H	1141	26 Nov	36.13	124.29	14.8
I <sup>a</sup>	1609	27 Nov	36.14	124.38	14.5
J	0035	01 Dec	35.56	124.49	13.9
K	1407	02 Dec	35.21	124.47	15.0
L	0241	04 Dec	34.41	124.57	15.2
M	1411	06 Dec	34.04	124.50	15.7

Note a: The drifter left the domain of Figure C.1

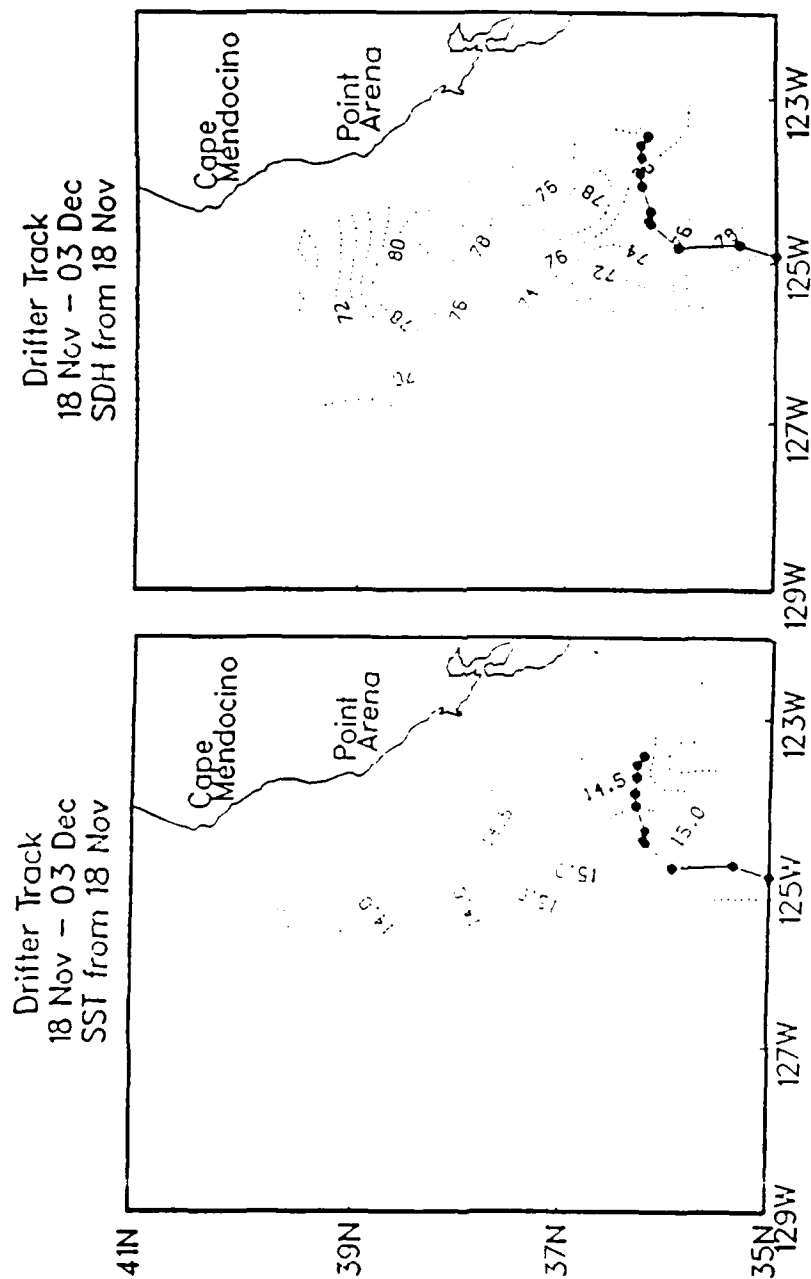


Figure C.1 Buoy track from 18 November to 6 December 1986 superimposed upon SST and SDH fields with central date of 18 November.

#### APPENDIX D: PRT-5 DATA SUBSAMPLING

An SST data set, derived from PRT-5 measurements on day 86313, was subsampled to quantify the effects of data density on OA model accuracy. (This set of data had more observations than any other during the OPTOMA 23 survey). The field was subsampled in three ways: first, by selecting alternate points, the data set was subsampled by factors of two (alternate); second, the fields were subsampled by a random selection process (random); and, third, the fields were subsampled by a "smart pick" process which used a priori knowledge of the field being analyzed (smart). For the latter, observations which were in the proximity of high gradient areas, or in maximum and minimum areas, were selectively retained. (The "smart pick" could have been influenced by climatology, persistence, or the subjective experience of an analyst and is related to the operational technique of "bogusing", i.e., the insertion of a feature into a field where there are no observations). The resulting data sets contained approximately 160 (full), 80 (half), 40 (quarter) and 20 (eighth) observations (Figure D.1). For comparison purposes, OA model parameters were kept constant, and both Gandin and inverse distance methods were used.

The Gandin OA, using the full data set, was the verification field. Qualitatively, two fields, the "eighth" inverse distance fields, alternate and random selection, were not similar to the other fields (Figures D.2 and D.3). The "full", "half", and "quarter" fields all reproduced the features in the verification field; the "smart" picks for

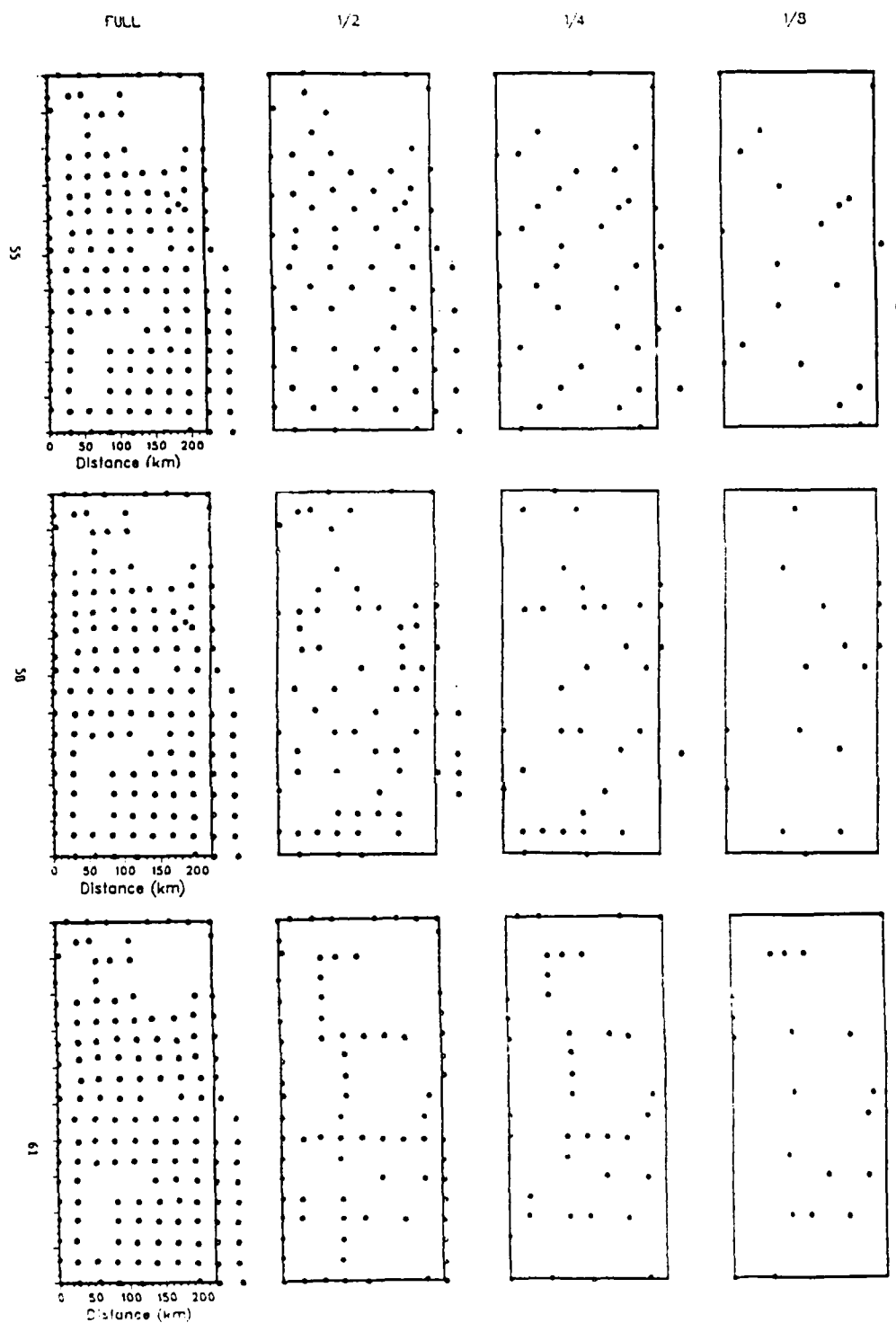


Figure D.1 PRT-5 data distribution using alternate (top), random (middle), and "smart pick" (bottom) methods of subsampling. The alternate method had more evenly distributed data; the "smart" method concentrated observations near features.

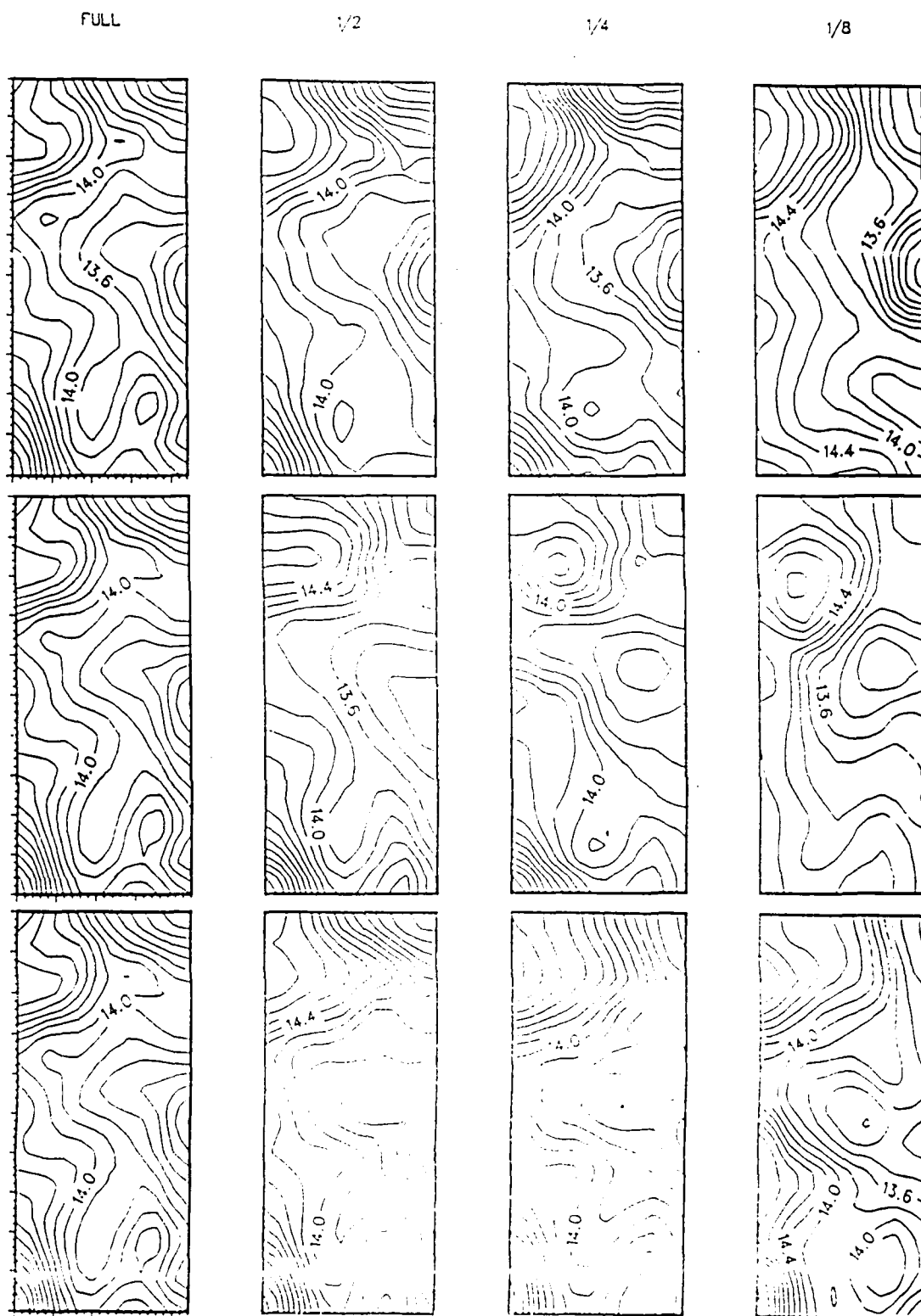


Figure D.2 OA (Gandin) PRT-5 fields. Alternate (top), random (middle), and smart (bottom) fields. Contour interval is 0.2 °C.

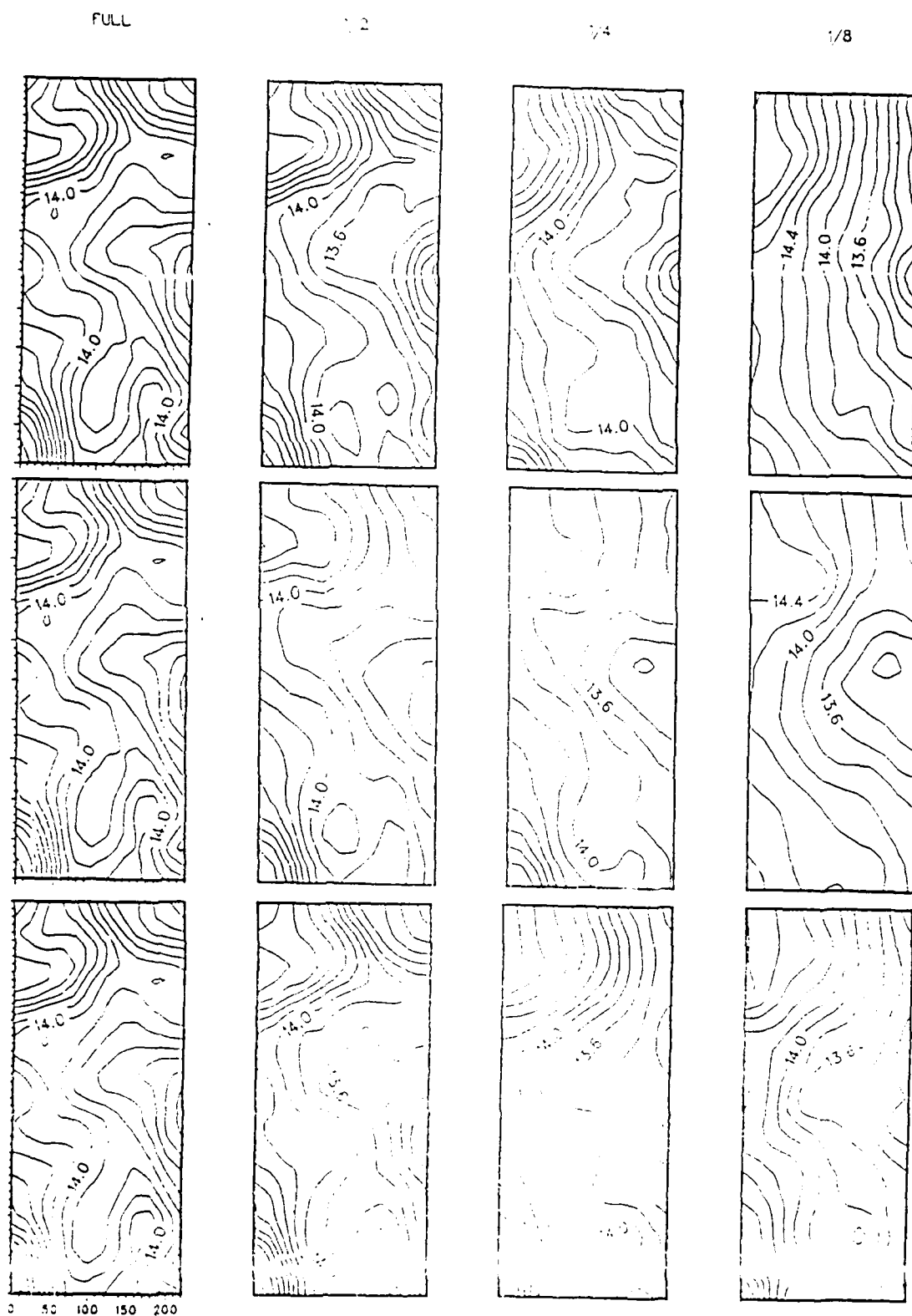


Figure D.3 OA (Inverse distance) PRT-5 fields. Alternate (top), random (middle), and smart (bottom) fields. Contour interval is 0.2 °C. No error estimate is available.

both the Gandin and inverse distance methods looked the best; the Gandin method looked better than the inverse distance method for all subsampled fields.

The OA error fields, generated by the Gandin method only, increased as the number of data points was reduced (Figure D.4). The average error was less than 5% for the full field; it increased to ca. 15% for the half-fields, 35% for the quarter-fields, and 45% for the eighth-fields. (The error for all fields was higher in the northeast, where an undercast prohibited measurements of the ocean surface). The error fields for the random data subsampling were higher than the error fields from the other subsamplings.

Quantitatively, all "half" fields, except the random selection, correlated well with the verification field (0.80 or higher). Generally, for each data density, the Gandin and inverse distance methods differed slightly. All "eighth" fields did not compare well with the verification field, but the best were the "smart" fields (Table 18).

With dense data fields, it appears that the selection of the OA method and the position of the observations are not crucial. With sparse data fields, the position of the observations and the choice of the OA method is more important; however, there are still large errors in the sparse fields.

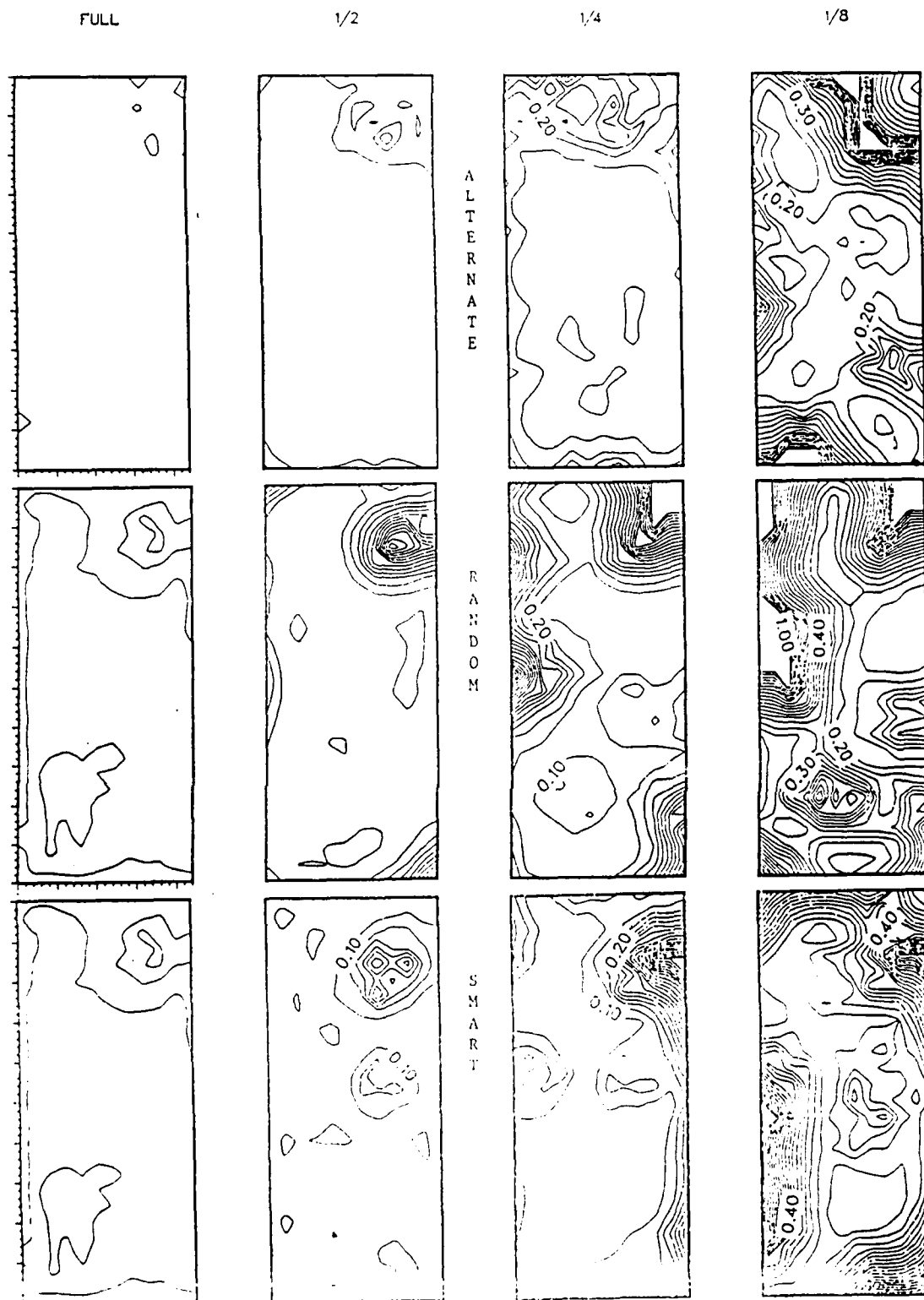


Figure D.4 OA (Gandin) error fields for PRT-5 data. Alternate (top), random (middle), and smart (bottom) fields. Contour interval is 5%.



TABLE 18. PRT-5 OA SUBSAMPLING COMPARISONS

## Gandin Method

Selection of Every Other Point (Alternate)

<u>OA Method</u>	<u>Data Set</u>	<u>MEAN</u>	<u><math>\sigma</math></u> <u>(°C)</u>	<u>CORR</u>	<u>MAE</u> <u>(°C)</u>	<u>RMS</u> <u>(°C)</u>
Gandin	full	13.9	0.8	1.00	0.0	0.0
Inv Dist	full	13.9	0.8	1.00	0.0	0.0
Gandin	1/2	13.7	0.8	0.84	0.6	1.0
Gandin	1/4	13.7	0.9	0.71	1.0	1.6
Gandin	1/8	13.9	0.9	0.51	1.7	2.7

Random Selection of Points (Random)

<u>OA Method</u>	<u>Data Set</u>	<u>MEAN</u>	<u><math>\sigma</math></u> <u>(°C)</u>	<u>CORR</u>	<u>MAE</u> <u>(°C)</u>	<u>RMS</u> <u>(°C)</u>
Gandin	full	13.9	0.8	1.00	0.0	0.0
Inv Dist	full	13.9	0.8	1.00	0.0	0.0
Gandin	1/2	14.0	0.8	0.79	0.8	1.3
Gandin	1/4	14.0	0.9	0.69	1.2	1.9
Gandin	1/8	13.8	0.9	0.47	1.8	3.1

"Smart Pick" (Smart)

<u>OA Method</u>	<u>Data Set</u>	<u>MEAN</u>	<u><math>\sigma</math></u> <u>(°C)</u>	<u>CORR</u>	<u>MAE</u> <u>(°C)</u>	<u>RMS</u> <u>(°C)</u>
Gandin	full	13.9	0.8	1.00	0.0	0.0
Inv Dist	full	13.9	0.8	1.00	0.0	0.0
Gandin	1/2	14.1	0.9	0.86	0.7	1.3
Gandin	1/4	13.8	0.9	0.73	0.9	1.6
Gandin	1/8	13.9	1.0	0.60	1.2	1.9

TABLE 18. (CONTINUED)

## Inverse Distance Method

Selection of Every Other Point (Alternate)

<u>OA</u> <u>Method</u>	<u>Data</u> <u>Set</u>	<u>MEAN</u>	<u><math>\sigma</math></u> <u>(°C)</u>	<u>CORR</u>	<u>MAE</u> <u>(°C)</u>	<u>RMS</u> <u>(°C)</u>
Gandin	full	13.9	0.8	1.00	0.0	0.0
Inv Dist	full	13.9	0.8	1.00	0.0	0.0
Inv Dist	1/2	13.7	0.8	0.80	0.7	1.2
Inv Dist	1/4	13.7	0.9	0.69	0.9	1.6
Inv Dist	1/8	13.9	0.9	0.20	1.4	2.3

Random Selection of Points (Random)

<u>OA</u> <u>Method</u>	<u>Data</u> <u>Set</u>	<u>MEAN</u>	<u><math>\sigma</math></u> <u>(°C)</u>	<u>CORR</u>	<u>MAE</u> <u>(°C)</u>	<u>RMS</u> <u>(°C)</u>
Gandin	full	13.9	0.8	1.00	0.0	0.0
Inv Dist	full	13.9	0.8	1.00	0.0	0.0
Inv Dist	1/2	14.0	0.8	0.72	0.8	1.4
Inv Dist	1/4	14.0	0.9	0.60	1.1	1.9
Inv Dist	1/8	14.0	0.9	0.37	1.5	2.7

"Smart Pick" (Smart)

<u>OA</u> <u>Method</u>	<u>Data</u> <u>Set</u>	<u>MEAN</u>	<u><math>\sigma</math></u> <u>(°C)</u>	<u>CORR</u>	<u>MAE</u> <u>(°C)</u>	<u>RMS</u> <u>(°C)</u>
Gandin	full	13.9	0.8	1.00	0.0	0.0
Inv Dist	full	13.9	0.8	1.00	0.0	0.0
Inv Dist	1/2	14.1	0.9	0.84	0.8	1.2
Inv Dist	1/4	13.8	0.9	0.71	1.2	2.1
Inv Dist	1/8	13.9	1.0	0.43	1.5	2.3

## APPENDIX E: SATELLITE IMAGES



Figure E.1 AVHRR IR image from NOAA-10, channel 4, of OPTOMA domain on Julian Day 86314 at 16:23 GMT.



Figure E.2 AVHRR IR image from NOAA-9, channel 4, of OPTOMA domain on Julian Day 86314 at 21:55 GMT. Land is masked white.



Figure E.3 AVHRR IR image from NOAA-9, channel 4, of OPTOMA domain on Julian Day 86315 at 12:03 GMT. Land is masked white.



Figure E.4 AVHRR IR image from NOAA-9, channel 4, of OPTOMA domain on Julian Day 86315 at 21:45 GMT.



Figure E.5 AVHRR IR image from NOAA-9, channel 4, of OPTOMA domain on Julian Day 86319 at 22:42 GMT.



Figure E.6 AVHRR IR image from NOAA-9, channel 4, of OPTOMA domain on Julian Day 86321 at 22:21 GMT.



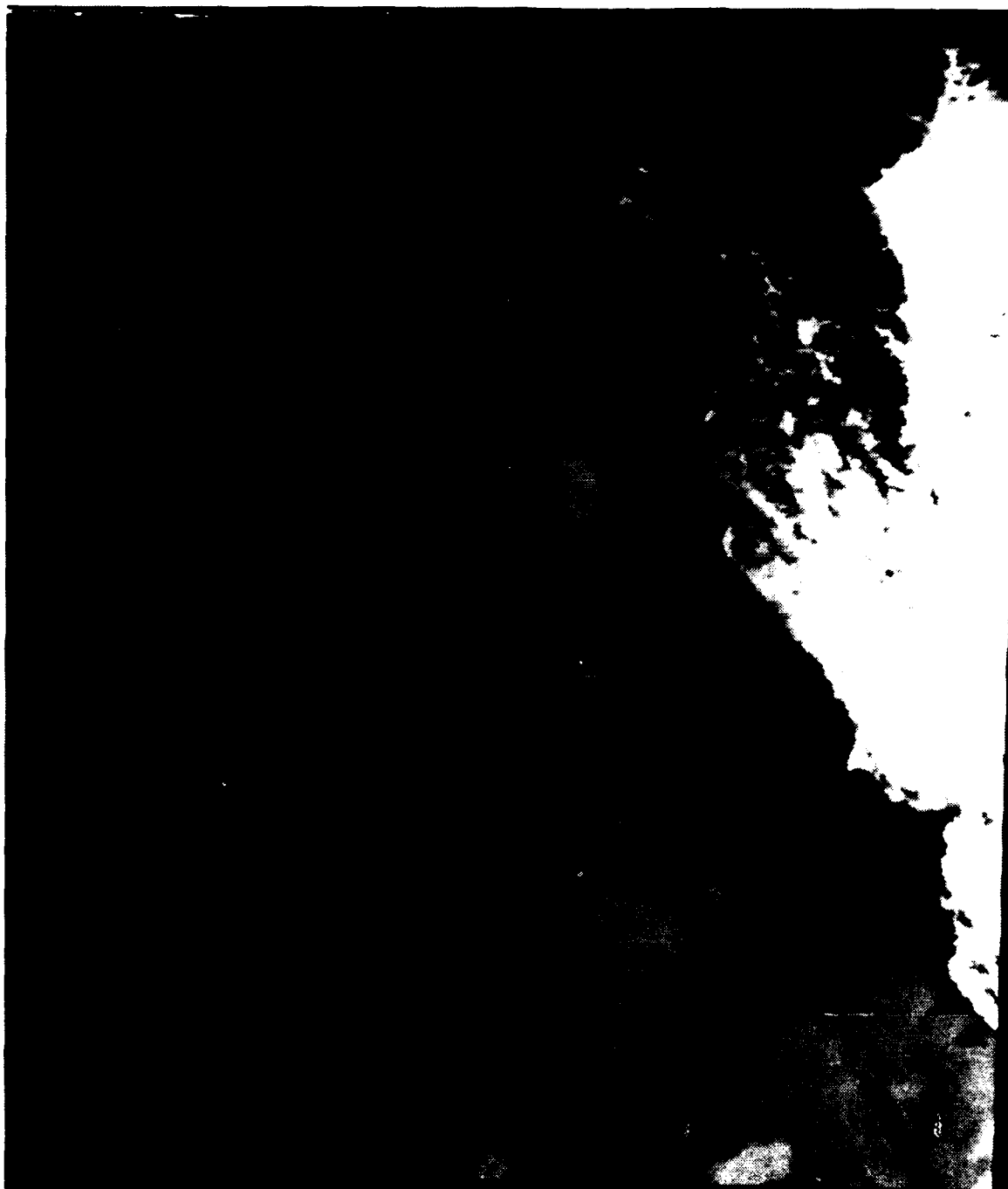


Figure E.7 AVHRR IR image from NOAA-9, channel 4, of OPTOMA domain on Juliar Day 86323 at 21:59 GMT.



Figure E.8 AVHRR IR image from NOAA-9, channel 4, of OPTOMA domain on Julian Day 86325 at 11:57 GMT. Land is masked white.

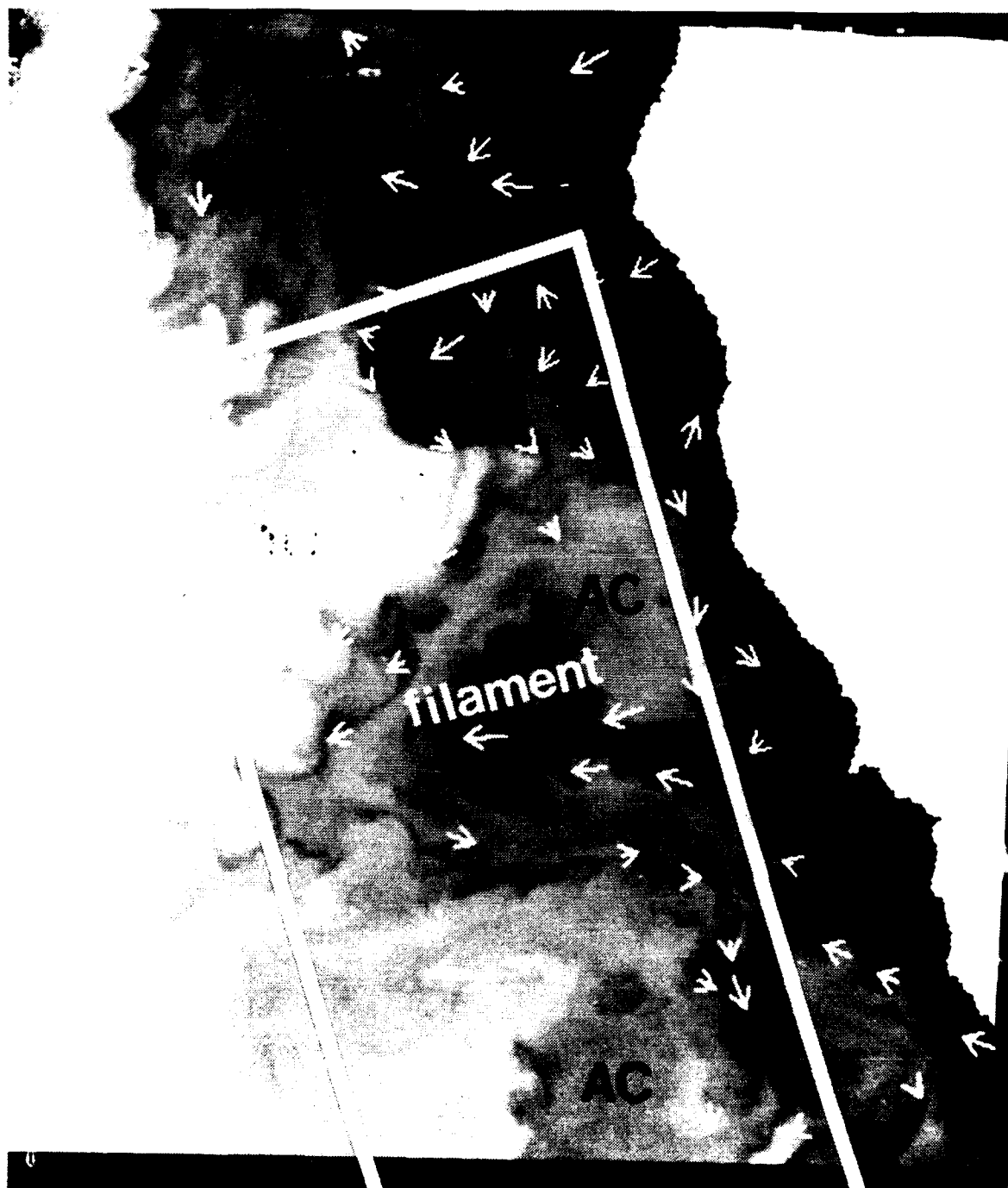


Figure E.9 Surface velocity vectors superimposed on channel 4 IR image from day 86315 (12:03 GMT). Vectors were calculated from day 86314 (16:23 GMT).  $\Delta t$  is ca. 20 hours. 10 cm/s scale in upper left corner. Land is masked white.

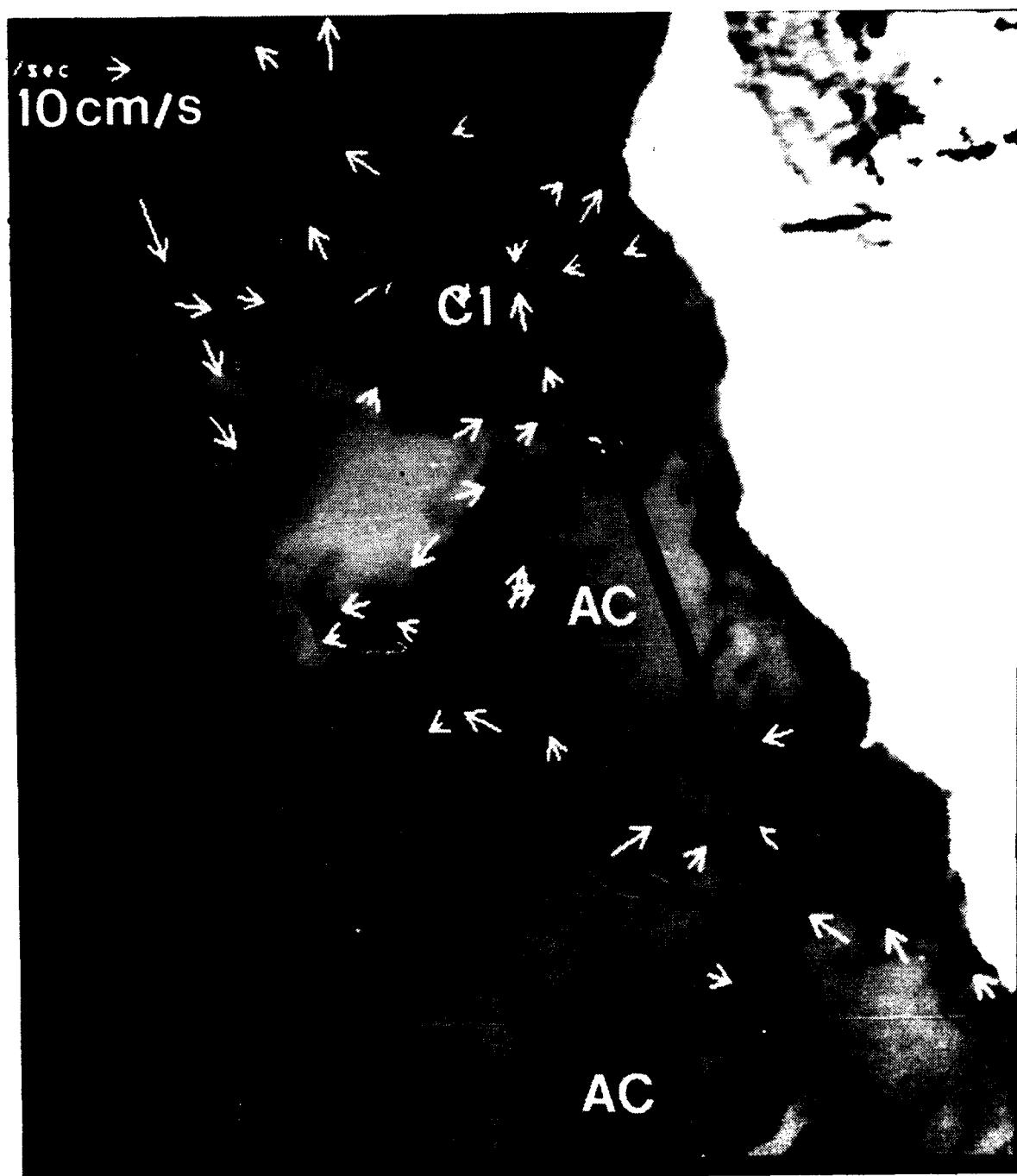


Figure E.10 Surface velocity vectors superimposed on channel 4 IR image from day 86315 (21:45 GMT). Vectors were calculated from day 86314 (16:23 GMT).  $\Delta t$  is ca. 29 hours. 10 cm/s scale in upper right corner.



Figure E.11 Surface velocity vectors superimposed on channel 4 IR image from day 86315 (12:03 GMT). Vectors were calculated from day 86314 (21:55 GMT).  $\Delta t$  is ca. 14 hours. 10 cm/s scale in upper left corner. Land is masked white.

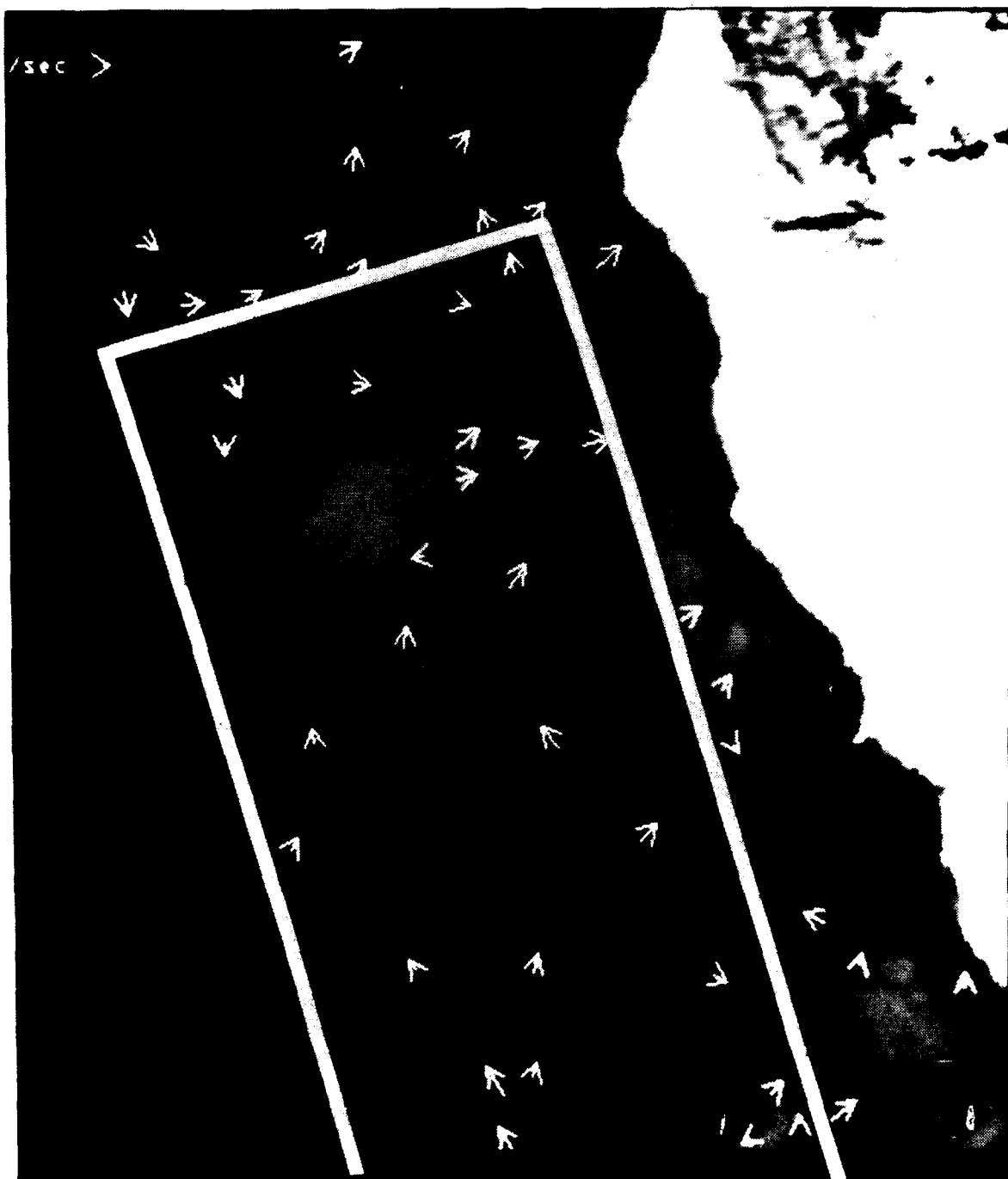


Figure E.12 Surface velocity vectors superimposed on channel 4 IR image from day 86315 (21:45 GMT). Vectors were calculated from day 86315 (12:03 GMT).  $\Delta t$  is ca. 10 hours. 10 cm/s scale in upper left corner.

## APPENDIX F: INVERSIONS

There were temperature inversions in about 10% of the OPTOMA 23 AXBT measurements. Some traces had multiple inversions. Three parameters describe the inversions: the intensity ( $\Delta T$  between the maximum temperature and the first above lying minimum), depth, and width. The intensities of the OPTOMA 23 inversions ranged from  $0.2$  to  $1.0^\circ \text{C}$ , the depths were typically between  $50$  and  $200 \text{ m}$ , and the widths averaged ca.  $15 \text{ m}$  (Table 19). Inversions capable of trapping low-frequency (ca.  $150 \text{ Hz}$ ) acoustic signals (i.e., those with a  $\Delta T$  greater than  $0.2^\circ \text{C}$  and a  $\Delta Z$  greater than  $5 \text{ m}$ ) were screened and plotted (Figure F.1).

Inversions in the CCS are common; 47% of the BT profiles near  $30^\circ \text{N}$  and  $125^\circ \text{W}$  over a 15-day period had inversions of  $0.5^\circ \text{C}$  or higher. The most common depth and width was  $100 \text{ m}$  and  $15 \text{ m}$ , respectively (Roden, 1964). These inversions were not associated with static instabilities (the temperature inversions were compensated by salinity inversions of the opposite sign). These were similar in size, strength, and location in the water column to inversions observed in the eastern Subtropical Front between  $30$  and  $35^\circ \text{N}$  (Roden, 1974).

The inversions from the first two flights on 9 and 10 November (OPTOMA23 P1 and P2) were clustered around the periphery of the two cool filaments. The same was true a week later on 16 November (OPTOMA23 P3) with the addition of an inversion in the center of the domain. Many more inversions were present both near the cool filaments and throughout the rest of the domain on 17 and 19 November (OPTOMA23 P4 and P5).

The location of most OPTOMA 23 inversions did not appear to be random and may have been areas of cool water subsidence, along the edges of the cool filament, or of mesoscale recirculation (Flament et al., 1985). Large changes in temperature and salinity associated with a cool filament, which were highly variable in space and time, were observed off Point Arena in July 1986 (Rienecker and Mooers, 1989). The observed depths of the OPTOMA 23 inversions were between the maximum depth of the cool filament, ca. 50 m, and the depth of influence of the jet, ca. 200 m.

Inversions in the subtropical latitudes were caused by differential advection of water of different origin. In regions of jets, the inversions occurred within the layer of strong velocity shear and may have been caused by turbulence (Roden, 1974). Differentiation, with respect to depth, of the equation for the conservation of temperature,  $T$ , gives insight into the mesoscale factors which give rise to inversions (Roden, 1964):

$$\delta/\delta t (\delta T/\delta z) = -\delta V_H/\delta z \nabla_H T + \delta \mu_H/\delta z \nabla_H^2 T \quad (\text{equation F.1}),$$

(1)                      (2)                      (3)

where, term (1) is the temporal rate of change of the temperature gradient with depth, term (2) is due to velocity shear and the temperature gradient, and term (3) is due to a depth-variable diffusion,



$\mu$ , and the Laplacian of the temperature distribution (it is assumed that  $\nabla_H \delta T / \delta z$  and  $\nabla_H^2 \delta T / \delta z$  are zero).

Term (2) will contribute to an inversion (i.e., term (1) less than zero) if the current shear is negative and a southward current flows from cold to warm water (as in the CCS). Term (3) will contribute to an inversion if the diffusion term increases with depth and there are high temperatures in the interior (as observed in anticyclonic features).

TABLE 19. OPTOMA 23 INVERSIONS (STRENGTHS AND WIDTHS GREATER OR EQUAL TO 0.2° C AND 5 M RESPECTIVELY)

JULIAN DATE	DAY NOV	TIME GMT	LAT (N)	LONG (W)	AXIS Depth	WIDTH (M)	STRENGTH (C)
86313	09	2107	39.3	125.3	72	8	0.2
86313	09	2318	38.5	125.2	63	23	0.3
86313	09	2329	38.4	125.3	82	6	0.2
86314	10	2108	35.6	123.2	111	35	1.0
86314	10	2140	35.5	125.2	61	11	0.2
86314	10	2330	36.6	124.3	76	10	0.6
86314	10	2341	36.5	123.5	100	10	0.2
86314	10	2355	36.1	123.1	70	12	0.3
86315	11	0003	36.0	124.5	64	18	0.5
86320	16	1913	39.2	126.1	80	10	0.3
86320	16	2015	36.6	123.3	203	7	0.2
86320	16	2040	35.5	123.5	203	6	0.2
86320	16	2237	39.2	124.6	135	21	0.3
86321	17	1935	37.5	124.1	225	17	0.2
86321	17	2231	39.2	126.1	94	16	0.3
86321	17	2336	38.4	126.1	60	17	0.5
86323	19	2208	36.2	124.2	86	6	0.2
86323	19	2255	36.2	123.4	84	14	0.2
86323	19	2349	35.5	124.2	191	9	0.2
86324	20	0039	37.1	124.5	88	7	0.2
86324	20	0102	36.1	125.3	83	8	0.2
86324	20	0208	37.3	123.2	170	40	0.5
86324	20	0306	35.3	125.3	42	13	0.3

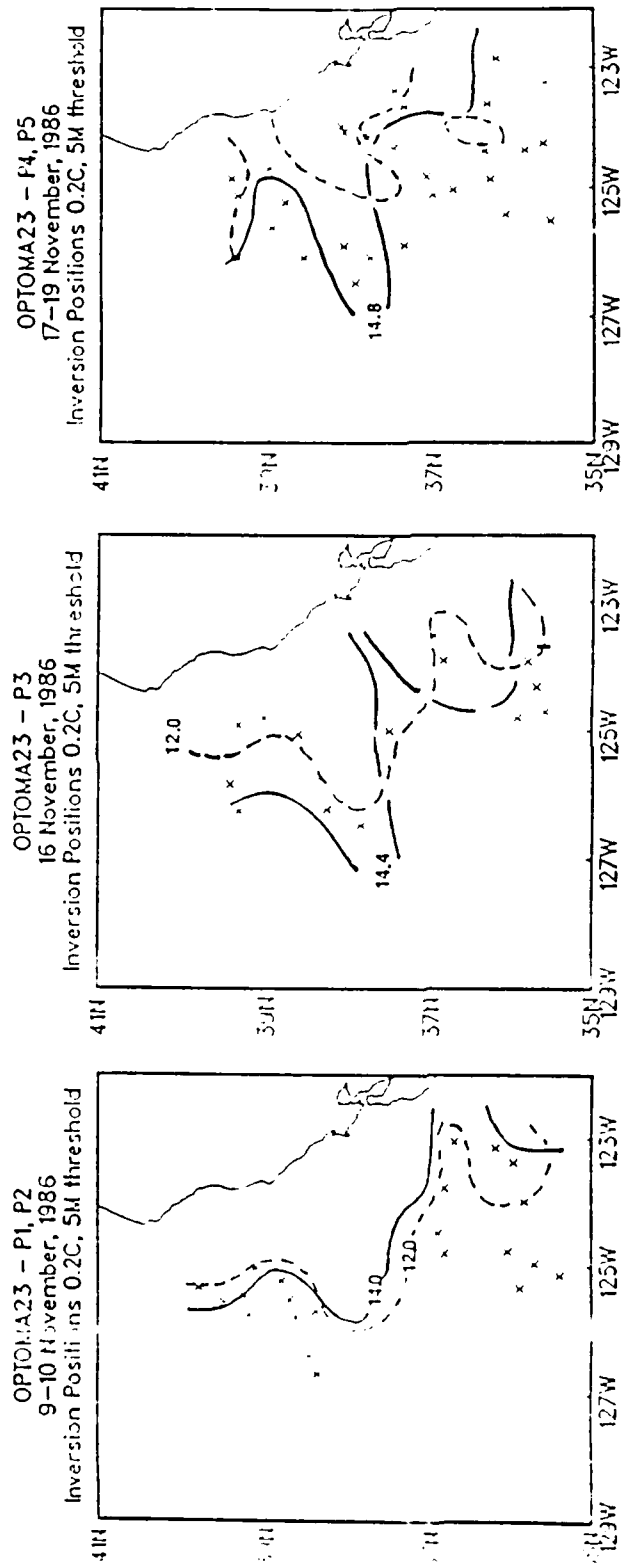


Figure F.1 Inversions (marked by X). OPTOMA 23P1 and P2 (left); 23P4 (center); 23P5 and P6 (right). Isotherms from SST OA (solid) T50 (dashed) outline the cool filaments.

# APPENDIX G. QG MODEL INPUTS AND DYNAMIC TOPOGRAPHY DATA SUBSAMPLING

## TABLE 20. EXAMPLE OF QG MODEL INPUTS

```

$ RUN QMODL1
1      TITLE(20A4)
GDEM CLIMATOLOGY
1
INPUT FIELD 3 LEVELS 50, 150, 400 M DH
1
FULL FIELD, WINDS, AND BOTTOM TOPOGRAPHY
2      ALPHA, BETA, AND KAPPA (BOTTOM FRICTION) 3F10.0
1.998  0.901  0.00
3      NUMBER OF LATERAL AND VERTICAL INTERVALS 3I5
      11      25      6
4      DEPTH INTERVALS
0.6667 0.6667 2.6667 6.22  8.22  8.22
5      STRATIFICATION SCALES (GAMMA AND SIGMA)
6.439  1.87  1.38  2.72  13.66  50.58  193.60  1030.30
6      FILTER (ORDER, FREQUENCY, NUMBER OF TIMES PER TIME STEP)
      4      1      1
7      PRAM
0.0      0.0      0.0      0.0      0.0      0.0865      0.0      0.0
0.0298  50000.  4000.  150.  0.0      0.0      0.0      1.0
8      DT, TSTART, TMAX, YBASIN
0.0036042  0.0  0.90
9      IFDIFF, IFPERT, IFRST, IFTOP, IFBOT, IFTVV, IFTREL, IFTWRT
      1      0      0      0      0      0      0      0
11     DIAGNOSTIC PRINTING
      0.865
12     PRINT ARRAYS
      1 .865
1 1 2 3
13     ARRAY PLOTS
      1 .0865
6 1 2 3 4 5 6
14     RDT
181.
15     ROTATION ANGLE
      38.
16     IFDH; IFEXT
      1      1
-9 END SPECS

```

TABLE 20. (Continued)

Explanation:

- (1) CARD 1 header,
- (2) CARD 2 advective and  $\beta$  scales, bottom friction,
- (3) CARD 3 total number of lateral gridpoints and vertical levels,
- (4) CARD 4 depth intervals (normalized by  $h_t$ , 150 m),
- (5) CARD 5 stratification scales,  $\Gamma^2$  and  $\sigma$ ,
- (6) CARD 6 Shapiro filter, the order, the number of repetitions of the filter each time it is called, and the interval in time steps between activations,
- (7) CARD 7 16 parameters:
  - PRAM(5), number of data sets to skip into the boundary data,
  - PRAM(6), time interval between successive boundary data sets,
  - PRAM(9), the Rossby Number ( $V/fd$ ),
  - PRAM(10), horizontal length scale,  $d$ ,
  - PRAM(11), average depth,  $L$ ,
  - PRAM(12), vertical length scale,  $H_t$ ,
  - PRAM(16), persisted of interpolated boundary conditions,
- (8) CARD 8 normalized time interval, beginning and ending times, basin scale,
- (9) CARD 9 8 switches:
  - finite differencing or collocation in depth,
  - calculate perturbation fields,
  - restart,
  - use top density information,
  - use bottom density information,
  - use top vertical velocity,
  - use bottom topography,
  - write unformatted output,
- (10) CARD 11 diagnostic printing,
- (11) CARD 12 number of printing cycles and frequency, number of levels to be printed, and a list, of the levels,
- (12) CARD 13 plotting (similar to CARD 12),
- (13) CARD 14 restart time,
- (14) CARD 15 angle of domain rotation.

TABLE 21. SUBSAMPLED OA DH FIELDS (FOR QG MODEL INPUT)<sup>1</sup> COMPARISONS

Day 86313 Full field:

	<u>MEAN</u> <sup>2</sup>	<u>STD DEV</u> <sup>2</sup>	<u>CORR</u>	<u>RMSE</u> <sup>2</sup>
Surface	0.76	.04	N/A	N/A
50 m	0.60	.03		
150 m	0.40	.02		
400 m	0.06	.00		

Day 86313 One-half "alternate" subsampled:

	<u>MEAN</u>	<u>STD DEV</u>	<u>CORR</u>	<u>RMSE</u>
Surface	0.74	.05	0.96	0.01
50 m	0.61	.03	0.97	0.01
150 m	0.39	.02	0.96	0.01
400 m	0.06	.00	0.95	0.01

Day 86313 One-quarter "alternate" subsampled:

	<u>MEAN</u>	<u>STD DEV</u>	<u>CORR</u>	<u>RMSE</u>
Surface	0.75	.03	0.73	0.03
50 m	0.60	.03	0.80	0.02
150 m	0.37	.03	0.89	0.02
400 m	0.06	.01	0.83	0.00

Day 86313 One-eighth "alternate" subsampled:

	<u>MEAN</u>	<u>STD DEV</u>	<u>CORR</u>	<u>RMSE</u>
Surface	0.76	.03	0.50	0.04
50 m	0.59	.02	0.70	0.03
150 m	0.41	.02	0.77	0.01
400 m	0.06	.00	0.53	0.00

Notes:

STD DEV - standard deviation;

CORR - correlation;

RMSE - Root Mean Square;

1 - Comparisons of subsampled fields are made with corresponding full field

2 - Units are dyn m.

TABLE 21. (CONTINUED)

## Day 86320 Full field:

	<u>MEAN</u> <sup>2</sup>	<u>STD DEV</u> <sup>2</sup>	<u>CORR</u>	<u>RMS</u> <sup>2</sup>
Surface	0.75	.03	N/A	N/A
50 m	0.60	.03		
150 m	0.40	.02		
400 m	0.06	.00		

## Day 86320 One-half "alternate" subsampled:

	<u>MEAN</u>	<u>STD DEV</u>	<u>CORR</u>	<u>RMSE</u>
Surface	0.76	.04	0.89	0.02
50 m	0.61	.04	0.91	0.02
150 m	0.38	.03	0.95	0.01
400 m	0.06	.01	0.94	0.00

## Day 86320 One-quarter "alternate" subsampled:

	<u>MEAN</u>	<u>STD DEV</u>	<u>CORR</u>	<u>RMSE</u>
Surface	0.74	.02	0.56	0.02
50 m	0.59	.02	0.54	0.02
150 m	0.41	.02	0.72	0.02
400 m	0.06	.00	0.75	0.00

## Day 86320 One-eighth "alternate" subsampled:

	<u>MEAN</u>	<u>STD DEV</u>	<u>CORR</u>	<u>RMSE</u>
Surface	0.77	.03	0.72	0.02
50 m	0.62	.02	0.76	0.02
150 m	0.39	.02	0.81	0.01
400 m	0.06	.00	0.72	0.00

## Notes:

STD DEV - standard deviation;

CORR - correlation;

RMSE - Root Mean Square;

1 - Comparisons of subsampled fields are made with corresponding full field

2 - Units are dyn m.

TABLE 21. (CONTINUED)

## Day 86323 Full field:

	<u>MEAN</u> <sup>2</sup>	<u>STD DEV</u> <sup>2</sup>	<u>CORR</u>	<u>RMS</u> <sup>2</sup>
Surface	0.76	.03	N/A	N/A
50 m	0.61	.03		
150 m	0.40	.02		
400 m	0.06	.00		

## Day 86323 One-half "alternate" subsampled:

	<u>MEAN</u>	<u>STD DEV</u>	<u>CORR</u>	<u>RMSE</u>
Surface	0.75	.02	0.88	0.02
50 m	0.58	.02	0.89	0.02
150 m	0.41	.01	0.93	0.01
400 m	0.06	.00	0.91	0.00

## Day 86323 One-quarter "alternate" subsampled:

	<u>MEAN</u>	<u>STD DEV</u>	<u>CORR</u>	<u>RMSE</u>
Surface	0.76	.03	0.63	0.03
50 m	0.58	.03	0.67	0.03
150 m	0.41	.02	0.71	0.02
400 m	0.06	.00	0.73	0.00

## Day 86323 One-eighth "alternate" subsampled:

	<u>MEAN</u>	<u>STD DEV</u>	<u>CORR</u>	<u>RMSE</u>
Surface	0.77	.05	0.57	0.05
50 m	0.60	.05	0.66	0.04
150 m	0.42	.04	0.78	0.03
400 m	0.05	.01	0.77	0.01

## Notes:

STD DEV - standard deviation;

CORR - correlation;

RMSE - Root Mean Square;

1 - Comparisons of subsampled fields are made with corresponding full field

2 - Units are dyn m.



TABLE 21. (CONTINUED)

## Day 86313 Full field:

	<u>MEAN</u> <sup>2</sup>	<u>STD DEV</u> <sup>2</sup>	<u>CORR</u>	<u>RMSE</u> <sup>2</sup>
Surface	0.76	.04	N/A	N/A
50 m	0.60	.03		
150 m	0.40	.02		
400 m	0.06	.00		

## Day 86313 One-half randomly subsampled:

	<u>MEAN</u>	<u>STD DEV</u>	<u>CORR</u>	<u>RMSE</u>
Surface	0.76	.04	0.96	0.01
50 m	0.60	.03	0.96	0.01
150 m	0.40	.02	0.96	0.01
400 m	0.06	.00	0.95	0.01

## Day 86313 One-quarter randomly subsampled:

	<u>MEAN</u>	<u>STD DEV</u>	<u>CORR</u>	<u>RMSE</u>
Surface	0.75	.03	0.72	0.03
50 m	0.59	.03	0.80	0.02
150 m	0.39	.03	0.89	0.02
400 m	0.06	.01	0.83	0.00

## Day 86313 One-eighth randomly subsampled:

	<u>MEAN</u>	<u>STD DEV</u>	<u>CORR</u>	<u>RMSE</u>
Surface	0.75	.02	0.50	0.04
50 m	0.59	.02	0.69	0.03
150 m	0.40	.02	0.78	0.01
400 m	0.06	.00	0.55	0.00

## Notes:

STD DEV - standard deviation;

CORR - correlation;

RMSE - Root Mean Square;

1 - Comparisons of subsampled fields are made with corresponding full field

2 - Units are dyn m.

TABLE 21. (CONTINUED)

## Day 86320 Full field:

	<u>MEAN</u> <sup>2</sup>	<u>STD DEV</u> <sup>2</sup>	<u>CORR</u>	<u>RMS</u> <sup>2</sup>
Surface	0.75	.03	N/A	N/A
50 m	0.60	.03		
150 m	0.40	.02		
400 m	0.06	.00		

## Day 86320 One-half randomly subsampled:

	<u>MEAN</u>	<u>STD DEV</u>	<u>CORR</u>	<u>RMSE</u>
Surface	0.75	.04	0.89	0.02
50 m	0.60	.04	0.92	0.02
150 m	0.39	.03	0.96	0.01
400 m	0.06	.01	0.94	0.00

## Day 86320 One-quarter randomly subsampled:

	<u>MEAN</u>	<u>STD DEV</u>	<u>CORR</u>	<u>RMSE</u>
Surface	0.75	.02	0.58	0.02
50 m	0.60	.02	0.59	0.02
150 m	0.40	.02	0.72	0.02
400 m	0.06	.00	0.75	0.00

## Day 86320 One-eighth randomly subsampled:

	<u>MEAN</u>	<u>STD DEV</u>	<u>CORR</u>	<u>RMSE</u>
Surface	0.76	.02	0.73	0.02
50 m	0.61	.02	0.75	0.02
150 m	0.40	.02	0.83	0.01
400 m	0.06	.00	0.73	0.00

## Notes:

STD DEV - standard deviation;

CORR - correlation;

RMSE - Root Mean Square;

1 - Comparisons of subsampled fields are made with corresponding full field

2 - Units are dyn m.

TABLE 21. (CONTINUED)

## Day 86323 Full field:

	<u>MEAN</u> <sup>2</sup>	<u>STD DEV</u> <sup>2</sup>	<u>CORR</u>	<u>RMS</u> <sup>2</sup>
Surface	0.76	.03	N/A	N/A
50 m	0.61	.03		
150 m	0.40	.02		
400 m	0.06	.00		

## Day 86323 One-half randomly subsampled:

	<u>MEAN</u>	<u>STD DEV</u>	<u>CORR</u>	<u>RMSE</u>
Surface	0.76	.02	0.88	0.02
50 m	0.60	.02	0.91	0.02
150 m	0.40	.01	0.94	0.01
400 m	0.06	.00	0.91	0.00

## Day 86323 One-quarter randomly subsampled:

	<u>MEAN</u>	<u>STD DEV</u>	<u>CORR</u>	<u>RMSE</u>
Surface	0.76	.03	0.64	0.03
50 m	0.60	.03	0.66	0.03
150 m	0.40	.02	0.72	0.02
400 m	0.06	.00	0.73	0.00

## Day 86323 One-eighth randomly subsampled:

	<u>MEAN</u>	<u>STD DEV</u>	<u>CORR</u>	<u>RMSE</u>
Surface	0.77	.05	0.56	0.05
50 m	0.61	.05	0.65	0.04
150 m	0.41	.04	0.78	0.03
400 m	0.06	.01	0.78	0.01

## Notes:

STD DEV - standard deviation;

CORR - correlation;

RMSE - Root Mean Square;

1 - Comparisons of subsampled fields are made with corresponding full field

2 - Units are dyn m.

TABLE 21. (CONTINUED)

## Day 86313 Full field:

	<u>MEAN</u> <sup>2</sup>	<u>STD DEV</u> <sup>2</sup>	<u>CORR</u>	<u>RMSE</u> <sup>2</sup>
Surface	0.76	.04	N/A	N/A
50 m	0.60	.03		
150 m	0.40	.02		
400 m	0.06	.00		

## Day 86313 One-half "smart pick" subsampled:

	<u>MEAN</u>	<u>STD DEV</u>	<u>CORR</u>	<u>RMSE</u>
Surface	0.76	.04	0.97	0.01
50 m	0.60	.03	0.97	0.01
150 m	0.40	.02	0.97	0.01
400 m	0.06	.00	0.96	0.01

## Day 86313 One-quarter "smart pick" subsampled:

	<u>MEAN</u>	<u>STD DEV</u>	<u>CORR</u>	<u>RMSE</u>
Surface	0.77	.03	0.74	0.03
50 m	0.61	.03	0.82	0.02
150 m	0.40	.03	0.90	0.02
400 m	0.06	.01	0.85	0.00

## Day 86313 One-eighth "smart pick" subsampled:

	<u>MEAN</u>	<u>STD DEV</u>	<u>CORR</u>	<u>RMSE</u>
Surface	0.75	.02	0.55	0.04
50 m	0.50	.02	0.70	0.03
150 m	0.40	.02	0.79	0.01
400 m	0.06	.00	0.58	0.00

## Notes:

STD DEV - standard deviation;

CORR - correlation;

RMSE - Root Mean Square;

1 - Comparisons of subsampled fields are made with corresponding full field

2 - Units are dyn m.

TABLE 21. (CONTINUED)

## Day 86320 Full field:

	<u>MEAN</u> <sup>2</sup>	<u>STD DEV</u> <sup>2</sup>	<u>CORR</u>	<u>RMS</u> <sup>2</sup>
Surface	0.75	.03	N/A	N/A
50 m	0.60	.03		
150 m	0.40	.02		
400 m	0.06	.00		

## Day 86320 One-half "smart pick" subsampled:

	<u>MEAN</u>	<u>STD DEV</u>	<u>CORR</u>	<u>RMSE</u>
Surface	0.75	.04	0.91	0.02
50 m	0.60	.04	0.93	0.02
150 m	0.40	.03	0.96	0.01
400 m	0.06	.01	0.94	0.00

## Day 86320 One-quarter "smart pick" subsampled:

	<u>MEAN</u>	<u>STD DEV</u>	<u>CORR</u>	<u>RMSE</u>
Surface	0.75	.02	0.60	0.02
50 m	0.60	.02	0.62	0.02
150 m	0.40	.02	0.74	0.02
400 m	0.06	.00	0.77	0.00

## Day 86320 One-eighth "smart pick" subsampled:

	<u>MEAN</u>	<u>STD DEV</u>	<u>CORR</u>	<u>RMSE</u>
Surface	0.76	.02	0.78	0.02
50 m	0.60	.02	0.77	0.02
150 m	0.40	.02	0.82	0.01
400 m	0.06	.00	0.80	0.00

## Notes:

STD DEV - standard deviation;

CORR - correlation;

RMSE - Root Mean Square;

1 - Comparisons of subsampled fields are made with corresponding full field

2 - Units are dyn m.

TABLE 21. (CONTINUED)

## Day 86323 Full field:

	<u>MEAN</u> <sup>2</sup>	<u>STD DEV</u> <sup>2</sup>	<u>CORR</u>	<u>RMS</u> <sup>2</sup>
Surface	0.76	.03	N/A	N/A
50 m	0.61	.03		
150 m	0.40	.02		
400 m	0.06	.00		

## Day 86323 One-half "smart pick" subsampled:

	<u>MEAN</u>	<u>STD DEV</u>	<u>CORR</u>	<u>RMSE</u>
Surface	0.76	.02	0.90	0.02
50 m	0.60	.02	0.92	0.02
150 m	0.40	.01	0.95	0.01
400 m	0.06	.00	0.92	0.00

## Day 86323 One-quarter "smart pick" subsampled:

	<u>MEAN</u>	<u>STD DEV</u>	<u>CORR</u>	<u>RMSE</u>
Surface	0.76	.03	0.67	0.03
50 m	0.60	.03	0.68	0.03
150 m	0.40	.02	0.75	0.02
400 m	0.06	.00	0.75	0.00

## Day 86323 One-eighth "smart pick" subsampled:

	<u>MEAN</u>	<u>STD DEV</u>	<u>CORR</u>	<u>RMSE</u>
Surface	0.77	.05	0.62	0.05
50 m	0.61	.05	0.68	0.04
150 m	0.41	.04	0.80	0.03
400 m	0.06	.01	0.78	0.01

## Notes:

STD DEV - standard deviation;

CORR - correlation;

RMSE - Root Mean Square;

1 - Comparisons of subsampled fields are made with corresponding full field

2 - Units are dyn m.

#### APPENDIX H: COMNAVOCEANCOM INDEPENDENT MODEL REVIEW PANEL (CIMREP)

The Harvard Open Ocean Model (HOOM), with feature model initialization, is currently in use at the Naval Oceanographic Office forecasting the 100 m position of the north wall of the Gulf Stream and its rings. The system, known as the Navy Operational Gulf Stream Model (NOGUSF) 1.0 or GULFCAST, provides a forecast once a week in a rectangular domain situated between ca. 30 and 46 N and 50 and 72 W.

NOGUSF 1.0 was delivered to the Naval Oceanographic Office in January 1989 for operational testing (i.e., an evaluation with operational resources) after a technical evaluation (i.e., a scientific, research quality evaluation) by the Navy Oceanographic and Atmospheric Research Laboratory (NOARL). During operational testing, seven-day forecasts had the same skill as persistence (Martinek, 1989).

The COMNAVOCEANCOM Independent Model Review Panel (CIMREP) was formed by the Commander, Naval Oceanography Command in April 1989 to evaluate NOGUSF 1.0 operational testing criteria, implementation procedures, model tendencies, strengths and weaknesses, and to recommend near and long-term improvements to upgrade model capabilities (Koehr, 1989). The panel was chaired by Dr William Schmitz (Woods Hole Oceanographic Institute), with the other members being: Dr Dana Thompson (NOARL), Dr Denny Kirwan (Old Dominion University), Dr John Hovermale (NOARL), and CDR Edward Johnson, USN (Institute for Naval Oceanography).

CIMREP met three times (20 April, 11 July, and 11 December 1989) and found that meander growth was overly rapid, phase and amplitude problems existed on the eastern boundary, and there were difficulties

with stream-ring interactions. The panel recommended changes in the feature model parameters, an increase in model resolution (vertical and horizontal), a shift in the domain, and an improvement in the amount and quality of the input data sets (Schmitz, 1989a, 1989b, and 1990). Additionally, CIMREP was influential in changing research priorities and in the drafting of a Memorandum of Understanding between COMNAVOCEANCOM and NOARL covering future model transition.

More details on CIMREP can be obtained through the Commander, Naval Oceanography Command staff, Mr Ray Partridge (601-688-4322).



# LIST OF REFERENCES

- Adamec, D., 1988: "Numerical Simulations of the Effects of Seamounts and Vertical Resolution on Strong Ocean Flows", J Phys Oceanogr, 18:258-269.
- Adamec, D., 1989: "Predictability of Quasi-geostrophic Ocean Flow; Sensitivity to Varying Model Vertical Resolution", J Phys Oceanogr, 19:1753-1764.
- Atmospheric Forcing of Ocean Circulation, 1988: Report of a Workshop at Tulane University, INO Report 89-1, 389 pages.
- Bakun, A., 1973: Coastal Upwelling Indices, West Coast of North America, NOAA Tech Report NMFS SSRF-671, 103 pages.
- Barrick, D.E., and C.T. Swift, 1980: "The SEASAT Microwave Instruments in Historical Perspective", IEEE J Ocean Eng, OE-5(2):74-79.
- Batteen, M.L., C.N.K. Mooers, and A.A. Bird, 1988a: "Effects of Sampling Strategies in Space and Time on Representation of Mesoscale Variability", (Submitted to J Geophys Res).
- Batteen, M.L., R.L. Haney, T.A. Tielking, and P.G. Renaud, 1988b: "A Numerical Study of Wind Forcing of Eddies and Jets in the California Current System", (Submitted to J Mar Res).
- Bernstein, R.L., 1982: "Sea Surface Temperature Estimation Using the NOAA-6 Advanced Very High Resolution Radiometer", J Geophys Res, 87:9455-9465.
- , L. Breaker, and R. Whritner, 1977: "California Current Eddy Formation: Ship, Air, and Satellite Results", Science, 195:353-359.
- Blumberg, A.F., and G.L. Mellor, 1987: "A Description of a Three Dimensional Coastal Circulation Model", Three-Dimensional Coastal Circulation Models, N. Heaps, editor, American Geophysical Union, 4:1-16.
- Boyd, J.D., 1986: Improved Depth and Temperature Conversion Equations for Sippican AXBT's, Naval Ocean Research and Development Activity Report 156, 10 pages.
- Breaker, L.C., 1986: A Note on Processing Sea Level Data, NPS Report 68-86-005, 15 pages.

- , 1983: "The Space-Time Scales of Variability in Oceanic Thermal Structure off the Central California Coast", Naval Postgraduate School Dissertation, 483 pages.
- , and Bratkovich, A., 1987: "Oceanographic Conditions along the California Coast Surrounding the Period of the Puerto Rico Oil Tanker Spill", (submitted to J Geophys Res)
- , and C.N.K. Mooers, 1986: "Oceanic Variability off the Central California Coast", Prog Oceanogr, 17:61-135.
- Bretherton, F.P., R.E. Davis, and C.B. Fandry, 1976: "A Technique for Objective Analysis and Design of Oceanographic Experiments applied to MODE-73", Deep-Sea Res, 23:559-582.
- Broenkow, W.W., 1982: "A Comparison Between Geostrophic and Current Meter Observations in a California Current Eddy", Deep-Sea Res, 29:1303-1311.
- Brown, O.B. and R.E. Cheney, 1983: "Advances in Satellite Oceanography", Rev Geophys, 21(5):1216-1230.
- Calman, J., 1987: "Introduction to Sea Surface Topography from Satellite Altimetry", John Hopkins APL Technical Digest, 8(2):206-211.
- Carter, E.F. and A.R. Robinson, 1981: Time Series of Synoptic Maps of the Western North Atlantic: A Space-Time Series Objective Analysis of Polymode XBT's, Div of Appl Sci, Harvard University, Report 15, 70 pages.
- Charney, J.G., R. Fjortoft, and J. von Neumann, 1950: "Numerical Integration of the Barotropic Vorticity Equation", Tellus, 2:237-254.
- Chelton, D.B., R.L. Bernstein, A. Bratkovich, and P.M. Kosro, 1987: "The Central California Coastal Circulation Study", EOS, 68(1):1-12.
- , P.A. Bernal, and J.A. McGowan, 1982: "Large Scale Interannual Physical and Biological Interaction in the California Current", J Mar Res, 40(4):1095-1125.
- Chen, C.T., and F.J. Millero, 1977: "Speed of Sound in Seawater at High Pressures", J Acoust Soc Amer, 62(5):1129-1135.
- Cheney, R.E., 1989: "Operational Monitoring of the Tropical Pacific", 11th GEOSAT Users Meeting, John Hopkins University, Applied Physics Laboratory, 23 March 1989.

- Ciandro, M.L., P.A. Wittman, A.A. Bird, and C.N.K. Mooers, 1986: Hydrographic Data from the OPTOMA Program; OPTOMA 22, NPS Technical Report, NPS-68-86-012, 48 pages.
- Colton, M.C., and C.N.K. Mooers, 1984: OPTOMA Program Interim Report: the Airborne Ocean Thermal Structure Mapping Project, NPS Technical Report, NPS-68-85-008, Monterey, California, 98 pages.
- Csanady, G.T., 1978: "The Arrested Topographic Wave", J Phys Oceanogr, 8:47-62.
- CTZ Group, 1988: "The Coastal Transition Zone Program", EOS, 69:698-707.
- Cummins, P.F., and L.A. Myzak, 1988: "A Quasi-Geostrophic Circulation Model of the Northeast Pacific. Part I: A Preliminary Numerical Experiment", J Phys Oceanogr, 18:1261-1286.
- Cummins, P.F., 1989: "A Quasi-Geostrophic Circulation Model of the Northeast Pacific. Part II: Effects of Topography and Seasonal Forcing", J Phys Oceanogr, 19:1649-1668.
- Data Base Description for Master Generalized Digital Environmental Model (GDEM): 1988, Naval Oceanographic Office OAML-DBD-20A, 15 pages.
- Davis, J.C., 1973: Statistics and Data Analysis in Geology, John Wiley and Sons, New York, 550 pages.
- Davis, T.M., K.A. Countryman, and M.J. Carron, 1986: "Tailored Acoustic Products Utilizing the NAVOCEANO GDEM (A Generalized Digital Environmental Model)", 36th Naval Symposium on Underwater Acoustics, San Diego, CA., T-15 to T-39.
- De May, P., and A.R. Robinson, 1987: "Assimilation of Altimeter Eddy Fields in a Limited-Area Quasi-Geostrophic Model", J Phys Oceanogr, 17:2280-2293.
- Deschamps, P.Y., and T. Phulpin, 1980: "Atmospheric Correction of Infrared Measurements of Sea Surface Temperature Using Channels 3.7, 11, and 12", Boundary-Layer Met, 18:131-143.
- , and R. Frouin, 1984: "Large Diurnal Heating of the Sea Surface observed by the HCMR experiment", J Phys Oceanogr, 14:177-184.
- Dorman, C.E. and J.F.T. Saur, 1978: "Temperature Anomalies between San Francisco and Honolulu, 1966-1974: Gridded by Objective Analysis", J Phys Oceanogr, 8:247-257.

- Douglas, B.C., and P.D. Gaborski, 1979: "The Sea State Correction for GEOS-3 and SEASAT Satellite Altimeter Data", Proceedings of the Thirteenth International Symposium on Remote Sensing of the Environment, 404-419.
- Emery, W.J., J.C. Thomas, M.J. Collins, W.R. Crawford, and D.L. Mackas, 1986: "An Objective Method of Computing Advective Surface Velocities from Sequential Satellite Images", J Geophys Res, 91:12,865-12,878.
- , W.G. Lee, and L. Magaard, 1984: "Geographic and Seasonal Distributions of Brunt-Vaisala Frequency and Rossby Radii in the North Pacific and North Atlantic", J Phys Oceanogr, 14:294-317.
- , and L.A. Mysak, 1980: "Dynamical Interpretation of Satellite-Sensed Thermal Features off Vancouver Island", J Phys Oceanogr, 10:961-970.
- , and A. O'Brien, 1978: "Inferring Salinity from Temperature or Depth for Dynamic Height Computations in the North Pacific", Atmos-Oceanogr, 16:348-366.
- Enfield, D.B., and J.S. Allen, 1980: "On the Structure and Dynamics of Monthly Mean Sea Level anomalies along the Pacific Coast of North and South America", J Phys Oceanogr, 10:557-578.
- Fiedler, P.C., 1988: "Surface Manifestations of Subsurface Thermal Structure in the California Current", J Geophys Res, 93:4975-4983.
- , G.B. Smith, and R.M. Laurs, 1985: "Fisheries Applications of Satellite Data in the Eastern North Pacific", Mar Fish Rev, 46:1-13.
- Flament, P., P.M. Kosro, and A. Huyer, 1988: "Mesoscale Variability off California as seen by GEOSAT", EOS, 69:1259.
- , L. Armi, and L. Washburn, 1985: "The Evolving Structure of an Upwelling Filament", J Geophys Res, 90:11,765-11,778.
- Flierl, G.R., 1978: "Correcting Expendable Bathythermograph (XBT) Data for Salinity Effects to Compute Dynamic Height in Gulf Stream Rings", Deep-Sea Res, 25:129-134.
- Gasparovic, R.F., 1983: Effects of Spatial Variability on Remotely Sensed Sea Surface Temperature, Applied Physics Laboratory, Johns Hopkins University, Rpt STD-R-822, 118 pages.

- Glenn, S., and A.R. Robinson, 1989: "Nowcasting and Forecasting of Oceanic Dynamic and Acoustic Fields", Computational Acoustics II, D. Lee, A. Cakmak, and R. Vichnevetsky, editors, Elsevier Science Publishing B.V.
- Glenn, S., A.R. Robinson, and M. Spall, 1987: "Recent Results from the Harvard Gulf Stream Forecasting Program", Oceanogr Mon Summary, 11:3.
- Godin, G., 1972, The Analysis of Tides, University of Toronto Press, Toronto, 264 pages.
- Hancock, D.W., 1980: "SEASAT Altimeter Sensor File Algorithms", IEEE J Ocean Eng, 5:93-99.
- Hawkins, J., 1989: "Use of SSMR Moisture fields in the NEPAC Experiment", 11th GEOSAT User's Meeting, Applied Physics Lab, Johns Hopkins University, 22 March 1989.
- Hickey, B. M., 1979: "The California Current System - Hypotheses and Facts", Prog Oceanogr, 8:191-279.
- Hickey, B.M., and N.E. Pola, 1983: "The Seasonal Alongshore Pressure Gradient on the West Coast of the United States", J Phys Oceanogr, 88:7623-7633.
- Holland, W.R., 1978: "The Role of Mesoscale Eddies in the General Circulation of the Ocean - Numerical Experiments Using a Wind-driven QG Model", J Phys Oceanogr, 8:363-392.
- Horton, C.W., 1982: Preliminary Report on Inferring the Path of the Subsurface Front of the Gulf Stream from Surface Infrared Observations, US NAVOCEANO Tech note 9100-9-81, 12 pages.
- Huyer, A., R.L. Smith, and B.M. Hickey, 1984: "Observations of a Warm Core Eddy off Oregon Jan-Mar 1978", Deep-Sea Res, 31:94-117.
- Ikeda, M., J.A. Johannessen, K. Lygre, and S. Sandven, 1989: "A Process Study of Mesoscale Meanders and Eddies in the Norwegian Coastal Current", J Phys Oceanogr, 19:20-35.
- , and Emery, W.J., 1984: "Satellite Observations in the California Current System off Oregon and Northern California", J Phys Oceanogr, 14:1434-1450.
- , W.J. Emery and L.A. Mysak, 1984: "Seasonal Variability in Meanders of the California Current System", J Geophys Res, 89:3487-3505.

- Johnson, J.E., P.A. Wittmann, C.N.K. Mooers, 1988: Hydrographic Data from the OPTOMA Program; OPTOMA 23, NPS Technical Report 68-88-01, 88 pages.
- Kang, Y.Q., and L. Magaard, 1980: "Annual Baroclinic Rossby Waves in the Central North Pacific", J Phys Oceanogr, 10:1159-1167.
- Kelly, Kathryn A., 1985: "Separating Clouds from Ocean in Infrared Images", Remote Sensing Env, 17: 67-83.
- , 1983, Swirls and Plumes or Application of Statistical Methods to Satellite Derived Sea Surface Temperatures, PhD Dissertation Scripps Institution of Oceanography, 293 pages.
- Koblinsky, C.J., J.J. Simpson, and T.D. Dickey, 1984: "An Offshore Eddy in the California Current System; Part 2 Surface Manifestation", Prog Oceanogr, 13:51-61.
- Koehr, J.E., 1989: COMNAVOCEANCOM ltr 3140 Ser 031: Gulfcast Operational Evaluation and Implementation, 11 April 1989.
- Kosro, P.M., A. Huyer, and P. Flament, 1988: "A Comparison Between Sea Surface Dynamic Topography from Altimetry and from Hydrography along the Coast of California", Poster Presentation at 10th GEOSAT Users Meeting, John Hopkins APL, 22-23 March 1988.
- Kuo, Y.H., E.G. Donall, and M.A. Shapiro, 1987: "Feasibility of Short Range Numerical Weather Prediction using Observations from a Network of Profilers", Mon Wea Rev, 115:2402-2427.
- Leese, J.A., C.A. Novak, and B.B. Clark, 1971: "An Automated Technique for Obtaining Cloud Motion from Geosynchronous Satellite Data using Cross Correlation", J App Met, 10:118-132.
- Legeckis, R.V., 1978: "A Survey of Worldwide Sea Surface Temperature Fronts detected by Environmental Satellites", J Geophys Res, 83:4501-4522.
- , 1979: "Satellite Observations of the Influence of Bottom Topography on Seaward Deflection of the Gulf Stream Off Charleston SC", J Phys Oceanogr, 9:483-497.
- , and J.M. Bane, Jr., 1983: "Comparison of TIROS-N Satellite and Aircraft Measurements of Gulf Stream Surface Temperature", J Geophys Res, 88:4611-4616.

- , and A.L. Gordon, 1982: "Satellite Observations of the Brazil and Falkland Currents - 1975 to 1976 and 1978", Deep-Sea Res, 29:375-401.
- Lentz, S., 1987: "A Description of the 1981, 1982 Spring Transition over the NOCAL Shelf", J Geophys Res, 92:1545-1567.
- Lorell, J., 1982: "Ionospheric Correction for SEASAT Altimeter Height Measurement", J Geophys Res, 87:3207-3212.
- Lybanon, M. and R.L. Crout, 1987: "The NORDA GEOSAT Ocean Applications Program", John Hopkins APL Technical Digest, 8:212-218.
- Lynn, R.J., and J.J. Simpson, 1987: "The California Current System: The Seasonal Variability of its Physical Characteristics", J Geophys Res, 92:12947-12966.
- Malanotte-Rizzoli, P, and W.R. Holland, 1985: "Gyre-Scale Acoustic Tomography: Modeling Simulation", J Phys Oceanogr, 15(4):416-438.
- Martinek, C.A., 1989, Commanding Officer ltr 3140 Ser OTTA/0550: Gulf Stream Forecast Operational Test Results, 20 July 1989.
- Mason, J.E., and A. Bakun, 1986: "Upwelling Index Update, U.S. West Coast, 33N-48N Latitude", NOAA Tech Memo NMFS 67, 4 pages.
- Maul, G., and M. Sidran, 1973: "Atmospheric Effects on Ocean Surface Temperature Sensing", J Geophys Res, 78:1911-1916.
- McClain, E.P., 1980: "Passive Radiometry of the Ocean from Space an Overview", Boundary Layer Met, 18:7-24.
- McWilliams, J.C., 1976: "Maps from the Mid-Ocean Dynamics Experiment Part I", J Phys Oceanogr, 6:810-827.
- Miller, R.N., A.R. Robinson and D.B. Haidvogel, 1983: "A Baroclinic Quasigeostrophic Open Ocean Model", J Comp Physics, 50:38-70.
- Minnett, P.J., 1986: "A Numerical Study of the Effects of Anomalous North American Atmospheric Conditions on the IR Measurement of SST from Space", J Geophys Res, 91:8509-8521.
- Mooers, C.N.K. and Robinson, A.R., 1984, "Turbulent Jets and Eddies in the California Current and Inferred Cross Shore Transports", Science, 223:51-53.

- Mysak, L.A., 1983: "Generation of Annual Rossby Waves in the North Pacific", J Phys Oceanogr, 13:1908-1923.
- Narimousa, S. and Maxworthy, T., 1985: "Two Layer Model of Shear Driven Coastal Upwelling in the Presence of Bottom Topography", J Fluid Mech, 159:503-531.
- Njoku, E.G., 1985, Satellite Derived Sea Surface Temperature: Workshop Comparisons", Bull Amer Met Soc, 66:274-281.
- Paulson, C.A. and J.J. Simpson, 1981: "The Temperature Difference Across the Cool Skin of the Ocean", J Geophys Res, 86:11044-11054.
- Palmen, E., and C.W. Newton, 1969: Atmospheric Circulation Systems: Their Structure and Physical Interpretation, Academic Press, New York, 603 pages.
- Peloquin, R., 1988, Long Range Plan Strategic Research and Development Plan for Navy Ocean Modeling and Prediction, 1988, Joint Sponsorship by The Office of the Chief of Naval Research and the Oceanographer of the Navy, 62 pages.
- Phoebus, P.A., 1988: "Improvements to the Data Selection Algorithms in the Optimum Thermal Interpolation System (OTIS)", NORDA Report 239, 18 pages.
- Pittenger, R.F., 1989: First Endorsement (Ser 961/9U5439326) on COMNAVOCEANCOM letter 3140 Ser 5/505 of 22 August 1989: Ocean Model Transition Recommendations, 03 October 1989.
- Rienecker, M.M. and C.N.K. Mooers, 1989: "Mesoscale Eddies, Jets, and Fronts off Point Arena, July 1986", J Geophys Res, 94:12544-12569.
- and C.N.K. Mooers, 1989: "A Summary of the OPTOMA Program's Mesoscale Ocean Prediction Studies in the California Current System", Mesoscale/Synoptic Coherent Structures in Geophysical Turbulence, J.C.J. Nihoul and B.M. Jamart, editors, pp. 519-547.
- , C.N.K. Mooers, and R.L. Smith, 1988: "Mesoscale Variability in Current Meter Measurements in the California Current System off Northern California", J Geophys Res, 93:6711-6734.



- , C.H. Reed, and C.N.K. Mooers, 1987: Mesoscale Variability in the California Current System during 1982 to 1986: Maps of Surface Dynamic Height, Sea Surface Temperature, Temperature at 50M, Mixed Layer Depth, and Depth of the 8C Isotherm from Observations during the OPTOMA Program, INO Technical Report 87-01, 138 pages.
- , C.N.K. Mooers, and A.R. Robinson, 1987: "Dynamical Interpolation and Forecast of the Evolution of Mesoscale Features off Northern California", J Phys Oceanogr, 17:1189-1213.
- and C.N.K. Mooers, 1986: "The 1982-1983 El Nino Signal off Northern California", J Geophys Res, 91:6597-6608.
- , C.N.K. Mooers, D.E. Hagan, and A.R. Robinson, 1985: "A Cool Anomaly off Northern California: An Investigation Using IR Imagery and In-Situ Data", J Geophys Res, 90:4807-4818.
- , C.N.K. Mooers, M.C. Colton, P.A. Wittmann, 1982: Hydrographic Data from the OPTOMA Program; OPTOMA1, NPS Technical Report, NPS68-84-005, 31 pages.
- Robinson, A.R., (ed.), 1983, Eddies in Marine Science, Springer Verlag, New York, 609 pps.
- , M.A. Spall, and N. Pinardi, 1988: "Gulf Stream Simulations and the Dynamics of Ring and Meander Processes", J Phys Oceanogr, 18(12):1811-1853.
- , and L.J. Walstad, 1987: "The Harvard Open Ocean Model: Calibration and Application to Dynamical Process, Forecasting, and Data Assimilation", App Numerical Math, 3:89-131.
- , and L.J. Walstad, 1987: "Altimetric Data Assimilation for Ocean Dynamics and Forecasting", Johns Hopkins APL Technical Digest, Vol 8(2):267-271.
- , M.A. Spall, W.G. Leslie, L.J. Walstad, and D.J. McGillicuddy, 1987: Gulfcasting: Dynamical Forecast Experiments for Gulf Stream Rings and Meanders November 1985 - June 1986, Harvard Open Ocean Model Reports Number 22, 34 pages.
- , J.A. Carton, N. Pinardi, and C.N.K. Mooers, 1986: "Dynamical Forecasting and Dynamical Interpolation - An Experiment in the California Current", J Phys Oceanogr, 16:1561-1579.
- , and W.G. Leslie, 1985: "Estimation and Prediction of Oceanic Eddy Fields", Prog Oceanogr, 14:485-510.

- , and K. Tu, 1981: "A Combined Statistical and Dynamical Approach to Regional Forecast Modeling of Open Ocean Currents", Ocean Prediction Workshop, Monterey, CA, 114-125.
- , and D. Haidvogel, 1980: "Dynamical Forecast Experiment with a Barotropic Open Ocean Model", J Phys Oceanogr, 10(12):1909-1928.
- Robinson, I.S., N.C. Wells, and H. Chamock, 1984: "The Sea Surface Thermal Boundary Layer and its Relevance to the Measurement of Sea Surface Temperature by Airborne and Spaceborne Radiometers", Int J Rem Sens, 5:19-45.
- Roden, G.I., 1984: "Mesoscale Sound Speed Fronts in the Central and Western Pacific in the Emperor Seamounts Region", J Phys Oceanogr, 14:1659-1669.
- Roden, G.I., 1974: "Thermocline Structure, Fronts, and Sea-Air Energy Exchange of the Trade Wind Region East of Hawaii", J Phys Oceanogr, 4:168-182.
- Roden, G.I., 1964: "Shallow Temperature Inversions in the Pacific Ocean", J Geophys Res, 69:2899-2914.
- Rosmond, T., 1989: "Evaluation of Navy Operational Meteorological Models", Summer Colloquium on Mesoscale Ocean Science and Prediction Part A, INO Report 90-1.
- Sailor, R.V., and A.R. LeSchack, 1987: "Preliminary Determination of the GEOSAT Radar Altimeter Noise Spectrum", John Hopkins APL Technical Digest, Vol 8(2):182-183.
- Satellite-Derived Sea Surface Temperature Workshop III, 1984: JPL Pub 85-63.
- Schmitz, W.J., Chairman CIMREP, 1989a: COMNAVOCEANCOM Independent Model Review Panel (CIMREP) Letter: GULFCAST Evaluation and Recommendations, 04 May 1989.
- Schmitz, W.J., Chairman CIMREP, 1989b: COMNAVOCEANCOM Independent Model Review Panel (CIMREP) Letter: GULFCAST Evaluation and Recommendations, 24 July 1989.
- Schmitz, W.J., Chairman CIMREP, 1989: COMNAVOCEANCOM Independent Model Review Panel (CIMREP) Letter: GULFCAST Evaluation and Recommendations, 15 January 1990.

- Shapiro, R., 1971: "The Use of Linear Filtering as a Parameterization of Atmospheric Diffusion", J Atmos Sci, 28:523-531.
- Simpson, J.J., C.J. Koblinsky, J. Pelaez, L.R. Haury, and D. Wisenhahn, 1986: "Temperature-Plant Pigment-Optical Relations in a Recurrent Offshore Eddy Near Point Conception, California", J Geophys Res, 91:12919-12936.
- , T.D. Dickey, and C.J. Koblinsky, 1984: "An Off-Shore California Current Eddy - Part I Interior Dynamics", Prog Oceanogr, 13:5-49.
- Smith, J.A., A.R. Robinson and C.N.K. Mooers, 1985: "Empirical and Dynamical Modes in the California Current System", J Atmos Ocean Tech, 2:491-507.
- Smith, R.L., G. Pittock, J. Fleischbein and R. Sill, 1986: Current Measurements from Moorings off Northern California: September 1984 - July 1985, ONR Data Report NR-083-102, 211 pages.
- Smith, S.D., 1988: "Coefficients for Sea Surface Wind Stress, Heat Flux, and Wind Profiles as a Function of Wind Speed and Temperature", J Geophys Res, 93:15467-15472.
- , 1981, Coefficients for Sea Surface Wind Stress and Heat Exchange, Bedford Institute of Oceanography, BI-R-81-19, 31 pages.
- Stage, S.A. and R.A. Weller, 1980: "The Frontal Air-Sea Interaction Experiment (Fastinex); Part I Background and Scientific Objectives", Bull Amer Met Soc, 66:1511-1520.
- Stramma, L., Cornillon, P. and J.F. Price, 1986: "Satellite Observations of SST Cooling by Hurricanes", J Geophys Res, 91:5031-5036.
- Strong, A.E. and E.P. McClain, 1984: "Improved Ocean Surface Temperature from Space - Comparison with Drifting Buoys", Bull Amer Met Soc, 65:138-142.
- Strub, P.T. and C. James, 1988: "Atmospheric Conditions During the Spring and Fall in the Coastal Ocean off Western United States", J Geophys Res, 93:15561-15584.
- Svejkovsky, J., 1988: "Sea Surface Flow Estimation from Advanced Very High Resolution Radiometer and Coastal Zone Color Scanner Satellite Imagery: A Verification Study", J Geophys Res, 93:6735-6743.
- Sverdrup, H., M. Johnson, and R. Fleming, 1942, The Oceans, Prentice Hall, 1087 pps.

- Tabata, S., 1978: "On the Accuracy of Sea-Air Temperature and Salinities Observed in the Northeast Pacific Ocean", Atmosphere-Oceanogr, 16(3):237-247.
- Tai, C.-K., W.B. White, and S. Pazan, 1989: "GEOSAT Crossover Analysis in the Tropical Pacific 2", J Geophys Res, 94:897-908.
- Tapley, B.D., 1982: "The SEASAT Altimeter Data and its Accuracy Assessment", J Geophys Res, 87:3179-3189.
- Teague, W.J. and P.J. Hogan, 1989: Regional Plots from the GDEM and Levitus Climatologies, NORDA Technical Note 361, 8 pages.
- Urick, R.J., 1982: Sound Propagation In The Sea, Peninsula Publishing Company, Los Altos, Ca., 225 pages.
- Vallis, G.K., B. Cornuelle, and W. Holland, 1987: "Dynamics and Predictability of a Model of the California Current Mesoscale", EOS, 68:1220.
- Van Woert, M., 1982: "The Subtropical Front: Satellite Observations during Fronts 80", J Geophys Res, 87:9523-9536.
- Vastano, A.C., and R.O. Reid, 1985: "Sea Surface Topography Estimation with Satellite Imagery", J Atm Ocean Tech, 2:393-400.
- , and R.L. Bernstein, 1984: "Mesoscale Features along the First Oyashio Intrusion", J Geophys Res, 89(C1):587-596.
- , and S.E. Borders, 1984: "Sea Surface Motion over an Anticyclonic Eddy in the Oyashio Front", Rem Sens of Environ, 16:87-90.
- Walstad, L.J., 1988: "Model Requirements for Ocean Data in support of Operational Forecasts", Pacific Congress in Marine Science and Technology Proceedings 1988, Workshop 2, page 42.
- Welander, P., 1957: "Wind Action on a Shallow Sea: Some Generalizations of Ekman's Theory", Tellus, 9:45-52.
- Werner, F.E., and B.M. Hickey, 1983: "The Role of a Longshore Pressure Gradient in Pacific Northwest Coastal Dynamics", J Phys Oceanogr, 13:395-10.
- White, W.B., and C.K. Tai, 1988: "Time and Space Scales of the Mesoscale Eddy Activity in the California Current Region from the GEOSAT Exact Repeat Mission", EOS, 69(44):1249.

- , and J.T. Saur, 1981: "A Source of Annual Baroclinic Waves in the Eastern Subtropical Pacific", J Phys Oceanogr, 11:1452.
- Wittmann, P.A., M.C. Colton, J.J. Rendine, and C.N.K. Mooers, 1985: Hydrographic Data from the OPTOMA Program; OPTOMA 18, NPS Technical Report, NPS-68-86-001, 48 pages.
- Wickham, J.B., A.A. Bird, and C.N.K. Mooers, 1987: "Mean and Variable Flow over the Central California Continental Margin", Continental Shelf Res, 7:827-849.
- Willmott, C.J., S.G. Ackleson, R.E. Davis, J.J. Feddema, K.M. Klink, D.R. Legates, J. O'Donnell, and C.M. Rowe, 1985: "Statistics for the Evaluation and Comparison of Models", J Geophys Res, 90:8995-9005.
- Wyllie, J.G., 1966: Geostrophic Flow of the California Current at the Surface and 200 m, CalCOFI Atlas 14, 12 pages, 288 charts.
- Wyrтки, K, L. Magaard, and J. Hager, 1976: "Eddy Energy in the Oceans", J Geophys Res, 81:2641-2646.

# INITIAL DISTRIBUTION LIST

	No. Copies
1. Defense Technical Information Center Cameron Station Alexandria, VA 22304-6145	2
2. Library, Code 0142 Naval Postgraduate School Monterey, CA 93943-5002	2
3. Dr C.N.K. Mooers OPAL/SERB UNH Durham, NH 03824-3525	2
4. Commanding Officer Naval Oceanographic Office SSC, MS 39529	1
5. Dr M. Carron Naval Oceanographic Office SSC, MS 39529	1
6. Mr R. Rhodes Naval Oceanographic Office SSC, MS 39529	1
7. Commanding Officer Naval Ocean Research and Development Activity SSC, MS 39529	1
8. Dr R.W. Garwood Oceanography Department Code 68Gd Naval Postgraduate School Monterey, CA 93943	1
9. Dr M.L. Batteen Oceanography Department Code 68Bv Naval Postgraduate School Monterey, CA 93943	1
10. Dr K.L. Davidson Meteorology Department Code 63Ds Naval Postgraduate School Monterey, CA 93943	1

11. Dr J.V. Sanders 1  
Physics Department Code 61Sd  
Naval Postgraduate School  
Monterey, CA 93943
  
12. CDR J.E. Johnson 3  
Institute for Naval Oceanography  
SSC, MS 39529-5005
  
13. Office of Naval Research 1  
800 N. Quincy Street  
Arlington, VA 22217
  
14. Oceanographer of the Navy 1  
Naval Observatory  
34th and Massachusetts Avenue NW  
Washington, D.C. 20390
  
15. Commander, Naval Oceanography Command 1  
SSC, MS 39529
  
16. Director 2  
Institute for Naval Oceanography  
SSC, MS 39529
  
17. Dr Kewal Puri 1  
Mathematics Department  
University of Maine  
326 Neville Hall  
Orono, Maine 04469
  
18. Dr Alan Robinson 1  
Center for Earth and Planetary Physics  
Harvard University  
Pierce Hall  
28 Oxford Street Room 100D  
Cambridge, MA 02138